

https://dspace.org/

A theoretical investigation of the structural, electronic and optical properties of transition metal chalcogenides

Abdulsalam, Mahmud

2015
http://hdl.handle.net/10539/19291

Downloaded from a DSpace repository. https://dspace.org/



A Theoretical Investigation of the Structural, Electronic and Optical Properties of Transition Metal Chalcogenides

by

Mahmud Abdulsalam

Supervisor

Professor Daniel Joubert

A thesis submitted to the Faculty of Science
University of the Witwatersrand,
in fulfilment of the requirements for the degree of
Doctor of Philosophy.
School of Physics,
University of the Witwatersrand,
Johannesburg.

October, 2015

Declaration

I declare that this thesis is my own unaided work. It is being submitted for the award of the Doctor of Philosophy in Physics at the University of Witwatersrand, Johannesburg. It contains the outcome of research under the supervision of Prof. Daniel P. Joubert. No part of this thesis has been or is being submitted for any degree at any other University.



Mahmud Abdulsalam

10:13 Wednesday 28th October, 2015

Abstract

Harvesting renewable energy and the miniaturisation of electronic components are among the major challenges of the 21st century. Transition metal chalcogenides (TMC) have interesting properties that are promising in meeting these challenges. It is therefore important to conduct a systematic theoretical study of the structural, electronic and optical properties of the transition metal chalcogenides as possible components of low dimensional transistors or as solar-energy harvesters. In this work, we present the detailed theoretical investigation of the structural, electronic and optical properties of transition metal chalcogenides M_yX_z, (where M = Hf, Zr, Tc or Re), (X = S, Se and Te), y and z are integers.

The structural properties of TMCs were studied using energy-volume relationship (equation of states (EOS)), equilibrium structural lattice parameters, formation and cohesive energies were extracted from the EOS. Mechanical stability test based on elastic constants and phonon dispersion relation were carried out to determine the strengths of the TMCs against mechanical distortions. The most stable structural configurations were used to investigate electronic properties through partial density of states (PDOS) and band structure analysis. Optical properties (absorption coefficients, refractivity, reflectivity) of some of the TMCs were then computed.

Our computations of the structural, electronic and the optical properties were based on density functional theory (DFT). Projector-Augmented wave (PAW) was used to mimic electron-ion interactions and generalised-gradient approximation was used in the exchange correlation functional. Van der Waal's correction terms proposed by Grimme (DFT-D2), Lundqvist and Langreth (vdW-DF) and Tkatchenko-Scheffler (vdW-TS) were used to account for long range dispersion forces in addition to PBE and its modified version for solids PBEsol. Optical properties were investigated at the many body (GW) and Bethe-Salpeter equation (BSE) levels of approximations.

Our results obtained are discussed within the theoretical frame work and compared with experimental and previous theoretical results where available.

Publications

1. **Electronic and optical Properties of semiconducting MX_3(M= Ti, Zr and Hf; X= S, Se, Te) first principle insight** *In preparation*
2. **Structural, Electronic and Optical Properties of $TcX_2(X{=}S, Se, Te)$ from first principles calculations** *Under review*
3. **Electronic and Optical Properties of monolayer MX_2(M= Zr, Hf; X= S, Se) from first principles calculations** *Under review*
4. **Structural and Electronic Properties of MX_3 (M= Ti, Zr and Hf; X= S, Se, Te) from first principles calculations** Eur. Phys. J. B (2015) 88: 177 http://dx.doi.org/10.1140/epjb/e2015-60005-x.
5. **Structural and electronic properties of iron doped technetium sulphide South Africa Institute of Physics 2014, Page 558-563** http://events.saip.org.za/getFile.py/access?resId=100&materialId=6&confId=34.

Presentations

1. 29th June - 3rd July 2015 Conference South African Institute of physics conference Boardwalk Convention Centre, Port Elizabeth, South Africa **Electronic and Optical Properties of monolayer MX_2(M= Zr, Hf; X= S, Se) from first principles calculations** Oral presentation

2. 19 - 30 Jan. 2015 Workshop 3rd African School on Electronic Structure Methods and Applications (ASESMA)University of the Witwatersrand, Johannesburg South Africa

3. 01- 05 December 2014 Conference/Workshop CHPC National Meeting 2014 Kruger National Park, Mpumalanga, South Africa **Structural and Electronic Properties of MX_3(M= Zr and Hf; X= S, Se) from first principles calculations** Poster presentation

4. 28 –29th Oct. 2014 Conference 6th Cross Faculty Graduate SymposiumUniversity of the Witwatersrand, Johannesburg, South Africa **Rhenium Chalcogenides: Insight from first principles calculations** Oral presentation

5. 29th July - 2nd Aug. 2013 Conference 5th Cross Faculty Graduate SymposiumUniversity of the Witwatersrand, Johannesburg South Africa **A theoretical Investigation of the Structural, electronic and Phase transition of Molybdenum Selenide** poster presentation

6. 08 - 12 July 2013 Conference South African Institute of physics conference University of Zululand, South Africa **Molybdenum Selenide compounds for solar energy application** poster presentation

7. 02 August 2013 Workshop Gauteng Electronic Structure Meeting University of the Witwatersrand, Johannesburg, South Africa oral presentation

Dedication

To my late grand parents Abdulkadir Sidi, Zuwaira Armaya'u and Hajiya Amina Nuhu Salihu may your souls rest in peace.

Acknowledgements

First I will like to begin by thanking Allah (SWT) for everything that he has done to me and making this research a reality.

I would like to express my sincere appreciation to my supervisor Professor Daniel P. Joubert, who introduced me to this interesting field of computations, patiently provided me with adequate materials, encourage and guide me to continue with the work at the time of difficulties and provided me with the best support I could wish for. I would like to say a big **Thank you**.

The support of the DST-NRF Centre of Excellence in National institute for theoretical physics (NITheP) towards this research is hereby acknowledged. Opinions expressed and conclusions arrived at, are those of the author and are not necessarily to be attributed to the CoE.

I would also like to acknowledge Center for High Performance Computing (CHPC) for providing me with the computational resources to perform some of the computations in this thesis.

Special thanks to Dr Mohammed Suleiman Hussein Suleiman, Dr George S. Manyali for their valuable assistance in the course of this research.

Thanks to Professor Richard Martins (University of Illinois) for a wonderful discussion in electronic properties of semiconductor, Professor Matteo Gatti (European Theoretical Spectroscopy Facility, France) and Professor Andrea Marini (European Theoretical Spectroscopy Facility, Spain) for discussion in optical properties. Your help is indeed priceless.

This acknowledgement will be complete without thanking my colleagues in the office Moise Dongho Nguimdo, Peter Egbele and Faris Mohammed among many fellow postgraduate students at the School of Physics for their stimulating discussions during coffee breaks.

It will be a failure on my side if I fall to express gratitude to my families at Wits Musalla. Without your prayers, jokes and enthusiasm, this research would have been more tedious task than I expect. I really appreciate your efforts.

The support from my South African family, in particular Ibrahim Usman, Dr Iyabo Usman and Professor Pedro is highly appreciated. *Na gode.*

The contribution of my secondary school teachers Malam Ibrahim Jika (May your soul rest in peace) and Malam Kabir Mustapha is highly appreciated, without your support, encouragement and advice I may not be where I am today. Thank you for all you have done to me.

List of Figures

5.1 K point convergence. . . . 37

5.2 Cut-off energy convergence. . . . 38

6.1 TcS_2 unit cell doubled in the Z-direction to show the layered structure. . . . 56

6.2 TcS_2 cohesive energy-volume graph calculated using (a) PBE, (b) PBEsol, (c) vdW-TS, (d) DFT-D2 and (f) vdW-DF. . . . 57

6.3 $TcSe_2$ cohesive energy-volume graph calculated using (a) PBE, (b) PBEsol, (c) vdW-TS, (d) DFT-D2 and (f) vdW-DF. . . . 58

6.4 $TcTe_2$ cohesive energy-volume graph calculated using (a) PBE, (b) PBEsol, (c) vdW-TS, (d) DFT-D2 and (f) vdW-DF. . . . 59

6.5 TcX_2 (X= S, Se and Te) phonon dispersion relation graph calculated using vdW-D2. . . . 63

6.6 vdW-D2 calculated specific heat capacity at constant volume and entropy for the TcX_2 (X= S, Se and Te) structures. . . . 64

6.7 Calculated vdW-D2 TcS_2 calculated electronic structure (a) band structure along high symmetry K-points, (b) spin projected TDOS, (c) PDOS of Tc(s,p,d) and (d) PDOS of S(s,p). . . . 65

6.8 Calculated MBJ $TcSe_2$ calculated electronic structure (a) band structure along high symmetry K-points, (b) spin projected TDOS, (c) PDOS of Tc(s,p,d) and (d) PDOS of Se(s,p). . . . 66

6.9 Calculated vdW-DF $TcTe_2$ calculated electronic structure (a) band structure along high symmetry K-points, (b) spin projected TDOS, (c) PDOS of Tc(s,p,d) and (d) PDOS of Se(s,p). . . . 66

6.10 Band gap volume relationship in TcX_2 (X= S, Se and Te) calculated from vdW-D2 relaxed structure. . . . 68

6.11 Primitive unit cell for technetium sulphide in the $P\bar{1}$ structure and the positions of the four Technetium atoms. . . . 70

6.12 Positions of Tc atoms. . . . 70

6.13 Structural volume per atom as a function of doping configuration. . . . 71

6.14 Formation energy per atom as a function of doping configuration. . . . 71

6.15 Band gap as a function of doping configuration for TcS_2 calculated with MBJ functional. 72

6.16 HfX_2 phonon dispersion relation graph calculated using vdW-TS. . . . 74

6.17 vdW-TS calculated specific heat capacity at constant volume and entropy for HfX_2 (X= S, Se and Te) structures. . . . 75

6.18 HfX_2 (X= S, Se) BSE calculated optical absorptions. . . . 76

6.19 High symmetry points used in HfX_2 (X = S, Se) band structure calculations. . . . 77

6.20 Monolayer HfX_2 (X= S, Se) BSE calculated optical absorptions. 79
6.21 HfX_3 structure. 80
6.22 HfX_3 cohesive energy-volume relation. 81
6.23 HfX_3 phonon dispersion relation graph calculated using vdW-TS. 85
6.24 vdW-TS calculated specific heat capacity at constant volume and entropy for HfX_3 (X= S, Se and Te) structures. 86
6.25 Calculated electronic properties of HfS_3 using MBJ functional band structure (a) band structure along high symmetry K-points, (b) spin projected TDOS, (c) PDOS of Hf(s,p,d) (d) PDOS of S (s,p). 87
6.26 MBJ $HfSe_3$ calculated band structure (a) band structure along high symmetry K-points, (b) spin projected TDOS, (c) PDOS of Hf(s,p,d) (d) PDOS of Se (s,p). 88
6.27 vdW-TS $HfTe_3$ calculated band structure (a) band structure along high symmetry K-points, (b) spin projected TDOS, (c) PDOS of Hf(s,p,d) (d) PDOS of Te (s,p). 88
6.28 GW HfS_3 calculated frequency-dependent optical spectra (a) real $\epsilon_{re}(\omega)$ and the imaginary $\epsilon_{im}(\omega)$ parts of the dielectric function, (b) reflectivity $R(\omega)$ and Transmitivity $T(\omega)$, (c) Refraction $\eta(\omega)$ and extinction coefficient $\kappa(\omega)$ and (d) absorption coefficient $\alpha(\omega)$. The visible range are shaded. 91
6.29 GW $HfSe_3$ calculated frequency-dependent optical spectra (a) real $\epsilon_{re}(\omega)$ and the imaginary $\epsilon_{im}(\omega)$ parts of the dielectric function, (b) reflectivity $R(\omega)$ and transmitivity $T(\omega)$, (c) refraction $\eta(\omega)$ and extinction coefficient $\kappa(\omega)$ and (d) absorption coefficient $\alpha(\omega)$. The visible range is shaded. 91
6.30 vdW-TS calculated Specific heat capacity at constant volume and entropy for the ZrX_2 (X= S, Se and Te) structures. 92
6.31 ZrX_2 phonon dispersion relation graph calculated using vdW-TS. 93
6.32 ZrX_2 (X= S, Se) BSE calculated optical absorptions. 95
6.33 Optical absorptions for Monolayer ZrX_2 (X= S, Se) calculated at the BSE level. 97
6.34 ZrX_3 structure. 98
6.35 Cohesive energy-volume relation for ZrX_3. 99
6.36 ZrX_3 phonon dispersion relation graph calculated using vdW-TS. 101
6.37 vdW-TS calculated specific heat capacity at constant volume and entropy for ZrX_3 (X= S, Se and Te) structures. 102
6.38 ZrS_3 vdW-TS calculated band structure (a) band structure along high symmetry K-points, (b) spin projected total density of states (TDOS), (c) partial density of states (PDOS) of Zr(s,p,d) (d) PDOS of S (s,p). 104
6.39 MBJ $ZrSe_3$ calculated band structure (a) band structure along high symmetry K-points, (b) spin projected TDOS, (c) PDOS of Zr(s,p,d) (d) PDOS of Se (s,p). 104
6.40 vdW-DF $ZrTe_3$ calculated band structure (a) band structure along high symmetry K-points, (b) spin projected TDOS, (c) PDOS of Zr(s,p,d) (d) PDOS of Te (s,p). 105

6.41 GW ZrS_3 calculated frequency-dependent optical spectra (a) real $\epsilon_{re}(\omega)$ and the imaginary $\epsilon_{im}(\omega)$ parts of the dielectric function, (b) reflectivity $R(\omega)$ and transmitivity $T(\omega)$, (c) refraction $\eta(\omega)$ and extinction coefficient $\kappa(\omega)$ and (d) absorption coefficient $\alpha(\omega)$. The visible range is shaded. 107

6.42 GW $ZrSe_3$ calculated frequency-dependent optical spectra (a) real $\epsilon_{re}(\omega)$ and the imaginary $\epsilon_{im}(\omega)$ parts of the dielectric function, (b) reflectivity $R(\omega)$ and transmitivity $T(\omega)$, (c) refraction $\eta(\omega)$ and extinction coefficient $\kappa(\omega)$ and (d) absorption coefficient $\alpha(\omega)$. The visible range is shaded. 107

6.43 TiX_3 structure. 108

6.44 TiX_3 cohesive energy-volume relation. 109

6.45 TiX_3 phonon dispersion relation graph calculated using vdW-TS. 111

6.46 vdW-TS TiS_3 calculated electronic structure (a) band structure along high symmetry K-points, (b) spin projected TDOS, (c) PDOS of Ti(s,p,d) and (d) PDOS of S(s,p). . . . 113

6.47 vdW-TS $TiSe_3$ calculated electronic structure (a) band structure along high symmetry K-points, (b) spin projected TDOS, (c) PDOS of Ti(s,p,d) and (d) PDOS of Se(s,p). . . . 113

6.48 vdW-DF $TiTe_3$ calculated electronic structure (a) band structure along high symmetry K-points, (b) spin projected TDOS, (c) PDOS of Ti(s,p,d) and (d) PDOS of Se(s,p). . . . 114

6.49 GW TiS_3 calculated frequency-dependent optical spectra (a) real $\epsilon_{re}(\omega)$ and the imaginary $\epsilon_{im}(\omega)$ parts of the dielectric function, (b) reflectivity $R(\omega)$ and transmitivity $T(\omega)$, (c) refraction $\eta(\omega)$ and extinction coefficient $\kappa(\omega)$ and (d) absorption coefficient $\alpha(\omega)$. The visible range is shaded. 116

6.50 $ReSe_2$ cohesive energy-volume graph calculated using (a) PBE, (b) vdW-TS and (c) vdW-DF. 118

6.51 Phonon dispersion of $ReSe_2$ calculated using the vdW-TS relaxed structure. 120

6.52 MBJ calculated $ReSe_2$ band structure (a) band structure along high symmetry K-points, (b) spin projected total density of states (TDOS), (c) partial density of states (PDOS) of Re(s,p,d) (d) PDOS of Se (s,p). 121

6.53 G_0W_0 $ReSe_2$ calculated frequency-dependent optical spectra (a) real $\epsilon_{re}(\omega)$ and the imaginary $\epsilon_{im}(\omega)$ parts of the dielectric function, (b) reflectivity $R(\omega)$ and transmitivity $T(\omega)$, (c) refraction $\eta(\omega)$ and extinction coefficient $\kappa(\omega)$ and (d) absorption coefficient $\alpha(\omega)$. The visible range is shaded. 122

List of Tables

5.1 Second order elastic constant. . . . 43

6.1 Calculated and experimental equilibrium parameters of TcX_2(X = S, Se and Te): lattice constants (a (Å) , b (Å), c (Å)), volume V_0 (Å^3), formation energy E_f per atom and cohesive energy E_{coh} per atom. . . . 60

6.2 calculated and experimental TcX_2 (X = S, Se and Te) nearest neighbour distances in Å. 61

6.3 TcX_2 (X= S, Se and Te) calculated elastic constants (GPa). . . . 62

6.4 Charge transfer for $TcX_2(X = S, Se, Te)$ in electronic charge (e) calculated using vdW-D2. Charge transfer numbers refer to atoms in the first and second columns respectively (See Fig. 6.1). . . . 65

6.5 Calculated and experimental indirect energy band gaps (in eV) of TcX_2 (X= S, Se and Te) structures. . . . 67

6.6 Calculated elastic constants (GPa) for HfX_2 (X = S, Se and Te). . . . 73

6.7 Calculated and experimental band gaps eV of HfX_2 (X= S, Se). . . . 75

6.8 Calculated and experimental direct band gaps eV of HfX_2 (X= S, Se). . . . 76

6.9 HfX_2 (X= S, Se) BSE calculated positions for A and B peaks in eV. . . . 77

6.10 HfX_2 (X= S, Se) BSE calculated binding energy for A and B excitons in eV. . . . 77

6.11 Monolayer HfX_2; X= S, Se band gap in eV. . . . 78

6.12 Monolayer HfX_2 (X= S, Se) BSE calculated excitation energies for A and B excitons in eV. . . . 79

6.13 Monolayer HfX_2 (X= S, Se) BSE calculated binding energy for A and B excitons in eV. 80

6.14 Calculated cohesive and formation energy/atom of HfX_3 (X = S, Se and Te) structures in (eV). . . . 82

6.15 Calculated and experimental equilibrium parameters of HfX_3(X= S, Se, Te): lattice constants [a (Å), b (Å), c (Å)], atomic volume V_0 (Å^3) and angle β°. . . . 83

6.16 calculated and experimental HfX_3 (X = S , Se and Te) structures nearest neighbour distances in Å unit see Figure 6.21. . . . 84

6.17 HfX_3 calculated elastic constants (GPa). . . . 84

6.18 Charge transfer for HfX_3 (X= S, Se, Te) in electronic charge (e) calculated using vdW-TS see Figure 6.21. . . . 87

6.19 Calculated and experimental energy band gaps (in eV) of HfX_3 (X= S, Se, Te). . . . 89

6.20 MBJ calculated minimum direct band gaps (in eV) of HfX_3 (X= S, Se, Te). . . . 90

6.21 Calculated elastic constants (GPa) for ZrX_2 (X = S, Se and Te). . . . 93

6.22 Calculated and experimental band gaps in eV for ZrX_2 (X= S, Se). . . . 94

6.23 Calculated and experimental direct band gaps in eV for bulk ZrX_2 (X= S, Se). 94
6.24 ZrX_2 (X= S, Se) BSE calculated positions for A and B peaks in eV. 95
6.25 ZrX_2 (X= S, Se) BSE calculated binding energy for A and B excitons in eV. 95
6.26 Monolayer ZrX_2 (X= S, Se) band gap in eV. 96
6.27 Positions for A and B peaks (in eV) calculated at the BSE level for Monolayer ZrX_2 (X= S, Se). 96
6.28 Monolayer ZrX_2 (X= S, Se) BSE calculated binding energy for A and B excitons in eV. 97
6.29 ZrS_3 like structures calculated cohesive and formation energy/atom in (eV). 98
6.30 Calculated and experimental equilibrium parameters of ZrX_3(X= S, Se, Te): lattice constants [a (Å), b (Å), c (Å)], atomic volume V_0 (Å^3) and angle β°. 100
6.31 Calculated and experimental nearest neighbour distances of ZrX_3 (X = S, Se and Te) in Å , see Figure 6.34. 101
6.32 Calculated elastic constants (GPa) for ZrX_3. 102
6.33 Charge transfer for ZrX_3 (X= S, Se, Te) in electronic charge (e) calculated using vdW-TS unit see Figure 6.34. 103
6.34 Calculated and experimental energy band gaps (in eV) of ZrX_3 (X= S, Se, Te). 105
6.35 MBJ calculated minimum direct band gaps (in eV) of ZrX_3 (X= S, Se, Te). 106
6.36 TiS_3 like structures calculated cohesive and formation energy/atom in (eV). 108
6.37 Calculated and experimental equilibrium parameters of TiX_3(X= S, Se, Te): lattice constants (a (Å), b (Å), c (Å)), atomic volume V_0 (Å^3) and angle β°. 110
6.38 Calculated and experimental TiX_3 (X = S, Se and Te) structures nearest neighbour distances in Å unit see Figure 6.43. 111
6.39 TiX_3 calculated elastic constants (GPa). 112
6.40 Charge transfer for TiX_3 (X= S, Se, Te) in the unit of electronic charge (e) obtained in vdW-TS calculations, see Figure 6.43. 113
6.41 Calculated and experimental energy band gaps (in eV) of TiX_3 (X= S, Se, Te). 114
6.42 MBJ calculated minimum direct band gaps (in eV) of TiX_3 (X= S, Se, Te). 115
6.43 Rhenium diselenide structural phases. 117
6.44 $ReSe_2$ calculated and experimental equilibrium lattice parameters. 118
6.45 Calculated nearest neighbour distance in (Å) units for $ReSe_2$. 119
6.46 Calculated elastic constants (GPa) for $ReSe_2$. 119
6.47 $ReSe_2$ calculated and experimental band gaps. 121

A.1 Doped technetium dichalcogenides structural system, volume, volume per atom, cohesive energy E_{coh}, cohesive energy E_{coh} per atom, formation energy per atom, band gap for DFT, band gap and magnetic moment per unit cell (μ) in Bohr magnetons. 127

Contents

1 Introduction **1**

1.1 Solar energy harvesting: The solar cell . . . 1

1.2 Transition metal chalcogenides . . . 3

1.3 Aims . . . 7

1.4 Thesis outline . . . 8

2 Density Functional Theory (DFT) **9**

2.1 Thomas-Fermi Model . . . 10

2.2 Hohenberg-Kohn Theorems (HK) . . . 11

2.3 Constrained search formalism . . . 14

2.4 Kohn-Sham Approach . . . 14

2.5 Exchange Correlation Functionals . . . 15

2.6 Van der Waals Corrections . . . 21

3 The GW Approximation **25**

3.1 Quasi-Particles . . . 25

3.2 Self Energy . . . 26

3.3 Green Function . . . 26

3.4 GW Approximation . . . 27

3.5 Bethe-Salpeter equation (BSE) . . . 28

4 Pseudo-potentials and the PAW Method **30**

4.1 Solution to K-S equation . . . 30

4.2 Pseudopotential . . . 32

4.3 Projector augmented waves (PAWS) . . . 33

5 Computational Details **36**

5.1 Outline of Calculations . . . 36

5.2 Test of convergence . . . 36

5.3 Equation of states . . . 38

5.4 Pressure phase transition . . . 39

5.5 Cohesive energy . . . 40
5.6 Formation energy . . . 41
5.7 Elastic constants . . . 41
5.8 Thermal properties . . . 44
5.9 Electronic density of State . . . 44
5.10 DFT band gap problem . . . 46
5.11 Optical properties . . . 47
5.12 Dielectric function . . . 50
5.13 GW and BSE methodology . . . 53

6 Results and discussions **55**
6.1 Technetium dichalcogenide . . . 55
6.2 Hafnium dichalcogenide . . . 73
6.3 Hafnium trichalcogenide . . . 79
6.4 Zirconium dichalcogenide . . . 91
6.5 Zirconium trichalcogenide . . . 97
6.6 Titanium trichalcogenide . . . 107
6.7 $ReSe_2$ . . . 116

7 Conclusions and Future Work **123**
7.1 Conclusion . . . 123
7.2 Future work . . . 126

A Doped TcS_2 Structures **127**

References **156**

1. Introduction

In this chapter, we introduce the current energy crises on the Earth, how the energy challenges may be overcome, properties of materials that may be used in harnessing the renewable sources of energy and the potential materials for harnessing the energy.

1.1 Solar energy harvesting: The solar cell

As a result of increased industrialisation and world population, energy consumption has risen tremendously over the last few decades, setting the possibility of exhausting fossil fuels such as coal, wood, oil and gas. This increase in human need for energy cannot be fulfilled by burning fossil fuel, which will increase the emission of carbon IV oxide (CO_2) in the atmosphere. Plants will not be able to convert all the CO_2 emitted into oxygen and bound carbon, leading to CO_2 accumulation in the atmosphere which further leads to negative effects to the environment like global warming and deforestation [1, 2, 3].

Among the anticipated consequences of an increase in atmospheric temperature are, but not limited to, increase in chemical and biological activities which can lead to faster bacterial growth, spread of diseases and corrosion in buildings. To limit these occurrences, CO_2 emission from man made activities has to be reduced by either reducing human energy consumption or adopting new ways of energy generation that emit less CO_2.

Solar energy is one of the alternative sources of energy that can be harnessed in lieu of fossil fuel. The energy from the sun is the purest form of renewable energy known to man, this energy made it possible to store energy in fossil fuels through a very long process of storing solar energy in plants and their decay process. The energy from the sun has been there for billions of years and will continue to be there for considerable amount of time in the future. The annual solar energy supply to the Earth has been estimated to be about 3×10^{24} J [4, 5, 6], whereas the world energy consumption is estimated to be around 4.29×10^{20} J [7]. Energy from the sun is unlimited. Harnessing it, does not constitute any hazard to the environment. To harness the solar energy, we need a device that can effectively convert the solar energy into the required form of energy.

A device which converts solar energy into electricity through the photovoltaic effect (a method of generation of current or voltage from sunlight) is known as solar cell/photovoltaic cell. In the photovoltaic

effect light is incident on the surface of a material, electrons in the valance bands of the material absorb the energy from the incident light, are excited, to the conduction band and become free electrons [8]. To prevent the recombination of the electrons with the holes (only materials in which electron-hole recombination can be prevented are good materials for solar cells), which can happen immediately the electrons are freed from the valance band, the freed electrons are accelerated into and collected in an external circuit by a built-in potential. The extra energy of the electron generates an electromotive force (EMF). The EMF drives the electrons through a load to do a work.

In order to extract the extra energy of the excited electrons, there must be an energy gap separation large enough compared to kT between the excited states of the material of the solar cell and the ground state [8]. Here k is Boltzmann's constant and T is temperature. The material, that can be suitable for solar energy application, should therefore have valence band and conduction band separated by atleast kT. Separation between these energy bands will serve to maintain the excited electron at a higher energy for a longer time compared to thermal relaxation time for the excited electrons to be exploited. Such a material with a separation between the valence band and the conduction band is called a semiconductor.

The generation of photovoltaic solar cells can be divided into three categories: First generation solar cells, which are based on silicon wafers with efficiency of about 10 to 25 $\%$ [9]. Despite the favourable efficiency of these solar cells, their cost of production is very high [9, 5, 10] when compared with the cost of other means of energy generation (1 \$/Wp). To reduce the cost of production, there was a gradual shift to thin-films (second generation solar cells). This offer the opportunity of reducing the cost of the material of the solar cell and its cost of deposition [11, 12]. Their efficiency is however, less than the efficiency of the first generation photovoltaic [11, 12]. The third generation solar cells were targeted toward reducing the production cost of the second generation solar cells and improving its efficiency at the same time [11, 13]. To improve the efficiency of the solar cell and overcome the well known limit of a single band gap material (the so-called Shockley Queisser limit) [14], we need multiple threshold devices like multi-colour or tandem (multi layer) solar cell [10, 11, 12]. Tremendous progress has been made in reducing the cost and improving the efficiency of the third generation solar cell and efficiencies of about 37.9 $\%$ to 40 $\%$ have been reported [15, 16]. To use a semiconductor in first and second generation photovoltaic material, it need to have an optimum band gap of about 1.5 eV [9], whereas a band gap that ranges from 0.5 eV to 3.0 eV are required in third generation solar cells [17, 18, 19, 20]. Transition metal chalcogenides are promising materials for these applications.

Transition metal chalcogenides are important inorganic materials with wide range of potential applica-

tions in the magnetic, electronic, catalytic and optical industry [21]. These materials can be divided into two categories: layered materials with van der Waal's spacing between the layers, which comprise two-third of transition metal chalcogenides and non-layered materials [22]. Some members of the family of transition metal chalcogenide are semiconductors with band gap falling within the infra red and the visible range of the spectrum and are therefore promising material for investigation as potential candidates for third generation solar cells.

1.2 Transition metal chalcogenides

The Transition Metal Chalcogenides (TMC) is a family of compounds with the formula M_yX_z, where M is a member of the transition metals (V, Nb, Ta, Cr, Mo, W, Mn, Tc or Re), while X represents a member of the chalcogen family (P, S, Se and Te), y and z are integers. They have a variety of potentially useful properties [23, 24, 25, 26, 27, 28, 29]. Depending on the transition metal and the chalcogen involved, layered transition metal chalcogenide (LTMC) can have properties ranging from semi-conducting to superconducting [23]. Layered bulk dichalcogenide crystal materials are composed of vertically stacked layers bonded together by weak van der Waal's forces, similar to the van der Waal's forces in graphite [30]. Owing to strong surface effects, the properties of these materials vary drastically with the number of layers in a sheet. The electrical and optical properties of these compounds can be tuned on demand by reducing or increasing the number of layers [31], which makes them potential candidates for tunable nano electronics [32]. It is possible to extract single dichalcogenide layers from bulk crystals systems [33, 34] and deposit them on substrates. Single layered MX_2 systems present an opportunity for a wide range of systems for studying mesoscopic transport in 2D and may find practical applications similar to those of graphene. Bulk WSe_2 has been used in the fabrication of photo-voltaic cells [35]. MoS_2 has been used in nano tubes [36] and nanowires [37], where they showed confinement effects in their electronic and optical properties. Fabrication of field effect transistors can be achieved through nanoscale semi-conducting dichalcogenides [34, 37, 38]. Superconducting $NbSe_2$ could be a model for studying superconductivity in low-dimensions, while TSi_2, $MoTe_2$ and WS_2 are semiconductors with variety of physical properties and potential electronic applications [21]. Shearing in MoS_2, $MoSe_2$, $MoTe_2$, WS_2, TaS_2, $NbSe_2$, $NiTe_2$, BN and Bi_2Te_2 can be utilized in lubrication [39]. MoS_2, $MoSe_2$, TSi_2, $MoTe_2$, WS_2, HfS_2, $HfSe_2$, TSi_3, ZrS_3, $ZrSe_3$, HfS_3, $HfSe_3$, ZrS_3 and $ZrSe_3$ are semiconductors and are potential candidates for third generation solar cells [21, 40, 41, 42, 43, 44, 45, 46, 47].

Transition metal chalcogenides have been studied extensively both theoretically and experimentally. For the purpose of this thesis, we decide to limit our investigations to chalcogenide of technitium, hafnium, zirconium, titanium and rhenium. Compounds that are yet to be fully theoretically investigated.

1.2.1 Technitium dichalcogenide

Following the crystal structure study of group VII transition metal chalcogenides by Alcock and Kjekshus [48], Widervanck and Jellinek [49] used Guinier powder data and Weissenberg diagram to establish the stoichiometry of technitium dichalcogenides compounds, i.e. TcS_2, $TcSe_2$ and $TcTe_2$. They proposed that TcS_2 and $TcSe_2$ have triclinic symmetry with space group $P\bar{1}$, their unit cell contains four units formula ($Z = 4$), which corresponds to the distortion of $Cd(OH)_2$ type cell, the Tc atoms has octahedral coordination forming Tc diamond shaped chains and that $TcTe_2$ has the same structure with a high temperature form of $MoTe_2$ with space group $P2_1/m$ having lattice parameters a and b double that of $MoTe_2$. However, *ab initio* calculations show that $TcTe_2$ with a triclinic structure which is iso-structural with TcS_2 and $TcSe_2$ is energetically more stable than the one with the $MoTe_2$ structure [22]. Lamfers et. al. [50] used single X-ray crystal diffraction methods and re-examined the crystal structure of TcS_2 and reported the same cell parameters as obtained by Widervanck and Jellinek [49].

Widervanck and Jellinek [49] reported the preparation of TcS_2, $TcSe_2$ and $TcTe_2$ by chemical transport reactions in a tube which is 20 cm long at a temperature of about 1080 to 1150°C for sulphide, 1000 to 1080°C for selenides and 840 to 980°C for the tellurides.

The structural and electronic properties of TcS_2 have been reasonably reported both theoretically and experimentally. However, there is scarce characterisation of the structural and electronic properties of $TcSe_2$ and $TcTe_2$ [51]. Added to the fact that the theoretical characterisation of TcS_2 reported by Fang et. al. [52] and Philippe et. al. [22], used the local density approximation and the generalized gradient approximation, respectively, of the density functional theory, methods known to underestimate the band gap of semiconductors by as much as 30 to 50 % and which do not take into account the long range dispersion forces between the layers of the TcS_2. The long range dispersion forces are a necessary ingredient for accurate description of the structural properties of layered materials like TcS_2, which in turn determines the electronic properties of the materials. There is therefore the need to carry out an accurate study of the structural and electronic properties of TcS_2, $TcSe_2$ and $TcTe_2$ with inclusion of the necessary van der Waal's correction terms and post DFT methods like GW approach that are known

to correct the DFT band gap error.

1.2.2 Hafnium chalcogenides

In preparation and characterisation, Hafnium chalcogenides share the same methods and properties as zirconium discussed in Section 1.2.3 and share the same structure with TiX_3 and TiX_2 discussed in Section 1.2.4 of this thesis.

The structural as well as the electronic properties of the semiconducting chalcogenides of zirconium and hafnium have been theoretically reported by a number of authors [40, 53, 54, 55, 56]. However, to the best of our knowledge, there is no reported theoretical investigation of the optical properties of these structures using many body perturbation theory in the GW approximation and the BSE (Bethe-Salpeter equation), a methods believed to be the most accurate in description of the electronic and optical properties of an extended systems [40, 57, 58, 59]. This leaves room for the need to conduct systematic studies of the optical properties of these structures at the GW level and the Solution of the Bethe-Salpeter equation (BSE) in the Tamm-Dancoff level of approximation.

To the best of our knowledge, there are few or no theoretical studies of the structural, electronic or optical properties of the trichalcogenides of zirconium or hafnium. This is surprising considering the interesting properties of the compounds and that they have attracted tremendous attention of researcher from both theory and experiment.

Monolayer HfS_2 and $HfSe_2$ were generated and their electronic and optical properties investigated in a similar way to their zirconium counterparts discussed in Section 1.2.3

1.2.3 Zirconium chalcogenides

The chalcogenides of zirconium have been prepared and experimentally characterised by a number of authors [60, 61, 62, 63, 64]. Theoretically, Jiang [40] characterised the structural and electronic properties of the dichalcogenides of these compounds. The structures (ZrS_2, $ZrSe_2$, $ZrTe_2$, ZrS_3, $ZrSe_3$ and $ZrTe_3$) can either be prepared by heating the reactants separately in a suitably design vessel, by direct reaction of accurately weighted quantities of their elements, by decomposing compounds with higher chalcogenides content to lower chalcogenides contents in a silica evacuated tube or through the methods of chemical transport reaction [62, 63]. ZrX_3 (X= S, Se and Te) shares the same structure as

HfX_3 discussed in Section 1.2.2 of this thesis.

The structural and electronic properties of ZrS_2 and $ZrSe_2$ have been extensively investigated both theoretically and experimentally [40, 53, 65, 54, 66, 55, 56]. The structures have been shown to be iso-structural [40, 53, 65, 54, 66, 55, 56] and they crystallises in a 1T-CdI_2 type structure with space group *164,* $P\bar{3}m1$ in which the metal atom is sandwiched between two sheets of the chalcogen atoms leading to X-M-X layers. Atoms within a layer are strongly held together by a covalent bond with weak ionic bond within the layers. It is therefore a surprise that, to the best of our knowledge, there is no reported theoretical reported study of the optical properties of these structures at the GW level and BSE level of approximation. Methods believed to be the state of the art in predicting the optical properties of materials.

To tune the electronic and optical properties of the ZrX_2 structures, their layers were slice down to monolayers and their electronic and optical properties investigated. The monolayer was generated by creating a space wide enough between the adjacent layers in the z-direction of the relaxed bulk structure. A vacuum region of 19 Å was used to isolate the layers along the c axis and was found sufficient to eliminate interaction between the layers.

1.2.4 Titanium chalcogenides

McTaggart and Wadsley [60], Brattas and Kjekshus [67] and Furuseth et. al. [64] prepared and characterised the structures of TiX_3 (X = S, Se and Te). The samples were prepared by heating a measures quantity of their samples in a closed, evacuated tube at a temperatures of about 600 °C. The structures were identified to be iso-structural to HfX_3 and ZrX_3 and their dichalcogenides structures have the same structure as the dichalcogenides of the hafnium and zirconium [63, 64, 68, 69, 70].

There is a need to conduct an accurate systematic first principle calculations of the electronic and optical properties of the TiX_3 structures.

1.2.5 Rhenium Selenides

The first production of rhenium selenide was reported by Henry et. al. [71], Alcock et. al. [48] characterized the crystal structure of $ReSe_2$, Wildevanck et. al. [49], Lamfers et. al. [50] and Wilson et. al. [21] independently characterised the structural as well as the electronic properties of quite a

number of rhenium selenide compounds.

Wildevanck et. al [49] reported preparation of the crystalline samples of $ReSe_2$ at a temperature of about 1100 °C by heating intimate mixtures of their elements in an evacuated quartz-glass tube.

The structural as well as electronic properties of $ReSe_2$ have been reported both theoretically and experimentally by a number of authors [50, 52, 72, 73, 74, 75, 76]. Unfortunately, none of the theoretical studies took into account the needed van der Waal's correction necessary for accurate description of the layered structures.

1.3 Aims

Motivated by the facts discussed in Section 1.2, the aims and objectives of this thesis are:

1. Numerical computation techniques will be employed to investigate the most stable structural configuration of transition metal chalcogenides using density functional theory. The systems that will be investigated include experimentally identified structures as well as a range of potential new structures. The most stable structures will be identified for further study. Binary compounds M_yX_Z (y and x are integer variables) where M=(Hf, Zr, Ti, Tc or Re) and X = (S, Se or Te) will be included in the study.

2. Further investigation on the stable structures will include

- Mechanical stability test using elastic constants and phonon band structures.
- Electronic structure calculations at the density functional theory and GW level of approximation with a hope of identifying systems with band-gaps in the optical range.
- Optical properties and excitation energies using the GW approximation and comparing our results with experiments, where available.
- Examining possible changes in electronic, structural and optical properties of subset of systems identified in the previous step when doped with another atom.
- Identify possible trends in the properties of the observed TMCs based on the obtained results.

1.4 Thesis outline

This thesis is organised as follows:

Chapter 1 provided a brief background on motivation for the research, transition metal chalcogenides and what is expected to be achieved at the end of the investigation.

Chapter 2 is devoted to the background of density functional theory, exchange correlation functional and van der Waal's correction terms in density functional theory.

Chapter 3 gives a brief description of the method used in the so-called GW calculations, formalism for calculating frequency dependent dielectric functions and the BSE.

In Chapter 4, methods of solving the well known Kohn-Sham equations are discussed and approximations used in the solution of the equations.

In Chapter 5, the practical ways by which the calculations were done are described.

Chapter 6 discusses and analyses the structural, mechanical, electronic and optical properties of the transition metal chalchogenides. Chapter 7 followed 6, where all the work is concluded and future work proposed.

Appendix A provides detailed information about the changes in the structural, formation and cohesive energies and electronic properties of doped TcS_2.

2. Density Functional Theory (DFT)

To understand the behaviour of a particular system, obtain information about the density of the system and understand how the system will respond to external perturbation, it is important to solve Schrödinger equation for that particular system. The exact solution of the equation is available only for a few number of small systems like particle in a box, hydrogen atom and a simple harmonic oscillator. The equation can not be solved exactly for many body systems. Density Functional Theory (DFT) solves the problem by using the electron density (which is a function of three spatial coordinates only), to calculate the energy of systems, thereby reducing computational cost and offering the possibility of calculating the chemical and physical properties of large solids, molecules and atoms. DFT is a quantum mechanical theory of investigating the electronic structure of many-body systems (atoms, solids and molecules) in their ground states. Like most quantum mechanical calculations, the aim of DFT is to find an approximate solution of the many-body time independent Schrödinger equation for electrons

$$\left[-\frac{\hbar^2}{2m}\sum_i \nabla_i^2 + \sum_i V_{ext}(\mathbf{r_i}) + \frac{\mathbf{1}}{\mathbf{2}}\sum_{\mathbf{i}\neq\mathbf{j}} \frac{\mathbf{e^2}}{|\mathbf{r_i}-\mathbf{r_j}|} - \mathbf{E}\right]\psi(\mathbf{r_1},...\mathbf{r_N}) = \mathbf{0} \tag{2.0.1}$$

where the external potential on electron i, due to nuclei Z$_I n$ of R_I is given by

$$V_{ext}(\mathbf{r_i}) = -\sum_{i,I} \frac{Z_I e^2}{|\mathbf{r_i}-\mathbf{R_j}|} \tag{2.0.2}$$

The first term in equation (2.0.1) above describes the kinetic energy of the system, while the second and the third terms are electron-nucleus Coulomb interaction and electron-electron repulsive Coulomb energies respectively. The r_i and r_j denote the positions of electrons in the system, e is the electronic charge, while Z_I and R_I are the atomic numbers and coordinates of the nuclei [77]. For a given location R_I of nuclei, the most important characteristics in describing the ground state electronic structure are the total energy E and the electronic density distribution $n(\mathbf{r})$. DFT has attracted interest from condensed matter physicists as well as chemists in recent years, due to the following reasons:

- it is much easier to work with a 3-dimensional density, $n(\mathbf{r})$, than a 3N-dimensional wave function, ψ, (N is the number of electrons)
- it is computationally simple and
- it can handle infinite periodic systems.

Understanding the electronic structure of matter relies on the understanding of the many body non-relativistic Schrödinger equation [78]. The Hamiltonian of the system of nuclei and electron in an system is given by:

$$\hat{H} = -\frac{\hbar^2}{2m_e}\sum_i \nabla_i^2 - \sum_{i,I}\frac{Z_I e^2}{|\mathbf{r_i} - \mathbf{R_I}|} + \frac{1}{2}\sum_{i\neq j}\frac{e^2}{|\mathbf{r_i} - \mathbf{r_j}|} - \sum_I \frac{\hbar^2}{2M_I}\nabla_I^2 + \frac{1}{2}\sum_{I\neq J}\frac{Z_I Z_J e^2}{|\mathbf{R_I} - \mathbf{R_J}|}$$

where variables representing electrons, with mass m_e are lower case and that of nuclei having charge Z_I and mass M_I by upper case. The mass of the electrons is much less than the mass of the nuclei. This suggests that electrons will reach equilibrium faster than the nuclei. In the Born-Oppenheimer approximation electrons are considered to be in equilibrium with the nuclei at any instant. This allows us to separate the degrees of freedom of the electrons and the nuclei [79] and the electronic part of the Hamiltonian can be written as

$$\hat{H} = -\frac{\hbar^2}{2m_e}\sum_i \nabla_i^2 - \sum_i V_{ext}(\mathbf{r_i}) + \frac{1}{2}\sum_{i\neq j}\frac{e^2}{|\mathbf{r_i} - \mathbf{r_j}|}. \tag{2.0.3}$$

Here the external potential, which is given by $V_{ext}(\mathbf{r_i})$ accounts for the electron interaction with the nuclei [78]. DFT is a ground state theory which considers the charge density as the relevant physical quantity [80]. Besides its simplicity, it is highly successful in describing structural and electronic properties in quite a number of materials.

The Schrödinger equation for the first principles (*ab-initio*) calculation is

$$i\hbar\frac{\partial\psi(\{\mathbf{r_i}\};t)}{\partial t} = \hat{H}\psi(\{\mathbf{r_i}\};t) \tag{2.0.4}$$

where $\psi(\{\mathbf{r_i}\};t)$ is the wave function for the electron.

2.1 Thomas-Fermi Model

Thomas [81] and Fermi [82] describe a way of calculating the energy of an electronic system exclusively in terms of its density. They proposed an expression for the total energy of an electronic system as an explicit function of density, electrons were considered as non-interacting particles in a homogeneous gas whose density is equal to the local density at any given point[83, 78]. The Thomas and Fermi model neglected the correlation and exchange among electrons. Dirac [84] formulated a local approximation

for the exchange which leads to an electron energy functional in an external potential V_{ext} given by

$$E_{TF}[n] = C_1 \int d^3r n(\mathbf{r})^{(5/3)} + \int d^3r V_{ext}(\mathbf{r}) n(\mathbf{r}) + C_2 \int d^3r n(\mathbf{r})^{(4/3)} + \frac{1}{2} \int d^3r d^3r' \frac{n(\mathbf{r}) n(\mathbf{r}')}{|\mathbf{r} - \mathbf{r}'|}, \tag{2.1.1}$$

where $\int d^3r n(\mathbf{r})^{(5/3)}$ is the local density approximation to the kinetic energy and $C_1 = \frac{3}{10}(3\pi^2)^{(2/3)} = 2.81$ Hatree, $\int d^3r n(\mathbf{r})^{(4/3)}$ is the exchange [85, 84] with $C_2 = -\frac{3}{4}(\frac{3}{\pi})^{(1/3)}$ = -0.739 Hatree and $\frac{1}{2}\int d^3r d^3r' \frac{n(\mathbf{r})n(\mathbf{r}')}{|\mathbf{r}-\mathbf{r}'|}$ is the classical electrostatic Hartree energy [78, 83]. In order to find the ground state energy and density, we need to minimize the functional E_{TF} in all possible values of $n(\mathbf{r})$ subject to the constraint that the integrated charge density equals the total number of electrons

$$\int d^3 n(\mathbf{r}) = N. \tag{2.1.2}$$

The solution of the unconstrained functional of the minimization can be found by the use of a Lagrange multiplier μ

$$\Omega_{TF}[n] = E_{TF}[n] - \mu \left\{ \int d^3r n(\mathbf{r}) - N \right\}, \tag{2.1.3}$$

The Lagrange multiplier μ represents the Fermi energy. If there is a small variation in density $\delta n(\mathbf{r})$, the condition for stationary point

$$\int d^3r n(\mathbf{r}) \Omega_{TF}[n(\mathbf{r})] + \delta n(\mathbf{r}) - \Omega_{TF}[n(\mathbf{r})] \rightarrow \int d^3r \left\{ \frac{5}{3} C_1 n(\mathbf{r})^{(2/3)} + V(\mathbf{r}) - \mu \right\} \delta n(\mathbf{r}) = 0 \tag{2.1.4}$$

where the total potential is given by $V(\mathbf{r}) = V_{ext}(\mathbf{r}) + V_{Hartree}(\mathbf{r}) + V_x(\mathbf{r})$. Since for any function $\delta n(\mathbf{r})$ eqn (2.1.4) must be satisfied, it is obvious that the will be stationary if and only if the potential and the density satisfies the relation

$$\frac{1}{2}(3\pi^2)^{(2/3)} n(\mathbf{r})^{(2/3)} + V(\mathbf{r}) - \mu = 0. \tag{2.1.5}$$

The Thomas-Fermi model has been used in equation of state of elements [78], but the approach begins with a crude approximation, missing important chemistry and physics of shell structure of atoms and molecules binding energy, for example. It can therefore be said to fall short of an accurate description of electrons in matter.

2.2 Hohenberg-Kohn Theorems (HK)

Hohenberg and Kohn's approach was to formulate DFT as an exact theory of many body systems [78]. It is applicable to systems of interacting particles in an external potential $V_{ext}(\mathbf{r})$ and it is applicable to

any system with electron and fixed nuclei in which the Hamiltonian can be written in the form

$$\hat{H} = \frac{-\hbar^2}{2m}\sum_i \nabla_i^2 + \sum_i V_{ext}(\mathbf{r_i}) + \frac{1}{2}\sum_{i\neq j}\frac{e^2}{|\mathbf{r}-\mathbf{r_j}|}. \tag{2.2.1}$$

DFT is based on the two theorems by Hohenberg and Kohn [86]. Hohenberg-Kohn Theorem I states that:

1. For any system, the ground state density $n_0(\mathbf{r})$ uniquely determines the external potential $V_{ext}(\mathbf{r})$ up to a constant. To prove this, HK used a general many body wave function to express the density and energy. They assumes two external potentials $V^1_{ext}(\mathbf{r})$ and $V^2_{ext}(\mathbf{r})$ which are different by more than a constant but lead to the same ground state density $n_0(\mathbf{r})$. It is expected that the two potentials should have different Hamiltonians, $\hat{H}^{(1)}$ and $\hat{H}^{(2)}$ with ground state wave functions $\psi^{(1)}$ and $\psi^{(2)}$ respectively hypothesized to give the same $n_0(\mathbf{r})$. It is expected that $\psi^{(2)}$ is not the ground state of $\hat{H}^{(1)}$, therefore

$$E^1 = \langle\psi^{(1)}|\hat{H}^{(1)}|\psi^{(1)}\rangle < \langle\psi^{(2)}|\hat{H}^{(1)}|\psi^{(2)}\rangle. \tag{2.2.2}$$

The inequality is strictly obeyed in a non-degenerate ground state, we can write $\langle\psi^{(2)}|\hat{H}^{(1)}|\psi^{(2)}\rangle$ as

$$\langle\psi^{(2)}|\hat{H}^{(1)}|\psi^{(2)}\rangle = \langle\psi^{(2)}|\hat{H}^{(2)}|\psi^{(2)}\rangle + \langle\psi^{(2)}|\hat{H}^{(1)} - \hat{H}^{(2)}|\psi^{(2)}\rangle \tag{2.2.3}$$

$$= E^2 + \int d^3r[V^1_{ext}(\mathbf{r}) - V^2_{ext}(\mathbf{r})]n_0(\mathbf{r}), \tag{2.2.4}$$

therefore

$$E^1 < E^2 + \int d^3r[V^1_{ext}(\mathbf{r}) - V^2_{ext}(\mathbf{r})]n_0(\mathbf{r}). \tag{2.2.5}$$

We can as well consider E^2 in a similar way by replacing the subscripts (1) with (2)

$$E^2 < E^1 + \int d^3r[V^2_{ext}(\mathbf{r}) - V^1_{ext}(\mathbf{r})]n_0(\mathbf{r}). \tag{2.2.6}$$

If we add eqn

$$E^1 + E^2 < E^1 + E^2. \tag{2.2.7}$$

Which proves the theorem that there can not be two different external potentials that give the same ground state charge density or the density at the ground state uniquely determines the external potential [87, 77]. Since $n(\mathbf{r})$ determines the external potential, it also determines the ground state wave function which can be obtained from the many body Schrödinger equation. It is worthy to note that we are still facing the problem of solving the many body Schrödinger equation in the presence of an external field.

2. Hohenberg-Kohn Theorem II states that: A universal functional $F_{HK}[n]$ of the energy E[n] in terms of the density $n(\mathbf{r})$ can be defined, which is valid for any external potential $V_{ext}(\mathbf{r})$; for a given $V_{ext}(\mathbf{r})$, the ground state energy of the system is the global minimum value of this functional, and the density $n(\mathbf{r})$ that minimizes the functional is the exact ground state density $n_0(\mathbf{r})$ [78]. To prove this theorem, the variational energy $E_{HK}[n]$ a density functional from HK theorem I, is:

$$E_{HK}[n] = T[n] + E_{int}[n] + \int d^3r V_{ext}(\mathbf{r})\, n(\mathbf{r}) \tag{2.2.8}$$

$$\equiv F_{HK}[n] + \int d^3r V_{ext}(\mathbf{r}) n(\mathbf{r}), \tag{2.2.9}$$

where the internal, potential and kinetic energies of the interacting electron are contained in the term $F_{HK}[n]$ and it is given by

$$F_{HK}[n] = T[n] + E_{int}[n], \tag{2.2.10}$$

which, by construction, must be same for all electron systems, irrespective of the external potential, since the kinetic and interaction energies of the system are functionals of the density only. Using the above discussion, if we consider a system with ground sate density $n_0(\mathbf{r})$ which corresponds to an external potential $V_{ext}(\mathbf{r})$, the expectation value of Hamiltonian of the system in the unique ground state with wave function $\psi^{(0)}$ will give HK functional

$$E^0 = E_{HK}[n^0] = \langle \psi^{(0)} | \hat{H}^{(0)} | \psi^{(0)} \rangle. \tag{2.2.11}$$

If we think of a different density $n^1(\mathbf{r})$ whose wave function is $\psi^{(1)}$. It will be clear that it will have have an energy E^1 which is higher than E^0 [78]. Therefore

$$E^0 = \langle \psi^{(0)} | \hat{H}^{(0)} | \psi^{(0)} \rangle < \langle \psi^{(1)} | \hat{H}^{(1)} | \psi^{(1)} \rangle = E^1. \tag{2.2.12}$$

It is, therefore, clear that the energy given by eqn (2.2.8) in terms of HK functional evaluated for the correct ground state density $n^0(\mathbf{r})$ is lower than the value of this expression for any other density $n(\mathbf{r})$.If the functional $F_{HK}[n^0]$ is known, minimizing the system total energy with respect to variation in density will give the exact ground state density and energy. However, HK theorem do not give any information on how the functional $F_{HK}[n]$ that gives the ground state energy can be constructed. The theorem can only be applied to a non degenerate system, even though, DFT is based upon it [78].

2.3 Constrained search formalism

Levy [88] and Lieb [89] redefined the universal functional of the energy in Hohenberg-Kohn formalism (ii) above as

$$F[n] = \min_{\psi \to n(r)} [\langle \psi | \hat{T} + \hat{V}_{int} | \psi \rangle] \tag{2.3.1}$$

which minimizes the energy over all $\mathbf{N}$-particle wave function ψ that yield a given density $n(\mathbf{r})$. The total energy functional E(n) for a specific system is then given by

$$E[n] = \int d\mathbf{r} V_{ext}(\mathbf{r}) n(\mathbf{r}) + F[n] \tag{2.3.2}$$

The ground state energy and density are obtained by minimizing $E[n]$ under the constraint $\int d\mathbf{r} n(\mathbf{r}) = N$, which implies that $d\mathbf{r} n(\mathbf{r})$ is the average number of electrons in a volume element $d\mathbf{r}$. In this way, Levy and Lieb restate the HK theorem and give more insight to the meaning of what the functional is as "the minimum of the sum of kinetic and interaction energies for all possible wave function with density $n(\mathbf{r})$. Unlike HK theorem, Levy and Lieb formalism is defined for all densities that correspond to anti-symmetric wave function and the restriction that the density has to be associated with the external potential is lifted [87]. Despite the success of the HK theorems, being the bedrock of DFT, it is only a proof that the electron density contains all the information needed to describe a molecular or electronic system. They failed to provide an insight on how the functional that produces the ground state energy can be constructed [87] and it also failed to provide a hint on the type of approximation to be used for the unknown functional. The constrained search formalism is of mere theoretical value and provides no solutions to the practical problem, searching through all possible wave function is practically impossible making

$$F[n] = \min_{\psi \to n(r)} [\langle \psi | \hat{T} + \hat{V}_{int} | \psi \rangle] \tag{2.3.3}$$

practically impossible to determine.

2.4 Kohn-Sham Approach

Kohn and Sham [90] reformulated the problem in a more familiar form and opened the way to practical applications of DFT by proposing the following ansatz

1. A system of interacting electrons is mapped on to an auxillary system of non-interacting electrons having the same ground state charge density $n(\mathbf{r})$ as the interacting system

2. the auxillary Hamiltonian is chosen to have the usual kinetic operator and an effective potential $V_{\texttt{eff}}(\mathbf{r})$ acting on an electron at a point $\mathbf{r}$.

For the Kohn-Sham system of non-interacting electrons, the ground state density is given by

$$n(\mathbf{r}) = 2\sum_i |\psi_i(\mathbf{r})|^2 \tag{2.4.1}$$

where the Kohn-Sham orbitals are the solutions of the one-particle Shrödinger equation

$$(-\frac{\hbar^2}{2m_e}\nabla^2 + V_{\texttt{KS}}(\mathbf{r}))\psi_i = \varepsilon_i\psi_i. \tag{2.4.2}$$

In this approach, the Kohn-Sham energy can be written as:

$$E_{KS}[n] = T_s[n] + \int d\mathbf{(r)}V_{ext}(\mathbf{r})n(\mathbf{r}) + E_H[n] + E_{XC}[n], \tag{2.4.3}$$

where the Hatree energy $E_H[n]$ is the Coulomb energy of the density $n(\mathbf{r})$ treated as a classical charge density

$$E_H[n] = \frac{1}{2}\int d\mathbf{(r)}d\mathbf{r\prime}\frac{n(\mathbf{r})n(\mathbf{r\prime})}{|\mathbf{r}-\mathbf{r\prime}|}, \tag{2.4.4}$$

and T_s is the independent-particle kinetic energy of non-interacting electron given by [91]

$$T_s = -\frac{\hbar^2}{2m}\ 2\sum_i \int \psi_i^*(\mathbf{r})\nabla^2\psi_i(\mathbf{r})dr. \tag{2.4.5}$$

The variational problem on the density $n(\mathbf{r})$ leads to the self-consistent Kohn-Sham equation [92], equation (2.4.2) with

$$V_{KS}(\mathbf{r}) = V_H(\mathbf{r}) + V_{XC}(\mathbf{r}) \tag{2.4.6}$$

where $V_{XC} = \frac{\delta E_{XC}}{\delta n(\mathbf{r})}$ and $V_H = \frac{\delta E_H}{\delta n(\mathbf{r})}$. This implies that if the universal density functional is known, the exact density and the ground state energy can be computed by solving the Kohn-Sham equation [78]. The effects of the correlation and exchange are grouped into the exchange correlation energy

$$E_{XC}[n] = \langle\hat{T}\rangle - T_s[n] + \langle V_{int}\rangle - E_H[n], \tag{2.4.7}$$

which follows from equations (2.3.3), (2.3.2) and (2.4.3).

2.5 Exchange Correlation Functionals

The exchange correlation energy contains all the terms that we are ignorant of and it also contains correction to the independent particle kinetic energy. A good approximation for the exchange correlation

may give a realistic electron density and ground state energy [93]. In the spin-unrestricted form, the Kohn-Sham equation becomes

$$[-\frac{\hbar^2}{2m_e}\nabla^2 + V_H(\mathbf{r}) + V_{XC}^{\sigma}(\mathbf{r})]\psi_i^{\sigma} = \varepsilon_i^{\sigma}\psi_i^{\sigma}, \tag{2.5.1}$$

where $\sigma =\uparrow$ or $\downarrow$ label the spin state.

For several decades, there were several attempts to construct approximate density functionals. Today, such functionals can be constructed semi-empirically through the adjustment of parameters from a given experimental data set [94, 93] or non-empirically through satisfaction of well known exact constraints. Improvements on density functional theory calculations led to the development hierarchy of exchange correlation functionals called "Jacobs ladder" [95]. The first four rungs on the ladder are:

1. Local Spin Density Approximation (LSDA)
2. Generalized Gradient Approximation (GGA)
3. meta-GGA
4. hybrid functionals.

2.5.1 Local Spin Density Approximation (LSDA)

LSDA was first proposed by Kohn and Sham [90], they proposed that a solid can sometimes be considered to be close to homogeneous electron gas (a hypothetical system, where electrons move on a positive background of charge density in a way that the ensemble is neutral electrically [87]), within this limit, it is believed that exchange and correlation effects are local in character, the exchange correlation energy is expressed as an integral over all surfaces. It is also assumed that the density at each point is the same as that of an electron gas of the same density [96]. The exchange correlation energy in this approximation is given by

$$E_{XC}^{LSDA}[n_\uparrow, n_\downarrow] = \int d^3\mathbf{r} n(\mathbf{r})\varepsilon_{xc}(n_\uparrow(\mathbf{r}), n_\downarrow(\mathbf{r})) \tag{2.5.2}$$

where $\varepsilon_{xc}(n_\uparrow, n_\downarrow)$ is the energy component in an electron gas with uniform spin densities $n_\uparrow$ and $n_\downarrow$ and $n(\mathbf{r})d^3\mathbf{r}$ is the average number of electrons in volume element $d^3\mathbf{r}$.

LSDA Exchange potential can be expressed as [97]

$$v_{xc}^{(LSDA)} = \frac{\delta E_{XC}^{LSDA}}{\delta n_\uparrow(\mathbf{r}), n_\downarrow(\mathbf{r})} = \varepsilon_{xc} + (n_\uparrow(\mathbf{r}), n_\downarrow(\mathbf{r}))\frac{\partial \varepsilon_{xc}(n)}{\partial n} \tag{2.5.3}$$

We need to determine the exchange correlation term of a uniform electron gas at a given density for practical applications of LSDA. This can be broken into the exchange ε_x and correlation ε_c parts as

$$\varepsilon_{xc} = \int d^3\mathbf{r} n(\mathbf{r}) \left[\varepsilon_x(n_\uparrow(\mathbf{r}), n_\downarrow(\mathbf{r})) + \varepsilon_c(n_\uparrow(\mathbf{r}), n_\downarrow(\mathbf{r}))\right] \tag{2.5.4}$$

where the exchange part, which is the electron exchange energy of a uniform electron gas at a given density, is given by Dirac the functional as [84]

$$\varepsilon_x = -\frac{3}{4}\sqrt[3]{\frac{3(n_\uparrow(\mathbf{r}), n_\downarrow(\mathbf{r}))}{\pi}}. \tag{2.5.5}$$

Ceperly and Alder [98] provide accurate values of ε_c through Quantum Monte Carlo simulations, analytic expressions for ε_c [99], are only known at high and low density limits [100]. The correlation energy in the high density limit is given by

$$\varepsilon_c = A \ln r_s + C + 0(r_s) \tag{2.5.6}$$

where A = 0.031091 and C = -0.046644 and r_s is Wigner-Seitzs radius and is related to the density by $\frac{4}{3}\pi r_s^3 = \frac{1}{n}$ At the low density limit, the correlation energy is given by

$$\varepsilon_c = -\frac{1}{2}\{\frac{g_0}{r_s} + \frac{g_1}{r_s^{3/2}} + ...\}, \tag{2.5.7}$$

where $g_0 = 0896$ and $g_1 = 1.325$ as deduced by Wigner. Vosko et. al. (VWN) [99], Perdew and Zunger (PZ81) [101], Cole and Perdew (CP) [102] and Perdew and Wang (PW92) [103] have used different approaches and different analytic expressions for ε_x to generate several LSDA correlation functionals.

LSDA is an *ab initio* method, and, by construction, is exact for a uniform system and has proven to be a very good approximation on systems of slowly varying density. For a real electronic system, whose density varies rapidly, it provide results with moderate accuracy, though, these densities are outside the range of the validity of the LSDA. After decades of the initial LSDA proposal, it remains a mere approximation for solid state calculations. LSDA describes successfully the ground state properties of metals and the Kohn-Sham eigenvalues are sometimes found to agree reasonably well with quasi-particle energies from experiments in photo-emission. However, LSDA tends to overestimate atomization energies and under-estimate bulk volumes [104].

2.5.2 Generalized Gradient Approximation (GGA)

GGA was developed to address the short comings of LSDA, it maintains all the features of LSDA and incorporate a correlation functional that is to correct the second order gradient expansion [105] in a slow

varying limit of density. With this correction, GGA partly takes into account changes in the electron density in the vicinity of the point of interest [106] and this is very important when points of consideration are near the nuclei, where the electron density is changing strongly. Energy functionals in GGA depend on the density and its gradient, and they also maintain the analytical properties of exchange correlation of the LSDA. The exchange correlation energy in GGA is given by:

$$E_{XC}^{GGA}[n_\uparrow, n_\downarrow] = \int dr f(n(\mathbf{r}), n_\uparrow(\mathbf{r}), n_\downarrow(\mathbf{r}), \nabla n_\uparrow(\mathbf{r}), \nabla n_\downarrow(\mathbf{r})), \tag{2.5.8}$$

while the exchange correlation potential is given by

$$V_{xc}^{\sigma}(\mathbf{r}) = \left[\epsilon_{xc} + n\frac{\partial \epsilon_{xc}}{\partial n}\right]_{\mathbf{r}_{m,\sigma}} + \sum_{m'}\left[n\frac{\partial \epsilon_{xc}}{\partial|\nabla n|}\frac{\nabla n}{|\nabla n|}\right]_{\mathbf{r}_{m',\sigma}} \mathbf{C}_{m'-m}. \tag{2.5.9}$$

There are different versions of GGA: Chevary, et. al. version (PW91) [107], Perdew, et. al. version (PBE) [108], Becke et. al. version (BLYP) [109]. However, for the purpose of this research, we are going to use the PBE parametrization because it solves the problem encountered by PW91 with a simple construction of a version of GGA exchange correlation for all parameters. The correlation functional in this derivation is given by

$$E_C^{GGA} = \int d^3n[\epsilon_C^{unif}(r_s, \xi) + H(r_s, \xi, t)], \tag{2.5.10}$$

r_s in the above equation represents local Seitz radius given by $n = \frac{3}{4\pi r_s^3} = \frac{k_f^3}{3\pi^2}$, relative spin polarization $\xi = \frac{n_\uparrow - n_\downarrow}{n}$ while t is a dimensionless density gradient quantity given by $\frac{|\nabla n|}{2\phi k_s n}$, here ϕ in the t is given by $\frac{[(1+\xi)^{\frac{2}{3}} + (1-\xi)^{\frac{2}{3}}]}{2}$ which is a spin scaling factor and Thomas-Fermi screening wave number $k_s = \sqrt{\frac{4k_f}{\pi a_0}}$ and $a_0 = \frac{\hbar^2}{me^2}$. Perdew, et. al. [108] classify the regions of density variation in to three:

1. Slow variation limit (second-order gradient is corrected in the region of slow variation in density).
2. Rapid variation limit (satisfied sum rule)

   and
3. Region of uniform scaling (logarithmic singularity of ϵ_C^{unif} is cancelled [110]).

All the three regions satisfy a simple ansatz:

$$H = (\frac{e^2}{a_0})\gamma\phi^3 \times \ln\left\{1 + \frac{\beta}{\gamma}t^2\left[\frac{1+At^2}{1+At^2+A^2t^4}\right]\right\}, \tag{2.5.11}$$

where

$$A = \frac{\beta}{\gamma}[e^{\left\{\frac{-\epsilon_C^{unif}}{(\frac{\gamma\phi^3 e^2}{a_0})}\right\}} - 1]^{-1}, \tag{2.5.12}$$

β is a constant $\backsimeq 0.066725$. Function of H takes its value from the point $t = 0$ and monotonically grow to $t = \infty$, consequently, $E_C^{GGA} \leqslant 0$ which at high density, under uniform scaling tends to

$$-\frac{e^2}{a_0}\int d^3r n\gamma\phi^3 \times \ln\left\{1 + \frac{1}{\frac{\chi s^2}{\phi^2} + \left(\frac{\chi s^2}{\phi^2}\right)^2}\right\}, \tag{2.5.13}$$

where s is defined as $\frac{|\bigtriangledown|n}{2k_f n} = \left(\frac{r_s}{a_0}\right)^{\frac{1}{2}}\frac{\phi t}{c}$ which is a dimensionless gradient of density, $c = (3\pi^2/16)^{(1/3)} \simeq 1.2277$, χ is given by $(\beta/\gamma)c^2 e^{-\omega/\gamma} = 0.72161$. GGA-PBE exchange energy is constructed from four condition:

1. $\xi = 0$ everywhere, given

$$E_x = \int d^3r n\epsilon_x^{unif}(n)F_x(s), \tag{2.5.14}$$

where $\epsilon_x^{unif} = -3e^2k_F/4\pi$. In order to restore the right limit of a uniform gas, $F_x(0)$ the enhancement factor is set to zero.

2. Spin scaling is obeyed by exact form of the exchange energy i.e. $E_x[n_\uparrow, n_\downarrow] = \{E_x[2n_\uparrow] + E_x[2n_\downarrow]\}/2$

3. LSDA gives an excellent approximation to exchange correlation energy for small changes in density, while gradient expansion did not. To maintain this LSDA feature

$$F_x(s) \longrightarrow 1 + \mu s^2, \tag{2.5.15}$$

where $\mu = \beta(\pi^2/3) \simeq 0.21951$ effect of exchange gradient coefficient must cancelled that of correlation.

4. If the enhancement factor $F_x(\xi = 1, s) = 2^{(1/3)}F_x(s/2^{(1/3)})$ grows slowly, but progressively with s, the condition below (Lieb-Oxford bound)

$$E_x[n_\uparrow, n_\downarrow] \geq E_{xc}[n_\uparrow, n_\downarrow] \geq -1.679e^2\int d^3r n^{4/3} \tag{2.5.16}$$

will be satisfied. A form of enhancement factor, which satisfies eqn (2.5.15) and (2.5.16) is

$$F_x(s) = 1 + \kappa - \kappa/(1 + \mu s^2/\kappa) \tag{2.5.17}$$

with $\kappa = 0.804$.

The GGA proposed by Perdew et. al. [108] maintains the characteristics of LSDA together with gradient corrected non-locality. However, PW91 features like second order correction to exchange and correlation energy in slow varying limit and non-uniform scaling of exchange energy that are considered less important are sacrificed [108]. GGA however, fails to simultaneously describe exchange correlation energy densities as well as correlation potentials correctly in the limit $\mathbf{r} \to \infty$, which calls for further improvement to the approximation.

2.5.3 meta-GGA

In meta-GGAs, the exchange correlation energy expression include the Laplacian of the spin density. The exchange correlation is now of the form

$$E_{XC}^{\text{MGGA}}[n_\uparrow, n_\downarrow] = \int d^3\mathbf{r} n e_{XC}^{\text{MGGA}}(n_\uparrow, n_\downarrow, \nabla n_\uparrow, \nabla n_\downarrow, \nabla^2 n_\uparrow, \nabla^2 n_\downarrow, \tau\uparrow, \tau\downarrow) \tag{2.5.18}$$

where $\tau_\sigma(\mathbf{r}) = \frac{1}{2}\sum_\alpha \theta(\mu - \epsilon_{\alpha\sigma})| \bigtriangledown \psi_{\alpha\sigma}(\mathbf{r})|^2$ is the Kohn-Sham orbital kinetic energy of electrons with spin σ. Meta-GGAs achieve very accurate atomization energies of molecules, surface energies of metals and lattice constant of solids. Despite these advances, there are difficulties in expressing the exchange part of the energy.

There are various meta-GGA flavours [111], among them TPSS [112], M06L [113] and Modified Becke Johnson potential (MBJ) [114]. The later is known to predict electronic properties at an accuracy comparable to hybrid and GW at a lower computational cost [115].

MBJ used local approximation to atomic exchange potential together with screening term in the form

$$V_{x,\sigma}(\mathbf{r}) = cV_{x,\sigma}(\mathbf{r}) + (3c-2)\frac{1}{\pi}\sqrt{\frac{5}{12}}\sqrt{\frac{2T(\mathbf{r})}{n_\sigma(\mathbf{r})}}. \tag{2.5.19}$$

Where n_σ is the electron density, T kinetic energy density and $V_{x,\sigma}(\mathbf{r})$ is the Becke-Roussel potential given by

$$V_{x,\sigma}(\mathbf{r}) = -\frac{1}{b_\sigma(\mathbf{r})}\left[1 - e^{-x_\sigma(\mathbf{r})}\right]. \tag{2.5.20}$$

The $V_{x,\sigma}(\mathbf{r})$ was introduced to model Coulomb potential created by exchange hole. It is purely local and determined by the electron density, its derivatives and kinetic energy density. The function b_σ in

[1] It is important to note that MBJ has no exchange correlation energy, it take its correlation energy from LSDA and thus its calculations can not be self consistent with respect to energy. It also become unstable in vacuum at points where the electron density and the kinetic energy approach zero [114].

the equation above is given by

$$b_\sigma = \left[\frac{x_\sigma^3 e^{-x}}{(8\pi n_\sigma)}\right]^{1/3}, \tag{2.5.21}$$

and

$$c = \alpha + \beta\left(\frac{1}{V_{cell}}\int_{cell}\frac{|\nabla n(\mathbf{r}')|}{n(\mathbf{r}')}d\mathbf{r}'\right)^{1/2} \tag{2.5.22}$$

2.5.4 Hybrid Functionals

Hybrid-GGAs introduced by Becke [116, 117] try to overcome the difficulties encountered by GGAs by including exchange energy from Hatree-Fock expression into local/semi-local GGA/LDA exchange and correlation functions. A part of the non-local exact Hatree-fock-like exchange

$$E_x^{HF}(\mathbf{r},\mathbf{r}\prime) = -\frac{1}{2}\sum_{i,j}\int\int d^3\mathbf{r}d^3\mathbf{r}'\frac{\phi_i^*(\mathbf{r})\phi_j(\mathbf{r})\phi_j^*(\mathbf{r}')\phi_i(\mathbf{r}')}{|\mathbf{r}-\mathbf{r}'|} \tag{2.5.23}$$

is mixed with complementary GGA / LDA semi-local/local approximate exchange correlation. The hybrid functional is written as

$$E_{xc}^{hyb} = \alpha E_x^{exact} + (1-\alpha)E_x^{GGA/LDA} + E_c^{GGA/LDA} \tag{2.5.24}$$

where α is the mixing factor and it control the exact E_x^{HF} included in to the hybrid functional.

2.6 Van der Waals Corrections

Standard exchange correlation functionals in density functional theory (LDA, GGA, meta-GGA and hybrid) describe bonds, structures, lattice constants and many other properties of molecules and solids with varying degree of accuracy. However, fail to account for long range electron correlations that are the primary cause of van der Waal's interactions, resulting from dynamical correlations between fluctuating charge distributions, which play a significant role in layered structures. There have been attempts to improve approximate functionals to account for van der Waal's effects on biomolecules, polymers and van der Waal's complexes [118, 119, 120, 121, 122].

2.6.1 DFT-D2

Grimme [119, 123] proposed a method of including a van der Waal's correction term to the conventional DFT energy term E_{KS-DFT} to give the total corrected energy E_{DFT-D}

$$E_{DFT-D} = E_{KS-DFT} + E_{disp} \tag{2.6.1}$$

where E_{disp} is the empirical dispersion correction to the DFT energy and is given by

$$E_{disp} = -s_6 \sum_{i=1}^{N_{at}-1} \sum_{j=i+1}^{N_{at}} \frac{C_6^{ij}}{R_{ij}^6} f_{dmp}(R_{ij}) \tag{2.6.2}$$

where N_{at} represents the number of atoms in a given system, C_6^{ij} dispersion coefficient for atom pair ij, s_6 scaling factor, which depends on the nature of the DFT approximation used, and R_{ij} are inter-atomic distances. A damping function f_{dmp} is added to avoid singularities for small values of R_{ij}, with

$$f_{dmp}(R_{ij}) = \frac{1}{1 + e^{-d\left(\frac{(R_{ij})}{(R_r)} - 1\right)}} \tag{2.6.3}$$

where R_r is the sum of atomic van der Waal's radii. The dispersion coefficients R_{ij} and C_6^{ij} are given by

$$R_{ij} = R_i + R_j \tag{2.6.4}$$

$$C_6^{ij} = \sqrt{C_6^i C_6^j} \tag{2.6.5}$$

respectively, where C_6^a is expressed in term of atomic ionization potential I_p and static dipole polarizability α as $C_6^a = 0.05 N I_p^a \alpha^a$, N has a value of 2, 10, 18, 36 and 54 for row 1-5 atoms of the periodic table. For PBE, s_6 has been optimized by least-square method to be 0.75. In the recent DFT-D method [122] more accurate dispersion coefficients are calculated through time dependent DFT by recurrent relation through the use of the Casimir-Polder equation

$$C_6^{ij} = \frac{3}{\pi} \int_0^\infty \alpha^i(i\omega)\alpha^j(i\omega) d\omega \tag{2.6.6}$$

where $\alpha^i(i\omega)$ is the average dipole polarizability at an imaginary frequency ω.

2.6.2 vdW-DF

Langreth et. al. [124, 125] proposed non-local correlation energies to account for the van der Waal's effect, the correlation energy being of the form

$$E_c^{nl}[n] = \int d^3\mathbf{r} \int d^3\mathbf{r}' n(\mathbf{r}) \phi(\mathbf{r}, \mathbf{r}') n(\mathbf{r}'). \tag{2.6.7}$$

The kernel ϕ is a function of $Rf(\mathbf{r})$ and $Rf(\mathbf{r}')$, where $R = |\mathbf{r} - \mathbf{r}'|$ and $f(\mathbf{r})$ is a function of $n(\mathbf{r})$ and its gradient.

2.6.3 TS + SCS

Tkatchenko et. al. [126] proposed a method of calculating dispersion coefficients from London type dispersion formula by rescaling polarizabilities and atomic dispersion coefficients. Their dispersion energy is similar to that of Grimme et. al. [119] and is given by

$$E_{disp} = -\frac{1}{2}\sum_{A=1}^{N}\sum_{B=1}^{N}\sum_{L}{}' \frac{C_{6AB}}{r^{AB,L}} f_{damp}(r^{AB,L}), \tag{2.6.8}$$

Here, $r^{AB,L} = |r^{A,0} - r^{B,L}|$ sums over all N atoms and unit cell translation $L = (l_1, l_2, l_3)$, the prime shows that for $L = 0, A \neq B$. The new feature in TS + SCS is in the computation of dispersion coefficient C_{6AB}^{TS} and static polarizabilities α_A^{TS} which are computed in the following way

$$\alpha_A^{TS} = \frac{V_A^{eff}}{V_A^{free}} \alpha_A^{free}, \tag{2.6.9}$$

the first term on the right hand sign represents the ratio of effective volume atom in molecule or solid V_A^{eff} that of a free non-interacting atom V^{eff}. In a similar way, by rationalizing the London dispersion formula, the effective dispersion of a free atom and atoms in a molecule can be computed by

$$C_{6AA}^{TS} = \left(\frac{V_A^{eff}}{V_A^{free}}\right)^2 C_{6AA}^{free}, \tag{2.6.10}$$

The Hirshfeld partition formula for all electrons density is then used to obtain the atomic volumes

$$\frac{V_A^{eff}}{V_A^{free}} = \frac{\int r^3 \omega_A(\mathbf{r}) n(\mathbf{r}) d^3(\mathbf{r}))}{\int r^3 n_A^{free}(\mathbf{r}) d^3(\mathbf{r})} \tag{2.6.11}$$

The n_A^{free} in the above equation represents the spherically average electron density of a neutral atom and ω_A the Hirshfeld weight by

$$\omega_A(\mathbf{r}) = \frac{n_A^{free}}{\sum_B n_B^{free}} \tag{2.6.12}$$

The sum here runs over all the atoms in the system. The dipole-dipole dispersion between unlike atoms is given by

$$C_{6AA} = \frac{2C_{6A}C_{6B}}{\left[\frac{\alpha_B}{\alpha_A}C_{6A} + \frac{\alpha_A}{\alpha_B}C_{6B}\right]} \tag{2.6.13}$$

To eliminate inaccurate interactions at close range distances, a damping function of the form is used

$$f_{damp}(r^{AB,L}) = \frac{1}{1 + e^{\left[-d\left(\frac{r^{AB,L}}{S_R R_{AB}^{eff}} - 1\right)\right]}} \tag{2.6.14}$$

where the d parameter is fixed at 20 and the scaling coefficient S_R, which is peculiar to the DFT exchange correlation functional used, has been optimised to be 0.94 for the PBE functional. R_{AB}^{eff} which stands for the sum of atomic radii is given by

$$R_{AB}^{eff} = R_A^{eff} + R_B^{eff} \tag{2.6.15}$$

and each can be calculated by rescaling free atom vdW radii as

$$R_A^{eff} = \left(\frac{\alpha_A^{TS}}{\alpha_A^{free}}\right)^{\frac{1}{3}} R_A^{eff} \tag{2.6.16}$$

R_A^{eff} is taken here to be the radius at which electron density of a free atom is the same as half the equilibrium distance in a dimer of noble gas atom in the same row in the periodic table as the atom under consideration. The term $\alpha_A^{SCS}(iw)$, is however, computed by solving screening equation self-consistently in the recent method of TS + SCS [127] through

$$\alpha_A^{SCS}(i\omega) = \alpha_A^{TS}(iw) - \alpha_A^{TS}(i\omega) \sum_{A \neq B} \tau_{A,B} \alpha_B^{CSS}(iw) \tag{2.6.17}$$

here, $\tau_{A,B}$ stands for the dipole interaction tensor and the effective frequency dependent polarizability is

$$\alpha_A^{TS}(iw) = \frac{\alpha_A^{TS}}{1 + \left(\frac{\omega}{\omega_A}\right)^2} \tag{2.6.18}$$

where ω_A is the mean excitation frequency given by

$$\omega_A = \frac{3}{4} \frac{C_{6AA}^{TS}}{\left(\alpha_A^{TS}\right)^2} \tag{2.6.19}$$

The TSC +SCS dispersion coefficient can be calculated from the Casimir-Polder integral as

$$C_{6AA} = \frac{3}{\pi} \int_0^\infty \alpha_A^{SCS}(i\omega) \alpha_A^{SCS}(i\omega) d\omega \tag{2.6.20}$$

and the van der Waal's radii R_A^{SCS} obtained by rescaling the TS radii

$$R_A^{SCS} = \left(\frac{\alpha_A^{SCS}}{\alpha_A^{TS}}\right)^{\frac{1}{3}} R_A^{TS}. \tag{2.6.21}$$

The value of S_R is optimized in a way similar to TS and found to be 0.97 for PBE functionals.

3. The GW Approximation

Generally speaking, properties of matter can be categorized into two groups: electronic ground state and electronic excited states. DFT describes exactly the ground state properties. It fails to describe excited properties of materials [92]. To be specific, for example, it underestimates band gaps in insulators and semiconductors by as much as fifty percent [78], yield wrong band order in some cases [128], there is significant deviation in DFT calculated optical spectra when compared with that of experiment [129] .

The error in the DFT calculated excited properties of material is because the eigenvalues of KS theory are Lagrangian parameters meant to ensure orthogonality of orbitals of particles. As such the eigenvalues should be considered as mathematical tools with no physical meaning except that the square of the eigenfunctions will sum to exact ground state density. In fact, there has been no formal justification that relates KS eigenvalues to dispersion energy of quasi-particles in solids, with exception that highest occupied KS eigenvalues has been identified to be the chemical potential of metals [130] and negative ionization energy for semiconductors and insulators [131, 92].

In order to overcome the shortcomings of DFT, many-body perturbation techniques can be used as post-DFT approximations to improve the calculated values of band gaps [57]. This approach is based on the concept of quasi-particles and the well known Green function method [132, 92].

Nevertheless, results from DFT calculations are ingredients to the GW approximation [133, 134, 135]. Eigenvalues and eigenfunctions from KS-DFT are used together with many body Green function techniques in construction of the electronic self energy in GW quasi-particle approximation [58].

3.1 Quasi-Particles

Electrons in solids repel each other through Coulombic potential, as a result the electron surrounds itself with a positively charged screening which, together with the electron, form a quasi-particle [92]. The quasi-particles interact with each other via a screened potential instead of the Coulombic potential. Quasi-particles therefore offer the opportunity of dealing with weakly interacting particles rather than a complicated system of strongly interacting particles.

3.2 Self Energy

The difference in energy between a quasi-particle and a bare particle is described in terms of the Self energy (energy of a bare particle interacting with itself through the polarization cloud that the particles generate in a many body system). Usually, the self energy accounts for exchange and correlation effects beyond the Hatree-Fock approximation, it is non local, energy dependent and non-Hermitian in general [92, 136]. It is not possible to determine the self energy of real systems exactly. However, it can be determined by approximations such as the screened interaction or the GW approximation proposed by Hedin [58]. The behaviour of quasi-particles is governed by an equation called the quasi-particle equation [137], written in the form

$$\left[-\frac{\hbar^2}{2m_e}\nabla^2(\mathbf{r}) + V_H(\mathbf{r}) + V_{ext}(\mathbf{r})\right]\Psi_i(\mathbf{r}) + \int dr'\Sigma(\mathbf{r},\mathbf{r}',E_i)]\Psi_i(\mathbf{r}') = E_i\Psi_i(\mathbf{r}), \tag{3.2.1}$$

where $\Sigma(\mathbf{r},\mathbf{r}',E_i)$ is the self energy, $V_H(\mathbf{r})$ is the Hartree potential of electrons given by

$$V_H(\mathbf{r}) = \int d\mathbf{r}'\frac{n(\mathbf{r}')}{|\mathbf{r}-\mathbf{r}'|}, \tag{3.2.2}$$

n is the electron density $V_{ext}(\mathbf{r})$ is the external potential from the ions, E_i and $\Psi_i(\mathbf{r}')$ are the quasi-particle energy and wave function respectively. The quasi-particle wave functions are obtained from KS-DFT ground state calculations, while the quasi-particle energy is given by

$$E_i = Re\left(\langle\Psi_i|H_{KS} - v_{xc}^{\sigma} + \Sigma_{GW}|\Psi_i\rangle\right) \tag{3.2.3}$$

3.3 Green Function

Significant physical information in many body theory can be extracted from a Green function [96]. Quasi-particle properties like lifetimes, energy and expectation values of single particle operators (total energy of many body system and density) are obtained from the single particle Green function [92].

In general, the Green function G of a linear operator $\mathcal{L}$ is given by [138]

$$[z - \mathcal{L}(r)]G(x,x';z) = \delta(x-x'), \tag{3.3.1}$$

where $\delta(x-x')$ is the Dirac delta function. If for example, and external potential acted on a single quantum particle, one will obtains

$$\left[-\frac{\hbar^2}{2m}\nabla^2 + V_{ext}(\mathbf{r}) - E\right]G^{(0)}(\mathbf{r},\mathbf{r}';E) = -\delta(\mathbf{r}-\mathbf{r}'). \tag{3.3.2}$$

It can be proved [83] that one particle Green function for many electron system satisfies

$$\left[-\frac{\hbar^2}{2m}\nabla^2 + V_{ext}(\mathbf{r}) - E\right] G(\mathbf{r},\mathbf{r}';E) + \int dr''\Sigma(\mathbf{r},\mathbf{r}'';E)G(\mathbf{r}'',\mathbf{r}';E) = -\delta(\mathbf{r}-\mathbf{r}'). \tag{3.3.3}$$

If the Hamiltonian is time dependant, G will explicitly depends on time difference $t-t'$, i.e. $G \equiv G(\mathbf{r},t;\mathbf{r}',\mathbf{t}')$. Fourier transforming the $G(\mathbf{r},t;\mathbf{r}',\mathbf{t}')$ with respect to $t-t'$ will lead to a function that is energy dependent [138].

Physically, one can interpret $G(\mathbf{r},t;\mathbf{r}',\mathbf{t}')$ as the probability of finding an electron at a point $\mathbf{r}$ in space and time t given that it was at $\mathbf{r}'$ at time t'.

If the value of $G_0(\mathbf{r}'',\mathbf{r}';E)$ for a reference related system is known exactly, the value of $G(\mathbf{r}'',\mathbf{r}';E)$ for any required real system can be obtain by many body perturbation theory through the use of the Dyson equation

$$G(\mathbf{r},\mathbf{r}';E) = G_0(\mathbf{r},\mathbf{r}';E) + \int\int d\mathbf{r_1}d\mathbf{r_2}G_0(\mathbf{r},\mathbf{r_1};E)\Delta\Sigma(\mathbf{r_1},\mathbf{r_2};E)G(\mathbf{r_2},\mathbf{r}';E), \tag{3.3.4}$$

where

$$\Delta\Sigma(\mathbf{r_1},\mathbf{r_2};E) = \Sigma(\mathbf{r_1},\mathbf{r_2};E) - v_0(\mathbf{r_1},\mathbf{r_2}) \tag{3.3.5}$$

is the perturbation on the system expressed via the interaction potential $v_0(\mathbf{r_1},\mathbf{r_2})$ of the reference system. For a non interacting electron system $v_0 = 0$ and $G(\mathbf{r}'',\mathbf{r}';E)$ can be shown to be:

$$G_0(\mathbf{r},\mathbf{r}';E) = \Sigma_i \left\{ \frac{\psi_i(\mathbf{r})\psi_\mathbf{i}^*(\mathbf{r}')}{E-E_i} \right\}, \tag{3.3.6}$$

with ψ_i and E_i being the solutions of single particle equation and eigenvalues, respectively, and the reference system is normally taken as the Kohn-Sham system.

3.4 GW Approximation

The Self energy can be obtained via the solution of the many body problem, the solution involves the two-particle Green's function [139], but this method is not practicable. The practicable way of obtaining the Self energy is the GW approximation proposed by Hedin [58] where the self energy is expanded in terms of dynamically screened Coulomb interaction but maintaining the first term in the expansion W.

$$\sum_{GW}(\mathbf{r},\mathbf{r}';t) \simeq iG(\mathbf{r},\mathbf{r}';t)W(\mathbf{r},\mathbf{r}';t), \tag{3.4.1}$$

in energy domain

$$\sum_{GW} = j \int dE' G(\mathbf{r}, \mathbf{r}'; E + E') W(\mathbf{r}, \mathbf{r}'; E) \tag{3.4.2}$$

The screened interaction is expressed in terms of bare the Coulomb interaction

$$W(\mathbf{r}, \mathbf{r}'; E) = v(\mathbf{r}, \mathbf{r}') + \int \int W(\mathbf{r}, \mathbf{r}'; E) P(\mathbf{r_1}, \mathbf{r_2}; E) v(\mathbf{r_2}, \mathbf{r}') d\mathbf{r_1} d\mathbf{r_2} \tag{3.4.3}$$

and in terms of the dielectric function

$$W(\mathbf{r}, \mathbf{r}'; E) = \int \int \epsilon^1(\mathbf{r}, \mathbf{r}'; E) v_2(\mathbf{r}, \mathbf{r_1}) d\mathbf{r_1}, \tag{3.4.4}$$

where the polarization P is given by

$$P(\mathbf{r}, \mathbf{r}'; E) = -jG(\mathbf{r}, \mathbf{r}'; E) G(\mathbf{r}', \mathbf{r}; E). \tag{3.4.5}$$

In practice, equations (3.3.5), (3.4.1), (3.4.3) and (3.4.5) are solved self consistently. The Random phase approximation (RPA) is normally used to calculate the dielectric function $\epsilon(\mathbf{r}, \mathbf{r}'; E)$. Frequency dependent RPA evolved from plasmon pole model to recent full RPA dielectric function [140].

The simplest approximation, sometimes denoted by G_0W_0, is to use the DFT eigenfunctions and eigenenergies to construct G and W. Other approximations result if the quasi-particle energies and/or wave functions are updated in a self-consistent cycle [128, 132, 141, 142].

In this work different GW approximations will be used to calculate the band gap and optical properties of semi-conducting transition metal chalcogenides. Comparison to experiment, where possible, will be used to benchmark the GW approximation for this study.

3.5 Bethe-Salpeter equation (BSE)

Recall that in Section 5.10 of this thesis, we discussed how DFT is ill equipped to describe the fundamental band gap of semiconductors and insulators, because DFT eigen-energies do not correspond to quasi-particle energies required to describe the process of addition or removal of electrons and how in Section 3.4, we described the GW level of approximation, which is used to to account for many body electron-electron interaction. This method describes accurately photo emission and inverse photo emission spectra. It however, fails in the description of optical excitations, where the number of electrons do not change [143, 144, 145]. To address this shortcoming, one need go beyond the GW one-particle

Green's function and account for two-particle Green's function by solving the well known BSE equation [143, 146, 147].

In wide band gap semiconductors, the screening is weak and the electron-hole interaction is expected to be very strong. One need the BSE to account for such electron-hole interaction in order to calculate optical absorption spectra [143, 148, 149]. In order to do this, one needs to use the results from the GW approximation and construct the statically screened-electron-hole interaction term $W\left(X,X';\omega=0\right)$ and the spectra of the single particle. The two particle BSE Hamiltonian is of the form:

$$H_{vc\mathbf{k},v'c'\mathbf{k}'}=\left(E_{c\mathbf{k}}-E_{v\mathbf{k}}\right)\delta_{vv'}\delta_{cc'}\delta_{\mathbf{k}\mathbf{k}'}+2\int\int d^3xd^3x'\Psi^*_{c\mathbf{k}}\left(\mathbf{X}\right)\Psi_{v\mathbf{k}}\left(\mathbf{X}\right)\times\overline{v}\left(\mathbf{X}-\mathbf{X}'\right)\Psi_{c'\mathbf{k}'}\left(\mathbf{X}'\right)\Psi^*_{v'\mathbf{k}'}\left(\mathbf{X}'\right)$$
$$-\int\int d^3xd^3x'\Psi^*_{c\mathbf{k}}\left(\mathbf{X}\right)\Psi_{v'\mathbf{k}'}\left(\mathbf{X}\right)$$
$$\times W\left(\mathbf{X},\mathbf{X}';\omega=0\right)\Psi_{c\mathbf{k}}\left(\mathbf{X}'\right)\Psi^*_{v'\mathbf{k}'}\left(\mathbf{X}'\right), \tag{3.5.1}$$

where $\overline{v}$ represents the bare Coulomb kernel given by [143] $\left(\frac{1}{|\mathbf{x}-\mathbf{x}'|}\right)$, $(E_{c\mathbf{k}},E_{v\mathbf{k}})$ are the single particle QP energies [148].

The polarization, in a number of BSE calculations [148, 150], is expanded in products of single particle conduction (c) and valence (v) bands states using DFT orbitals.

4. Pseudo-potentials and the PAW Method

4.1 Solution to K-S equation

In Chapter 2, we have shown how we can express observables in a many-body problem into equal observables in a single-particle problem. However, there is great task of expressing infinite number of mobile non-interacting electrons in a static potential of infinite ions or nuclei. In order to do this, two difficulties need to be overcome:

1. For each of the infinite number of electrons, wave function has to be calculated.

2. Because the electronic wave functions stretches over the whole solid, the basis set needed for the expansion of each of the wave functions has to be infinite.

The two problems can be overcome by doing calculations on periodic systems and using the famous Bloch's theorem for electronic wave function.

4.1.1 Bloch's Theorem

States that the electronic wave function of a periodic solid can be expressed as the product of the Bravais lattice periodicity and its plane waves. i.e.

$$\psi_k(\mathbf{r}) = e^{[\mathbf{ik.r}]} f_i(\mathbf{r}) \tag{4.1.1}$$

where $e^{[\mathbf{ik.r}]}$ is the plane waves and $f_i(\mathbf{r})$ the lattice periodicity. The expansion of the periodic part of the cell can be done using discrete form of plane wave basis sets, in which the wave vector and the reciprocal lattice vectors are the same. i.e.

$$f_i(\mathbf{r}) = \sum_G C_{i,\mathbf{G}} e^{i[\mathbf{G.r}]}, \tag{4.1.2}$$

where G stands for the reciprocal lattice vector, given by $\mathbf{G.L} = 2\pi m$ for all lattice vectors of the crystal L and m is an integer. The electronic wave function can now be expressed in term of plane waves as

$$\psi_k(\mathbf{r}) = \sum_G C_{i,\mathbf{k}+\mathbf{G}} e^{[i(\mathbf{k}+\mathbf{G}).\mathbf{r}]}. \tag{4.1.3}$$

It is now clear that the problem of solving K-S equation has been reduced to that of calculating a finite number of electronic wave functions in a unit cell.

By using plane waves as basis set for electronic wave functions, K-S equations assumes a very simple form. Putting (4.1.1) into (2.4.1) and integrating over r, one obtains a secular equation

$$\sum_{G}\left[\frac{\hbar^2}{2m}|\mathbf{k}+\mathbf{G}|^2\delta_{\mathbf{G}\mathbf{G}'}+V^{\sigma}_{\mathbf{R}}(\mathbf{G}-\mathbf{G}')\right]C_{i,\mathbf{k}+\mathbf{G}'}=\varepsilon_i C_{i,\mathbf{k}+\mathbf{G}'}. \tag{4.1.4}$$

From eqn. (4.1.4) above, we can see that the kinetic energy matrix element is diagonal in the reciprocal space and the different potentials can be described in term of Fourier transforms. The solution of the equation can be obtained through the diagonalization of the Hamiltonian matrix with elements in the brackets of eqn above.

4.1.2 Cut-off energy

The choice of $\frac{\hbar^2}{2m}|\mathbf{k}+\mathbf{G_c}|^2$ (cut-off energy) in equation (4.1.4) determine the size of the matrix, the cut-off energy is the highest kinetic energy of plane waves included in summing the K-S eigen states.

Having reduced the problem of solving K-S equation into that of calculating finite a number of electronic wave functions in a unit cell, we are now facing the problem of solving the electronic problem for an infinite number of Bloch states: there are infinite k points in the first Brillouin zone (primitive cell in reciprocal space) of the periodic lattice. There are nearby k vectors that carry the same information as the infinite Bloch states, making it possible to reproduce desired physical property at desired computational accuracy by using the wave function at the finite k point in the Brillouin zone [83, 151].

4.1.3 K points and Brillouin zone

From the symmetric properties of the wave function, it is clear that there are classes of k points in which the wave function and the phase factor are in phase with the periodicity of the unit cell of the solid. In order to determine the reciprocal lattice vectors of such a cell, we need a set of three smallest independent k points, so also for the primitive cell vectors.

If Ω is the unit cell volume, the first Brillouin zone is given by

$$\Omega_R = b_1.(b_1\times b_3)=\frac{(2\pi)^3}{\Omega}. \tag{4.1.5}$$

Monkhorst-Pack [152] and Chadi and Cohen [153] devised an accurate method of sampling the Brillouin zone. By using any of these methods, we can get better approximation to the total energy and electronic potential of a semiconductor or an insulator by calculating their electronic states at a very small number

of k points. It is however, more difficult to calculate the total energy and the electronic potential if the system is metallic due to a dense set of k points needed to define the Fermi surface [83].

4.2 Pseudopotential

Electrons in solids can be divided into core (highly localized) and valence (extended and responsible for bonding) electrons. It is believed that the physical properties of solids depends more on valence electrons than core electrons [96, 154, 83]. Pseudopotential approximation uses this advantage and replaces the core electrons and strong ionic potential with a weaker pseudopotential that acts on a set of pseudo wave functions in place of the true valence wave function. The pseudo wave function mimics the potential of the valence and core electronic states [155, 156, 157].

Let $|\psi_c\rangle$ and $|\psi_v\rangle$ be the exact solution to Schrödinger equation for core and valence electron respectively. Then

$$\widehat{H}|\psi_n\rangle = E_n|\psi_n\rangle, \tag{4.2.1}$$

where $n = c, v$. In order to maintain the orthogonality that exists between the valence and core wave functions, the wave function of the valence oscillates rapidly in the vicinity filled by the core electron from the strong potential in the region. The valence orbitals can therefore be expressed as a sum of a smooth function and an oscillating function due to this orthogonality.

$$|\psi_v\rangle = |\varphi_v\rangle + \sum_c \alpha_{cv}|\psi_c\rangle, \tag{4.2.2}$$

here $\alpha_{cv} = -\langle\psi_c|\varphi_v\rangle$, re-writing Schrödinger equation for the smooth orbital, we have

$$\widehat{H}|\varphi_v\rangle = E_v|\varphi_v\rangle + \sum_c (E_c - E_v)\,|\psi_c\rangle\langle\psi_c|\varphi_v\rangle. \tag{4.2.3}$$

The equation (4.2.3) shows that $|\varphi_v\rangle$ satisfy Schrödinger-like equation with energy dependent pseudo-Hamiltonian

$$\widehat{H}^{PK} = \widehat{H} - \sum_c (E_c - E)\,|\psi_c\rangle\langle\psi_c|. \tag{4.2.4}$$

From eqn (4.2.4), we can identify the pseudopotential $\widehat{w}^{PK}$ as

$$\widehat{w}^{PK}(E) = \widehat{v} - \sum_c (E_c - E)|\psi_c\rangle\langle\psi_c|. \tag{4.2.5}$$

$\widehat{v}$ stands for the true potential of the system and $\sum_c (E_c - E)|\psi_c\rangle\langle\psi_c|$ the repulsive potential which makes the pseudopotential near the core much weaker than the true potential.

Philips and Kleinman [78, 158, 159] suggested that pseudopotential can be cast into the form

$$w(\mathbf{r},\mathbf{r}') = \sum_{l}\sum_{m=-l} Y^{*}_{lm}(\widehat{\mathbf{r}})w_l(r,r')Y_{lm}(\widehat{r'}) \tag{4.2.6}$$

Y_{lm} represents spherical harmonics, and eqn (4.2.6) shows that w_l is angular momentum l dependent. Kleinman and Bylander [160] expresses it in a separable form as

$$w_l(r,r') = v_l(r)v_l(r'), \tag{4.2.7}$$

with semi local form

$$w(r,r') = w_l(r)\delta(r-r'). \tag{4.2.8}$$

To achieve more realistic pseudopotential, Topp and Hopfield [161, 162] put forward a suggestion that a pseudopotential should be adjusted in such a way that they can accurately describe charge density. As a result, today's pseudopotential are generated by inverting the free Schrödinger equation for a given system and forcing the pseudo wave function to be similar to the true wave function after a given distance r_l. The pseudo wave function are also forced to be norm conserving. The eigen energy values of the pseudopotential should have the same value as the true valence eigen values. The last three imposed condition can be expressed as

$$R^{PP}_{l}(r) = R^{AE}_{n}(r), \qquad if \qquad r > r_l, \tag{4.2.9}$$

$$\int_0^{rl} dr|R^{PP}_{l}(r)|^2 r^2 = \int_0^{rl} dr|R^{AE}_{nl}(r)|^2 r^2, \qquad for \qquad r < r_l \tag{4.2.10}$$

and

$$\varepsilon^{PP}_{l} = \varepsilon_n l^{AE}. \tag{4.2.11}$$

The additional condition imposed on the pseudo potential is that its wave function must not have nodal surfaces.

These conditions leads to the construction of pseudopotential that are norm-conserving and semi-local that only depend on the reference system electronic energy level ε^{AE}_{l}.

4.3 Projector augmented waves (PAWS)

PAW was introduced by Blöch in 1994 [163], the approach decomposes the all electron wave function into a smooth pseudo wave function, and a rapidly varying localized contribution within the core, while retaining its all electron character.

In PAW, the relationship between the pseudo and the true wave functions are given by the linear transformation:

$$|\varphi_{AE}\rangle = |\tilde{\varphi}_{PS}\rangle + \sum_i \left(|\Phi_{iAE}\rangle) - |\tilde{\Phi}_{iPS}\rangle\right) \langle \tilde{p}_i|\tilde{\varphi}_{PS}\rangle. \tag{4.3.1}$$

The φ_{PS} (pseudo wave functions) are variational quantities, index i stands for atomic site $\mathbb{R}$. The Φ_{iAE} all electron (AE) partial waves are derived for the reference atom, it is expected that $\tilde{\Phi}_{iPS} = \Phi_{iAE}$ outside the core radius and the two should continuously match inside the core radius, r_c^l, which is usually chosen to be half nearest neighbour distance [164, 165]. Due to linearity, the projection operators are required to satisfy a bi orthogonality condition

$$\langle \tilde{p}_i|\tilde{\varphi}_{PS}\rangle = \delta_{ij} \tag{4.3.2}$$

The charge density of the AE can be derived from eqn (4.3.1)

$$\eta(\mathbf{r}) = \tilde{\eta}(\mathbf{r}) + \eta^1(\mathbf{r}) - \tilde{\eta}^1(\mathbf{r}), \tag{4.3.3}$$

where the pseudo charge density is obtained from a pseudo wave functions on plane wave grid

$$\eta(\mathbf{r}) = \sum_n f_n \langle \tilde{\varphi}_{PS}|\mathbf{r}\rangle\langle \mathbf{r}|\tilde{\varphi}_{PS}\rangle, \tag{4.3.4}$$

and the pseudized charged densities η^1 and $\tilde{\eta}^1$ are evaluated using radial grid and are defined as

$$\eta^1\mathbf{r} = \sum_{(i,j)} \rho_{i,j} \langle \Phi_i|\mathbf{r}\rangle\langle \mathbf{r}|\Phi_j\rangle, \tag{4.3.5}$$

$$\tilde{\eta}^1\mathbf{r} = \sum_{(i,j)} \rho_{i,j} \langle \tilde{\Phi}_i|\mathbf{r}\rangle\langle \mathbf{r}|\tilde{\Phi}_j\rangle, \tag{4.3.6}$$

where $\rho_{i,j}$ is the occupancies for each augmentation (i,j), which are calculated from pseudo wave function by applying the projector function

$$\rho_{i,j} = f_n \sum_n \langle \tilde{\varphi_n}|\tilde{p_i}\rangle\langle \tilde{p_j}|\tilde{\varphi_n}\rangle. \tag{4.3.7}$$

In a complete set of projector operators, within the augmentation spheres $\eta^1 = \tilde{\eta}^1$.

The total energy is expressed as a sum of a smooth functions $\tilde{E}$ which is evaluated on a regular grid in Fourier or real space and two one-centre contributions denoted by E^1 and $\tilde{E}^1$, which are evaluated on the radial grid in angular momentum representation. The total energy is given by

$$E = \tilde{E} + E^1 - \tilde{E}^1, \tag{4.3.8}$$

with $\tilde{E}$, E^1 and $\tilde{E^1}$ defined as

$$\begin{aligned}\tilde{E} = &\sum_n f_n \langle \tilde{\varphi}_n| - \frac{1}{2}\Delta|\tilde{\varphi}_n\rangle + E_{xc}\left[\tilde{n}+\hat{n}+\tilde{n}_c\right] + E_H\left[\tilde{n}+\hat{n}\right] \\ &+ \int v_H\left[\tilde{n}_{zc}\right]\left[\tilde{n}\mathbf{r}+\hat{n}\mathbf{r}\right]d\mathbf{r} + U\left(\mathbf{R}, Z_{ion}\right),\end{aligned} \tag{4.3.9}$$

$$\begin{aligned}\tilde{E^1} = &\sum_{(i,j)} \rho_{ij}\langle \tilde{\phi}_i| - \frac{1}{2}\Delta|\tilde{\phi}_j\rangle + \overline{E_{xc}\left[\tilde{n}^1+\hat{n}+\tilde{n}_c\right]} + \overline{E_H\left[\tilde{n}^1+\hat{n}\right]} \\ &+ \int_{\Omega_r} v_H\left[\tilde{n}_{zc}\right]\left[\tilde{n}^1(\mathbf{r})+\hat{n}(\mathbf{r})\right]d\mathbf{r},\end{aligned} \tag{4.3.10}$$

$$E^1 = \sum_{(i,j)} \rho_{ij}\langle \phi_i| - \frac{1}{2}\Delta|\phi_j\rangle + \overline{E_{xc}\left[n^1+n_c\right]} + \overline{E_H\left[n^1\right]} + \int_{\Omega_r} v_H\left[n_{zc}\right] n^1(\mathbf{r})d\mathbf{r}, \tag{4.3.11}$$

where $\tilde{n}_c$ is the electronic core density, n_c the frozen core density, n_{zc} point charge density of the nuclei given by $n_{zc} = n_z + n_c$ and satisfy the condition

$$\int_{\Omega r} n_{zc}(\mathbf{r})d^3\mathbf{r} = \int_{\Omega r} \tilde{n_{zc}}(\mathbf{r})d\mathbf{r}. \tag{4.3.12}$$

5. Computational Details

5.1 Outline of Calculations

Throughout this work, the software Vienna-ab intio Simulation Package (VASP) [94, 166, 167] was used to perform electronic structure calculations. The Projector-augmented-wave approach (PAW) [163, 165] as implemented in VASP was used to describe electron-ion interaction. Both local density and generalised gradient approximations [101, 108, 168] were used for the exchange correlation functional. Typical DFT exchange correlation functional do not account properly for the van der Waals interactions, which are the dominant forces that determine inter layer separations in layered materials. The van der Waals correction terms proposed by Tkatchenko et. al. [126], Grimme et. al. [119, 122] and Langreth et. al. [124] were used to describe long range dispersion forces in such layered structures. Different suitable set of Monkorst-Pack mesh [152] were chosen for geometry optimisation in each structure.

5.2 Test of convergence

A numerical calculation is said to be well converged when its produces a result that is approximately equal to the true solution of the mathematical problem [169, 170]. There are two parameters that need to be converged in any DFT calculation: k points (k spacing) with respect to total energy and plane waves cut off energy (the number of basis functions) with respect to total energy.

5.2.1 K point convergence

As we have seen in Section 4.1.3, there are accurate ways by which the Brillouin zone can be sampled. Appropriate Brillouin zone sampling is important in order to strike a balance between computational accuracy and efficiency. The nature of the system under study determines the way the Brillouin zone is to be sampled: metallic systems require denser kpoints as compared to semiconductors and insulators. The "smearing method" also affects the choice of kpoints. This makes it necessary to converge kpoints with respect to energy and achieve a desired accuracy. An example of k-points convergence with respect to energy is depicted in Fig. 5.1. In this research, the tetrahedron method [171, 172] with Blöchl correction was used, a method known to converge kpoints rapidly and give accurate description of energies and

electronic density [172].

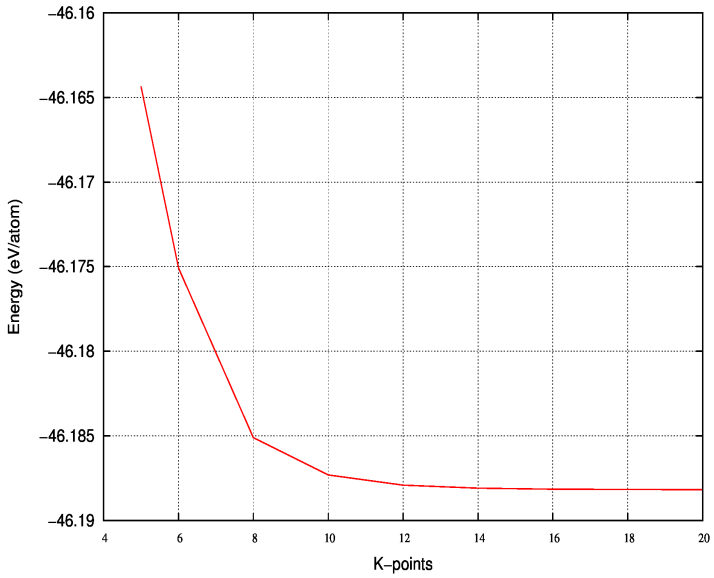


Figure 5.1: K point convergence.

5.2.2 Cut-off energy convergence

As we have seen in Section 4.1.2 that not all the kinetic energy in the solution of K-S equation are included in the calculations and that in the solution of equation (4.1.1), evaluating the solution of K-S equation at any point in k space, requires summation of infinite different possible values of G. This can not be realistic for practical calculation. Luckily, the function in the equation appears to have the same interpretation as Schrödinger equation, with solution of the form

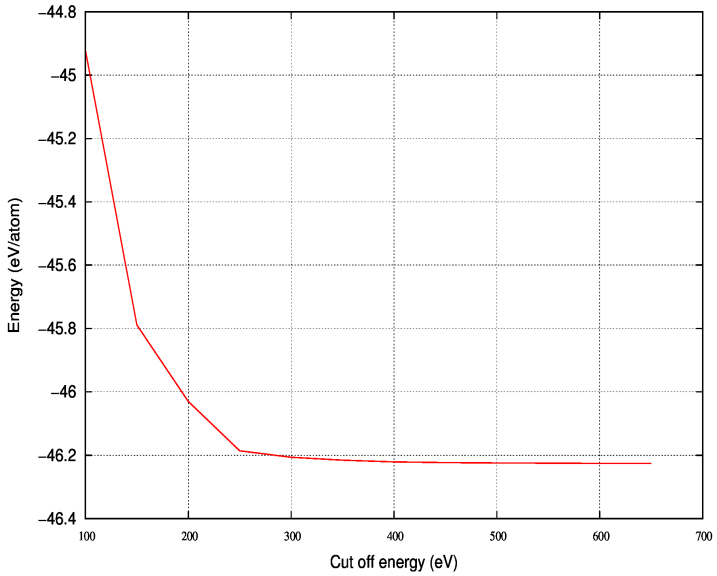


Figure 5.2: Cut-off energy convergence.

$$E = \frac{\hbar^2}{2m}|\mathbf{k} + \mathbf{G_c}|^2. \tag{5.2.1}$$

It is therefore logical to expect that lower energy solutions are more important than higher energy solutions. This accord us the opportunity to truncate the infinite sum in the equation (5.2.1) and include energies with values less than

$$E_{cut} = \frac{\hbar^2}{2m}\mathbf{G}^2_{cut}. \tag{5.2.2}$$

A sample of cut-of energy convergence graph is shown in Fig. 5.2.

5.3 Equation of states

Understanding the pressure, volume, temperature (P-V-T) relationship (equation of state (eos)) is of importance to both basic and applied scientist [173, 174]. There are many theoretical and semi empirical description of equation of state [174]. In this research, third order-Birch-Murnaghan eos was used [175]. The third order-Birch-Murnaghan eos, which is the simplest form of eos predicts bulk modulus B_0, which measures the material ability to resist change in volume due to uniform expansion of compression

$$B_0 = -V\left(\frac{\partial P}{\partial V}\right)_T, \tag{5.3.1}$$

which when differentiated with respect to pressure gives a dimensionless parameter B_0'

$$B_0' = \left(\frac{\partial B_0}{\partial P}\right)_T . \tag{5.3.2}$$

The quantity B_0' tests the dependence of the bulk modulus at equilibrium on pressure, it can be measured experimentally and can be used to test the accuracy of our ab-inition calculations. We should remember that we can express pressure as a function of energy as

$$P(V) = -\left(\frac{\partial E}{\partial V}\right)_S . \tag{5.3.3}$$

The system is said to be at equilibrium when its pressure is zero and all quantities are donated the subscript "0". Energy in Birch-Murnaghan eos is expressed as

$$E(V) = E_0 + \frac{9V_0B_0}{16}\left\{\left[\left(\frac{V_0}{V}\right)^{\frac{2}{3}} - 1\right]^3 B_0' + \left[\left(\frac{V_0}{V}\right)^{\frac{2}{3}} - 1\right]^2 \left[6 - 4\left(\frac{V_0}{V}\right)^{\frac{2}{3}}\right]\right\} , \tag{5.3.4}$$

where E_0 and V_0 are equilibrium energy and volume at zero pressure. Using eqn (5.3.3), we can express pressure in Birch-Murnaghan eos as

$$P(V) = \frac{3B_0}{2}\left[\left(\frac{V_0}{V}\right)^{\frac{7}{3}} - \left(\frac{V_0}{V}\right)^{\frac{5}{3}}\right]\left\{1 + \frac{3}{4}(B_0' - 4)\left[\left(\frac{V_0}{V}\right)^{\frac{2}{3}} - 1\right]\right\} . \tag{5.3.5}$$

It should be noted that the only quantity calculated from DFT directly is the energy (cohesive energy) at zero temperature, whereas B_0' and B_0 are related to energy-volume curve and measure its curvature about the equilibrium volume.

To calculate the equilibrium lattice parameters of our structures and study their eos, we performed the calculations in two steps: in the first step, we relaxed the structural atoms and generate a guess equilibrium volume. In the second step, we performed a static DFT calculation by fixing the atomic positions using Blöchl tetrahedron correction. We then used least-square method to fit the cohesive energy as a function of volume on eqn (5.3.4), where the quantities B_0, E_0 , V_0 and B_0' are the fitting parameters. The energy, elastic properties and equilibrium structural parameters can then be easily obtained by performing calculations at the equilibrium volume.

5.4 Pressure phase transition

Application of external pressure to a solid material will cause the distance between its atom to decrease, which has the tendency to cause structural changes in the solid material. The Helmholtz free energy

$$F(V,T) = E(V,T) - TS(V,T), \tag{5.4.1}$$

where temperature (T) and volume (V) are independent variable and the Gibbs free energy

$$G(P,T) = H(P,T) - TS(P,T), \tag{5.4.2}$$

where the temperature and pressure (P) are the independent variables with the enthalpy defined by

$$H = E + PV, \tag{5.4.3}$$

are the basic quantities needed to determine the stability of the possible new structure [78]. For a structural phase transition to occur between two structures at constant pressure, the enthalpy of the two structures must be equal [176, 78].

From eqn (5.4.3), the cohesive energy of the two structures must be the same

$$E_1 + PV_1 = E_2 + PV_2, \tag{5.4.4}$$

for them to have the same enthalpy. Using eqn (5.3.3), we can see that for the two structures to satisfy the aforementioned condition, they must share a common tangent on the plot of cohesive energy as a function of volume for different phases of the same material or use eqn (5.4.4) and plot enthalpy curves. The point where the curves crosses gives the transition pressure [177].

5.5 Cohesive energy

In solids, cohesive energy (binding energy) is defined as the energy needed to dismantle the solid into its constituent atoms, with the atoms infinitely separated [170, 176, 178, 179]. In *ab-initio* calculations, the cohesive energy is the difference between the calculated total energy of a unit cell and total energy of its isolated atoms [170, 180, 181] and it is given by

$$E_{coh} = E_{(crystal)} - E_{(atoms)} = E_{(crystal)} - \sum_{atom} E_{atom}^{isolated}. \tag{5.5.1}$$

In transition metal chalcogenide, cohesive energy per formula unit can be written as

$$E_{coh}^{tran_mChal_n} = \frac{E_{solid}^{tran_mChal_n} - Z \times \left(mE_{atom}^{tran} + nE_{atom}^{Chal}\right)}{Z \times (m+n)}. \tag{5.5.2}$$

where Z is the number of $tran_mChal_n$ in a unit cell of the considered transition metal chalcogenide, E_{atom}^{tran} and E_{atom}^{Chal} are atomic energies of the transition metal and the chalcogenide respectively, m and n are integers (stoichiometric weight).

It should be noted that for eqn (5.5.2) to have any physical meaning, the same level of accuracy must be used in calculating both the atomic and the crystal energies [182, 183]. In this research, cohesive energy was extracted from the fitting of the third order Birch-Murnaghan eos and it is used to predict structural stability.

5.6 Formation energy

Apart from cohesive energy, another factor used in predicting the relative stability of our structures is formation energy. Formation energy is defined as the energy released when individual atoms condenses to form a solid [170, 184]. The use of formation energy as a test for the formation of a structure and its phases relative thermodynamic stability is a common practice in *ab-initio* calculations [182], and it is obtained from the difference between the energy of the products $E_{coh}(product)$ (cohesive energy of the products) and the reactants cohesive energy $E_{coh}(reactants)$ [185, 170] given by

$$E_f = \sum E_{coh}(product) - \sum E_{coh}(reactant), \tag{5.6.1}$$

the most stable state at a specified temperature of the reactants should be used in predicting the formation energy [186].

If a solid M_mN_n is formed as a result of a reaction between the solid state of a transition metal M_m heated at a temperature of about 600 ° [60] and N_2 chalcogenide gaseous state through the reaction

$$mM^{solid} + \frac{n}{2}N_2^{gas} \leftrightharpoons M_mN_n^{solid}, \tag{5.6.2}$$

the formation energy eqn (5.6.1) will be

$$E_f(M_mN_n^{solid}) = E_{coh}(M_mN_n^{solid}) - \frac{mE_{coh}(M^{solid}) + \frac{n}{2}E_{coh}(N_2^{gas})}{m+n} \tag{5.6.3}$$

where the energy $E_f(M_mN_n^{solid})$ is the same as the cohesive energy in eqn (5.5.2)

The method described in Section 5.3 was used to determine the cohesive energy per atom of the studied structures.

5.7 Elastic constants

The study of the elastic properties of solid material are of great interest to researchers and technological industries [187], the knowledge of the elastic constants provides information about the structural stability,

mechanical properties, strain, fracture toughness, stress, load deflection and the strength of the material [188, 189]. We presented a brief discussion of elastic constant here with a view to establish stability or otherwise of our structures.

5.7.1 Hooke's law

In Hooke's law, elastic constants C are related to strain ε and stress σ by the relation

$$\sigma = C\varepsilon \tag{5.7.1}$$

In DFT, elastic constants are derived from the total energy of a strained crystal, which is expressed as

$$E = E_0 + V_0 \left(\sum_{ij} \sigma_{ij}\varepsilon_{ij} + \frac{1}{2} \sum_{ijkl} C_{ijkl}\varepsilon_{ij}\varepsilon_{kl} \right) \tag{5.7.2}$$

where E_0 and V_0 are the total energy and volume of the crystal in the unstrained state σ_{ij} and ε_{ij} are the stress and strain tensors, respectively with indices i, j, k and l which run over x, y and z.

The stress tensor σ_{ij} is defined as

$$\sigma_{ij} = \frac{1}{V_0} \left(\frac{\partial E}{\partial \varepsilon_{ij}} \right), \tag{5.7.3}$$

the elastic constant tensor C_{ijkl} is defined as

$$C_{ijkl} = \frac{1}{V_0} \left(\frac{\partial^2 E}{\partial \varepsilon_{ij}} . \varepsilon_{kl} \right)_{\varepsilon=0}, \tag{5.7.4}$$

at a point where the energy is minimized. The tensor σ_{ij} is defined as

$$\sigma_{ij} = \sum_{kl} C_{ijkl}\varepsilon_{kl}, \tag{5.7.5}$$

Eqn (5.7.5) is a generalized form of Hooke's law that relates strain and stress in a linear relation. Voigt notation [190] uses symmetry to reduce the order of the tensor, in this notation, the six dimensional vector is represented as

$$(\sigma_{xx}, \sigma_{yy}, \sigma_{zz}, \sigma_{yz}, \sigma_{xz}, \sigma_{xy}) \equiv (\sigma_1, \sigma_2, \sigma_3, \sigma_4, \sigma_5, \sigma_6), \tag{5.7.6}$$

and the strain tensor given by

$$\boldsymbol{\varepsilon} = \begin{bmatrix} \varepsilon_{xx} & \varepsilon_{xy} & \varepsilon_{xz} \\ \varepsilon_{yx} & \varepsilon_{yy} & \varepsilon_{yz} \\ \varepsilon_{zx} & \varepsilon_{zy} & \varepsilon_{zz} \end{bmatrix}, \tag{5.7.7}$$

is represented as

$$\varepsilon = (\varepsilon_{xx}, \varepsilon_{yy}, \varepsilon_{zz}, \varepsilon_{yz}, \varepsilon_{xz}, \varepsilon_{xy}) \equiv (\varepsilon_1, \varepsilon_2, \varepsilon_3, \varepsilon_4, \varepsilon_5, \varepsilon_6), \tag{5.7.8}$$

with

$$C_{ijkl} = C_{\alpha\beta} \qquad for \qquad \alpha, \beta = 1, 2, 3, 4, 5, 6. \tag{5.7.9}$$

In any crystal, there are at most twenty one independent elastic constants, which can be reduced depending on the symmetry of the crystal. Table 5.1 summarizes the number of the independent elastic constants for possible crystal symmetries.

Table 5.1: Second order elastic constant.

Lattice type	No. of independent elastic constants	Independent elastic constants
Cubic	3	C_{11}, C_{12}, C_{44}
Hexagonal	5	C_{11}, C_{12}, C_{13}, C_{33}, C_{44}
Rhombohedral I	6	C_{11}, C_{12}, C_{13}, C_{14}, C_{33}, C_{44}
Rhombohedral II	7	C_{11}, C_{12}, C_{13}, C_{14}, C_{15}, C_{33}, C_{44}
Tetragonal I	6	C_{11}, C_{12}, C_{13}, C_{33}, C_{44}, C_{66}
Tetragonal II	7	C_{11}, C_{12}, C_{13}, C_{16}, C_{33}, C_{44}, C_{66}
Orthorhombic	9	C_{11}, C_{12}, C_{13}, C_{22}, C_{23}, C_{33}, C_{44}, C_{55}, C_{66}
Monoclinic	13	C_{11}, C_{12}, C_{13}, C_{15}, C_{22}, C_{23}, C_{25}, C_{33}, C_{35}, C_{44}, C_{46}, C_{55}, C_{66}
Triclinic	21	C_{11}, C_{12}, C_{13}, C_{14}, C_{15}, C_{16}, C_{22}, C_{23}, C_{24}, C_{25}, C_{26}, C_{33}, C_{34}, C_{35}, C_{36}, C_{44}, C_{45}, C_{46}, C_{55}, C_{56}, C_{66}

Max Born [191, 192] and Grimvall et. al. [193] proposed that a crystalline structure need to satisfy the following stability criterion before it can attain stability (under the harmonic approximation, if there are no external forces):

1. All its phonon frequencies are positive for all considered wave vectors.
2. Elastic energies obtained from the solution of eqn. (5.7.2), must always be positive ($E > 0, \forall \varepsilon \neq 0$).

Félix and François-Xavier [194] used the above conditions to extract the necessary and sufficient condition needed for crystal stability and formulate them as:

1. the matrix C must be positive definite;
2. all the eigenvalues of the matrix C must be positive
3. leading principal minors of the matrix C should be positive;
4. arbitrary set of minors of the matrix C should be positive

5.8 Thermal properties

The specific heat capacity of a system within harmonic approximation is defined as [195]

$$\begin{aligned} C_V &= \left(\frac{\partial E}{\partial T}\right)_V \\ &= \sum_{\mathbf{q}\nu} k_{\mathrm{B}} \left(\frac{\hbar\omega(\mathbf{q}\nu)}{k_{\mathrm{B}}T}\right)^2 \frac{\exp(\hbar\omega(\mathbf{q}\nu)/k_{\mathrm{B}}T)}{[\exp(\hbar\omega(\mathbf{q}\nu)/k_{\mathrm{B}}T)-1]^2}, \end{aligned} \tag{5.8.1}$$

where T is temperature and k_{B} is Boltzmann constant. The summation sign runs over all the normal modes. The specific heat capacity is related to the heat content of the system, which is in turn determine by phonon.

The entropy of the system is given by:

$$\begin{aligned} S &= -\frac{\partial F}{\partial T} \\ &= \frac{1}{2T}\sum_{\mathbf{q}\nu} \hbar\omega(\mathbf{q}\nu)\coth(\hbar\omega(\mathbf{q}\nu)/2k_{\mathrm{B}}T) - k_{\mathrm{B}}\sum_{\mathbf{q}\nu}\ln\left[2\sinh(\hbar\omega(\mathbf{q}\nu)/2k_{\mathrm{B}}T)\right] \end{aligned} \tag{5.8.2}$$

5.9 Electronic density of State

One of the most important quantities used in describing electronic state of materials is called the band structure [169, 196]. It provides information about the arrangement of electrons, and it clarifies how electrons in a system responds to external perturbation, like emission or absorption of photons. Information about the total energy of a system can be extracted from it, from which a number of thermodynamic and material properties can be extracted [196].

An important concept used in the analysis of the band structure is the density of state (DOS) as function of energy [196]. It contains information about the band structure of the material for all possible positions kpoints in a very simple form [169]. The density of states $g(\epsilon)$ can be defined as the number of electronic states in a unit volume per unit energy [170]. In the energy range $[\epsilon, \epsilon + d\epsilon]$, the density of states is defined such that $g(\epsilon)d\epsilon$ is the number of energy states within the given range per unit volume. However, since the wave vector **k** are used to characterise the energy states, we have to sum all the number of states having energy within the interval of interest. Taking into account the spin degeneracy factor 2 and normalizing by the volume Ω of the solid, we can express the density of states as

$$g(\epsilon)d\epsilon = \frac{1}{\Omega}\sum_{\mathbf{k},\epsilon_k\varepsilon[\epsilon,\epsilon+d\epsilon]} 2 = \frac{2}{(2\pi)^3}\int_{\epsilon_k\varepsilon[\epsilon,\epsilon+d\epsilon]} d\mathbf{k}. \tag{5.9.1}$$

If ϵ_k has special symmetry with respect to k, then eqn (5.9.1) reduces to $\frac{1}{\pi^2}k^2dk$. Spherical coordinates in reciprocal space were used to arrive at this. Since energy in free electron model is not dependent on angular orientation of wave vector, i.e.

$$\epsilon_k = \frac{\hbar^2|\mathbf{k}|^2}{2m_e} \Longrightarrow \frac{m_e}{\hbar^2}d\epsilon,\ k = \left(\frac{2m_e\epsilon}{\hbar^2}\right)^{\frac{1}{2}}, \tag{5.9.2}$$

for energy value $\epsilon_k \varepsilon[\epsilon, \epsilon + d\epsilon]$. Eqns (5.9.1) and (5.9.2) gives density of state in a simple spherical symmetry 3D case of the form

$$g(\epsilon)d\epsilon = \frac{1}{2\pi^2}\left(\frac{2m_e\epsilon}{\hbar^2}\right)^{\frac{3}{2}}\sqrt{\epsilon}. \tag{5.9.3}$$

For practical purposes in crystal, ϵ_k is used from band structures calculation in place of eqn (5.9.3), leading to density of states of the form

$$\begin{aligned} g(\epsilon)d\epsilon = \frac{1}{\Omega}\sum_{n,\mathbf{k}} 2\delta\left(\epsilon - \epsilon_{\mathbf{k}}^{(n)}\right) &= \frac{2}{(2\pi)^3}\sum_n \int \delta\left(\epsilon - \epsilon_{\mathbf{k}}^{(n)}\right) d\mathbf{k} \\ &= \frac{2}{(2\pi)^3}\sum_n \int_{\epsilon_{\mathbf{k}}^{(n)}=\epsilon} \frac{1}{|\nabla_{\mathbf{k}}\epsilon_{\mathbf{k}}^{(n)}|} dS_{\mathbf{k}}. \end{aligned} \tag{5.9.4}$$

The integral in the last part of eqn (5.9.4) is integrated over surface δ_k in k-space, where $\epsilon_{\mathbf{k}}^{(n)}$ is constant and has the same value as ϵ and the vector $\nabla_{\mathbf{k}}\epsilon_{\mathbf{k}}^{(n)}$ is normal to $S_{\mathbf{k}}$ and having magnitude that is equal to rate of change of $\epsilon_{\mathbf{k}}^{(n)}$ in the normal direction. In real crystals, the number of unit cells are practically infinite if the crystal is large, this makes the spacing between the allowed wave vectors $\mathbf{k}$ to be very small, this makes it possible for us to replace the summation over the $\mathbf{k}$ vectors with an integral in the second part of eqn (5.9.4). We can see that from eqn (5.9.4), the denominator has roots that are of first order and has a finite contribution to the integral over the 2D smooth dimensional surface given by $S_{\mathbf{k}}$. The roots establish sharp features in the density of states called van Hove singularities [78, 178, 196, 197], the singularities are established at points where the density of states changes continuously [169]. It is, however, possible to detect the presence of energy gap, if the valence and conduction band are well separated.

If we define the total density of states as

$$g(\varepsilon) = \frac{\mathrm{d}I(\varepsilon)}{\mathrm{d}\varepsilon}, \tag{5.9.5}$$

where $I(\varepsilon)$ is the number of states with energy up to ε) and imposing the normalisation condition that

$$N = \int_{-\infty}^{E_F} g(\varepsilon)\ \mathrm{d}\varepsilon = I\left(E_F\right) \tag{5.9.6}$$

where N represents the number of valence electron per unit cell, we can readily obtain the Fermi energy from eqn (5.9.4) and (5.9.6). But it is easier to calculate density of states from eqn (5.9.6) in VASP [170] as

$$g(\varepsilon) = \frac{I(\varepsilon) - I(\varepsilon - \Delta\varepsilon)}{\Delta\varepsilon} \tag{5.9.7}$$

$\Delta\varepsilon$ is the difference in energy between two grid points. It is expected that this scheme should exactly conserve the number of electrons N

Information about the total density of states $g(\varepsilon)$ can be broken down into partial (projected) density of states using data obtained from wave functions [198]. If a given charge which corresponds to a given wave function is divided into individual atomic contributions, the projected density of states can be written in the form of $n^t(\varepsilon)$, where t is the atomic label.

5.10 DFT band gap problem

DFT is normally used in the electronic structure calculation of atoms, solids and molecule. Electron density is the key factor from which the ground state properties are determined. It provides information about forces and stresses, which can in turn allow structural relaxation of the system. Depending on the exchange correlation functional used, DFT accurately predicts equilibrium atomic positions and lattice parameters to an accuracy of about 95 $\%$. It however, fails in the prediction of band gap and excitation energies. Band gap calculated using DFT are underestimated by as much as 50 $\%$ [57].

The DFT underestimation of band gap is however, not surprising, this is because DFT KS eigenvalues are completely artificial: they are eigenvalues of a non-interacting system, chosen in such a way to give a density equal to that of the many body interacting system. Thus, the eigenvalues have no physical significance, but in practice, the comparison of the eigenvalues to the band structure was motivated by the similarity of KS band structure and that of real systems for quite a number of materials.

In DFT, the band gap is defined for an N electron system as the difference between the ionization energy (defined as $I = E^{(0)}_{N-1} - E^{(0)}_N \equiv -\epsilon_{HOMO}$) and the electron affinity (defined as $A = E^{(0)}_N - E^{(0)}_{N+1} \equiv -\epsilon_{LUMO}$) i.e.

$$E_{gap} = I - A = \epsilon_{LUMO} - \epsilon_{HOMO}, \tag{5.10.1}$$

where the LUMO and HOMO are the lowest unoccupied and highest occupied molecular orbitals respectively.

For non-interacting system, we can easily write the difference in the orbital energies as

$$E_{gap}^{KS} = \varepsilon_{N+1}^{(KS)}(N) - \varepsilon_{N}^{(KS)}(N). \tag{5.10.2}$$

We can get the exact KS gap from eqn (5.10.1) and (5.10.2) as

$$E_{gap} = \left(\varepsilon_{N+1}^{(KS)}(N) - \varepsilon_{N}^{(KS)}(N)\right) + \left(\varepsilon_{N+1}^{(KS)}(N+1) - \varepsilon_{N+1}^{(KS)}(N)\right) = E_{gap}^{KS} + \Delta_{xc}, \tag{5.10.3}$$

where Δ_{xc} is defined as

$$\Delta_{xc} = \left(\left.\frac{\delta E_{xc}[\eta]}{\delta \eta(\mathbf{r})}\right|_{N+1} - \left.\frac{\delta E_{xc}[\eta]}{\delta \eta(\mathbf{r})}\right|_{N} \right), \tag{5.10.4}$$

and it is the difference between the energies of the $(N+1)$ th KS orbital of the neutral and ionized electron system and it corresponds to the known neglected derivative discontinuity by exchange correlation functional when the number of particles changes by an integer [131, 199]. This discontinuity is responsible for the difference between the experimental band gap and the KS gap [131, 200, 201, 202]. The evaluation of the exchange correlation potential ($V_{xc}(\mathbf{r} = \frac{\delta E_{xc}}{\delta \eta(\mathbf{r})})$) at the point $(N+1)$ is to ensure that this discontinuity is captured at an integer particle number (N). In LDA and GGA, the value of Δ_{xc} is always zero. The fundamental gap obtained from these approximations is always purely KS gap, which is the reason why their gap is all the times underestimated when compared with experimental band gap [200].

5.11 Optical properties

In solids, optical properties provide a unique opportunity for the experimental study of band structures, excitations, defects, impurity levels, magnetic excitations and lattice vibration [203]. In these kind of experiments, observables, like light scattering, reflectivity, absorption or transmission can be measured [203]. Based on the evaluation of these quantities, we can measure quantities like the optical conductivity $\sigma(\omega)$, fundamental excitation frequencies, or the dielectric function $\epsilon(\omega)$. These studies enable us to characterize the materials and provide us with a range of possible technological applications of the materials [129, 204], photovoltaics, light emitting devices and material for laser technology for example. It is therefore eminent to accurately describe such materials using an efficient *ab initio* method. It is important to efficiently calculate the frequency-dependent microscopic polarizability matrix χ, which is crucial for a post-DFT approach implementation. In GW calculations, frequency-dependent macroscopic dielectric constants are of crucial importance and they are required for integrating analytically within

the long wavelength limit $(q = 0)$ the Coulomb singularity of the self and correlation energies. The dielectrically screened interaction potentials are of great importance, when excitonic effects are to be included in describing optical properties [129, 132, 170, 205].

5.11.1 Linear response theory

In order to obtain a good description of DFT exchange correlation energy and in calculating reflectance difference spectra, we need to determine how the material responds to external perturbation. If the perturbation is weak when compared to the internal electric field of the ions, we can describe the induced change in density in terms of perturbation theory using a term linearly dependent on the applied perturbation.

The response function $\chi\left(\mathbf{r}, \mathbf{r}', t - t'\right)$ is the key quantity needed to describe the change in density δn at a point $(\mathbf{r}, t)$, if there is a small change in external potential δv_{ext} at a point $(\mathbf{r}', t')$. The change in density is assumed in linear response theory to be:

$$\delta n\left(\mathbf{r}, t\right) = \int dt' \int d^3r' \chi\left(\mathbf{r}, \mathbf{r}', t - t'\right) \delta v_{ext}\left(\mathbf{r}', t'\right), \tag{5.11.1}$$

where the linear response function χ is given by

$$\chi\left(\mathbf{r}, \mathbf{r}', t - t'\right) = \frac{\delta n\left(\mathbf{r}, t\right)}{\delta v_{ext}\left(\mathbf{r}', t'\right)}. \tag{5.11.2}$$

It will be easy for one to calculate the response function $\chi^{KS}\left(\mathbf{r}, \mathbf{r}', t - t'\right)$ in KS-DFT, which describes how a KS system responds to a very small change in the effective KS potential $v_{eff}[n]$,

$$\delta n\left(\mathbf{r}, t\right) = \int dt' \int d^3r' \chi^{KS}\left(\mathbf{r}, \mathbf{r}', t - t'\right) \delta v_{eff}\left(\mathbf{r}', t'\right), \tag{5.11.3}$$

$$\chi^{KS}\left(\mathbf{r}, \mathbf{r}', t - t'\right) = \frac{\delta n\left(\mathbf{r}, t\right)}{\delta v_{eff}\left(\mathbf{r}', t'\right)}. \tag{5.11.4}$$

It is, however, required that the KS electron density and that of the physical system should be the same and the change in the time dependent density of the physical and the reference system must be the same. In order to be able to express χ^{KS} explicitly in terms of χ, one may need to introduce an exchange correlation kernel f_{xc} given by

$$f_{xc}[n_0]\left(\mathbf{r}, \mathbf{r}', t - t'\right) = \left.\frac{\delta v_{xc}\left(\mathbf{r}, t\right)}{\delta n\left(\mathbf{r}', t'\right)}\right|_{n=n_0}, \tag{5.11.5}$$

the time dependent exchange correlation functional $v_{xc}(\mathbf{r},t)$ is then written in term of ground state density $n_0(\mathbf{r})$ as

$$v_{xc}(\mathbf{r},t) = v_{xc}[n_0+\delta n](\mathbf{r},t) = v_{xc}[n_0](\mathbf{r}) + \int dt' \int d^3r' f_{xc}[n_0]\left(\mathbf{r},\mathbf{r}',t-t'\right)\delta n\left(\mathbf{r}',t'\right), \quad (5.11.6)$$

by requirement eqn (5.11.3) and (5.11.1) are the same and since the effective potential can be written in the form $v_{eff}[n](\mathbf{r},t) = v_{ext}[n](\mathbf{r},t) + v_H[n](\mathbf{r},t) + v_{xc}[n](\mathbf{r},t)$, where v_H is the Hartree potential, we can write them as

$$\begin{aligned} \int dt' \int d^3r' \chi\left(\mathbf{r},\mathbf{r}',t-t'\right)\delta v_{ext}\left(\mathbf{r}',t'\right) = \\ \int dt' \int d^3r' \chi^{KS}\left(\mathbf{r},\mathbf{r}',t-t'\right)\{\delta v_{ext}\left(\mathbf{r}',t'\right) + \delta v_H\left(\mathbf{r}',t'\right) + \delta v_{xc}\left(\mathbf{r}',t'\right)\}, \end{aligned} \quad (5.11.7)$$

using the chain rule, we can re-write $\delta v_H(\mathbf{r}',t')$ and $\delta v_{xc}(\mathbf{r}',t')$ in the form

$$\begin{aligned} \delta v_H\left(\mathbf{r}',t'\right) &= \int dt_1 dt_2 \int d^3r_1 d^3r_2 \frac{\delta v_H\left(\mathbf{r}',t'\right)}{\delta n\left(\mathbf{r}_1,t_1\right)} \frac{\delta n\left(\mathbf{r}_1,t_1\right)}{\delta v_{ext}\left(\mathbf{r}_2,t_2\right)} \delta v_{ext}\left(\mathbf{r}_2,t_2\right) \\ &= \int dt_1 dt_2 \int d^3r_1 d^3r_2 \frac{e^2}{|\mathbf{r_1}-\mathbf{r}'|} \chi\left(\mathbf{r}_1,\mathbf{r}_2,t_1-t_2\right)\delta v_{ext}\left(\mathbf{r}_2,t_2\right), \end{aligned} \quad (5.11.8)$$

$$\begin{aligned} \delta v_{xc}\left(\mathbf{r}',t'\right) &= \int dt_1 dt_2 \int d^3r_1 d^3r_2 \frac{\delta v_{xc}\left(\mathbf{r}',t'\right)}{\delta n\left(\mathbf{r}_1,t_1\right)} \frac{\delta n\left(\mathbf{r}_1,t_1\right)}{\delta v_{ext}\left(\mathbf{r}_2,t_2\right)} \delta v_{ext}\left(\mathbf{r}_2,t_2\right) \\ &= \int dt_1 dt_2 \int d^3r_1 d^3r_2 f_{xc}\left(\mathbf{r}',\mathbf{r}_1,t'-t_1\right)\left(\mathbf{r}_1,\mathbf{r}_2,t_1-t_2\right)\delta v_{ext}\left(\mathbf{r}_2,t_2\right). \end{aligned} \quad (5.11.9)$$

By using eqn (5.11.8) and (5.11.9), re-naming the integrating variable and going to frequency space, eqn (5.11.7) can be written in the form

$$\begin{aligned} \chi\left(\mathbf{r},\mathbf{r}',\omega\right) = \chi^{KS}\left(\mathbf{r},\mathbf{r}',\omega\right) \\ + \int d^3r_1 d^3r_2 \chi^{KS}\left(\mathbf{r},\mathbf{r}_1,\omega\right)\left(\frac{e^2}{|\mathbf{r}_1-\mathbf{r}_2|} + f_{xc}\left(\mathbf{r}_1,\mathbf{r}_2,\omega\right)\right)\chi\left(\mathbf{r}_2,\mathbf{r}',\omega\right). \end{aligned} \quad (5.11.10)$$

Eqn (5.11.10) is called Dyson equation. To evaluate the response function of an interacting electron system, the KS response function is calculated and the interacting response function is estimated thereafter using the Dyson equation and an (approximated) exchange correlation kernel f_{xc}. The simplest approximation to the exchange correlation kernel is called the Hartree approximation or random phase approximation (RPA) [140], where f_{xc} is neglected (i.e. $f_{xc}=0$) [206]. In this approximation, the electrons are assumed to respond to external perturbation independently [57] and the only contributing term is the Hartree term δv_H, while other interactions on the electrons cancel out due to their random phases [78].

5.12 Dielectric function

5.12.1 Macroscopic dielectric function

In an isotropic material, the instantaneous response to change in electric field E is given by

$$\mathbf{E} = \varepsilon^{-1}\mathbf{E}_{ext}, \tag{5.12.1}$$

where ε is the dielectric function and E_{ext}, the external field/perturbation. The quantity ε is a second rank tensor. In a homogeneous (macroscopic) material, the solution of eqn (5.12.1) is a product of frequency space and momentum. To properly analyse the situation, the total potential on the system is divided into induce v_{ind} and external potential v_{ext},

$$v_{tot} = v_{ext} + v_{ind}, \tag{5.12.2}$$

we can therefore re-write eqn (5.12.1) in the form

$$v_{tot} = \varepsilon^{-1}v_{ext}, \tag{5.12.3}$$

where v_{tot} is the sum total of the screened potential derived from the external and induced charged densities $\mathbf{E} = -\nabla v_H$ and $\mathbf{E}_{ext} = -\nabla v_{ext}$. If the external field is weak (linear response regime), we can assume that there is a linear relationship between the induced charge and the external potential of the form

$$\eta_{ind} = \chi v_{ext} \qquad (\chi = reducible \quad polarazability) \tag{5.12.4}$$

$$\eta = Pv_{tot} \qquad (P = irreducible \quad polarazability). \tag{5.12.5}$$

We can then write the relationship between the dielectric function ε and the inverse of the dielectric function ε^1 as

$$\varepsilon = \frac{v_{ext}}{v_{tot}} = \frac{v_{tot} - v_{ind}}{v_{tot}} = 1 - v\frac{\eta_{ind}}{v_{tot}} = 1 - vP \tag{5.12.6}$$

$$\varepsilon^{-1} = \frac{v_{tot}}{v_{ext}} = \frac{v_{ext} + v_{ind}}{v_{ext}} = 1 + v\frac{\eta_{ind}}{v_{ext}} = 1 + v\chi. \tag{5.12.7}$$

Where the two polarizabilities are related by

$$1 = \varepsilon\varepsilon^{-1} = (1 - vP)(1 + v\chi) \rightarrow \chi = P + Pv\chi. \tag{5.12.8}$$

We can now see that eqn (5.12.8) and (5.11.10) have the same form and that from eqn (5.12.6) and (5.12.7), we can calculate the dielectric function if we know the response function of the system to change in total or external potential.

5.12.2 Microscopic dielectric function

Response function in a periodic system on a coarse scale is homogeneous and macroscopic electric field of the system follows the external perturbation periodicity, unlike the microscopic electric field which rapidly oscillates on the scale of a primitive cell. It is therefore of great importance to differentiate between the functions. Dielectric function can be formally written in the form:

$$E(\mathbf{r},\omega) = \int d^3\mathbf{r}' \varepsilon^{-1}_{mac}(\mathbf{r}-\mathbf{r}',\omega) E_{ext}(\mathbf{r}',\omega), \tag{5.12.9}$$

where E_{ext} and E are external and total macroscopic electric fields connected by macroscopic dielectric function ε_{mac}. The microscopic electric field at the atomic level $e(\mathbf{r},\omega)$ is given by

$$e(\mathbf{r},\omega) = \int d^3\mathbf{r}' \varepsilon^{-1}_{mic}(\mathbf{r},\mathbf{r}',\omega) E_{ext}(\mathbf{r}',\omega). \tag{5.12.10}$$

The microscopic dielectric function is invariant only under lattice translation vector and it is the quantity that is accessible directly in *ab initio* calculations. We can use the invariant property of the microscopic dielectric constant to show that

$$e(\mathbf{q}+\mathbf{K},\omega) = \sum_{\mathbf{K}'} \varepsilon^{-1}(\mathbf{q}+\mathbf{K},\mathbf{q}+\mathbf{K}',\omega)\mathbf{E_{ext}}(\mathbf{q}+\mathbf{K}',\omega) = \sum_{\mathbf{K}'} \varepsilon^{-1}_{\mathbf{K},\mathbf{K}}(\mathbf{q},\omega)\mathbf{E_{ext}}(\mathbf{q}+\mathbf{K}',\omega), \tag{5.12.11}$$

since the microscopic dielectric function can be obtained easily from *ab initio* calculation, one may wish to calculate the macroscopic dielectric function using the following relation:

$$\varepsilon^{-1}_{mac}(\mathbf{q},\omega) = \mathbf{e}(\mathbf{q}+\mathbf{K}',\omega)\delta_{G,0}. \tag{5.12.12}$$

In real solids, local field effects arise due to the rapid variation of microscopic electric fields over a unit cell of the solid. As a result, the macroscopic field, which happens to be the average of the microscopic over a given region which is large enough when compared with the solid lattice constant and small when compared with the wavelength $\frac{2\pi}{q}$, is in general not the same as the local field polarizing charges in the crystal [206, 207].

5.12.3 Real and imaginary parts of the dielectric function

We can use the sum over δ-like Lorentzian peaks of width η and $\omega = \varepsilon_{m\mathbf{k}} - \varepsilon_{n\mathbf{k}}$ as transition energy, which is weighted using a transition probability $|\langle u_{m\mathbf{k}+\mathbf{q}}|u_{n\mathbf{k}}\rangle|^2$ to evaluate the imaginary and real parts

of the macroscopic dielectric function ($\varepsilon = \varepsilon^{(1)} + j\varepsilon^{(2)}$), where

$$\varepsilon^{(2)}(\hat{\mathbf{q}},\omega) = \frac{4\pi^2 e^2}{\Omega} \lim_{q\to 0} \frac{1}{q^2} \sum_{nm\mathbf{k}} 2f_{n\mathbf{k}} |\langle u_{m\mathbf{k}+\mathbf{q}} | u_{n\mathbf{k}} \rangle|^2 \left[\delta(\varepsilon_{m\mathbf{k}} - \varepsilon_{n\mathbf{k}} - \omega) - \delta(\varepsilon_{m\mathbf{k}} - \varepsilon_{n\mathbf{k}} + \omega)\right], \tag{5.12.13}$$

the subscripts n and m denote valence and conduction bands, respectively and $u_{n\mathbf{k}}$ represents the periodic part of the orbitals at a point k [208, 209]. When $q \to 0$, the imaginary part of the dielectric function will still depend on direction of $\overrightarrow{q}$, which can be described using a vector $\hat{\mathbf{q}} = \frac{\mathbf{q}}{|\mathbf{q}|}$. We can then introduce a direction tensor of the form $\varepsilon_{\alpha\beta}$ and set

$$\varepsilon^{(2)}(\hat{\mathbf{q}},\omega) = \sum_{\alpha,\beta} \hat{\mathbf{q}}_\alpha \varepsilon^{(2)}_{\alpha\beta}(\hat{\mathbf{q}},\omega)\hat{\mathbf{q}}_\beta. \tag{5.12.14}$$

We can then express the imaginary part of the dielectric function in term of Cartesian $\varepsilon_{\alpha\beta}$ as

$$\varepsilon^{(2)}(\hat{\mathbf{q}},\omega) = \frac{4\pi^2 e^2}{\Omega} \lim_{q\to 0} \frac{1}{q^2} \sum_{nm\mathbf{k}} 2f_{n\mathbf{k}} \langle u_{m\mathbf{k}+\mathbf{e}_{\alpha q}} | u_{n\mathbf{k}} \rangle \langle u_{n\mathbf{k}} | u_{m\mathbf{k}+\mathbf{e}_{\beta q}} \rangle \left[\delta(\varepsilon_{m\mathbf{k}} - \varepsilon_{n\mathbf{k}} - \omega) - \delta(\varepsilon_{m\mathbf{k}} - \varepsilon_{n\mathbf{k}} + \omega)\right]. \tag{5.12.15}$$

Using Hilbert transformation, the real part of the dielectric function $\varepsilon^{(1)}$ can be expressed via Kramer-Kronig relation:

$$\varepsilon^{(1)} = 1 + \frac{2}{\pi} P \int_0^\infty \frac{\varepsilon^{(2)}(\omega')\omega'}{\omega'^2 - \omega^2} d\omega'. \tag{5.12.16}$$

5.12.4 Absorption coefficient, refractive index and reflectivity

Measurement of light absorption is among the most useful techniques in optical measurements in solids. If, for example, light with intensity I_0 passes through a material of thickness z, after which it has a new intensity $I(z)$, the decrease in the intensity of the light can be expressed as [203, 210]

$$dI = -\alpha dz \times I(z). \tag{5.12.17}$$

Integrating equation (5.12.17) will give what is known as Beer's law:

$$I(z) = I_0 e^{-\alpha z}, \tag{5.12.18}$$

where the quantity α is called the absorption coefficient defined as the fraction of power absorbed in a given unit length of a material.

It can be shown that the intensity of the light $I(z)$ is proportional to the square of the optical field. It then follows that, the intensity in the medium will decrease exponentially with decay constant of

magnitude $2 \times \left(\frac{\kappa\omega}{c}\right)$. Comparing this equation to Beer's law, we can write that:

$$\alpha = \frac{2\kappa\omega}{c} = \frac{4\pi\kappa}{\lambda}, \tag{5.12.19}$$

where the quantity λ is the wavelength of light in a vacuum and κ is called the extinction coefficient and is related to the complex part of the refractive index. Equation (5.12.19) shows that α and κ are directly proportional.

The refractive index is defined as the N of the material is the ratio of the speed of light c in vacuum to the speed v in a given material:

$$N = \frac{c}{v}. \tag{5.12.20}$$

For a plane wave, its group velocity in the medium v is equal to its phase velocity i.e. $v = \frac{\omega}{q}$, where $\mathbf{q}$ is wave vector given by:

$$\mathbf{q} = \frac{\omega}{c}\left[\varepsilon_1\mu_1 + i\frac{4\pi\mu_1\sigma_1}{\omega}\right]^{\frac{1}{2}}\mathbf{n_q}, \tag{5.12.21}$$

where ω is frequency, $\mathbf{n_q}$ is unit vector in the direction of the wave vector $\mathbf{q}$.

Putting eqn. (5.12.21) in to (5.12.20), and replacing $\frac{4\pi\sigma_1}{\omega}$ with ε_2 we get

$$N = \frac{c}{v} = \frac{c}{\omega}q = \left[\varepsilon_1\mu_1 + i\frac{4\pi\mu_1\sigma_1}{\omega}\right]^{\frac{1}{2}} = \left[\mu_1\left(\varepsilon_1 + i\varepsilon_2\right)\right]^{\frac{1}{2}} = n + i\kappa. \tag{5.12.22}$$

Reflectivity R is normally derived from the complex part of the refractive index from the Fresnel equation:

$$R = \left|\frac{\tilde{n} - 1}{\tilde{n} + 1}\right|^2 = \left|\frac{n + i\kappa - 1}{n + i\kappa + 1}\right|^2 \tag{5.12.23}$$

5.13 GW and BSE methodology

Within the level of GW-PAW frame work discussed in Section 4.3, the calculation of the dynamically screened interaction requires a number of empty conduction band states. 996 empty bands were used for MX_3(M= Ti, Zr and Hf; X= S, Se, Te) and $ReSe_2$ calculations, 504 and 192 for bulk and monolayer MX_2(M= Zr and Hf; X= S, Se), respectively. Throughout the calculations, we start with normal DFT, where we calculate the unperturbed KS energies and eigenstates, to reduce computational cost. We then calculate the dielectric functions by employing a single shot G_0W_0, where the self consistent KS DFT orbitals and eigenvalues are used to construct the dynamically screened interaction W_0 and the Green's function G_0 and then solving the quasi particle (QP) equation iteratively. The simple G_0W_0 was

adopted where the screening W and the orbital for the Green's function are kept at the DFT level and the QP energies are calculated using first order perturbation theory. This method is known to predict fundamental band gaps with an accuracy of $\pm$ 10 $\%$ [211, 212] when compared with experimental values.

In order to calculate the optical spectra, BSE calculations using the Tamm Dancoff approximation on the basis of a free qausielectron-quasihole were performed. Five highest valence bands and five lowest conduction bands were found to be enough to converge the heights of the first two energy peaks in the bulk and monolayer MX_2(M= Zr, Hf; X= S, Se,) structures.

6. Results and discussions

In this chapter, the results obtained are presented and discussed.

6.1 Technetium dichalcogenide

It follows from the discussion of the preparation and structural properties of TcX_2 (X = S, Se and Te) in Section 1.2.1 of this thesis. Here, we report the structural, mechanical, electronic and optical properties of these compounds.

6.1.1 Equilibrium and Structural Properties

Structural relaxation of TcS_2, $TcSe_2$ and $TcTe_2$ was done using the PBE, PBEsol, vdW-TS, vdW-D2 and vdW-DF DFT approximations. Different functionals were used in order to identify the ones that will predict lattice parameters that are in best agreement with experiment. The results obtained are also compared with other theoretical calculations. The cohesive energy-volume relationship (EOS) calculated using the different DFT approximations for the structures are displayed graphically in Figures 6.2, 6.3 and 6.4 for TcS_2, $TcSe_2$ and $TcTe_2$, respectively. From the data, the equilibrium structural properties are extracted and presented in Table 6.1. Since the compounds are iso-structural as established in Section 1.2.1 of this thesis, only the TcS_2 relaxed structure, with the unit cell doubled in the Z-direction to show the layered nature of the structures is presented in Fig. 6.1. The structural parameters obtained are compared with experiment [50] and theory [22], where available.

From Figures, 6.2, 6.3 and 6.4, we observed that, the cohesive energy graphs obtained from PBE-GGA and its modified version PBEsol (also based on GGA), due to their inability to account for long range dispersion forces, tend to overestimate equilibrium volumes as it is well known [213] in layered structures. The PBEsol has the same analyticity as PBE but with two parameters changed to satisfy constraint conditions in solids [214]. This is what caused curves in sub-figure (a) part of 6.2, 6.3 and 6.4 to be flat, because the layers of the structures decouple at higher volumes and larger inter-layer separation. However, our PBE result is in agreement to that reported by Weck et. al. [22] which is also based on PBE. This suggests the necessity of including the van der Waal's correction term, for accurate description of layered structures like TcS_2. We observed that vdW-D2 (which combined conventional

PBE functional with empirical dispersion correction term to account for long range dispersion forces [119, 122, 215]) predicts structural lattice parameters and volumes that are closer to the experimental values, where the data is available for comparison. For example, in TcS_2, the interlayer distance c from vdW-D2 is only 0.08 Å larger than the experimental one, whereas it is 1.13 Å, 0.16 Å, 0.22 Å larger with PBE, PBEsol and vdW-DF, respectively, and 0.42 Å less than the experimental value in the case of vdW-TS. The difference between our PBE interlayer distance c and that of reference [22] may be as a result of difference in the input parameters or pseudopotential. We also note that, vdW-TS (which is built to account for van der Waal's interaction using system-dependent dispersion coefficients obtained from first principle calculations [214]) underestimates the equilibrium volume when compared with the experiment, where available. The vdW-TS volume is 8.06 % less than the experimental volume while vdW-DF (a nonlocal correlation functional that accounts for long range interaction [124, 125, 216]) overestimates the equilibrium volume by 6.79 % for TcS_2. The vdW-D2 volume in TcS_2 is 2.12 % greater than the experimental volume and this is the best theoretical result for this compound. From Figures 6.2, 6.3 and 6.4, the equilibrium properties of the structures are extracted and listed in Table 6.1.

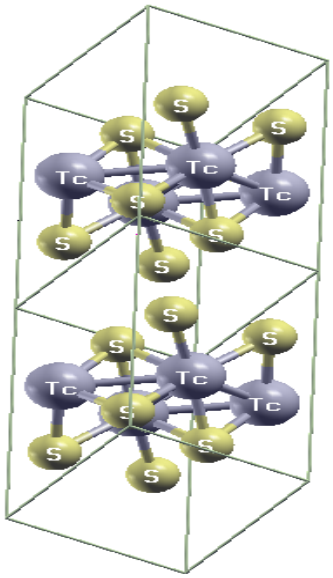


Figure 6.1: TcS_2 unit cell doubled in the Z-direction to show the layered structure.

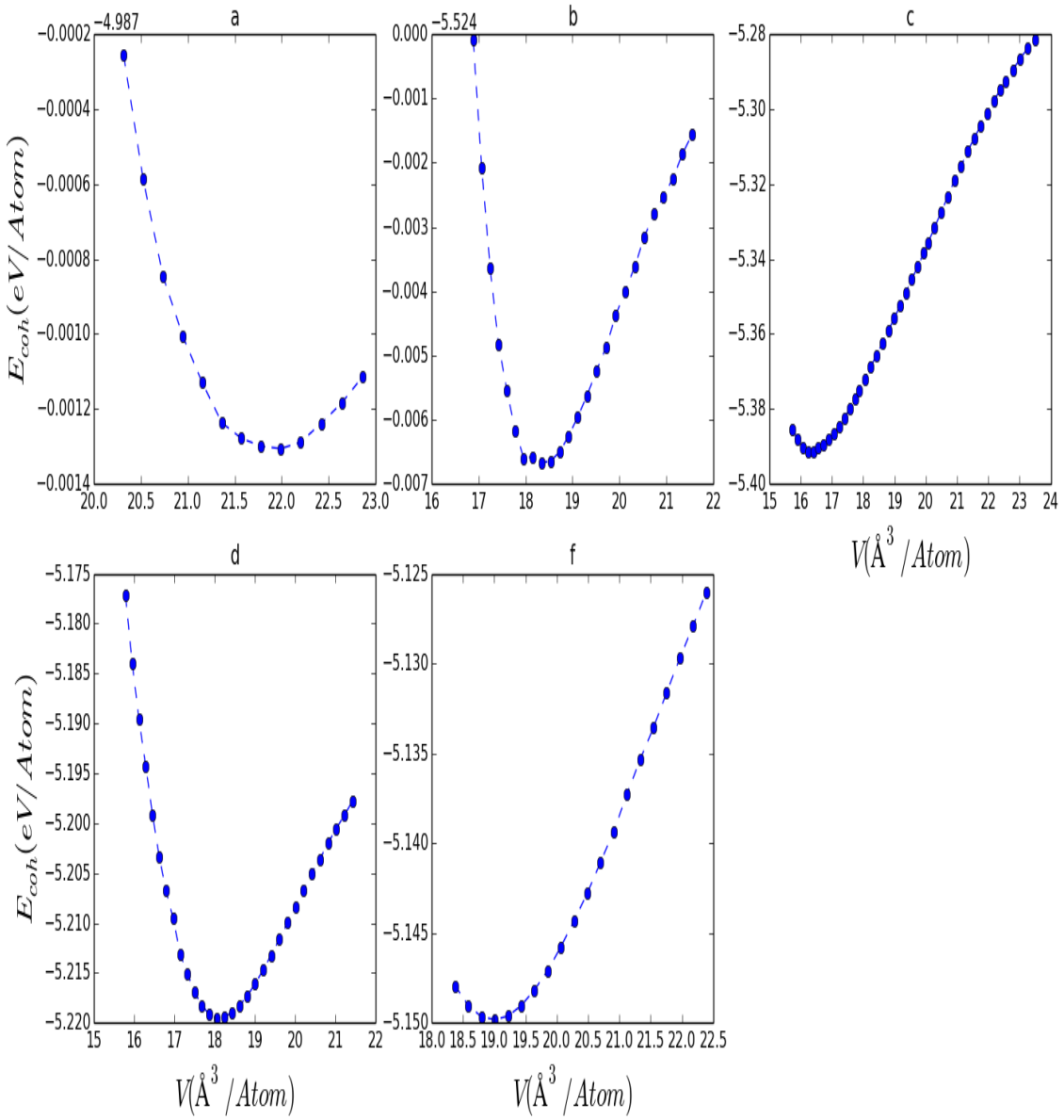


Figure 6.2: TcS_2 cohesive energy-volume graph calculated using (a) PBE, (b) PBEsol, (c) vdW-TS, (d) DFT-D2 and (f) vdW-DF.

From Table 6.1, using the vdW-D2 obtained structural lattice parameters, for example, we observe how the TcX_2 (X = S, Se and Te) structural lattice parameters (*a, b* and *c*) increase as one goes down from S to Te in the same group of the periodic table. This increase in the lattice parameters, leads to an increase in volume in the structures as can be observed from the table. The increase in volume may be

explained by the fact that as one moves down a particular group in the periodic table, the atomic volume increases. This is consistent with the information in Table 6.2, where we see that as we move down the group in the periodic table (i.e. from S to Te), the shortest nearest neighbour distances between the atoms increase.

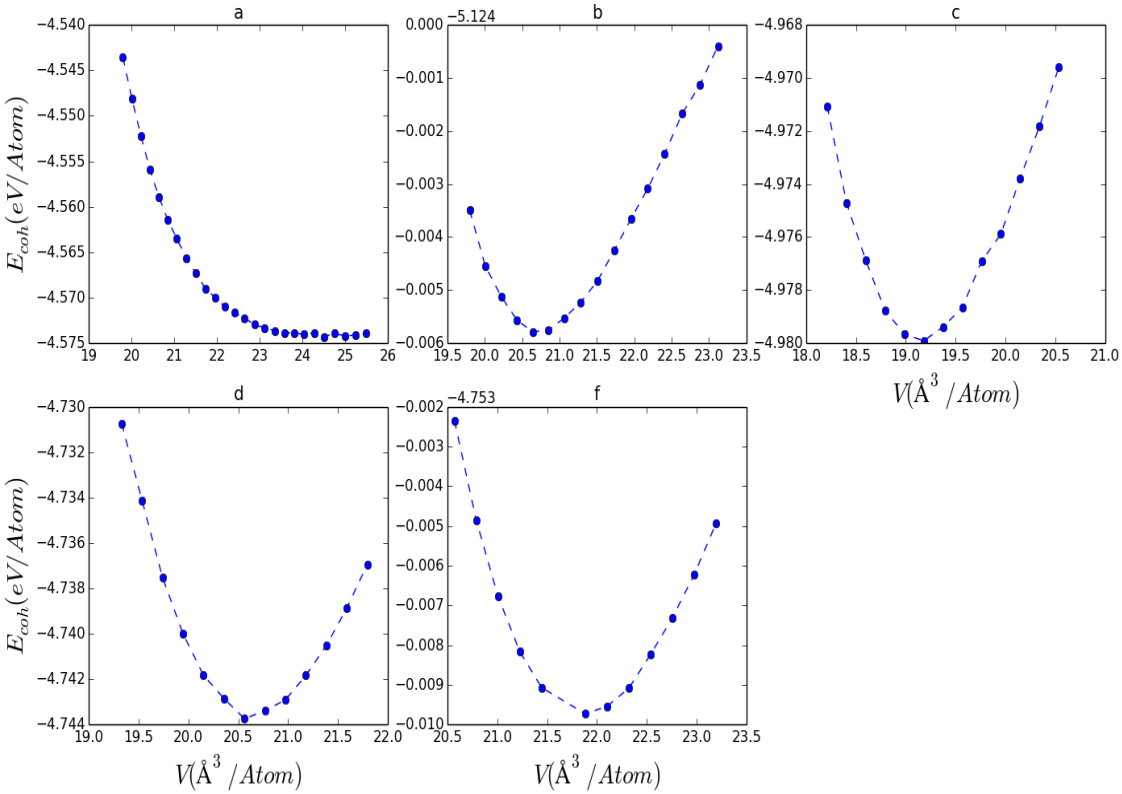


Figure 6.3: $TcSe_2$ cohesive energy-volume graph calculated using (a) PBE, (b) PBEsol, (c) vdW-TS, (d) DFT-D2 and (f) vdW-DF.

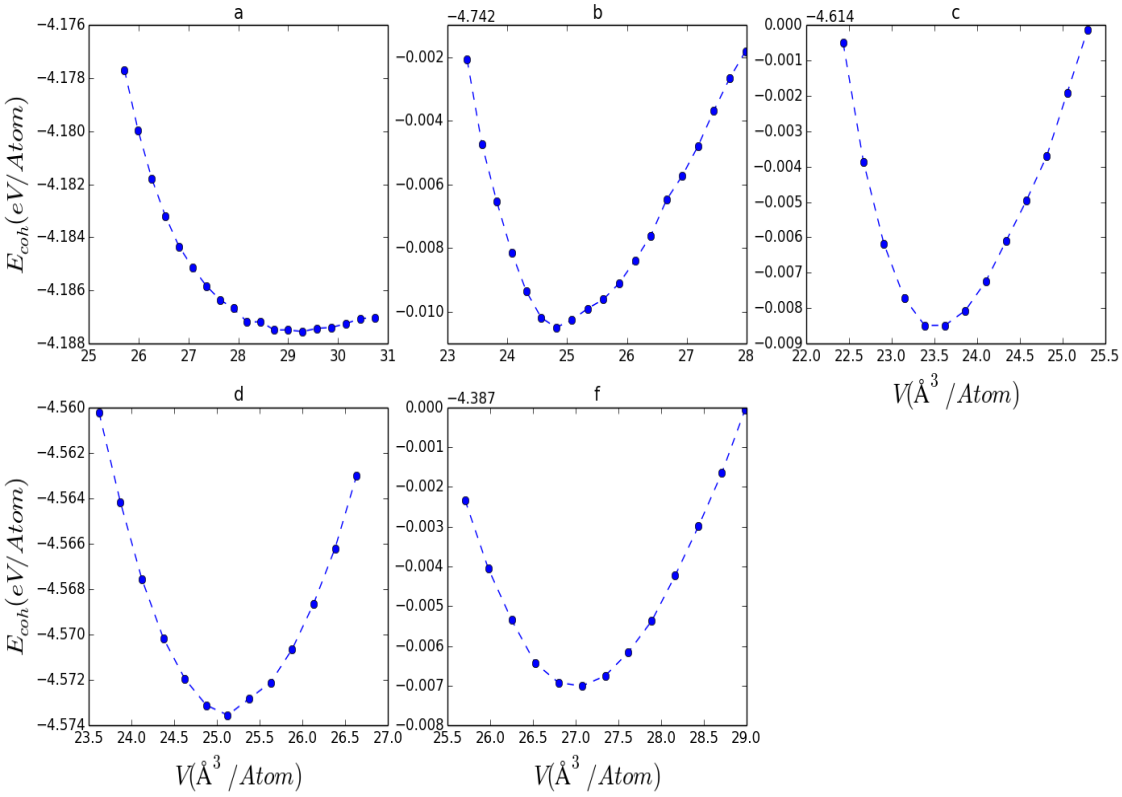


Figure 6.4: $TcTe_2$ cohesive energy-volume graph calculated using (a) PBE, (b) PBEsol, (c) vdW-TS, (d) DFT-D2 and (f) vdW-DF.

Table 6.2 list the bond length of the TcS_2 like structures. The nearest neighbour distance controls the physical properties of the structures like bond strength, melting point, elasticity and charge transfer. It is established that the larger the bond length, the larger the bulk modulus [217], which in turn determines the stiffness or structural rigidity and that the shorter the nearest neighbour distance, the more likely that there will be charge transfer in the structure [218].

6.1.2 Mechanical and thermal properties

As discussed in Section 5.7, in order to determine stability of a given structure, one needs to examine the phonon band structure and elastic constants. It is therefore important, to accurately calculate the elastic constants and evaluate them for determining the stability of a given material. In order to test the stability of the TcX_2 (X= S, Se and Te), their underlying phonon dispersion relation and elastic

Table 6.1: Calculated and experimental equilibrium parameters of TcX_2(X = S, Se and Te): lattice constants (a (Å) , b (Å), c (Å)), volume V_0 (Å^3), formation energy E_f per atom and cohesive energy E_{coh} per atom.

Functional	*a (Å)*	*b (Å)*	*c (Å)*	V_0 *(Å^3)*	E_f *(eV/atom)*	E_{coh} *(eV/atom)*	α°	β°	γ°
				TcS_2					
PBE	6.39	6.50	7.78	261.84	-0.66	-5.00	67.85	101.7	118.82
PBEsol	6.31	6.42	6.81	220.68	-0.66	-5.00	65.76	102.99	118.77
vdW-TS	6.38	6.51	6.23	196.20	-0.79	-5.40	59.82	104.39	118.74
DFT-D2	6.37	6.47	6.73	217.92	-0.62	-5.23	63.86	103.47	118.85
vdW-DF	6.43	6.54	6.87	227.88	-0.69	-5.15	64.27	103.38	118.91
Other PBE	6.42 [a]	6.52 [a]	7.07 [a]	234.4 [a]			64.7 [a]	102.9 [a]	118.9 [a]
Exp.	6.37 [b]	6.46 [b]	6.65 [b]	213.39 [b]			62.94 [b]	103.61 [b]	119.00 [b]
				$TcSe_2$					
PBE	6.64	6.77	8.07	295.20	-0.52	-4.59	68.24	101.66	118.80
PBEsol	6.56	6.69	6.90	248.76	-0.52	-4.59	70.14	103.24	118.77
vdW-TS	6.66	6.79	6.62	229.68	-0.60	-4.99	61.22	104.27	118.76
DFT-D2	6.64	6.75	7.00	248.04	-0.48	-4.88	64.51	103.40	118.83
vdW-DF	6.70	6.83	7.29	266.88	-0.52	-4.70	66.22	103.24	118.89
Other PBE	6.67 [a]	6.80 [a]	7.42 [a]	267.10 [a]			65.00 [a]	102.90 [a]	118.80 [a]
				$TcTe_2$					
PBE	7.07	7.22	8.24	348.36	-0.27	-4.20	71.77	102.49	118.91
PBEsol	6.98	7.12	7.34	300.00	-0.27	-4.20	70.50	103.24	118.95
vdW-TS	7.11	7.20	7.12	282.72	-0.28	-4.63	62.39	104.17	118.92
DFT-D2	7.12	7.22	7.39	301.68			65.52	103.51	119.01
vdW-DF	7.13	7.27	7.62	324.12	-0.22	-4.32	70.11	103.15	119.04
Other PBE	7.10	7.24	7.91	324.70			65.90	102.80	118.90

a = reference [22], b = reference [50]

constants were calculated. The vdW-D2, an approximation which predicted equilibrium volume in best agreement with experiment was used in the computation of the phonon band structures. The phonon band structures of the TcX_2 (X= S, Se and Te) are depicted in Figure 6.5 and the elastic constants obtained are listed in Table 6.3.

From Figure 6.5, can see that, the phonon dispersion relation for the TcX_2 (X = S, Se and Te) have no imaginary phonon frequencies and thus have satisfied one of the necessary stability criteria discussed in Section 5.7.

From Table 6.3, the elastic constants obtained have also satisfied the stability criteria discussed in Section 5.7. We can therefore, say that the structures are stable against distortions. We also observe

Table 6.2: calculated and experimental TcX_2 (X = S, Se and Te) nearest neighbour distances in Å.

Functional	Tc - Tc	Tc - S (Å)	S - S(Å)
		TcS_2	
PBE	2.67	2.28	3.07
PBEsol	2.80	2.40	3.21
vdW-TS	2.94	2.49	3.37
vdW-D2	2.85	2.42	3.25
vdW-DF	2.82	2.39	3.24
Other PBE	2.72 [a]	2.31 [a]	-
Expriment	2.70 [b]	2.23 [b]	-
		$TcSe_2$	
Functional	Tc - Tc	Tc - Se (Å)	Se - Se(Å)
PBE	2.61	2.31	3.06
PBEsol	2.73	2.42	3.20
vdW-TS	2.85	2.50	3.34
vdW-D2	2.78	2.44	3.23
vdW-DF	2.72	2.40	3.20
Other PBE		2.43 [a]	-
Expriment	-	-	-
		$TcTe_2$	
Functional	Tc - Tc	Tc - Te (Å)	Te - Te(Å)
PBE	2.55	2.33	3.08
PBEsol	2.64	2.44	3.20
vdW-TS	2.76	2.51	3.31
vdW-D2	2.71	2.45	3.23
vdW-DF	2.63	2.41	3.20
Other PBE	2.85 [a]	2.81 [a]	-
Expriment	-	-	-

a = reference [22] and b = reference [50]

that the structure has large in plane elastic constants C_{11} and C_{22} values and that weak inter-layer forces may be responsible for preventing the structure from attaining large out of plane elastic constants. For example, C_{33} with van der Waal's correction (vdW-TS, vdW-D2 and vdW-DF) is typically about four times the ones without the van der Waal's correction.

The phonon contribution to the heat capacity of TcX_2 (X = S, Se and Te) was evaluated using the calculated phonon frequencies determined from density functional perturbation theory [219]. The graph

Table 6.3: TcX_2 (X= S, Se and Te) calculated elastic constants (GPa).

	C_{11}	C_{12}	C_{13}	C_{14}	C_{15}	C_{16}	C_{22}	C_{23}	C_{24}	C_{25}	C_{26}	C_{33}	C_{34}	C_{35}	C_{36}	C_{44}	C_{45}	C_{46}	C_{55}	C_{56}	C_{66}
										TcS_2											
PBE	1661	315	132	93	330	-159	1338	245	530	7.29	-155	94	120	65	83	254	54	69	174	205	568
PBEsol	1666	317	131	92	332	-160	1349	245	532	9.76	-155	88	119	64	82	252	53	70	171	205	570
vdW-TS	2447	485	534	135	143	-163	2163	419	360	-24	-109	972	174	159	92	379	41	70	646	256	734
vdW-D2	2144	421	314	79	274	-159	1852	339	518	-1.11	-151	419	78	74	81	261	47	82	320	213	678
vdW-DF	1963	388	274	83	303	-175	1594	363	550	-4.15	-163	350	104	91	94	296	51	76	295	225	633
										$TcSe_2$											
PBE	1406	278	119	81	259	-130	1095	202	450	-0.47	-131	83	107	62	66	213	47	52	159	169	468
PBEsol	1406	278	119	81	259	-130	1095	202	450	-0.47	-131	83	107	62	66	213	47	52	159	169	468
vdW-TS	1998	433	496	88	118	-154	1741	401	409	-31	-131	810	151	181	85	300	31	65	549	224	577
vdW-D2	1765	364	342	41	166	-138	1462	369	436	-15	-138	520	54	93	88	256	44	57	349	181	526
vdW-DF	1650	348	263	57	223	-135	1330	321	451	-22	-126	335	67	64	77	235	50	55	258	176	524
										$TcTe_2$											
PBE	1151	223	118	68	227	-93	1011	149	335	25	-101	109	67	45	53	163	32	52	124	133	405
PBEsol	1118	240	96	56	219	-91	976	162	340	7.35	-98	45	61	30	54	158	38	52	117	129	393
vdW-TS	1619	360	422	31	75	-102	1476	295	332	-19	-112	545	90	159	54	190	17	66	478	176	435
vdW-D2	1399	323	362	-4.84	58	-60	1343	300	277	-29	-66	530	8.23	65	62	153	29	62	359	129	429
vdW-DF	1249	296	190	27	186	-78	1118	234	316	2.37	-89	275	28	52	58	182	29	51	206	120	430

of the structural specific heat capacity at constant volume against temperature is depicted in Figure 6.6. From the Figure, we note that the specific heat capacity of $TcSe_2$ is the first to approach a constant value (Dulong and Petit law) at a temperature of about 410 K, followed by TcS_2, at a temperature of about 430 K, then $TcTe_2$, at a temperature of about 450 K. It is also observed that, over the range of the observed temperatures, the specific heat capacity of the structures are of the order $C_v[TcSe_2] < C_v[TcS_2] < C_v[TcTe_2]$. This is consistent with the phonon dispersion relation of the structures displayed in Figure 6.6.

Since the TcX_2 (X= S, Se and Te) structures investigated are semiconductors, it is expected that their heat capacities at low temperature will be dominated by the phonon contribution. The electronic contributions are expected to be significant when there is sufficient thermal energy to excite the electronic degrees of freedom. This will only take place when the thermal energy kT (k is Boltzmann constant and T is temperature) is of the same order as the band gap of the structures.

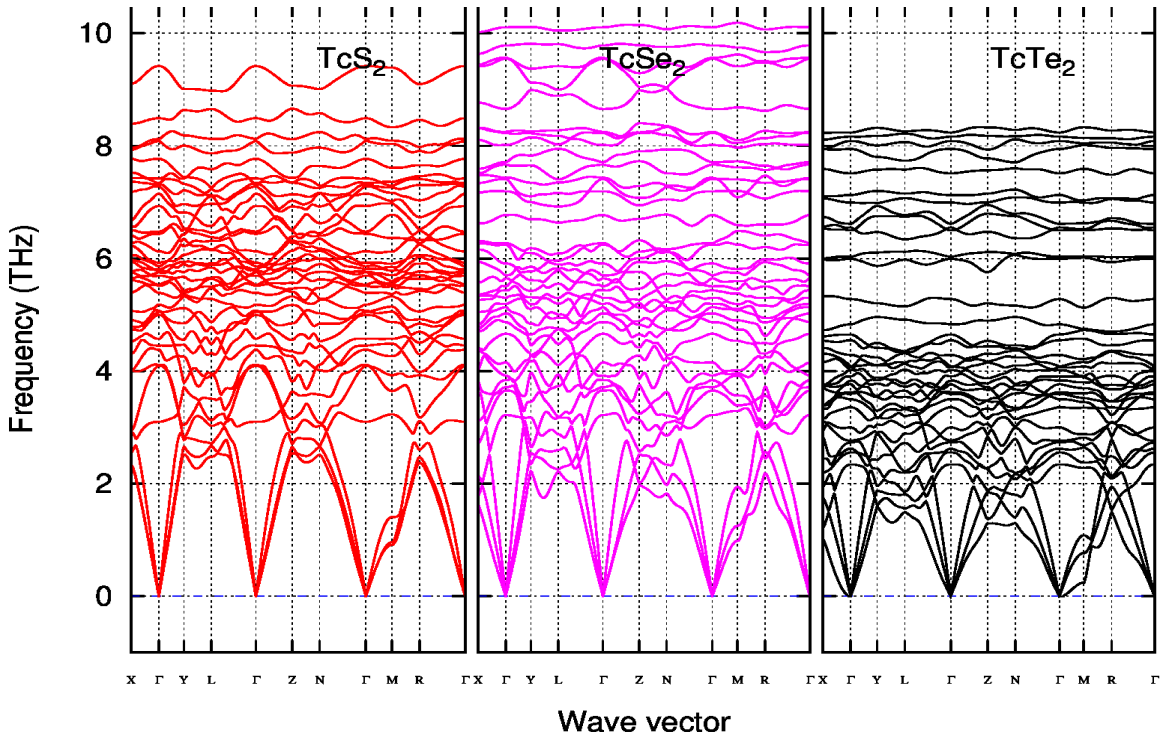


Figure 6.5: TcX_2 (X= S, Se and Te) phonon dispersion relation graph calculated using vdW-D2.

From subfigure 6.6 (b), we can note that entropy of these structures increases steadily with increase in temperature, the entropy is also observed to increase with increase in volume of the structures as we move down the chalcogenide group in the periodic table (i.e. $S[TcS_2] < S[TcSe_2] < STcTe_2$). This is consistent with Boltzmann's entropy law, discussed in Section 5.8 of this thesis, where the increase in micro-states of a system bring about increase in entropy.

6.1.3 Electronic properties

In trying to understand the nature of the electronic properties of technetium dichalcogenide structures, their underlying electronic structure, bonding and possible charge transfer were analysed using partial charge calculation in Bader partitions [220, 221, 222]. The electronic charge transfer was calculated for the vdW-D2 DFT approximation only, since this functional predicts structural parameters in best agreement with experiment than other approximations considered.

Bader charge analysis indicates that there is a significant charge transfer in these technetium structures. The charge transfer between the transition metal (Tc) and its corresponding dichalcogenides (X) is summarized in Table 6.4. From the table, we can see that the charge transfer from the Tc metal to

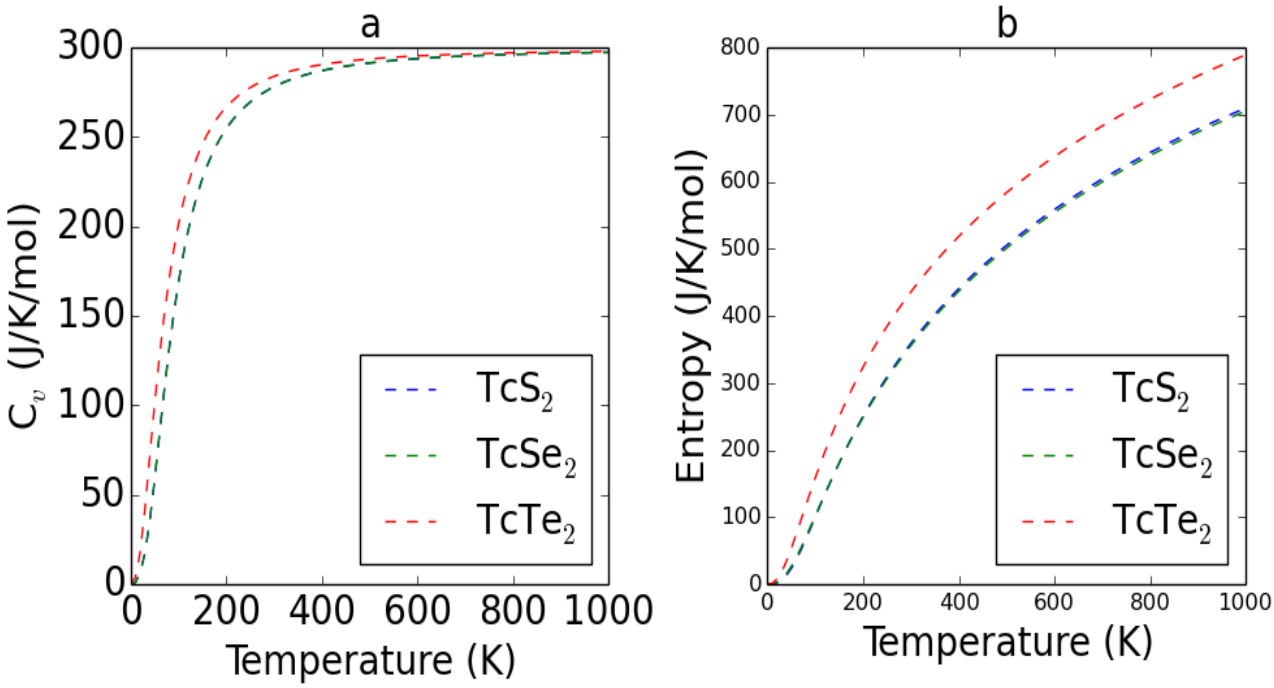


Figure 6.6: vdW-D2 calculated specific heat capacity at constant volume and entropy for the TcX_2 (X= S, Se and Te) structures.

the chalcogen atom decreases as one goes down the group in the periodic table, i.e., from S to Se to Te, suggesting that the bonding between the structures is becoming less ionic with increasing atomic number of the chalcogen atom. The decrease in charge transfer may be correlated with the increasing distance between the transition metal and chalcogen atoms as shown in Table 6.2 and discussed in Section 6.1.2.

To understand the electronic properties of the TcX_2 (X = S, Se and Te) structures, their underlying electronic band structures, total density of states (TDOS) and partial density states (PDOS) were calculated and shown in Figures 6.7, 6.8 and 6.9. However, due to the similarity of the graphs obtained from the approximations considered, only results from one of the functionals will be shown in each instance. Having observed that the structures are not magnetic (electrons occupy spin up and spin down equally), it is sufficient to show only spin up density of states and spin up band diagrams. Plotting the electronic band structure along the high symmetry k-points accord us the opportunity of extracting the nature of the electronic band gap of the structures. Using the PDOS plots, we can obtain information about the orbital character of the bands. The TDOS and PDOS are plotted using an arbitrary scale.

Table 6.4: Charge transfer for $TcX_2(X = S, Se, Te)$ in electronic charge (e) calculated using vdW-D2. Charge transfer numbers refer to atoms in the first and second columns respectively (See Fig. 6.1).

	TcS_2	$TcSe_2$	$TcTe_2$
Tc1, Tc2	0.91	0.61	0.18
Tc3, Tc4	0.92	0.61	0.18
X1, X2	-0.52	-0.36	-0.12
X3, X4	-0.45	-0.30	-0.07
X5, X6	-0.42	-0.27	-0.08
X7, X8	-0.44	-0.29	-0.08

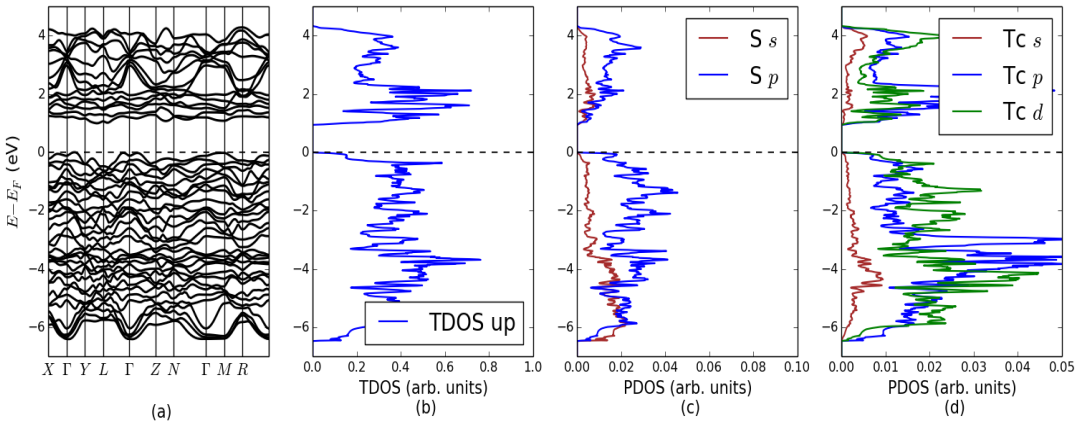


Figure 6.7: Calculated vdW-D2 TcS_2 calculated electronic structure (a) band structure along high symmetry K-points, (b) spin projected TDOS, (c) PDOS of Tc(s,p,d) and (d) PDOS of S(s,p).

Fig. 6.7 shows that TcS_2 is a semiconductor Fig. 6.7 (a) shows its conduction band minimum (CBM) at a point between Y and L of the high symmetry k-points and its valence band maximum (VBM) at a point between Γ and M of the high symmetry k-points, leading to an indirect DFT vdW-D2 band gap of $E_g = 0.99$ eV. Fig. 6.7 (b) depicts the spin projected TDOS, (Fig. 6.7 (c) and (d) show the PDOS[1], from it, we can see that the dominant orbitals at the conduction band minimum are Tc(s) and hybridized S(s and p) with little contribution from hybridized Tc (p and d). The valence band maximum, on the other hand is dominated by S (p) with little contribution from S (s) Tc (s) and hybridized Tc (p and d).

Fig. 6.8 shows that $TcSe_2$ is also a semiconductor Fig. 6.8 (a) shows its conduction band minimum

[1]It is important here to note that sub-figure (c) and (d) are plotted using a different scale. This is to make sure that individual atomic contributions to the density of states are clear in the sub-figures

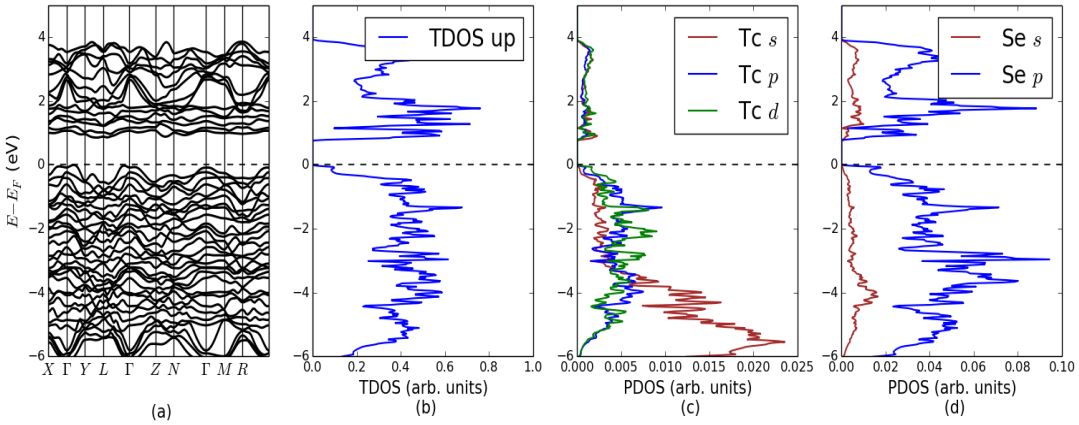


Figure 6.8: Calculated MBJ $TcSe_2$ calculated electronic structure (a) band structure along high symmetry K-points, (b) spin projected TDOS, (c) PDOS of Tc(s,p,d) and (d) PDOS of Se(s,p).

(CBM) at a point between Y and L of the high symmetry k-points and its valence band maximum (VBM) at a point between Γ and Y of the high symmetry k-points, leading to an indirect DFT band gap of $E_g = 0.86$ eV. Fig. 6.8 (b) show the TDOS, Fig. 6.8 (c) and (d) show the PDOS. The dominant orbitals at the CBM are Se(p) with slight contribution from hybridized Tc (s) and Se (s). The VBM is dominated by Se (p) with little contribution from Tc (d).

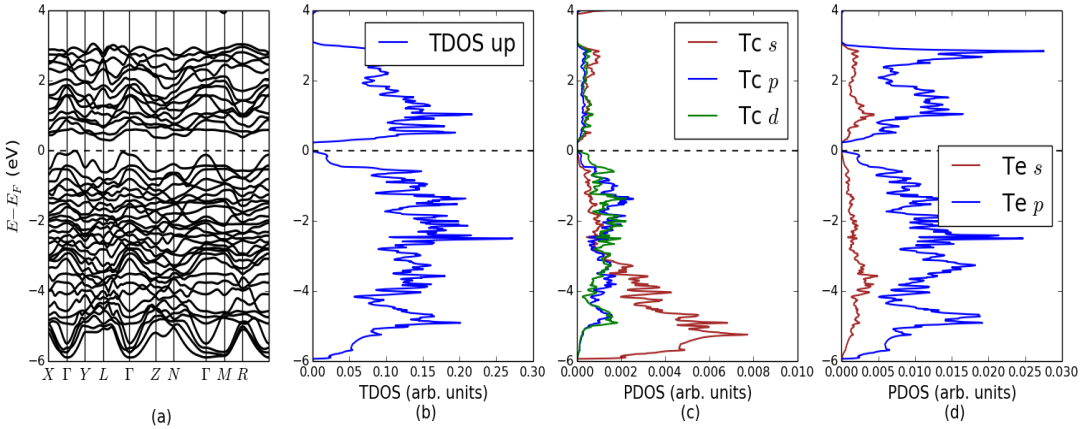


Figure 6.9: Calculated vdW-DF $TcTe_2$ calculated electronic structure (a) band structure along high symmetry K-points, (b) spin projected TDOS, (c) PDOS of Tc(s,p,d) and (d) PDOS of Se(s,p).

Fig. 6.9 depict that $TcTe_2$ is a semiconductor Fig. 6.9 (a) shows its CBM at a point betwen Y and L of the high symmetry k-points and VBM at a point between Γ and Y of the high symmetry k-points, leading to an indirect DFT band gap of $E_g = 0.30$ eV. Fig. 6.9 (b) shows the TDOS, Fig. 6.9 (c) and (d) shows the PDOS. The dominant orbitals at the CBM are Te(p) with slight contribution from Tc

(s). The VBM is dominated by Te (p) with little contribution from Tc (s and d).

Careful look at Figures 6.7, 6.8 and 6.9 reveal that the three TcX_2 materials share a common feature: they are all indirect band gap semiconductors with CBM between Y and L of the high symmetry k-points and VBM between Γ and Y of the high symmetry k-points.

Even though KS-DFT plays a very important role in predicting the properties of material at their ground states, it fails to provide an accurate description of the electronic properties of materials as discussed in Section 5.10. In trying to have a better prediction of the band gaps of the TcX_2 (X = S, Se and Te) structures, their band gaps were calculated using the modified Becke-Johnson potential (MBJ) [212] (a method known to predict band gaps at an accuracy comparable to hybrid and GW at less computational cost), a hybrid functional (HSE06) and G_0W_0 (this method has been described as state-of-the-art method for accurate fundamental band gap calculations, as observed in some extended systems and shown to be true by direct and inverse photo-emission spectroscopy). The relaxed structures obtained from vdW-D2, an approximation we note to provide lattice structural parameters with an accuracy comparable to the experiment, were used for the MBJ, HSE06 and the G_0W_0 calculations. The band gaps obtained are listed in Table 6.5 and compared with the available optical absorption edge reported [50]. It is important to note here that the absorption edge may not necessarily correspond to the fundamental band gap of the structures as observed in a number of transition metal dichalcogenides [223, 224, 225, 226, 227].

Table 6.5: Calculated and experimental indirect energy band gaps (in eV) of TcX_2 (X= S, Se and Te) structures.

Structure	PBE	PBEsol	vdW-TS	vdW-D2	vdW-DF	MBJ	HSE	G_0W_0	Other PBE	Exp.
TcS_2	1.18	1.11	0.52	0.99	1.02	1.10	1.83	1.59	0.90 [a]	1.00 [b]
$TcSe_2$	0.99	0.83	0.36	0.70	0.82	0.86	0.69	1.32	0.80 [a]	0.88 [b]
$TcTe_2$	0.57	0.11	Metallic	0.07	0.30	0.20	0.38	0.63	0.30 [a]	-

a = reference [22], b = reference [50]

The difference in the vdW-TS, vdW-D2 and vdW-DF band gaps may not be unconnected with the difference in the structural equilibrium volumes predicted by the different approximations as earlier explained and shown in Figure 6.10. It is expected in these type of structures that the band gap will increase with increase in volume of the structure. We can understand the band gap volume relationship in these structures when we compare the volume predicted by the approximations considered in Table 6.1 and their corresponding band gaps in Table 6.5 or by looking at the band gap volume relationship

in Figure 6.10 extracted from vdW-D2 calculated structures.

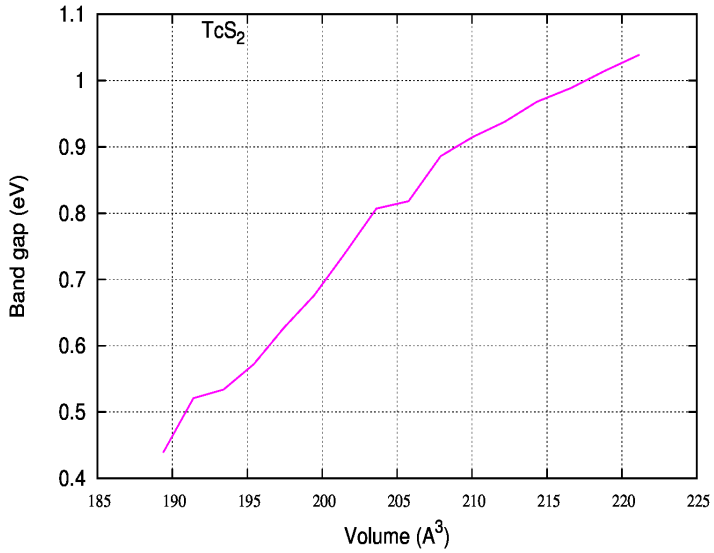


Figure 6.10: Band gap volume relationship in TcX_2 (X= S, Se and Te) calculated from vdW-D2 relaxed structure.

It is important to note here that TcS_2 and $TcSe_2$ having band gap between 0.63 eV and 1.59 eV are promising material for third generation solar cells as discussed in Section 1.1 of this thesis.

To the best of our knowledge, this is the first time where the structural and the electronic properties of TcX_2 (X = S, Se and Te) with inclusion of vander Waal's correction are reported. The vander Waal's correction terms are necessary for accurate description of the structural parameter and the accurate determination of the electronic properties relies heavily on the accurate determination of the structural parameters. And this is the first time that the electronic properties of these structures are reported beyond DFT.

6.1.4 Doping

In order to maximise the practical application of TcS_2 in nano-devices, solar energy applications and other electronic applications, their electronic and optical properties can be modulated by: the application of external fields, forces, alloying [228, 229], modified layer stacking or doping [230, 231, 232, 233, 234, 235]. Recently, investigations have proven that application of strain can change the band gap of some TMDCs from indirect to direct, while transition from semi-conductor to metal has also been observed

in some TMDCs [236, 237]. The band gap of these materials may also be tuned by the application of external electric fields [238, 239].

To achieve a possible modification of the electronic properties of TcS_2, we substitute the Tc with Fe in TcS_2. This is based on Hick's [240] rule for solubility, the ionic radius of the host and intercalating metal and should be close and the doped metal should come from a group adjacent to the host metal in the periodic table. Based on this, we decided to investigate substitutional doping of TcS_2 by replacing selected Tc atoms by Fe atoms, an element from the adjacent group in the periodic table, having one electron more than Tc in its d-shell. We calculated the DFT electronic band structure of $Tc_{1-x}SFe_x$ and $Tc_{1-x}Fe_xS$ (x = 0.125, 0.25, 0.375, or 0.5), corresponding to a sub set of configurations for 12.5%, 25% 37.5% and 50% Fe doping respectively by considering modifications of the primitive unit cell forming supercells in different directions by doubling the structural lattice parameter (*a, b or c* in Table 6.1). The structures were relaxed using vdW-D2 approximation, an approximation we note to predict lattice structural parameters with an accuracy comparable to the experiment (see Table 6.1). As observed in Table 6.5, MBJ predict the band gaps of these type of structures with an accuracy that is comparable to experiment, thus, we decided to limit our band gap calculations to vdW-D2 and MBJ approximations. We note that in the bulk structures, there are the two Tc atomic positions that have different environments. This leads to five, twenty nine, thirty eight, and sixty two distinct doping configurations for the 12.5%, 25% 37.5% and 50% Fe-doping configurations considered respectively. For example, using Figure 6.11, showing the TcS_2 structure and Figure 6.12 showing the positions of technetium in TcS_2 unit cell, the possible doping configurations of the unit cell are listed in Table A.1 of the appendix. To summarise the table, the volume per atom as a function of doping configuration, formation energy per atom as a function of doping configuration and band gaps as a function of doping configuration are shown pictorially in Figures 6.13, 6.14 and 6.15, respectively. It is important to mention here that the configurations are arranged according to their size of MBJ band gap in Figure 6.13 and not according to the percentage of the doping. We observed that there is no strict relationship that exists between the percentage of doping or the location of the dopant atom with the band gap of the structure. Detailed information about the band gap, doping position and percentage can be found in Table A.1.

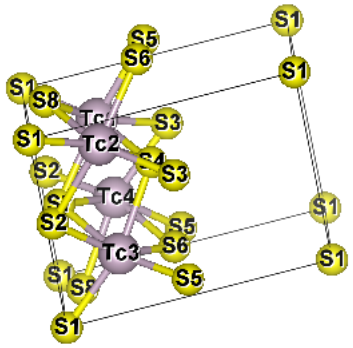


Figure 6.11: Primitive unit cell for technetium sulphide in the $P\bar{1}$ structure and the positions of the four Technetium atoms.

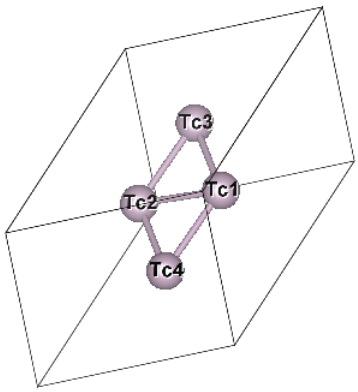


Figure 6.12: Positions of Tc atoms.

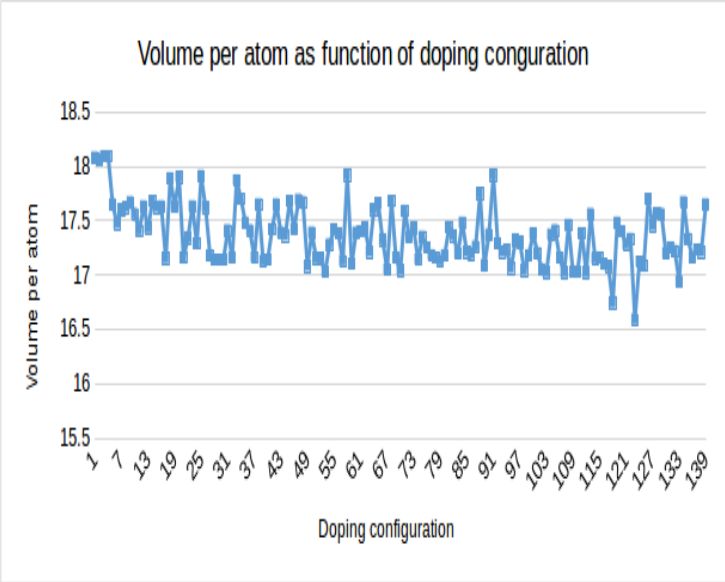


Figure 6.13: Structural volume per atom as a function of doping configuration.

From Figure 6.13, we can observe how the variation of the percentage of the dopant and doping positions affect the volume of the doped system. It is therefore expected that the electronic properties of the new structure will change as a result of the volume change of the new structure.

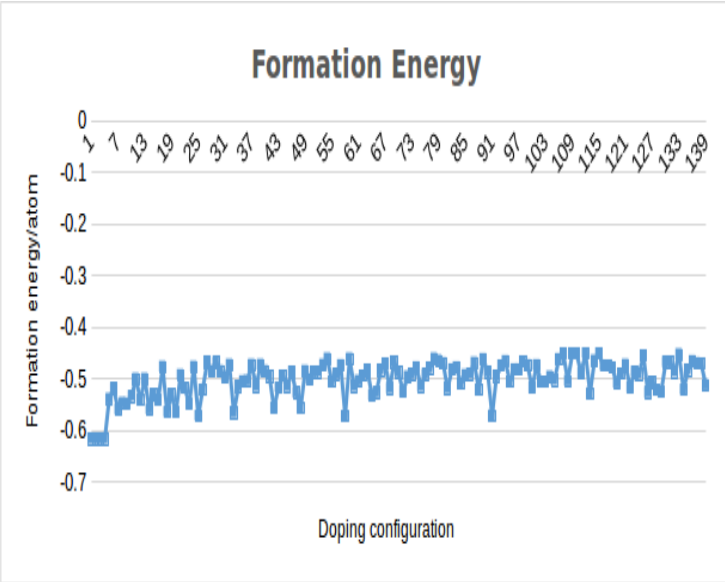


Figure 6.14: Formation energy per atom as a function of doping configuration.

Formation and cohesive energy were used to determine the stability of the doped structures in Table A.1, from the table and Figure 6.14, we observed that the formation and cohesive energy obtained for the

investigated systems are all negative. A positive value of any of the two energies at a given temperature and pressure signifies instability in the structure and tendency of the structure to decompose to its constituent solid components. On the other hand, the more negative the value of the energies, the more stable the structure is. Our results in Table A.1 and pictorially depicted in Figure 6.14 suggests that the doped structures are stable with respect to decomposition to their components and that the formation energy of the new structure is dependent on the percentage of the dopant atom and the position of the doped atom.

We note that there is induced magnetisation in some of the doped structures and that the magnetic moments are almost entirely confined to the Fe and Tc atoms. Magnetic moments associated with other atoms are negligible. The magnetic semiconductors are materials of interest in the field of spintronics. We also note that TcS_2 and majority its Fe doped derivatives studied in this report are indirect band gap materials, the direct band gap systems are quite few. Direct gap materials are of importance for optical absorption without phonon assistance. We also note that the doped systems have potential applications in third generation solar cells as discussed in Section 1.1.

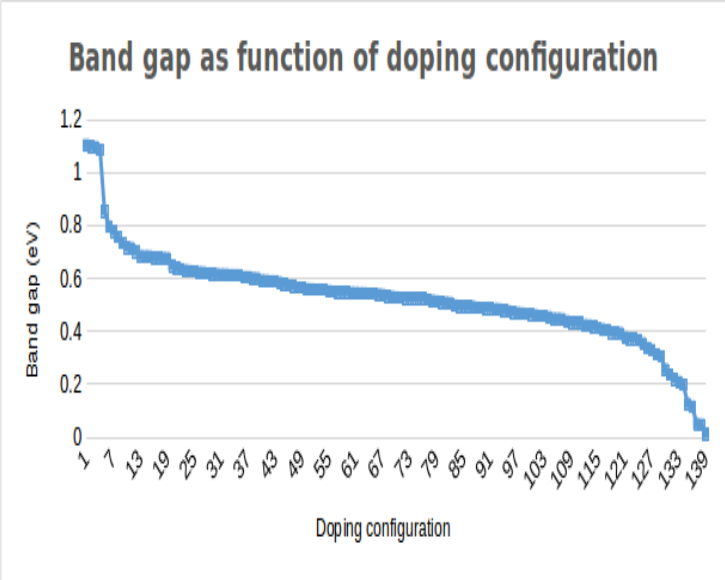


Figure 6.15: Band gap as a function of doping configuration for TcS_2 calculated with MBJ functional.

From Figure 6.15, we observed that doping TcS_2 decreases the band gap of the parent material, the band gap of the new structure depends on the amount of dopant Fe introduced into the parent material and the position where the dopant are placed in the structure.

6.2 Hafnium dichalcogenide

The structures of this family of compounds has been discussed in Section 1.2.2 of this thesis. We will only report simulations of the mechanical, thermal, as well as the optical properties of these family of structures. It is, however, our belief that, for accurate description of properties of these structures, it is important to begin with an accurate description of their structural properties. Since the structures are layered, they were relaxed using vdW-TS and vdW-DF. It was found that the vdW-TS lattice structural parameters are surprisingly in good agreement with the experimental reported structural parameters, with an error that is less than 3 $\%$. We therefore decide to adopt the vdW-TS structural parameters for all our subsequent calculations.

6.2.1 Mechanical and thermal properties

In order to examine the stability of the HfX_2 structures against mechanical distortions, their elastic and phonon properties were determined. The elastic constants of the structures are listed in Table 6.6 and the phonon dispersion plots shown in Figure 6.16 .

The necessary and sufficient conditions for the stability of a hexagonal crystals are:

$$C_{11} > \mid C_{12} \mid \quad 2C_{13}^2 < C_{33}\,(C_{11} + C_{12}) \quad C_{44} > 0. \tag{6.2.1}$$

Table 6.6: Calculated elastic constants (GPa) for HfX_2 (X = S, Se and Te).

		C_{11}	C_{12}	C_{13}	C_{33}	C_{44}
HfS_2	vdW-TS	1326	217	50	315	105
	vdW-DF	1358	253	56	284	60
$HfSe_2$	vdW-TS	1032	192	50	318	95
	vdW-DF	1099	224	79	305	59
$HfTe_2$	vdW-TS	621	199	69	219	138
	vdW-DF	1062	258	374	1228	388

From Table 6.6, we note that HfX_2 has satisfied one of the necessary and sufficient conditions for crystal stability discussed in Section 5.7. From Figure 6.16, we observe that HfX_2 have no imaginary phonon frequencies in all the considered brillouin zone. We may therefore assume that the structures are stable against mechanical distortions.

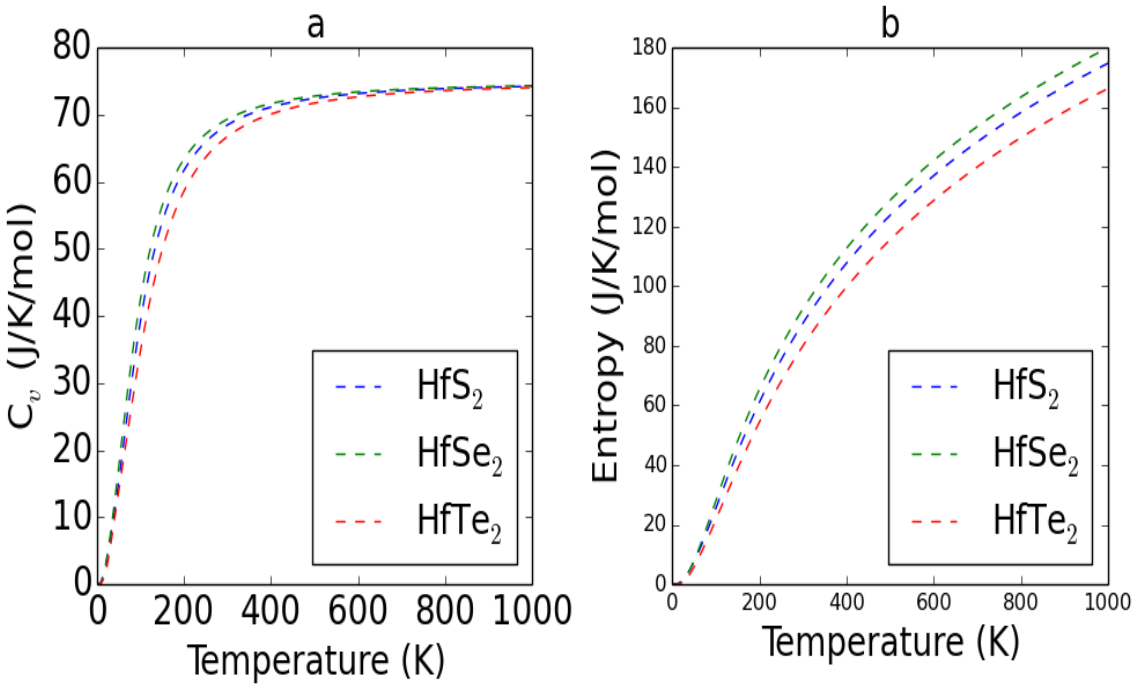


Figure 6.16: HfX_2 phonon dispersion relation graph calculated using vdW-TS.

Results for the specific heat capacity at constant volume for the HfX_2 structures are shown in Figure 6.17. From the Figure, the heat capacity of $HfSe_2$ is the first to approach a constant value (Dulong and Petit law) at about 260 K. It is also observed that $C_v[HfSe_2] < C_v[HfS_2] < C_v[HfTe_2]$. These relationships are consistent with the relative phonon frequencies shown in Figure 6.16 (i.e. the number of lower lying energy states in $HfSe_2$ are more than that of HfS_2, which in turn is higher than that of $HfTe_2$). Since the structures are semiconducting, the heat capacity at low temperatures is expected to be dominated by the vibrational degrees of freedom. The electronic contributions will only become relevant when the thermal energy kT is sufficient to excite the electronic degrees of freedom, where k is Boltzmann's constant and T is the temperature.

6.2.2 Electronic and Optical properties

For accurate determination of the optical properties of a structure, it is important to start from an accurate description of its electronic properties. As such we compare our calculated electronic properties (which is used as input to the optical properties calculations) with the reported theoretical and experimental electronic properties of the HfX_2 structures. The experimental band gaps are mainly ex-

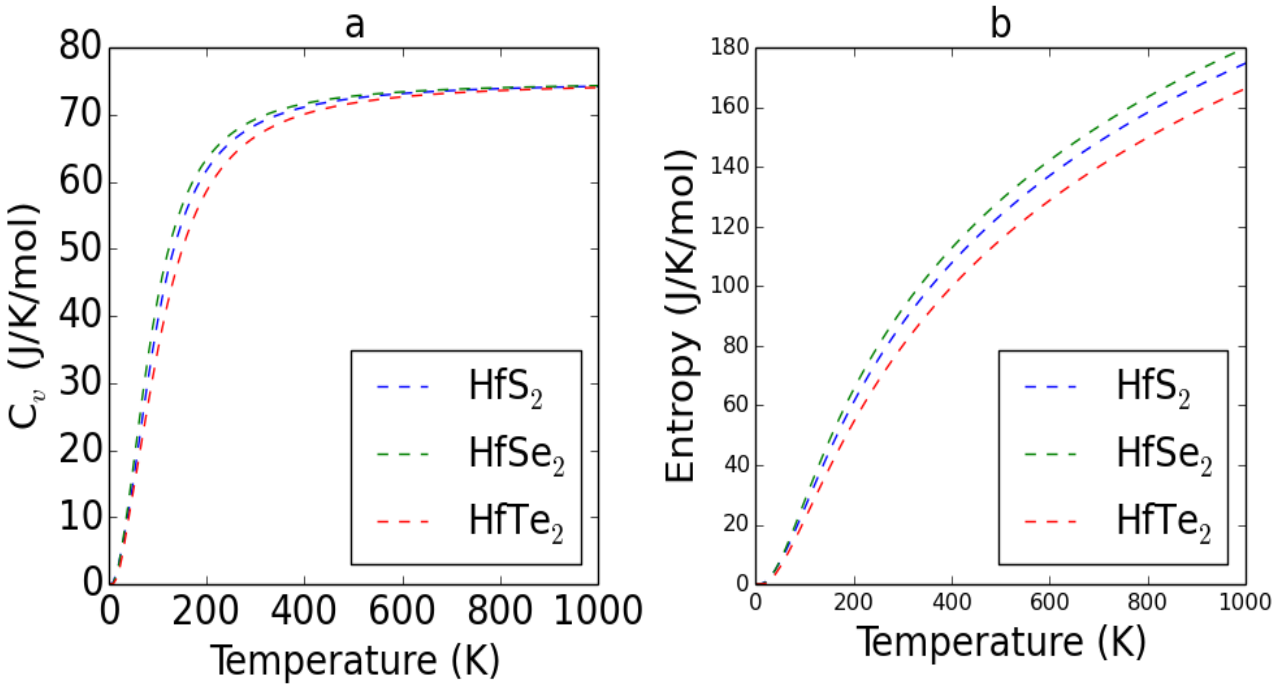


Figure 6.17: vdW-TS calculated specific heat capacity at constant volume and entropy for HfX_2 (X= S, Se and Te) structures.

tracted from optical (reflectivity, thermoreflectance, transmission, or absorption) experiments. Tables 6.7 and 6.8 list the calculated and experimental indirect and direct band gaps of the HfX_2 structures, respectively. From the tables, we observed that our calculated band gaps are in good agreement with the reported calculated and experimental band gaps (optical band gaps) of the structures, suggesting we have a good starting point for the computation of the optical properties. The difference between our results and that of Jiang [40] may be as a result of the fact that they did not account for long range dispersion forces in relaxing their structures or the difference in pseudopotentials used in the computations. Also, the difference between our calculated values and the experimental ones may be as a result of the difference in the input parameters of the structure.

Table 6.7: Calculated and experimental band gaps eV of HfX_2 (X= S, Se).

	GW	Other GW	Exp.
HfS_2	1.79	1.96 [a]	1.96 [b], 2.13 [c], 1.80 [d], 1.87 [e]
$HfSe_2$	1.08	1.26 [a]	1.13 [b], 1.15 [d]

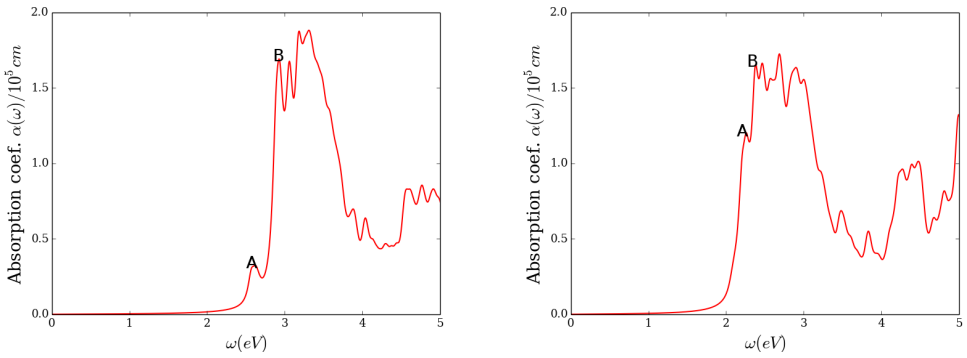
a = reference [40], b = reference [241], c = reference [242], d = reference [243] and e = reference [244]

In order to calculate the binding energies of the excitons in HfX_2, their optical absorption spectra were calculated at the BSE level of approximation, the positions of the fist two peaks were compared with the GW calculated direct band gaps. Figure 6.18 depicts the absorption spectra of the structures. From the Figure, we note that HfS_2 starts to absorb photons at about 1.57 eV of the ultra-violet region of the spectrum and that there is a downward shift in absorption energy as we move from sulphur to selenium.

Table 6.8: Calculated and experimental direct band gaps eV of HfX_2 (X= S, Se).

Band gap	GW	Other GW	Exp.
HfS_2	2.78	2.92 [a]	2.60 [b], 2.87 [c]
$HfSe_2$	2.19	2.27 [a]	2.02 [c]

a = reference [40], b = reference [242] and c = reference [245]



(a) Bulk HfS_2 optical absorption (b) Bulk $HfSe_2$ optical absorption

Figure 6.18: HfX_2 (X= S, Se) BSE calculated optical absorptions.

The binding energies of the excitons can then be determined by subtracting the energies that correspond to the first two peaks in Figures 6.18a and 6.18b from the GW direct band gaps in Table 6.8. The positions of the first two peaks are listed in Table 6.9 and their corresponding binding energies in Table 6.10. Negative binding energy in the table may be attributed to resonant exciton corresponding to that energy level. It is important to note that the absorption edge of these structures is lower than their GW band gaps, as expected from the inclusion of the interaction between the electron and hole quasiparticles in the BSE approximation.To the best of our knowledge, this is the first time where the optical properties of HfX_2 (X = S and Se) is reported at the BSE level of approximation.

It is important to note that HfS_2 and $HfSe_2$ having band gaps of 1.96 eV and 1.26 eV, respectively start

Table 6.9: HfX_2 (X= S, Se) BSE calculated positions for A and B peaks in eV.

	HfS_2	$HfSe_2$
E_A	2.61	2.26
E_B	2.94	2.38

Table 6.10: HfX_2 (X= S, Se) BSE calculated binding energy for A and B excitons in eV.

	HfS_2	$HfSe_2$
E_B^a	0.17	-0.07
E_B^b	-0.16	-0.19

to absorb light within the infra red and the red region of spectrum are promising materials for first and third generation solar photovoltaic applications.

In order to use the materials in photovoltaic application, we may need to investigate the life time of the excitons of the structures.

6.2.3 Monolayer HfX_2 (X = S, Se) Electronic and Optical properties

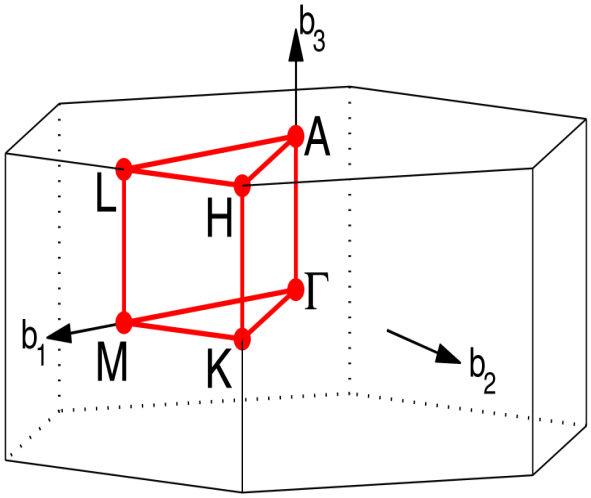


Figure 6.19: High symmetry points used in HfX_2 (X = S, Se) band structure calculations.

Our calculated fundamental electronic band gap of monolayer HfX_2 (X= S, Se) structures are listed in Table 6.11. The monolayers of these structures were found to be indirect band gap semiconductors,

their conduction band minimum lie at the A and valence band maximum at the M points of the high symmetry points, respectively. The Brillouin zone of the structures is shown in Figure 6.19. From the table we note that our calculated PBE electronic band gaps are in good agreement with those reported in [246]. The difference in our band gaps and that of reference [246] is less than 10 $\%$. The difference between our calculated band gap and that of reference [246] may be as a result of the small difference in our relaxed lattice parameters. However, we have no experimental or GW fundamental band gaps to compare our results with.

Table 6.11: Monolayer HfX_2; X= S, Se band gap in eV.

	HfS_2	$HfSe_2$
PBE	1.22	0.67
GW	2.02	0.93
Direct GW gap	3.07	2.31
Other PBE	1.27 [a]	0.61 [a]

a = reference [246]

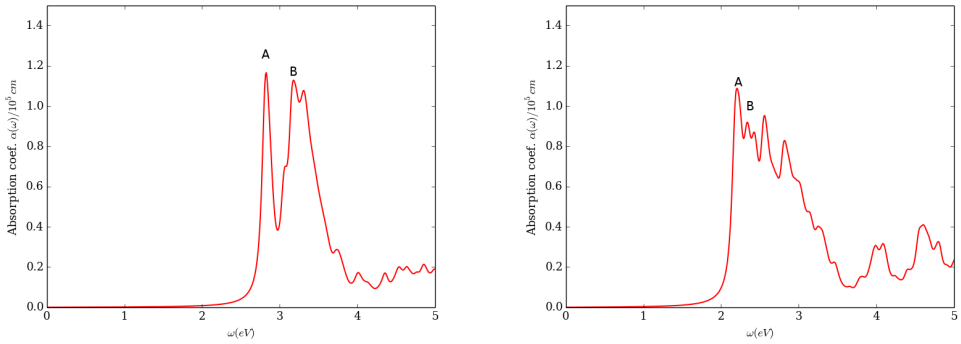
In order to determine the optical properties, the absorption spectra of the monolayer HfX_2 family of structures were calculated at the BSE level of approximation. The results are plotted in Figure 6.20a and 6.20b. From the figures, we can note that monolayer HfS_2 starts to absorb photons in the ultra-violet region of the spectrum and that there is a downward shift in energy absorption energy as we move from sulphur to selenium.

For the binding energies of the energetically lowest lying excitons, the energies of the peaks in the BSE calculated absorption coefficient were compared with the quasi-particle energies obtained from the GW calculations. The positions of the first two peaks are listed in Table 6.12. Again, the binding energies of the excitons are estimated by subtracting the lowest BSE absorption peak energy from the GW direct band gap energy, i.e. E_A^a = (GW direct gap) -E_A and E_B^b = (GW direct gap) -E_B. These binding energies are listed in Table 6.13. We observed that on moving from bulk to monolayer in these compounds, the binding energies increase. This is consistent with the decrease in the screening and stronger interaction between electron and hole quasi-particles in the mono-layer. This becomes clear when we compare Tables 6.9 and 6.13. Negative binding energies suggest a resonant exciton at the corresponding energy level.

To the best of our knowledge, this is the first time ever that the electronic properties and the optical properties of the monolayer HfX_2 (X= S, Se) are reported at the GW and the BSE levels of approxima-

Table 6.12: Monolayer HfX_2 (X= S, Se) BSE calculated excitation energies for A and B excitons in eV.

	HfS_2	$HfSe_2$
E_A	2.84	2.20
E_B	3.17	2.60



(a) HfS_2 optical absorption (b) $HfSe_2$ optical absorption

Figure 6.20: Monolayer HfX_2 (X= S, Se) BSE calculated optical absorptions.

tions, respectively. The structures have band gaps that can be utilised in the manufacture of tandem solar cells and the structures are good absorbers of light. These qualities advantageous in multilayer solar cells.

6.3 Hafnium trichalcogenide

The structure of this family of compounds was discussed in Section 1.2.2 of this thesis. Since the structure is layered, we decided to use two different van der Waal's correction terms to study the structural properties of the compounds. The van der Waal's correction terms are necessary for accurate description of the structural properties of a layered structures. Details about the need of van der Waal's correction term for accurate description of layered structural parameters was given in Section 6.1 of the thesis.

Table 6.13: Monolayer HfX_2 (X= S, Se) BSE calculated binding energy for A and B excitons in eV.

	HfS_2	$HfSe_2$
E_B^a	0.23	0.11
E_B^b	-0.1	-0.29

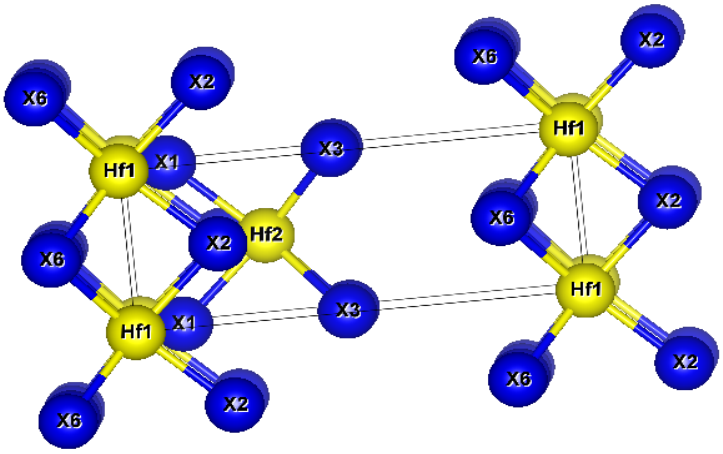
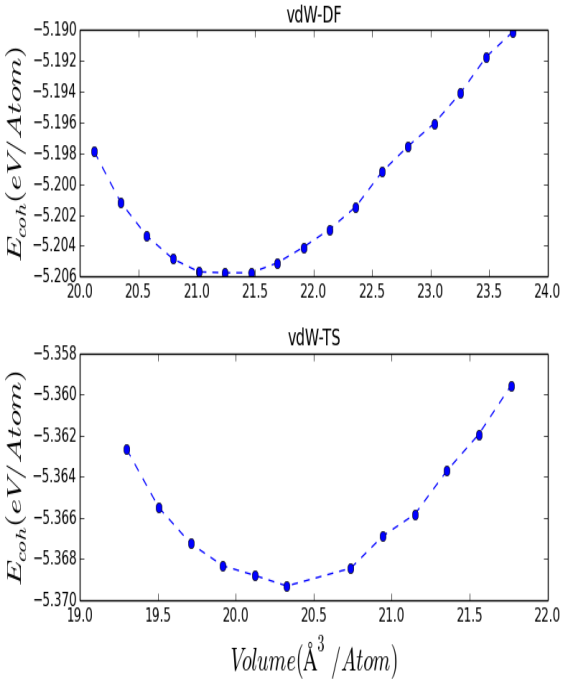
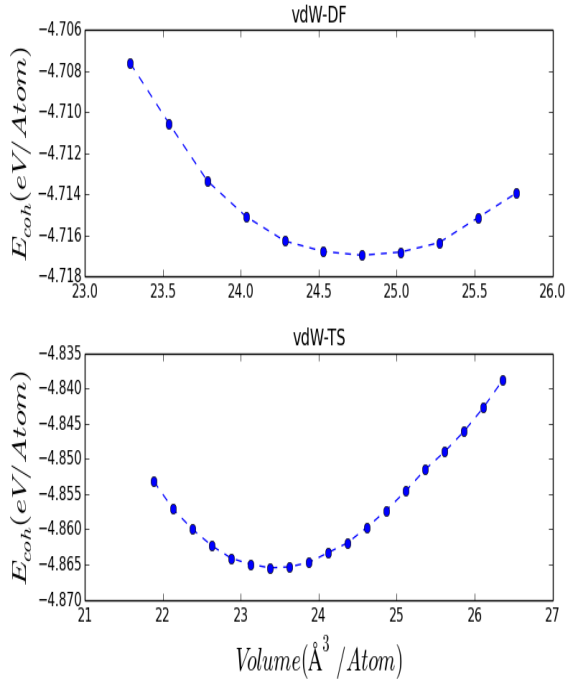


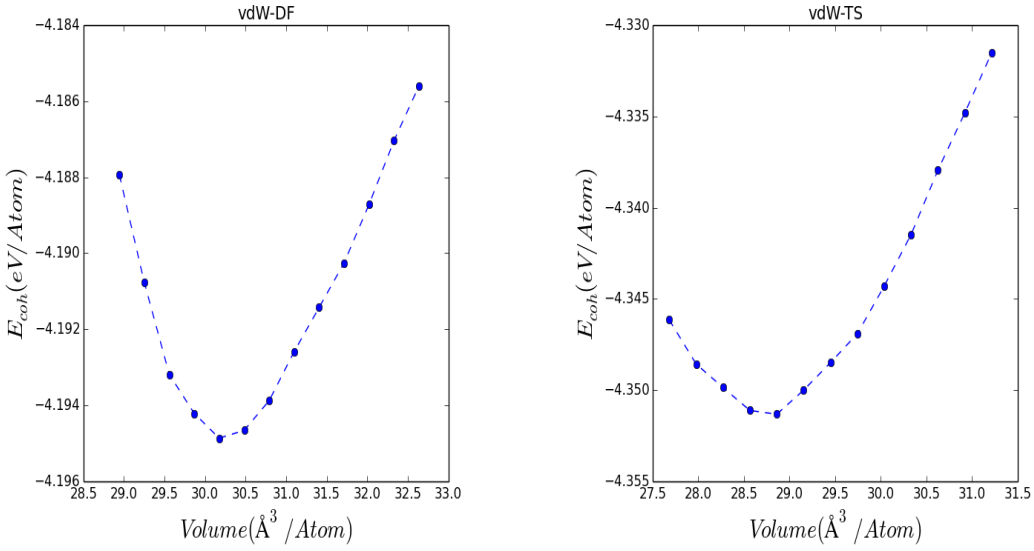
Figure 6.21: HfX_3 structure.



(a) HfS_3 cohesive energy-volume graph calculated using (a) vdW-TS and (b) vdW-DF



(b) $HfSe_3$ cohesive energy-volume graph calculated using (a) vdW-TS and (b) vdW-DF



(c) $HfTe_3$ cohesive energy-volume graph calculated using (a) vdW-TS and (b) vdW-DF

Figure 6.22: HfX_3 cohesive energy-volume relation.

The graph of cohesive energy against volume for HfS_3, $HfSe_3$ and $HfTe_3$ calculated using vdW-TS and

vdW-DF are plotted and shown in Fig. 6.22. The HfX_3 cohesive energy was calculated by subtracting the energy of its constituents isolated atoms from the HfX_3 total energy of a unit crystal at equilibrium lattice constant as discussed in Section 5.5. The cohesive energy and formation energy calculated are listed in Table 6.14. From the table, we can see that both the cohesive energy and the formation energies are negative, an indication that the reactions leading to the formation of these structures are an exothermic reactions, suggesting that these structures can be readily formed from their constituent atoms as observed experimentally [60, 63, 67, 247, 69]. From the table, we also observe that both the cohesive and formation energies per atom of the HfX_3 (X = S, Se and Te) structures decrease in magnitude as the atomic number of the chalcogen atom increases, indicating that the compounds are relatively less stable with increasing atomic number of the chalcogen atom. The unit cell of the HfX_3 structure is displayed in Figure 6.21

Table 6.14: Calculated cohesive and formation energy/atom of HfX_3 (X = S, Se and Te) structures in (eV).

	Functional	HfS_3	$HfSe_3$	$HfTe_3$
Cohesive energy	vdW-TS	-5.30	-4.87	-4.35
	vdW-DF	-5.49	-4.72	-4.20
Form. energy	vdW-TS	-1.14	-0.94	-0.50
	vdW-DF	-1.30	-1.05	-0.62

The equilibrium lattice parameters are given in Table 6.15, where we observe that these lattice parameters agree well with the measured experimental values [67, 63] . The inter-layer distances are overestimated in both vdW-TS and vdW-DF approximations, which may be interpreted as the inability of the dispersion correction terms used in the calculations to accurately account for the long range dispersion forces in these structures. We note that vdW-TS predicts volumes that are closer to the experimental values in each case and also predicts lattice parameters that are in better agreement with the experimental values in most cases.

We can therefore conclude that the vdW-TS approximation predicts structural parameters in better agreement when compared to experiment for HfX_3 (X= S, Se and Te) systems. Qualitative trends in the change of volume and lattice parameters as functions of chalcogenide atom, however, are the same for the two approximations.

Table 6.15: Calculated and experimental equilibrium parameters of HfX_3(X= S, Se, Te): lattice constants [a (Å), b (Å), c (Å)], atomic volume V_0 (Å^3) and angle β°.

	Functional	*a (Å)*	*b (Å)*	*c (Å)*	V_0 *(Å^3)*	β°
	vdW-TS	5.06	3.62	9.34	162.32	96.62
HfS_3	vdW-DF	5.17	3.62	9.16	170.40	96.86
	Experiment	5.09 [a]	3.59 [a]	8.97 [a]	162.80 [a]	97.38 [a]
	vdW-TS	5.31	3.73	9.52	187.12	97.18
$HfSe_3$	vdW-DF	5.49	3.76	9.67	198.00	97.02
	Experiment	5.39 [a]	3.72 [a]	9.43 [a]	187.30 [a]	97.78 [a]
	vdW-TS	5.85	3.90	10.12	229.36	97.84
$HfTe_3$	vdW-DF	6.02	3.95	10.26	241.84	97.85
	Experiment	5.88 [a]	3.90 [a]	10.06 [a]	228.50 [a]	97.98 [a]

a = reference [67]

The shortest distances between the metal and the chalgonedide in the HfX_3 (X = S, Se and Te) structures are listed in Table 6.16. We can infer from this table, that the distance between the metal and the chalcogenide increases as we move down the chalcogenide group in the periodic table, which is consistent with what was observed in the volume change of the structures.

6.3.1 Mechanical and thermal properties

The structural mechanical stability of HfX_3 was determined by calculating their phonon dispersion relation and elastic constants. Fig. 6.23 shows the HfX_3 phonon dispersion curves, calculated based on vdW-TS functional, an approximation identified to produce volume at an accuracy that is comparable to experiment.

From this figure, we observe that all the phonon frequencies of the structures are positive, the structures therefore satisfy one of the elastic stability conditions discussed in Section 5.7.

In a monoclinic crystal, the independent elastic constants as discussed in Section 5.7 are C_{11}, C_{12}, C_{13}, C_{15}, C_{22}, C_{23}, C_{25}, C_{33}, C_{35}, C_{44}, C_{55}, C_{66}, and C_{46}. Conditions for mechanical stability are [248, 249] $[C_{11}+C_{22}+C_{33}+2(C_{12}+C_{13}+C_{23})]>0$, $C_{11}>0$, $C_{22}>0$, $C_{33}>0$, $C_{44}>0$, $C_{55}>0$, $C_{66}>0$, $C_{33}C_{55}-C_{35}^2>0$, $C_{44}C_{66}-C_{46}^2>0$, $C_{22}+C_{33}-2C_{23}>0$, $[C_{22}(C_{33}C_{55}-C_{35}^2)+2C_{23}C_{25}C_{35}-C_{23}^2C_{55}-C_{55}^2C_{33}]>0$ and $\{2[C_{15}C_{25}(C_{33}C_{12}-C_{13}C_{23})+$

Table 6.16: calculated and experimental HfX_3 (X = S , Se and Te) structures nearest neighbour distances in Å unit see Figure 6.21.

Functional	Hf - Hf	Hf - X (Å)	X - X(Å)
HfS_3			
vdW-TS	4.19	2.60	2.16
vdW-DF	4.33	2.68	2.17
Experiment	4.37 [a]	2.99 [a]	2.10 [a]
$HfSe_3$			
vdW-TS	4.40	2.72	2.40
vdW-DF	4.38	2.69	2.40
Experiment	4.55 [a]	2.70 [a]	
$HfTe_3$			
vdW-TS	4.48	2.73	2.64
vdW-DF	4.49	2.71	2.61
Experiment	-	-	-

a = reference [67]

Table 6.17: HfX_3 calculated elastic constants (GPa).

		C_{11}	C_{12}	C_{13}	C_{15}	C_{22}	C_{23}	C_{25}	C_{33}	C_{35}	C_{44}	C_{46}	C_{55}	C_{66}
HfS_3	vdW-TS	980	198	73	83	1387	117	0.80	324	-33	119	22	73	309
	vdW-DF	1000	209	99	107	1502	144	13	408	-14	165	24	71	324
$HfSe_3$	vdW-TS	1011	175	87	160	1137	122	-3.51	397	-27	126	67	28	187
	vdW-DF	863	176	112	81	1230	154	7.95	423	-4.25	133	4.85	145	260
$HfTe_3$	vdW-TS	1135	134	158	115	852	149	-7.84	494	-24	240	-42	119	79
	vdW-DF	884	114	111	51	876	99	-15	412	-37	206	-10	102	146

$C_{15}C_{35}(C_{22}C_{13} - C_{12}C_{23}) + C_{25}C_{35}(C_{11}C_{23} - C_{12}C_{13})] - [C_{15}^2(C_{22}C_{33} - C_{23}^2) + C_{25}^2(C_{11}C_{33} - C_{13}^2) + C_{35}^2(C_{11}C_{22} - C_{12}^2)] + C_{55}g\} > 0$

where $g = C_{11}C_{22}C_{33} - C_{11}C_{23}^2 - C_{33}C_{12}^2 + 2C_{12}C_{13}C_{23}$.

The HfX_3 calculated elastic constants are listed in Table 6.17, from the table, we can see that all the listed elastic constants satisfy the stability criteria discussed in Section 5.7. These structures, are

therefore, stable against mechanical distortions. We also note that the in-plane elastic constants C_{11} and C_{22} are considerably larger than the of out-of-plane elastic constant C_{33}, reflecting the larger resistance to in-plane distortions compared to out-of-plane distortions. This is because, in most layered materials, forces between atoms in the same layer are known to be, to a large extent, greater than forces between atoms in different layers. The negative elastic constants observed for some non-diagonal elements may be as a result of the low symmetry of the monoclinic structure [250].

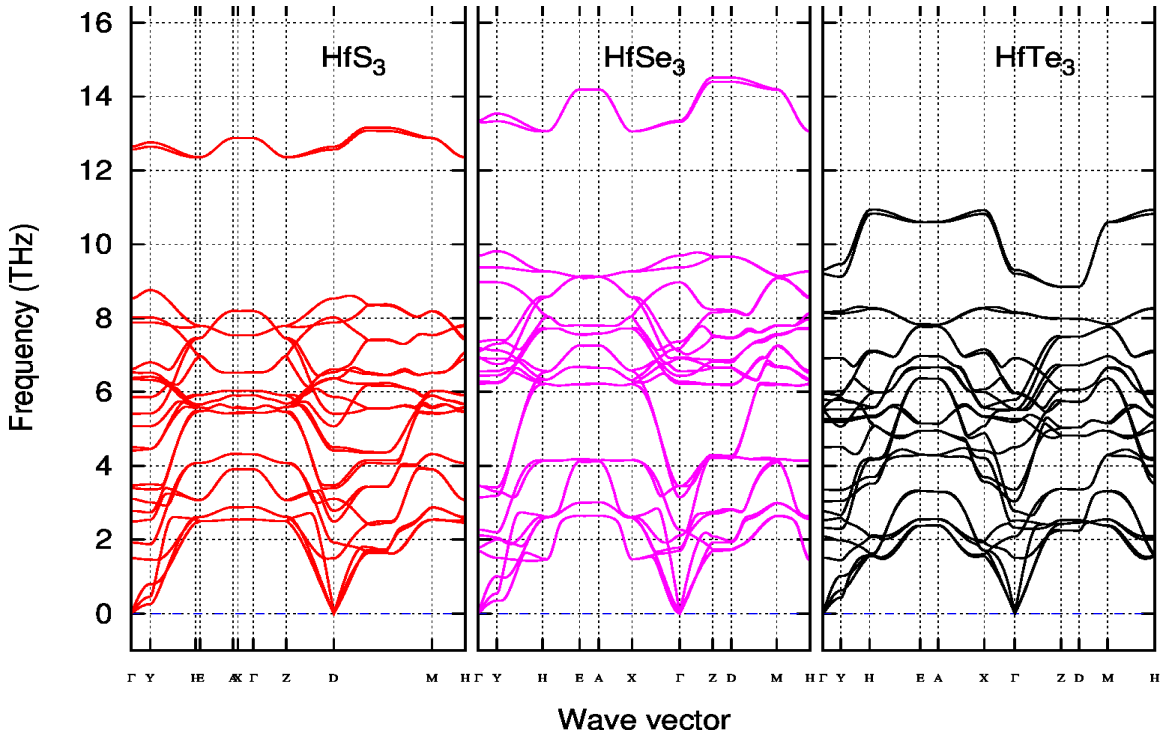


Figure 6.23: HfX_3 phonon dispersion relation graph calculated using vdW-TS.

The phonon contribution to the heat capacity of the HfX_3 (X= S, Se, Te) compounds were computed based on their phonon frequencies. Results for specific heat capacity at constant volume for the structures are shown in sub-figure 6.24 (a). From the figure, the heat capacity of $HfSe_3$ is the first to approach a constant value (Dulong and Petit law) at about 750 K. It is also observed that $C_v[HfSe_3] < C_v[HfS_3] < C_v[HfTe_3]$. These relationships are consistent with the relative phonon frequencies shown in Figure 6.23.

For the semiconducting systems shown in sub-figure 6.23 (a), the heat capacity at low temperatures is dominated by the vibrational degrees of freedom. The electronic contributions only become relevant when the thermal energy is sufficient to excite the electronic degrees of freedom. This happens when

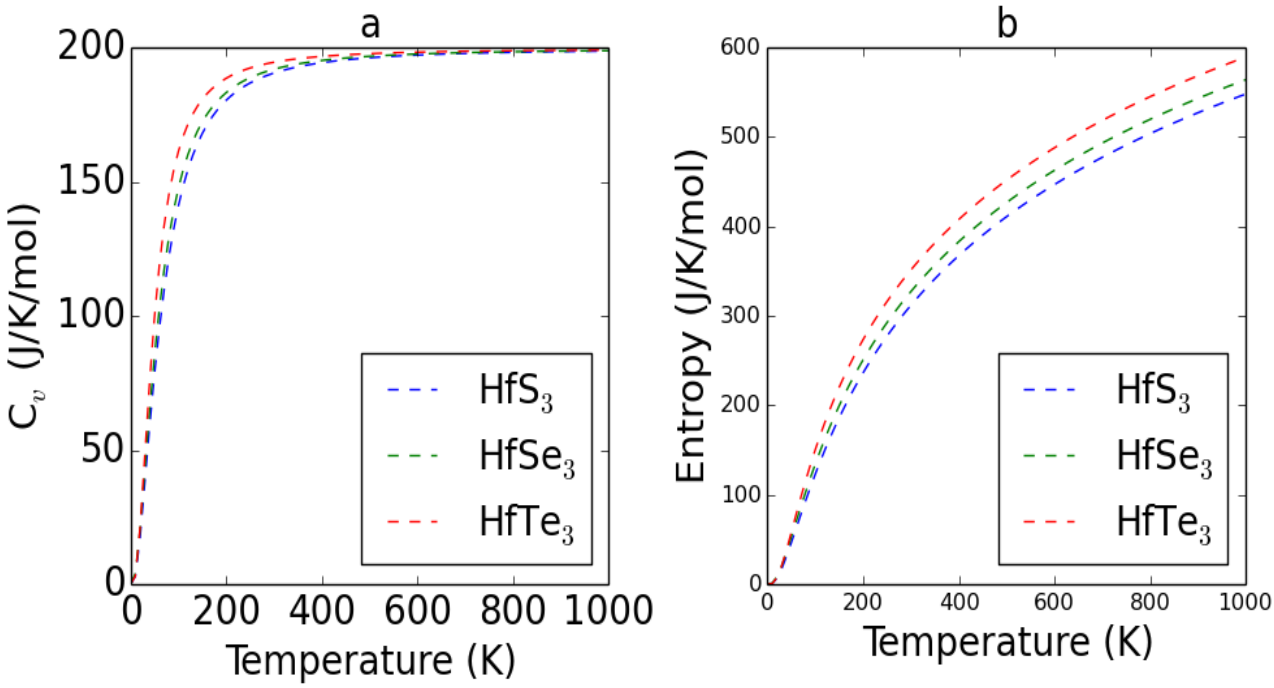


Figure 6.24: vdW-TS calculated specific heat capacity at constant volume and entropy for HfX_3 (X= S, Se and Te) structures.

the thermal energy, kT (k is Boltzmann constant and T, temperature) is of the order of the band gap. Since kT $\sim$ 0.03 eV at room temperature (300 K), the electronic excitations are expected to make an insignificant contribution to the heat capacity at room temperature for these semi-conducting systems. Anharmonic effect are likely to become important with an increase in temperature before the electronic contributions start to play a role.

As we can observe in the sub-figure 6.23 (b), the entropy of the HfX_3 (X= S, Se and Te) structures increases in a steady manner with increasing temperature and with unit cell volume expansion of the structures: the volume of the structures increases on moving from S to Te in the periodic table as observed in Table 6.15. These observations are in agreement with the fact that increase in a unit cell volume of a structure, will result in producing large number of micro states W in the system, leading to logarithmic a increase in the system entropy in accordance with a Boltzmann's equation for entropy $S = k \ln W$.

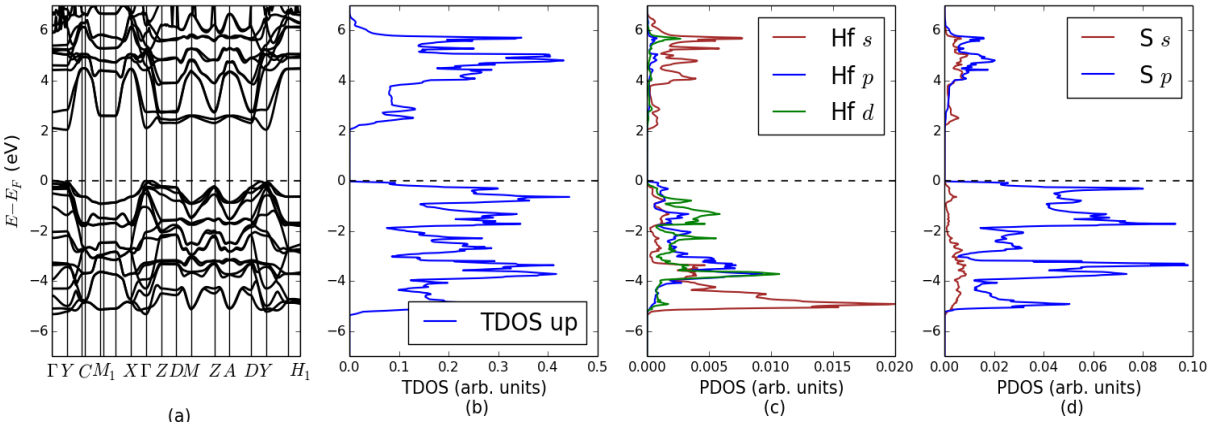


Figure 6.25: Calculated electronic properties of HfS_3 using MBJ functional band structure (a) band structure along high symmetry K-points, (b) spin projected TDOS, (c) PDOS of Hf(s,p,d) (d) PDOS of S (s,p).

6.3.2 Electronic properties

To understand the electronic properties of Hafnium trichalcogenides, their electronic structure and charge transfer were analysed from partial charges calculated in Bader partitions [220, 221, 222]. The electronic charge transfer was calculated using only vdW-TS van der Waal's approximation.

Using Bader charge analysis, it is observed that there is significant charge transfer in the structures. The charge transfer between the Hafnium and the chalcogenides is summarized in Table 6.18. We observed that the charge transfer from the hafnium to the chalcogenide atoms decreases from S to Se to Te, indicating that the bonding becomes less ionic as one goes down the chalcogenide group in the periodic table. The decrease in charge transfer may be correlated with the increasing distance between the transition metal and chalcogen atoms as observed in Table 6.16.

Table 6.18: Charge transfer for HfX_3 (X= S, Se, Te) in electronic charge (e) calculated using vdW-TS see Figure 6.21.

	HfS_3	$HfSe_3$	$HfTe_3$
Hf1, Hf2	1.99	1.83	1.54
X1, X2	-1.05	-0.95	-0.75
X3, X4	-0.46	-0.44	-0.40
X5, X6	-0.48	-0.44	-0.39

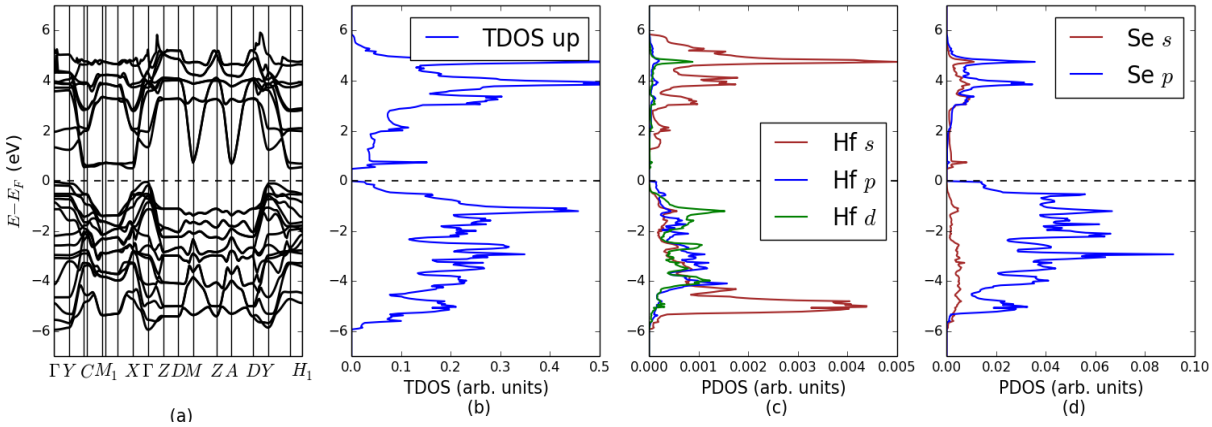


Figure 6.26: MBJ $HfSe_3$ calculated band structure (a) band structure along high symmetry K-points, (b) spin projected TDOS, (c) PDOS of Hf(s,p,d) (d) PDOS of Se (s,p).

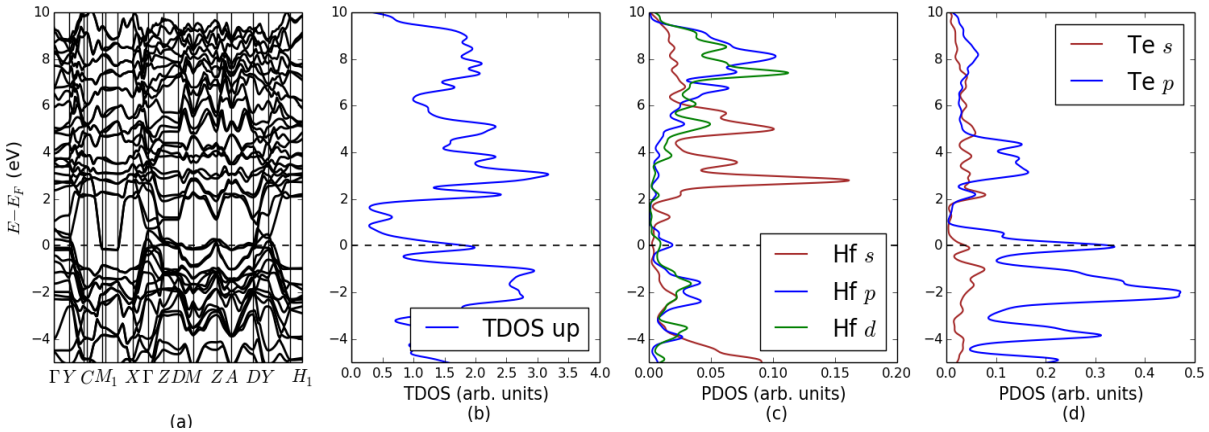


Figure 6.27: vdW-TS $HfTe_3$ calculated band structure (a) band structure along high symmetry K-points, (b) spin projected TDOS, (c) PDOS of Hf(s,p,d) (d) PDOS of Te (s,p).

The band structure and spin projected density of states (DOS) of the HfX_3 structures are plotted in Figures 6.25 to 6.27 and partial density of states (PDOS) in sub-figures (c) and (d) [2]. In the figures, spin projected total density of states (TDOS) are depicted in sub-figures (b) in each case. In all the HfX_3 structures, due to non-magnetic nature of the structures, electrons occupy the spin up and spin down bands equally, leading to a zero spin-polarized density of states, as such only one component of the spin contribution is shown.

The valence band maximum is taken as the zero energy reference for HfS_3 and $HfSe_3$. Due to the

[2] It is important here to note that sub-figure (c) and (d) are plotted using a different scale. This is to make sure that individual atomic contributions to the density of states are clear in the sub-figures

similarity of the details in the calculated band structures, total and partial density of states for the different approximations, the band structures are shown for one representative approximation only in each case.

The semiconducting structures, HfS_3 and $HfSe_3$ have a common feature: they are indirect band gap semiconductors. The valence band maxima of HfS_3 is at Γ and conduction band minima at Y, the valence band maxima at Z and the conduction band minima of $HfSe_3$ is at a point between X and Γ of the high symmetry points and valence band minima at X.

Table 6.19: Calculated and experimental energy band gaps (in eV) of HfX_3 (X= S, Se, Te).

Structure	vdW-TS	vdW-DF	MBJ	Others	Exp.	HSE06	G_0W_0
HfS_3	1.09	1.21	2.04 (2.00)	-	-	1.82	2.17
$HfSe_3$	0.28	0.01	0.55 (0.46)		-	0.60	0.58
$HfTe_3$	Metallic	Metallic	Metallic	-	-	Metallic	Metallic

From the figures, we see that the valence bands at the band gap edge of the sulphides are composed mainly of S s type orbitals with a small contribution from the transition metal s states, while the conduction band gap edge of the selenides is composed mainly of Se p mixed with little of Se d and s states and the s state of the transition metal.

The electronic band gaps of the HfX_3 structures are summarised in Table 6.19. The vdW-TS relaxed structure, which is observed to be in closer agreement to experimental values are used in the MBJ calculations (with the inclusion of spin-orbit coupling) hybrid calculations, G_0W_0 calculations and all the subsequent calculations that come thereafter. Results obtained from the spin-orbit coupling calculations are in parenthesis. It is noted that due to inversion symmetry in the structures, the spin degeneracy in the structures is lifted. The most pronounced effect of spin-orbit coupling is in $HfSe_3$, where it reduces the electronic band gap by about 0.1 eV. The difference between the band gap obtained from vdW-TS and vdW-DF may be connected with the difference in the volumes obtained from the two approximations as the band gaps in these types of structures are assumed to be volume dependent. We observed that PBE band gaps are about 0.32 eV less than the MBJ, HSE06 and the G_0W_0 band gaps. This is not surprising, as it is always expected that the PBE should underestimate the experimental band gap by up to about 50 $\%$. We however could not get experimental band gaps to compare our results with.

The direct band gap of an indirect band gap material is of importance for optical absorption without

phonon assistance . The MBJ calculated direct band gaps were obtained for the structures relaxed using the vdW-TS functional, an approximation that predicts structural parameters that are typically close to experimental values.

Table 6.20: MBJ calculated minimum direct band gaps (in eV) of HfX_3 (X= S, Se, Te).

	HfS_3	$HfSe_3$	$HfTe_3$
MBJ	2.12 (3.1) [e]	1.08	Metallic

e = reference [251]

Looking at the calculated band gaps of the HfX_3 (X= S and Se), we can conclude that these structures having band gaps in the range of 0.5 eV to 2 eV are promising materials for the manufacture of third generation solar cells.

6.3.3 Optical properties

G_0W_0 calculation was carried out on the semiconducting HfX_3 structures and the frequency-dependent optical spectra obtained is displayed in Figures 6.28 and 6.29. In the figures, the optical regions (visible part of the spectrum) is shaded. We see an gradual increase in the real part of the dielectric functions while that of the imaginary part gradually shifts downward within the energy ranges considered. Both have their peaks outside the visible part of the spectrum.

The transmitivity $T(\omega)$ and reflectivity $R(\omega)$ of HfS_3 and $HfSe_3$ are shown in part (b) of sub-figures 6.28 and 6.29. We find the transmitivity in the range $0.84 \geq T(\omega)) \geq 0.78$ for HfS_3 and $0.69 \geq T(\omega) \geq 0.6$ for $HfSe_3$. Thus these structures are good transmitters. In the visible range, the structures has maximum reflectivity $R(\omega)$ at about 3.10 eV ($\backsim 400nm$) for HfS_3 and 2 eV ($\backsim 620nm$) of the visible range of the spectrum corresponding to violet and orange respectively.

In sub-figures 6.28 (c) and 6.29 (c), we can see that the refraction $\eta(\omega)$ and extinction coefficient $\kappa(\omega)$ have similar frequency dependence as the real $\epsilon_{re}(\omega)$ and the imaginary $\epsilon_{im}(\omega)$ parts of the dielectric function as expected.

Sub-figure 6.28 (d) and 6.29 (d), depict the absorption coefficient $\alpha(\omega)$.From these sub-figures, we note that the HfS_3 and $HfSe_3$ start to absorb incident radiation at the 1.07 eV and 0.5 eV range of the spectrum, respectively. As such, they may be potential materials for third generation solar cells.

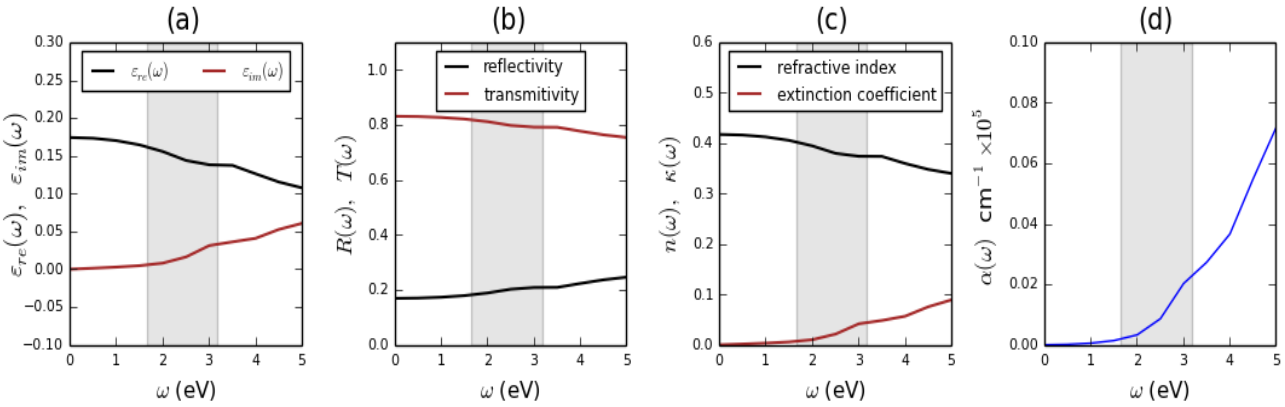


Figure 6.28: GW HfS_3 calculated frequency-dependent optical spectra (a) real $\epsilon_{re}(\omega)$ and the imaginary $\epsilon_{im}(\omega)$ parts of the dielectric function, (b) reflectivity $R(\omega)$ and Transmitivity $T(\omega)$, (c) Refraction $\eta(\omega)$ and extinction coefficient $\kappa(\omega)$ and (d) absorption coefficient $\alpha(\omega)$. The visible range are shaded.

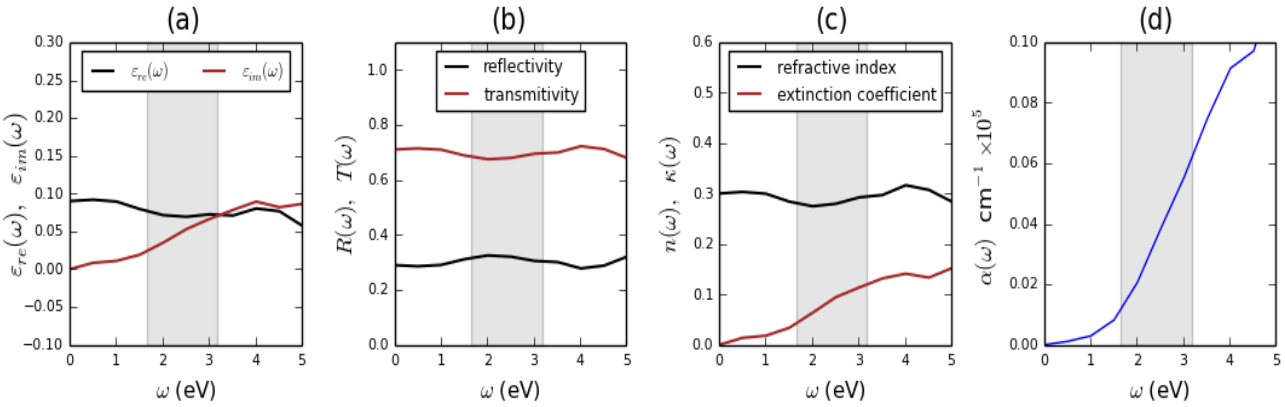


Figure 6.29: GW $HfSe_3$ calculated frequency-dependent optical spectra (a) real $\epsilon_{re}(\omega)$ and the imaginary $\epsilon_{im}(\omega)$ parts of the dielectric function, (b) reflectivity $R(\omega)$ and transmitivity $T(\omega)$, (c) refraction $\eta(\omega)$ and extinction coefficient $\kappa(\omega)$ and (d) absorption coefficient $\alpha(\omega)$. The visible range is shaded.

To the best of our knowledge, this is the first time where the structural, electronic and optical properties of HfX_3 (X = S, Se and Te) are reported at the atomic level.

6.4 Zirconium dichalcogenide

The structures and preparation of the ZrX_2 family has been discussed in Section 1.2.3 of this thesis. It was established that the structural and the electronic properties of the structures have been extensively

investigated theoretically and experimentally. We therefore decided to fill in the missing gap by reporting the mechanical, thermal, as well as the optical properties of these family of structures. For accurate description of these properties of the structures, we relaxed the structures using vdW-TS and vdW-DF. It was found that vdW-TS lattice structural parameters are surprisingly in good agreement with the experimental reported structural parameters, with an error that is less than 3 %. We therefore decide to adopt the vdW-TS structural parameters for all our subsequent calculations.

6.4.1 Mechanical and thermal properties

Having discussed the preparation and the structures of the ZrX_2 in Section 1.2.3, the mechanical, thermal as well as the optical properties of the structures are reported here.

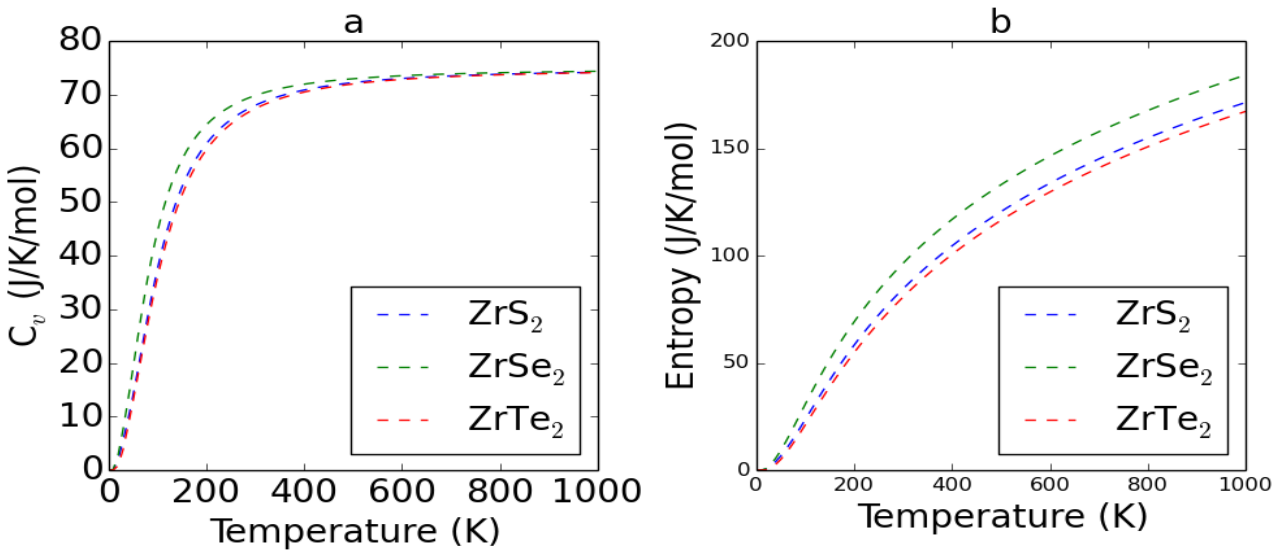


Figure 6.30: vdW-TS calculated Specific heat capacity at constant volume and entropy for the ZrX_2 (X= S, Se and Te) structures.

From Table 6.21, we observe that the calculated elastic constants of ZrX_2 structures satisfy one of the necessary and sufficient conditions for hexagonal crystal stability discussed in Sections 6.2.1 and 5.7 of this thesis.

From Figure 6.31, we note that the the ZrX_2 phonon dispersion curves have no imaginary phonon frequencies, thus, satisfying the last necessary and sufficient condition for hexagonal crystal stability. We can therefore say that the structures are stable against mechanical distortions.

Table 6.21: Calculated elastic constants (GPa) for ZrX_2 (X = S, Se and Te).

		C_{11}	C_{12}	C_{13}	C_{33}	C_{44}
ZrS_2	vdW-TS	1334	235	87	454	111
	vdW-DF	1264	244	59	293	65
$ZrSe_2$	vdW-TS	1052	196	92	474	152
	vdW-DF	1004	218	53	263	60
$ZrTe_2$	vdW-TS	596	170	103	512	132
	vdW-DF	633	212	93	93	171

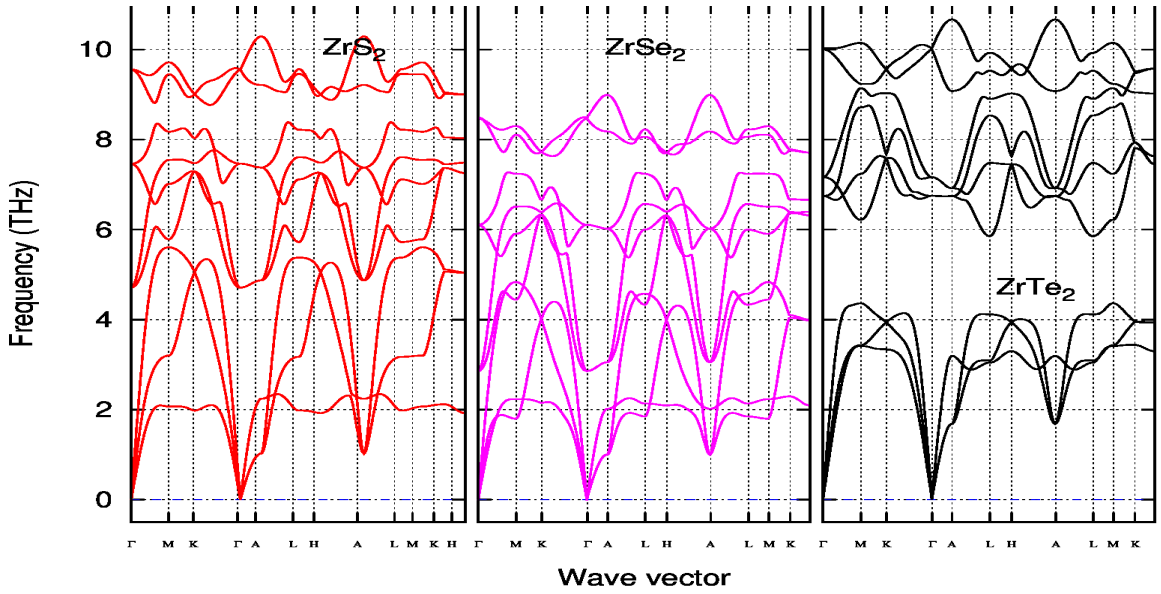


Figure 6.31: ZrX_2 phonon dispersion relation graph calculated using vdW-TS.

The specific heat capacity at constant volume for the ZrX_2 structures calculated from the phonon frequencies calculated from density functional perturbation theory are shown in Figure 6.30. From the figure, we observe that the specific heat capacity of $ZrSe_2$ is the first to approach a constant value (Dulong and Petit law) at about 300 K. It is also observed that $C_v[ZrSe_2] < C_v[ZrS_2] < C_v[ZrTe_2]$. These relationships are consistent with the relative phonon frequencies shown in Figure 6.31. In semiconducting materials, heat capacity at low temperatures is expected to be dominated by the vibrational degrees of freedom. The electronic contributions will only become relevant when the thermal energy kT is sufficient to excite the electronic degrees of freedom (k is Boltzmann's constant and T is the temperature).

6.4.2 Electronic and Optical properties

As discussed in Section 6.2.2, the electronic properties of ZrX_2 are calculated and compared with the theoretical and experimental values reported. Our calculated GW values are then used as input for the computation of the optical properties. Table 6.22 lists band gaps of the ZrX_2 structures. From the table, we observe that our calculated band gaps are in good agreement with both the theoretical and experimental literature band gaps, providing a good starting point for the computation of the optical properties. The experimental band gaps were extracted from various optical experiments. The difference between our calculated band gap and those in literature may be as a result of differences of pseudopotentials used in the computation or the differences in the approximations used in relaxing the structures. The direct band gaps of the structures needed for the determination of the binding energies of the energetically lowest lying excitons are listed in Table 6.23.

Table 6.22: Calculated and experimental band gaps in eV for ZrX_2 (X= S, Se).

Band gap	GW	Other GW	Exp.
ZrS_2	1.51	1.80 [a]	1.68 [b] 1.70 [c], 1.78 [d]
$ZrSe_2$	1.18	1.12 [a]	1.20 [c], 1.10 [e], 1.18 [f]

a = reference [40], b = reference [241], c = reference [252], d = reference [242], e = reference [253] and f = reference [254]

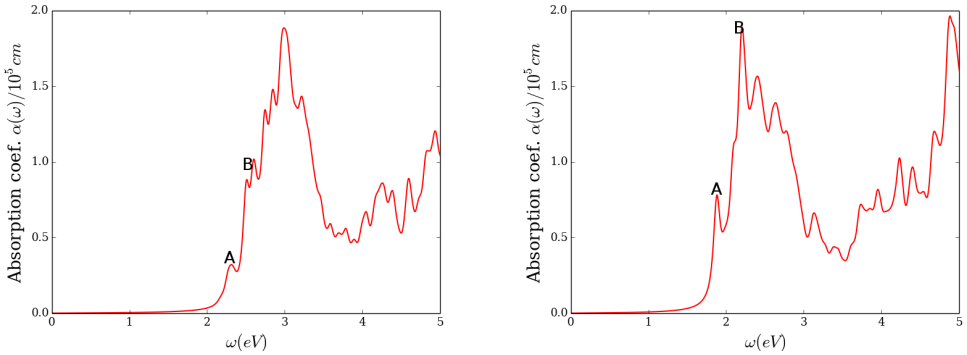
Table 6.23: Calculated and experimental direct band gaps in eV for bulk ZrX_2 (X= S, Se).

Band gap	GW	Other GW	Exp.
ZrS_2	2.32	2.61 [a]	2.10 [b], 2.48 [c]
$ZrSe_2$	2.02	1.94 [a]	1.65 [d], 1.2 [e], 1.1 [f]

a = reference [40], b = reference [254], c = reference [245], d = reference [255], e = reference [252] and f = reference [253]

In order to determine the optical properties, the absorption spectra of the ZrX_2 family of structures were calculated at the BSE level of approximation. The optical absorptions of the structures are shown in Figure 6.32 and the position of the first two peaks of the optical absorption spectra are listed in Table 6.24. From the figure, we observed that ZrS_2 starts to absorb photons in the infra red region of the spectrum and that there is a downward shift in energy absorption ZrX_2 as we move from X = sulphur to X = selenium in these family of structures.

The positions of the first two lower lying excitons in Figure 6.32 were subtracted from the GW calculated



(a) Bulk ZrS_2 optical absorption (b) Bulk $ZrSe_2$ optical absorption

Figure 6.32: ZrX_2 (X= S, Se) BSE calculated optical absorptions.

Table 6.24: ZrX_2 (X= S, Se) BSE calculated positions for A and B peaks in eV.

	ZrS_2	$ZrSe_2$
E_A	2.33	1.88
E_B	2.52	2.22

direct band gap and the binding energies obtained are listed in Table 6.25. We observed that ZrS_2 has only resonant excitons within the spectrum considered while $ZrSe_2$ has both resonant and binding excitons.

Table 6.25: ZrX_2 (X= S, Se) BSE calculated binding energy for A and B excitons in eV.

	ZrS_2	$ZrSe_2$
E_B^a	-0.01	0.14
E_B^b	-0.20	-0.50

Based on our reported band gaps in Table 6.22 and the optical absorption spectra in Figure 6.32b, ZrS_2 and $ZrSe_2$ are promising material for the manufacture of third photovoltaic solar cells.

To the best of our knowledge, this work is the first to investigate, theoretically the optical properties of ZrS_2 and $ZrSe_2$ at the BSE level of approximation.

6.4.3 Monolayer ZrX_2 (X = S, Se) Optical properties

Following the same procedure used in calculating the optical properties of monolayer HfX_2 structures and discussed in Section 6.2.3, the optical properties of monolayer ZrX_2 (X= S and Se) were calculated,

the calculated PBE and GW band gaps are listed in Table 6.26. However, we have no experimental results to compare with, the only available information is that of Li et. al. [256], where the authors used their HSE06 band gap and predicted the experimental band gap of monolayer ZrS_2 to be between 1.7 to 1.93 eV, which is in good agreement with our GW indirect band gap result.

Table 6.26: Monolayer ZrX_2 (X= S, Se) band gap in eV.

	ZrS_2	$ZrSe_2$
PBE	0.80	0.26
GW	1.95	2.53
Direct GW gap	2.83	2.53
Others	1.10 [a], 1.93 [b]	0.45 [a]

a = reference [246] and b = reference [256]

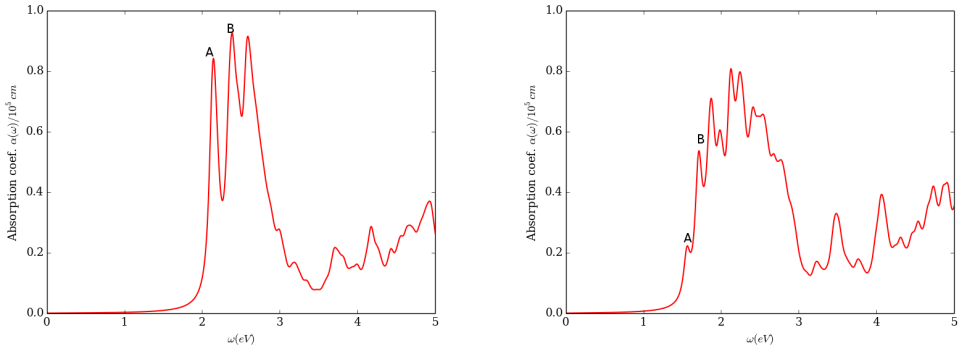
Monolayer ZrS_2 was found to be an indirect band gap material with valence band maximum which lies at Γ and conduction band minimum at A points of the high symmetry k-points whereas $ZrSe_2$ is a direct band gap semiconductor with both valence and conduction bands at the Γ points of the high symmetry k-points. The high symmetry k-points of the structures are similar to those of HX_2 (X= S, Se) and are shown in Figure 6.19. In order to calculate the binding energy of the excitons in the ZrS_2 structures, we therefore need to calculate its direct band gap, which is also listed in Table 6.26.

In order to determine the binding energies of the structures, their optical absorption spectra were computed and plotted in Figure 6.33, from the figures, the BSE calculated positions of the first two peaks were extracted and listed in Table 6.27. The BSE absorption spectra for ZrS_2 and $ZrSe_2$ are shown in Figure 6.33a and 6.33b, respectively, and the BSE transition binding energy listed in Table 6.28.

Table 6.27: Positions for A and B peaks (in eV) calculated at the BSE level for Monolayer ZrX_2 (X= S, Se).

	ZrS_2	$ZrSe_2$
E_A	2.15	1.57
E_B	2.40	1.71

From Figure 6.33, we note that ZrS_2 and $ZrSe_2$ start to absorb photons in the infra red region of the spectrum and that there is a downward shift in energy absorption energy as we move from sulphur to selenium.



(a) ZrS_2 optical absorption (b) $ZrSe_2$ optical absorption

Figure 6.33: Optical absorptions for Monolayer ZrX_2 (X= S, Se) calculated at the BSE level.

Table 6.28: Monolayer ZrX_2 (X= S, Se) BSE calculated binding energy for A and B excitons in eV.

	ZrS_2	$ZrSe_2$
E_B^a	0.68	0.96
E_B^b	0.43	0.82

The monolayer structures of ZrS_2 and $ZrSe_2$ having band gaps of 1.95 eV and 2.53 eV are promising material for the manufacture of third generation photovoltaic solar cells. Their optical absorption spectra point to the fact that the structures are good absorbers of light in the infra red region of the spectra.

To the best of our knowledge, this is the first theoretical investigation of the electronic and optical properties of ZrS_2 and $ZrSe_2$ at the GW and the BSE level of approximation.

6.5 Zirconium trichalcogenide

The structure and methods of preparation of ZrX_3 (X = S, Se and Te) structures have been discussed in Section 1.2.3 of this thesis. A unit cell of the structure doubled in the *c* direction is shown in Figure 6.34.

The cohesive - energy volume (equation of states) relationship for ZrX_3 structures is calculated and plotted in Figure 6.35. The cohesive and formation energies for the equilibrium structures are listed in Table 6.29 and the structural equilibrium lattice parameters in Table 6.30. From the graphs and the tables, we can see the similarities between the HfX_3 structures discussed in Section 6.3 and ZrX_3. This may not be unconnected with the fact that the structures are isostructural [63, 64, 68, 69, 70].

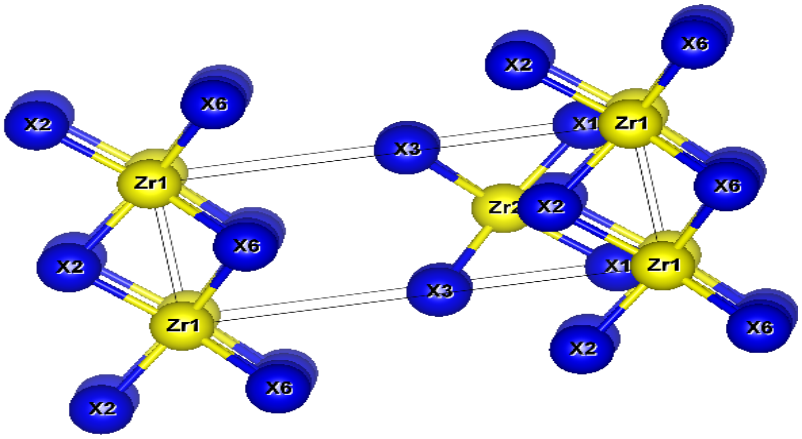


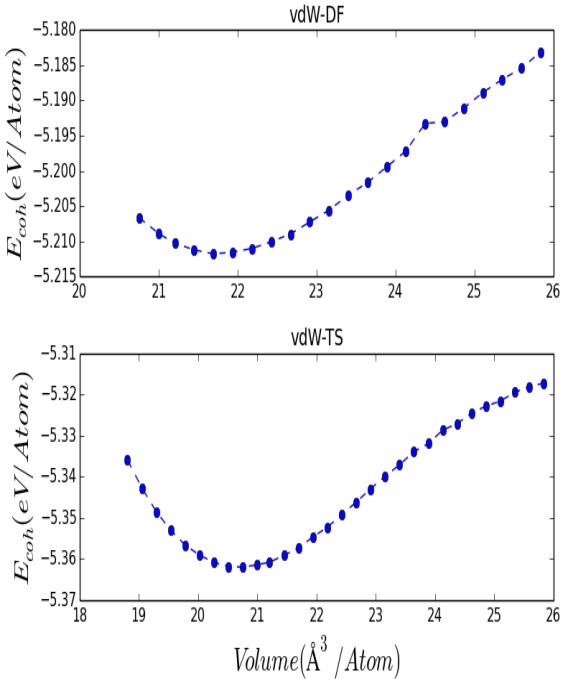
Figure 6.34: ZrX_3 structure.

Table 6.29: ZrS_3 like structures calculated cohesive and formation energy/atom in (eV).

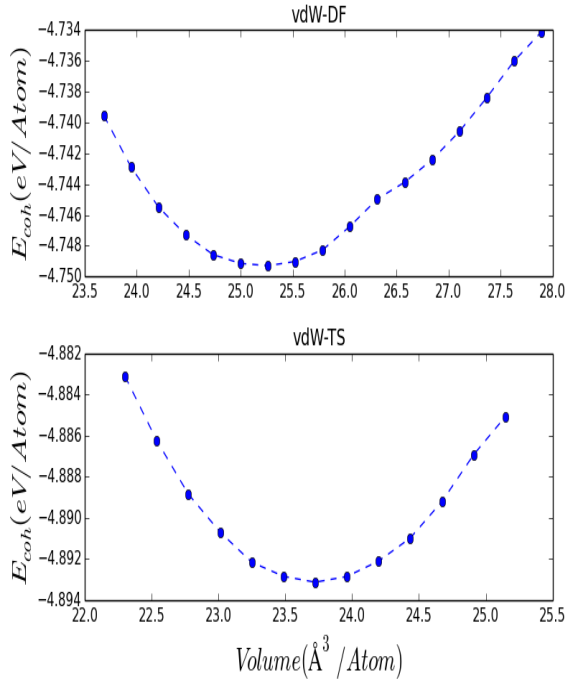
		ZrS_3	$ZrSe_3$	$ZrTe_3$
Cohesive energy	vdW-TS	-5.36	-4.89	-4.42
	vdW-DF	-5.21	-4.75	-4.26
Form. energy	vdW-TS	-1.15	-0.97	-0.57
	vdW-DF	-1.37	-1.14	-0.74

In Table 6.30, we see how the two different approximations (vdW-TS and vdW-DF) predict the structural lattice parameters. We note that the vdW-TS structural parameters are in better agreement with experiment and that both approximations overestimate the *c*-lattice parameter, which determines the inter-layer distance of the layered structures.

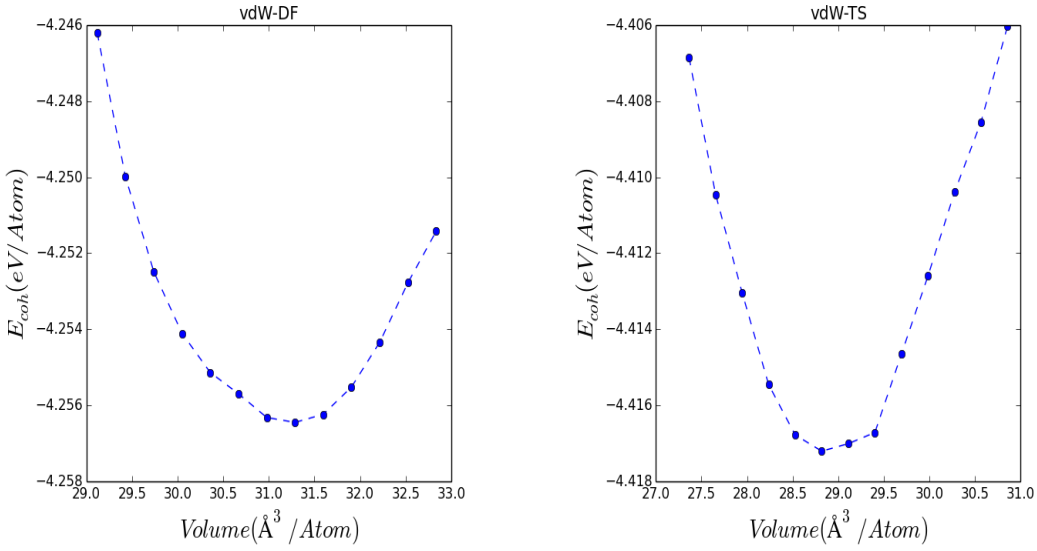
From Table 6.29, we note that the cohesive energy and formation energy follow the same trend and



(a) ZrS_3 cohesive energy-volume graph calculated using (a) vdW-TS and (b) vdW-DF



(b) $ZrSe_3$ cohesive energy-volume graph calculated using (a) vdW-TS and (b) vdW-DF



(c) $ZrTe_3$ cohesive energy-volume graph calculated using (a) vdW-TS and (b) vdW-DF

Figure 6.35: Cohesive energy-volume relation for ZrX_3.

we can therefore, use any of them to determine the stability of the structures. Since both energies

are negative, we may conclude that the structures can be formed. We also note that, as observed in the HfX_3 structures, both the cohesive and formation energies per atom decreases in magnitude as the atomic number of the chalcogen atom increases, indicating that the compounds are relatively less stable with increasing atomic number of the chalcogen atom.

Table 6.30: Calculated and experimental equilibrium parameters of ZrX_3(X= S, Se, Te): lattice constants [a (Å), b (Å), c (Å)], atomic volume V_0 (Å^3) and angle β°.

	Functional	*a (Å)*	*b (Å)*	*c (Å)*	V_0 *(Å^3)*	β°
	vdW-TS	5.04	3.63	9.05	164.74	96.95
ZrS_3	vdW-DF	5.21	3.66	9.15	173.04	96.05
	Experiment	5.12 [a]	3.62 [a]	8.98 [a]	165.40 [a]	97.28 [a]
	vdW-TS	5.33	3.76	9.59	190.56	96.68
$ZrSe_3$	vdW-DF	5.52	3.80	9.70	201.28	96.82
	other theory	5.41 [b]	3.77 [b]	9.45 [b]		97.50 [b]
	Experiment	5.39 [a]	3.72 [a]	9.43 [a]	187.30 [a]	97.48 [a]
	vdW-TS	5.85	3.92	10.17	230.8	97.75
$ZrTe_3$	vdW-DF	6.04	3.99	10.42	248.72	97.97
	Experiment	5.89 [a]	3.93 [a]	10.10 [a]	231.50 [a]	97.82 [a]

a = reference [67], b = reference [247]

Table 6.31 lists the shortest distances between the atoms of the ZrX_3 structures. Looking at the table, we can note how the distances between the atoms increase with increase in the atomic number of the chalcogenide atoms. This may be attributed to the increase in atomic radius and consequently volume as one goes down a particular group in the periodic table.

6.5.1 Mechanical and thermal properties

To test for the stability of the ZrX_3 structures, their phonon dispersion curves were calculated using density functional perturbation theory and the underlying phonon band structures are shown in Figure 6.36. From the figure, we observe that the structures have no imaginary phonon frequencies, thereby satisfying one of the necessary conditions for stability as discussed in Section 5.7 of this thesis. Because it is possible that imaginary phonon frequency can arise in a structure as a result of structural phase transition, further studies were done on the elastic constants of the structures. The structural elastic

Table 6.31: Calculated and experimental nearest neighbour distances of ZrX_3 (X = S, Se and Te) in Å , see Figure 6.34.

Functional	Zr - Zr	Zr - X (Å)	X - X(Å)
ZrS_3			
vdW-TS	4.39	2.71	2.17
vdW-DF	4.34	2.69	2.14
Experiment	4.41[a]	2.79[a]	2.09 [a]
$ZrSe_3$			
vdW-TS	4.43	2.72	2.38
vdW-DF	4.38	2.70	2.33
Experiment	4.58 [a]	2.79 [a]	2.33 [a]
$ZrTe_3$			
vdW-TS	4.51	2.74	2.62
vdW-DF	4.47	2.71	2.54
Experiment	4.84 [a]	2.77 [a]	2.78 [a]

a = reference [67]

constants are listed in Table 6.32.

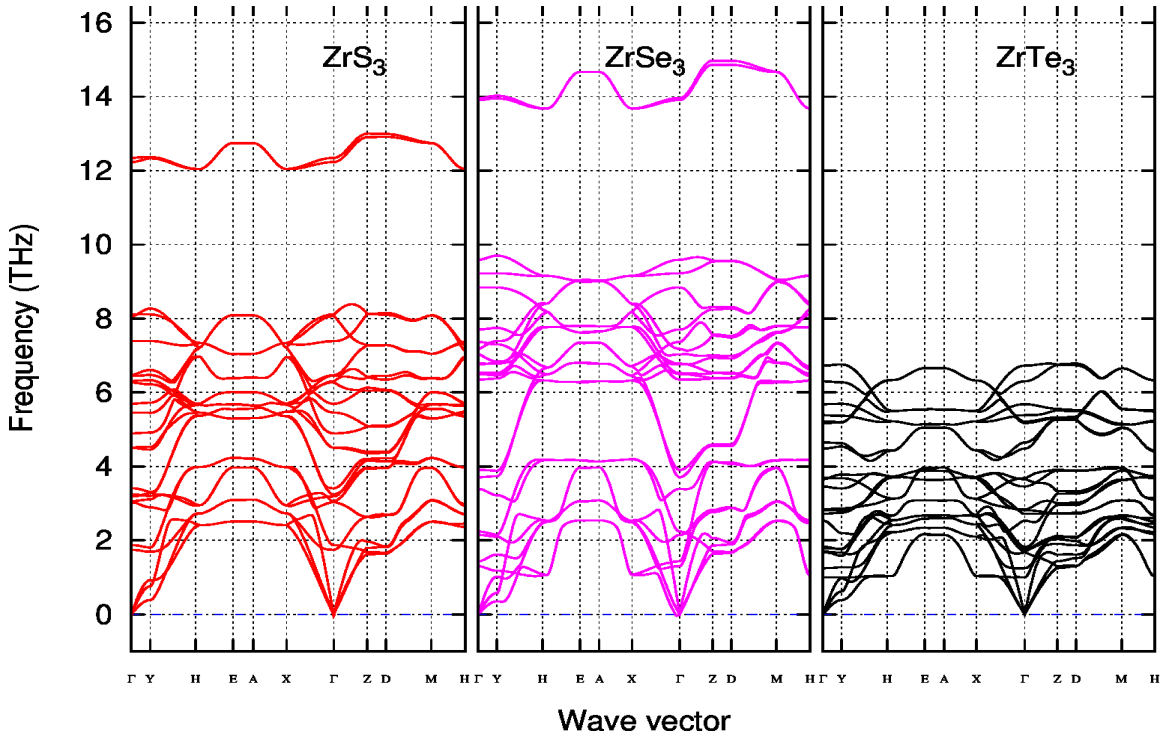


Figure 6.36: ZrX_3 phonon dispersion relation graph calculated using vdW-TS.

From Table 6.32, we can see that the elastic constants obtained satisfy the stability criteria discussed in

Section 5.7 and that the behaviour of the ZrX_3 structures elastic constants is similar to the behaviour observed in HfX_3 structures. We may therefore conclude that the structures are stable against mechanical distortions.

Table 6.32: Calculated elastic constants (GPa) for ZrX_3.

		C_{11}	C_{12}	C_{13}	C_{15}	C_{22}	C_{23}	C_{25}	C_{33}	C_{35}	C_{44}	C_{46}	C_{55}	C_{66}
ZrS_3	vdW-TS	986	212	110	111	1385	163	7.75	444	-25	149	23	76	270
	vdW-DF	962	207	111	86	1403	142	-2.10	392	-22	135	20	73	283
$ZrSe_3$	vdW-TS	972	195	127	129	1129	180	-3.00	524	-29	172	-7.96	73	184
	vdW-DF	825	164	109	68	1131	132	-11	416	-26	78	46	97	190
$ZrTe_3$	vdW-TS	883	-58	-134	55	609	-79	-33	213	-74	234	-53	75	126
	vdW-DF	811	103	78	97	838	121	-3.28	358	-12	153	-2.22	88	186

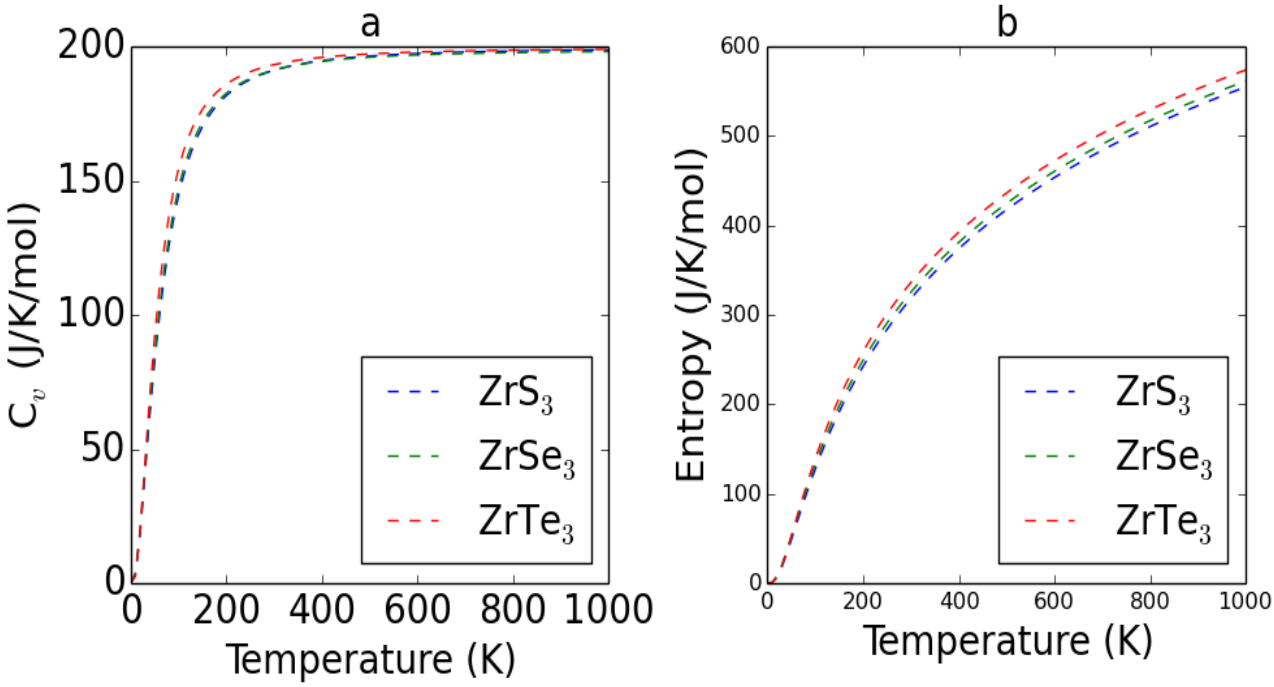


Figure 6.37: vdW-TS calculated specific heat capacity at constant volume and entropy for ZrX_3 (X= S, Se and Te) structures.

Results from density functional perturbation theory were used to predict the phonon contribution to the heat capacity of the ZrX_3 (X= S, Se, Te) compounds based on their phonon frequencies. The specific heat capacity at constant volume are shown in sub-figure 6.37 (a). From the figure, the heat capacity of ZrS_3 is the first to approach a constant value (Dulong and Petit law) at a temperature of about 720 K. Over the range of the observed temperature, it is also found that $C_v[ZrSe_3] < C_v[ZrS_3] < C_v[ZrTe_3]$.

As discussed in Section 6.3.1, the heat capacity of the semiconducting member of these structures structures will be dominated by vibrational contributions at lower temperature and the electronic contribution to the specific heat will only manifest after a given temperature.

The entropy of these structures share the same trend as observed in HfX_3 structures and discussed in Section 6.3.1.

6.5.2 Electronic properties

In order to elucidate the electronic properties of ZrX_3 structures, their possible charge transfer has been studied using Bader charge analysis [220, 221, 222]. The charge transfers in the structures are listed in Table 6.33. From the table, we can see how the charge transfer decreases as one move from sulphur to selenium, this may not be unconnected with the increasing atomic volume of the atoms as one goes down their group in the periodic table.

Table 6.33: Charge transfer for ZrX_3 (X= S, Se, Te) in electronic charge (e) calculated using vdW-TS unit see Figure 6.34.

	ZrS_3	$ZrSe_3$	$ZrTe_3$
Zr1, Zr2	1.99	1.80	1.51
X1, X2	-1.07	-0.94	-0.75
X3, X4	-0.47	-0.44	-0.39
X5, X6	-0.46	-0.42	-0.37

The band structure diagrams and spin projected density of states (DOS) of the semiconducting stable ZrX_3 family structures are plotted in Figures 6.38 to 6.40. Spin projected total density of states (TDOS) are shown in sub-figures (b) in each case. In all the cases, because the structures are non-magnetic, electrons occupy the spin up and spin down bands equally, leading to a zero spin-polarized density of states, we showed only one component of the spin contribution.

The ZrX_3 have some common features: they are all indirect band gap semiconductors. The ZrS_3 has

its conduction band minimum at Y and valence band maximum at a point between Γ and Z of the high symmetry points. $ZrSe_3$ has conduction band minimum at Γ and and valence band maximum at Z.

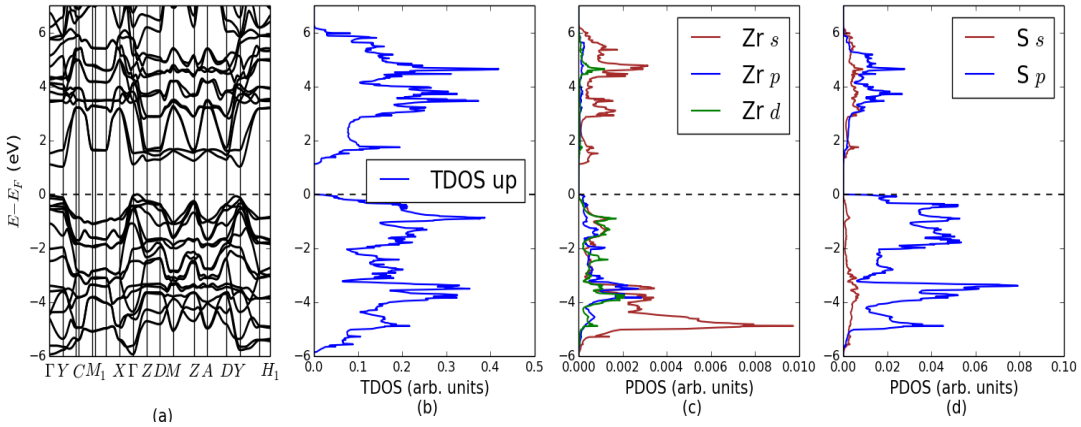


Figure 6.38: ZrS_3 vdW-TS calculated band structure (a) band structure along high symmetry K-points, (b) spin projected total density of states (TDOS), (c) partial density of states (PDOS) of Zr(s,p,d) (d) PDOS of S (s,p).

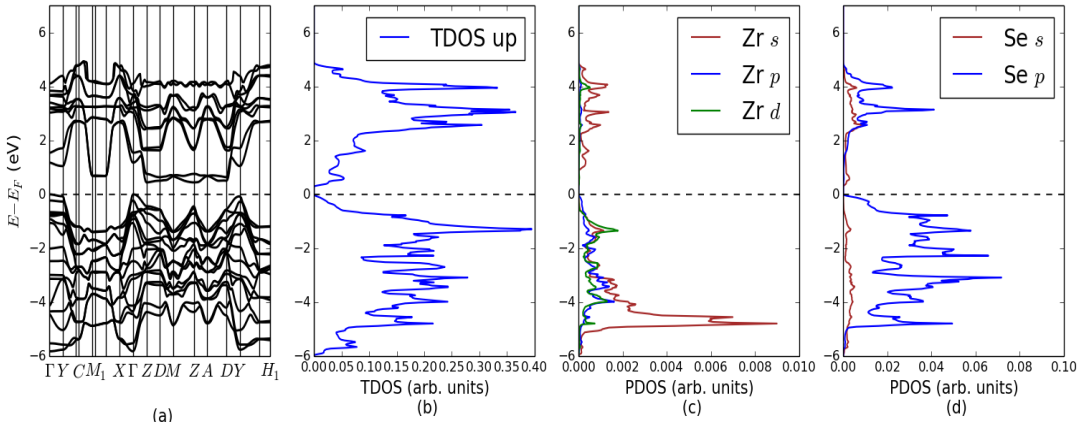


Figure 6.39: MBJ $ZrSe_3$ calculated band structure (a) band structure along high symmetry K-points, (b) spin projected TDOS, (c) PDOS of Zr(s,p,d) (d) PDOS of Se (s,p).

The conduction band edge of the Zirconium compounds is dominated by hybridized chalcogene (p and s) with little contribution from transition metal (s).

From Table 6.34, we see that as we go down the chalcogenide group in the periodic table, the electronic band gap of the structures decreases due to a decrease in electro-negativity of the chalcogen atoms (the atoms with dominant contribution at the band edges) as obtained in a number of structures [262]. We

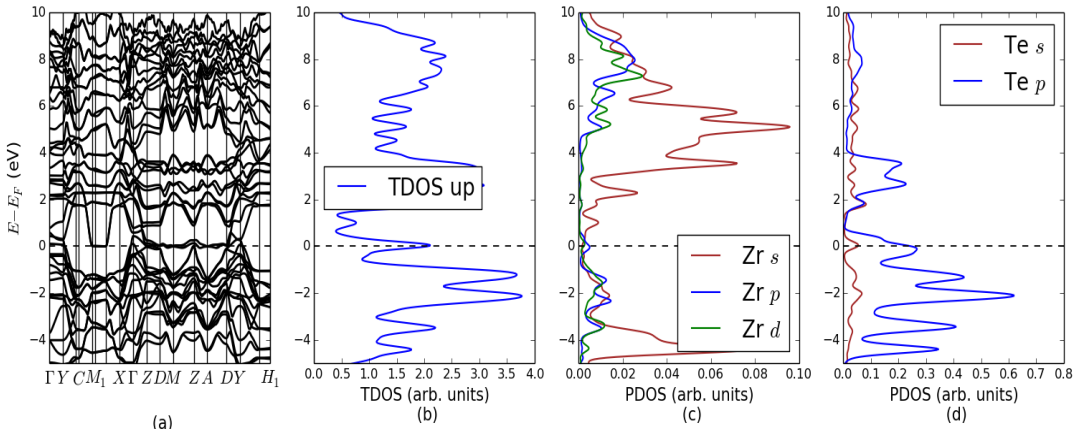


Figure 6.40: vdW-DF $ZrTe_3$ calculated band structure (a) band structure along high symmetry K-points, (b) spin projected TDOS, (c) PDOS of Zr(s,p,d) (d) PDOS of Te (s,p).

Table 6.34: Calculated and experimental energy band gaps (in eV) of ZrX_3 (X= S, Se, Te).

Structure	vdW-TS	vdW-DF	MBJ	G_0W_0	Others	Exp.
ZrS_3	1.02	1.20	1.80 (1.78)	2.37	-	2.0 [c] 2.01 [e, f]
$ZrSe_3$	Metallic	0.34	0.44 (0.41)	Metallic	1.3 [d]	1.1 [g, h]
$ZrTe_3$	Metallic	Metallic	Metallic	-	-	-

c = reference [257], d = reference [247], e = reference [258], f = reference [259], g = reference [260] and h = reference [261]

also observed that vdW-TS, vdW-DF and MBJ band gaps are respectively, about 0.98, 0.8 and 0.2 eV less than the experimental gap (optical band gap) in ZrS_3. The experimental band gap is about 0.36 eV less than the calculated G_0W_0 fundamental band gap. The vdW-TS relaxed structure, which we observed to be in closer agreement to the reported experimental values were used for the MBJ calculations)with and without inclusion of spin-orbit coupling), hybrid calculations, the G_0W_0 calculation, and all the subsequent calculations that come thereafter. Results obtained from the spin-orbit coupling are in parenthesis. It is noted that due to inversion symmetry in the structures, the spin degeneracy in the structures is lifted. The most pronounced effect of spin-orbit coupling is in $ZrSe_3$, where it reduces the electronic band gap by about 0.03 eV. The difference between the band gap obtained from vdW-TS and vdW-DF may be connected with the difference in the obtained volumes of the two approximations as band gap in these type of structures are assumed to be volume dependent.

The direct band gap of these kind of structures is useful in optical absorption without phonon assistance.

Table 6.35: MBJ calculated minimum direct band gaps (in eV) of ZrX_3 (X= S, Se, Te).

	ZrS_3	$ZrSe_3$	$ZrTe_3$
MBJ	1.89 (2.5) [d, f]	1.25 (1.47) [g] [d]	Metallic

d = reference [247], f = reference [263] and g = reference [261]

The MBJ calculated direct band gap of the ZrX_3 structures are listed in Table 6.35.

From Table 6.34, we observed that ZrS_3 have G_0W_0 band gap of about 2.37 eV, whereas $ZrSe_3$ have metallic character, respectively. ZrS_3, may therefore, be a promising material for third generation photovoltaic applications.

6.5.3 Optical properties

G_0W_0 calculated optical properties for the semiconducting ZrX_3 family are displayed in Figure 6.41 and 6.42, and shown in sub-figures of 6.41 (a) and 6.42 (a). The real $\epsilon_{re}(\omega)$ and the imaginary $\epsilon_{im}(\omega)$ part of the ZrX_3 functions have their peaks outside the optical regions of the white light spectrum.

In sub-figures of 6.41 (b) and 6.42 (b), the reflectivity $R(\omega)$ reached its peaks at 2.79 eV ($\sim$ 450 nm), for ZrS_3 and 2.01 eV ($\sim$ 620 nm) for $ZrSe_3$ which are blue and violet regions, respectively. With transmitivity $0.82 \leqslant T(\omega) \leqslant 0.78$ for ZrS_3 and $0.70 \leqslant T(\omega) \leqslant 0.67$ for $ZrSe_3$, we may conclude that the structures are good transmitters in the infra red and the red regions of the spectrum, respectively.

From subfigure 6.41 (c) and 6.42 (c), we see the expected similarity between the refraction $\eta(\omega)$ and extinction coefficient $\kappa(\omega)$ in 6.41 and 6.42 subfigure (a) as expected.

In 6.41 and 6.42 subfigure (d), the absorption coefficient $\alpha(\omega)$ are shown, where we can notice that ZrS_3 and $ZrSe_3$ absorb energy at 1.63 eV and 0.68 eV of the spectrum of the light and may not be good candidates for solar energy application.

Looking at the optical spectra of ZrS_3 and $ZrSe_3$, we can observe that the structures can be used as absorber within the visible range of the spectrum of light.

To the best of our knowledge, this is the first work in which the structural, electronic and optical properties of ZrX_3 (X = S, Se and Te) are reported at the atomic level. In order to calculate more accurate optical properties of the structures, one needs to include electron-hole interaction in the computations and this can only be done at the BSE level of approximation.

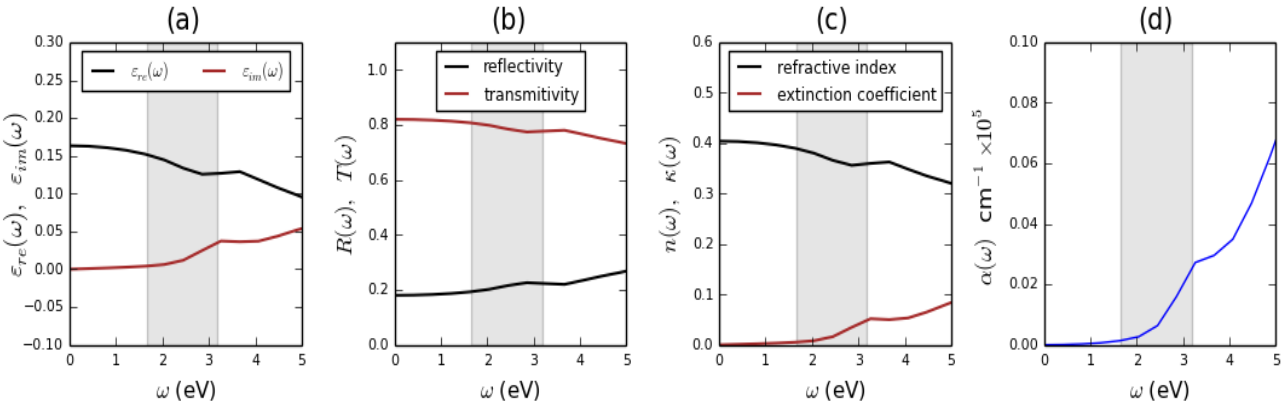


Figure 6.41: GW ZrS_3 calculated frequency-dependent optical spectra (a) real $\epsilon_{re}(\omega)$ and the imaginary $\epsilon_{im}(\omega)$ parts of the dielectric function, (b) reflectivity $R(\omega)$ and transmitivity $T(\omega)$, (c) refraction $\eta(\omega)$ and extinction coefficient $\kappa(\omega)$ and (d) absorption coefficient $\alpha(\omega)$. The visible range is shaded.

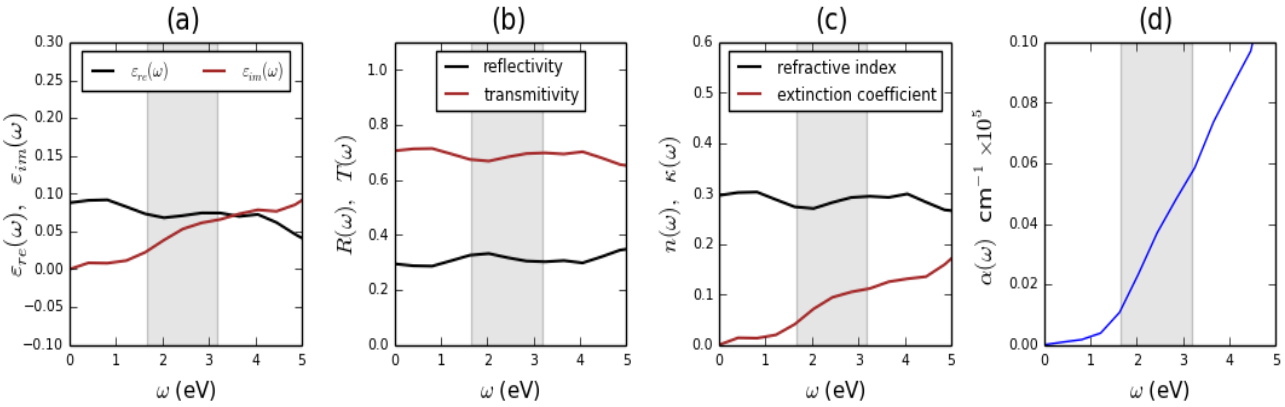


Figure 6.42: GW $ZrSe_3$ calculated frequency-dependent optical spectra (a) real $\epsilon_{re}(\omega)$ and the imaginary $\epsilon_{im}(\omega)$ parts of the dielectric function, (b) reflectivity $R(\omega)$ and transmitivity $T(\omega)$, (c) refraction $\eta(\omega)$ and extinction coefficient $\kappa(\omega)$ and (d) absorption coefficient $\alpha(\omega)$. The visible range is shaded.

6.6 Titanium trichalcogenide

The structure and methods of preparation of TiX_3 (X = S, Se and Te) structures have been discussed in Section 1.2.4 of this thesis and its structure is shown in Figure 6.43.

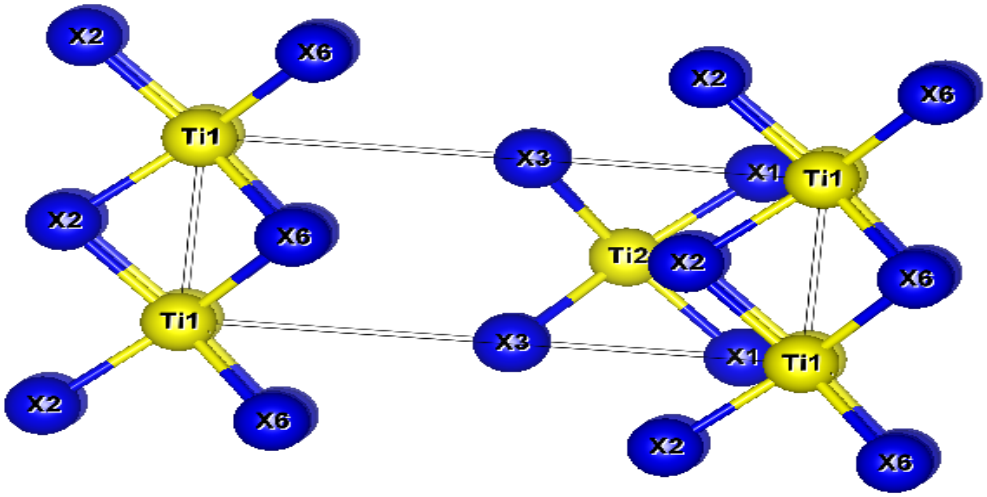


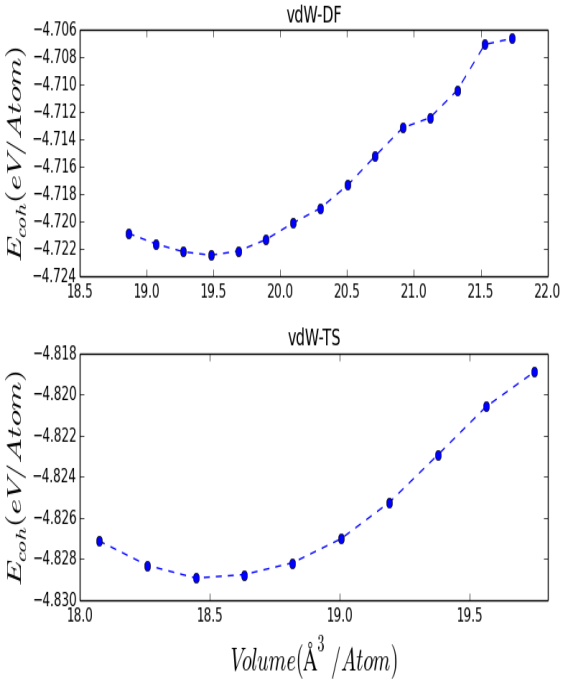
Figure 6.43: TiX_3 structure.

TiX_3 equation of states (energy-volume equation) calculated from the different approximations considered are shown in Figure 6.44. The corresponding structural cohesive, formation energies and equilibrium lattice parameters extracted from the graphs are listed in Tables 6.36 and 6.37 respectively.

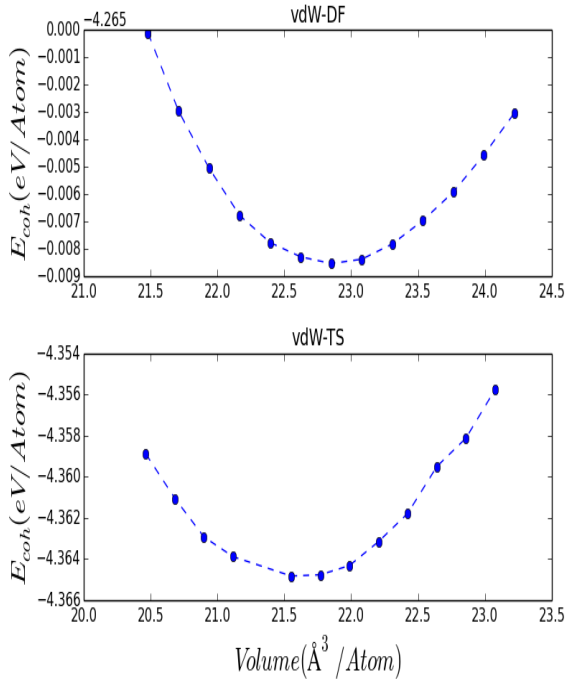
Table 6.36: TiS_3 like structures calculated cohesive and formation energy/atom in (eV).

		TiS_3	$TiSe_3$	$TiTe_3$
Cohesive energy	vdW-TS	-4.83	-4.37	-3.92
	vdW-DF	-4.72	-4.37	-3.81
Form. energy	vdW-TS	-1.09	-0.87	-0.47
	vdW-DF	-1.07	-1.13	-0.49

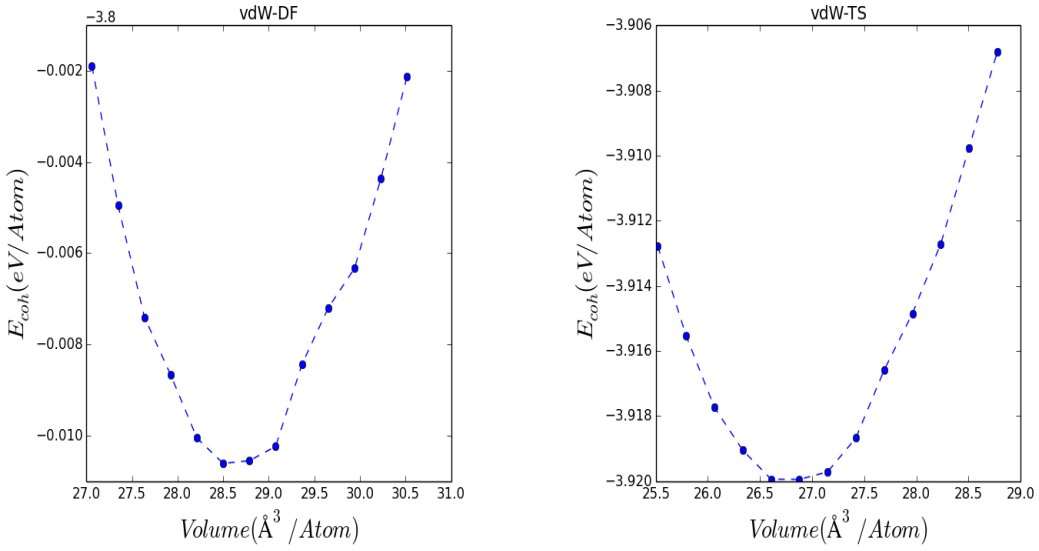
The negative values of the cohesive and formation energies in Table 6.36 points to the possibility of the formation of the structures and that the structures are stable. We note that the formation energy and cohesive energies follows the same trend in the structures.



(a) TiS_3 cohesive energy-volume graph calculated using (a) vdW-TS and (b) vdW-DF



(b) $TiSe_3$ cohesive energy-volume graph calculated using (a) vdW-TS and (b) vdW-DF



(c) $TiTe_3$ cohesive energy-volume graph calculated using (a) vdW-TS and (b) vdW-DF

Figure 6.44: TiX_3 cohesive energy-volume relation.

In Table 6.37, we can note that vdW-TS predicts the structural parameters in better agreement to

Table 6.37: Calculated and experimental equilibrium parameters of TiX_3(X= S, Se, Te): lattice constants (a (Å), b (Å), c (Å)), atomic volume V_0 (Å^3) and angle $\beta°$.

	Functional	*a (Å)*	*b (Å)*	*c (Å)*	V_0 *(Å^3)*	$\beta°$
	vdW-TS	4.92	3.39	8.93	147.92	96.63
TiS_3	vdW-DF	5.06	3.43	9.00	155.12	96.86
	Other DFT	4.98 [a]	3.39 [a]	8.89 [a]		97.24 [a]
	Experiment	4.97 [c]	3.43 [c]	8.71 [c]		97.74 [c]
	vdW-TS	5.24	3.53	9.40	172.40	97.64
$TiSe_3$	vdW-DF	5.42	3.58	9.49	182.72	97.94
	Experiment	-	-	-	-	-
	vdW-TS	5.82	3.72	10.00	214.24	98.20
$TiTe_3$	vdW-DF	5.99	3.81	10.11	228.72	97.71
	Experiment	-	-	-	-	-

a reference [264], c = reference [63]

experiment where available, the error in the vdW-TS lattice parameter is less than 3 %. We can also observed that the volume of the structures increases as we move from S to Te in the periodic table as observed in HfX_3 and ZrX_3 structures, which may be due to the fact that the structures are iso-structural [63, 64, 68, 69, 70]. They therefore share a common trend in behaviour.

Table 6.38 list the nearest neighbour distances in the TiX_3 structures. From the table, we can see how the nearest neighbour distances in the structures decreases as we move from S to Te in the periodic table, which is consistent with increase in volume as observed in Table 6.37.

6.6.1 Mechanical stabilty

In order to test for the stability of the TiX_3 structures, as it is established that relaxing a structures does not imply stability, phonon dispersion relation and the elastic constants of the structures were calculated. The obtained phonon band structures are displayed in Figure 6.45 and the elastic constants listed in Table 6.39.

Table 6.38: Calculated and experimental TiX_3 (X = S, Se and Te) structures nearest neighbour distances in Å unit see Figure 6.43.

Functional	Ti - Ti	Ti - X (Å)	X - X(Å)
TiS_3			
vdW-TS	4.36	2.67	2.21
vdW-DF	4.34	2.64	2.19
Experiment	-	2.45 [a]	-
$TiSe_3$			
vdW-TS	4.43	2.68	2.43
vdW-DF	4.40	2.65	2.39
Experiment	-	-	-
$TiSe_3$			
vdW-TS	4.58	2.69	2.69
vdW-DF	4.57	2.67	2.64
Experiment	-	-	-

a = reference [265]

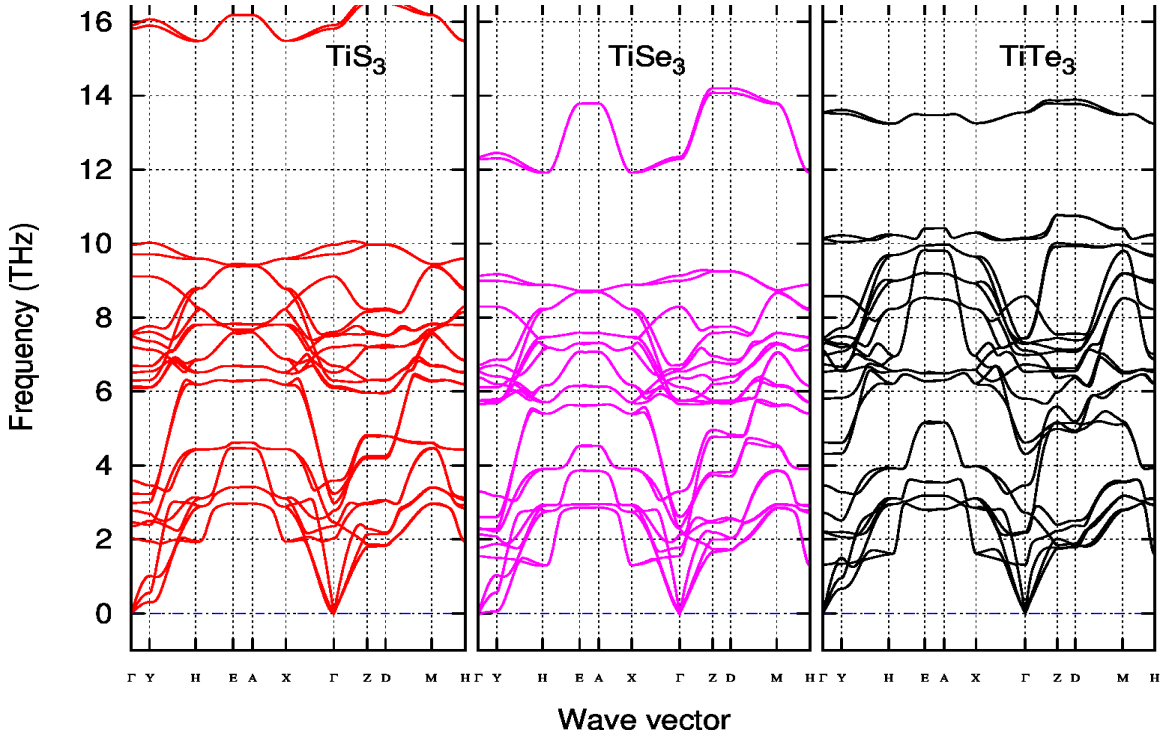


Figure 6.45: TiX_3 phonon dispersion relation graph calculated using vdW-TS.

Looking at the Figure 6.45, one can confirmed that all the observed structures have no imaginary phonon phonon frequencies, we can therefore say that they have satisfied one of the needed and necessary conditions for stability.

Table 6.39: TiX_3 calculated elastic constants (GPa).

		C_{11}	C_{12}	C_{13}	C_{15}	C_{22}	C_{23}	C_{25}	C_{33}	C_{35}	C_{44}	C_{46}	C_{55}	C_{66}
TiS_3	vdW-TS	1235	212	110	128	1549	155	-0.54	517	-55	210	16	96	323
	vdW-DF	954	182	90	102	1501	122	4.19	419	-33	165	12	61	304
$TiSe_3$	vdW-TS	1189	203	124	95	1281	175	15	564	10	281	-2.23	161	291
	vdW-DF	833	155	71	83	1236	132	3.34	409	-6.04	233	-6.82	59	266
$TiTe_3$	vdW-TS	1255	94	106	154	663	174	-16	390	-24	119	25	96	178
	vdW-DF	843	77	88	139	780	139	16	366	5.44	172	-2.95	10	143

From the elastic constants obtained in Table 6.39, one can confirm that all the structures have satisfied the elastic stability criteria with both DFT functional and are, therefore, mechanically stable against distortions. As we expected, for all the TiX_3 systems examined, the in-plane elastic constants C_{11} and C_{22} obtained are larger than the of out-of-plane elastic constant C_{33}, reflecting the larger resistance to in-plane distortions compared to out-of-plane distortions. This is because, in most layered materials, forces between atoms in the same layer are known to be, to a large extent, greater than forces between atoms in different layers. The negative elastic constants observed for some non-diagonal elements may be as a result of the low symmetry of the monoclinic structure [250].

6.6.2 Electronic properties

To understand the detailed electronic properties of the TiX_3 structures, the underlying charge transfer was analysed and band gap calculated. Table 6.40 lists the charge transfer between the atoms in the TiX_3 structures. As observed earlier on, in structures considered iso-structural to TiX_3 [63, 64, 68, 69, 70], we note that the charge transfer between the structures decreases with increase in atomic volume of the structures.

The band structure diagrams and spin projected density of states (DOS) of the stable TiX_3 family

Table 6.40: Charge transfer for TiX_3 (X= S, Se, Te) in the unit of electronic charge (e) obtained in vdW-TS calculations, see Figure 6.43.

	TiS_3	$TiSe_3$	$TiTe_3$
Ti1, Ti2	1.62	1.48	1.25
X1, X2	-0.87	-0.76	-0.76
X3, X4	-0.38	-0.36	-0.34
X5, X6	-0.37	-0.35	-0.33

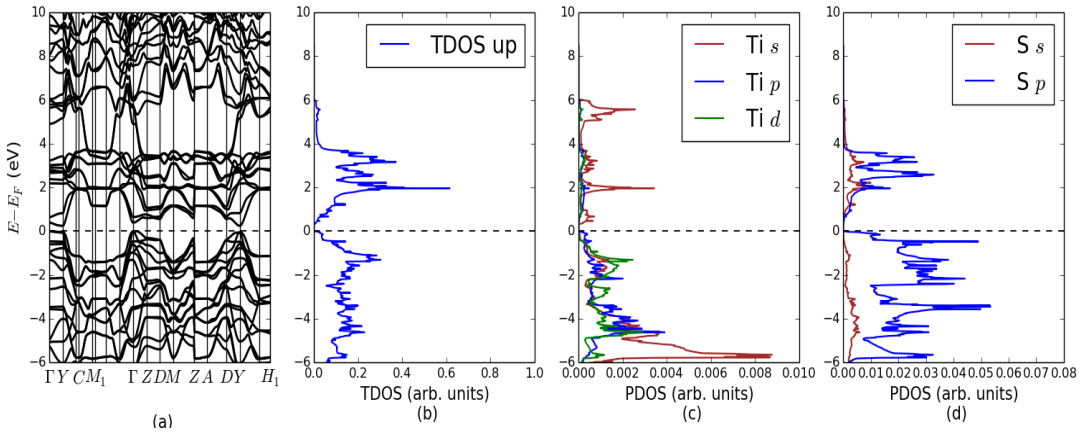


Figure 6.46: vdW-TS TiS_3 calculated electronic structure (a) band structure along high symmetry K-points, (b) spin projected TDOS, (c) PDOS of Ti(s,p,d) and (d) PDOS of S(s,p).

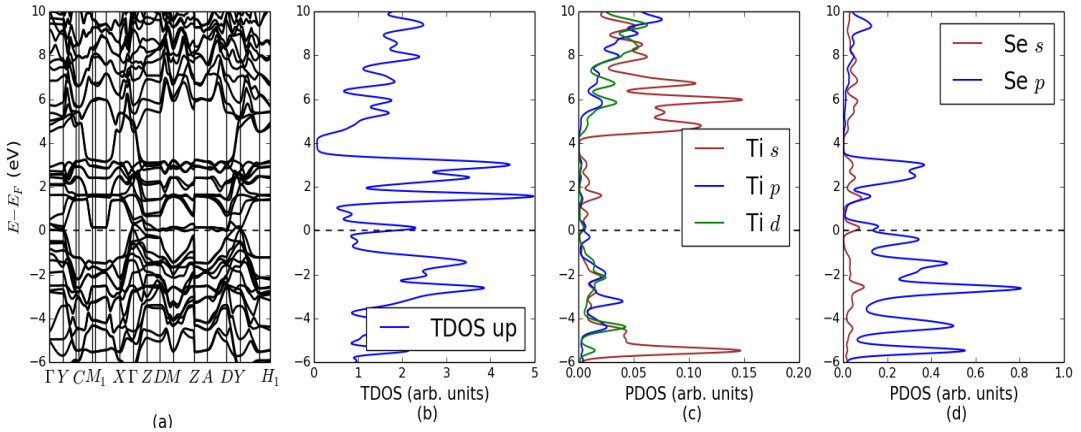


Figure 6.47: vdW-TS $TiSe_3$ calculated electronic structure (a) band structure along high symmetry K-points, (b) spin projected TDOS, (c) PDOS of Ti(s,p,d) and (d) PDOS of Se(s,p).

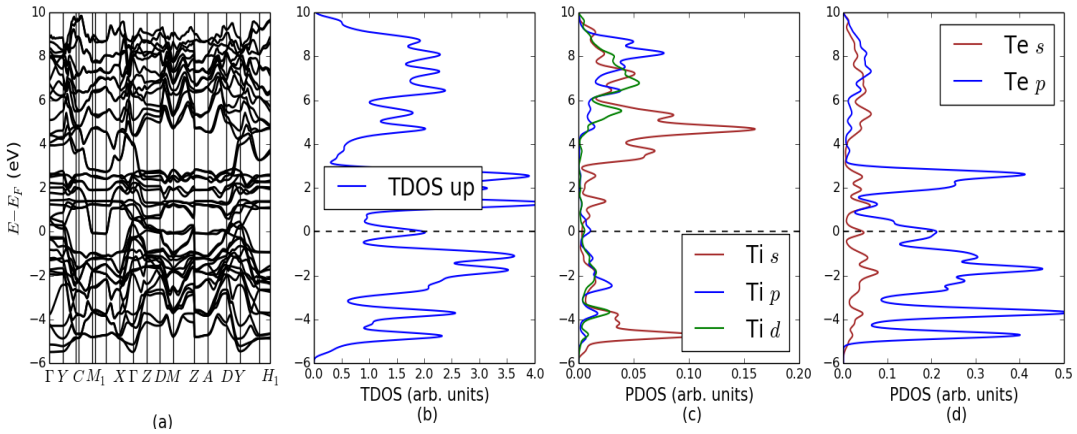


Figure 6.48: vdW-DF $TiTe_3$ calculated electronic structure (a) band structure along high symmetry K-points, (b) spin projected TDOS, (c) PDOS of Ti(s,p,d) and (d) PDOS of Se(s,p).

structures are plotted in Figures 6.46 to 6.48. Spin projected total density of states (TDOS) are shown in sub-figures (b) in each case. Electrons occupy the spin up and spin down bands equally because the structures are not magnetic, as observed in HfX_3 and ZrX_3. This lead to zero spin polarized density of states, making it sufficient to show only one component of the spin projected density of states. The valence band maximum is taken as the zero energy reference.

The semi conducting TiS_3 conduction band minimum is observed to be between Γ and Z and its valence band maximum at Y. The dominant orbital at the band gap edge of the TiS_3 are mainly composed of S s type orbitals with a small contribution from the Ti s states. The band gaps of the TiX_3 structures are listed in Table 6.41 and the direct band gap of the structures in Table 6.42.

Table 6.41: Calculated and experimental energy band gaps (in eV) of TiX_3 (X= S, Se, Te).

Structure	vdW-TS	vdW-DF	MBJ	Others (HSE06)	Exp.	GW
TiS_3	0.24	0.31	0.87 (0.85)	0.94 [a] 1.02 [c]	0.9 [b], 1.35 [d]	1.34
$TiSe_3$	Metallic	Metallic	Metallic	-		
$TiTe_3$	Metallic	Metallic	Metallic	-		

a = reference [42], b = reference [265], c = reference [264] and d= reference [263]

From the Table 6.41, we observed that PBE grossly underestimates the band gap of TiS_3, MBJ and HSE06 underestimate the band gap by about 0.5 eV and 0.41 eV, respectively, whereas G_0W_0 underestimate it by only about 0.01 eV. The vdW-TS relaxed structure, which we observed to be in close agreement to experimental values were used for the MBJ (with and without inclusion of spin-orbit cou-

pling), hybrid calculations, G_0W_0 calculation and all the subsequent calculations that come thereafter. Results obtained from the spin-orbit coupling are in parenthesis. It is noted that due to inversion symmetry in the structures, the spin degeneracy in the structures is lifted. The difference between the band gap obtained from vdW-TS and vdW-DF may be connected with the predicted volumes difference of the two approximations as band gap in these type of structures are assumed to be volume dependent.

Table 6.42: MBJ calculated minimum direct band gaps (in eV) of TiX_3 (X= S, Se, Te).

	TiS_3	$TiSe_3$	$TiTe_3$
MBJ	0.90	Metallic	Metallic

6.6.3 Optical properties

The optical properties for the semiconducting TiS_3 calculated at the G_0W_0 level are displayed in Figure 6.49. Sub-figure of (a) 6.49 shows the real $\epsilon_{re}(\omega)$ and the imaginary $\epsilon_{im}(\omega)$ parts of the TiS_3 functions have their peaks outside the optical regions of the white light spectrum.

In sub-figure of 6.49 (b), the reflectivity $R(\omega)$ reached its peaks at 3.19 eV ($\sim$ 390 nm), which correspond to the violet region of the spectrum, with transmitivity $0.33 \geq T(\omega) \geq 0.23$. We may conclude that the structure is a good transmitter in the infra red and the red region of the spectrum.

From subfigure 6.49 (c), we can see the similarity between the refraction $\eta(\omega)$ and extinction coefficient $\kappa(\omega)$ and sub-figure 6.49 (a) as expected.

In 6.49 sub-figure (d), the absorption coefficient $\alpha(\omega)$ is shown, where we notice that TiS_3 absorbs all the incident energy in the spectrum of the visible light and may not be a good candidate for solar energy application.

The G_0W_0 calculated band gap of 1.35 eV in TiS_3 points to the fact that the structures can be used as a possible component of first, second and third generation photovoltaic. The optical absorption spectrum of the structure, shows that it absorbs all radiation within the visible range of the spectrum of light. It also have low reflectivity.

To the best of our knowledge, this is the first time where the structural, electronic and optical properties of TiX_3 (X = S, Se and Te) are reported at the atomic level. In order to calculate more accurate optical properties of the structures, one needs to include electron-hole interaction in the computations and this

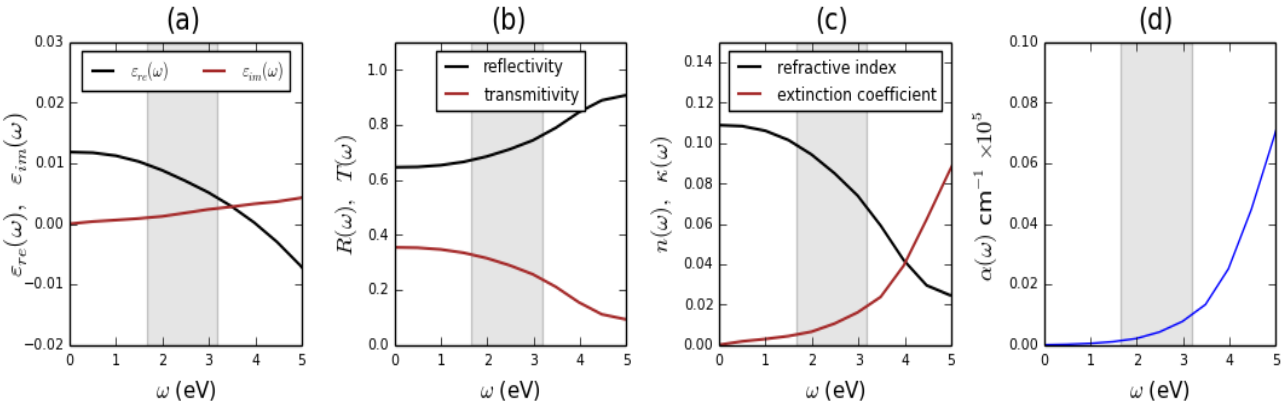


Figure 6.49: GW TiS_3 calculated frequency-dependent optical spectra (a) real $\epsilon_{re}(\omega)$ and the imaginary $\epsilon_{im}(\omega)$ parts of the dielectric function, (b) reflectivity $R(\omega)$ and transmitivity $T(\omega)$, (c) refraction $\eta(\omega)$ and extinction coefficient $\kappa(\omega)$ and (d) absorption coefficient $\alpha(\omega)$. The visible range is shaded.

can only be done at the BSE level of approximation.

6.7 $ReSe_2$

6.7.1 Potential new $ReSe_2$ structures

The same compound may exist in different structural phases with different energies and stabilities. In order to find the most stable structural modification of $ReSe_2$, different possible structural phases of the compound are considered. There are different ways by which a possible new stable structural phase can be determined: for known experimentally reported structure, the search is straight forward. In a situation where there is no experimentally reported phase, choice of the possible structural phases can be governed by physical and chemical intuition. The Periodic Table of elements is used as a starting point for this reasoning. For example, elements that belong to the same group in the periodic table have the same number of electrons in their outer orbitals (valence electrons). It is known that these outer electrons determine both physical and chemical properties of the elements. It is therefore, possible to expect similar characteristics from such elements in the same group. As such, one element in the group can be used to replace another element in the same group in any known existing structure. For example, manganese and rhenium belong to the same group in the periodic table, $MnSe_2$ crystallises into a cubic structure, it is therefore possible to replace the Mn in $MnSe_2$ with Re with the hope of checking the

possible existence of $ReSe_2$ in a cubic structure. The vdW-TS functional, a approximation known to predict structural parameters at an accuracy comparable to experiment in layered structures, was used to calculate the properties of these different possible potential structural modifications and are listed in Table 6.43.

Table 6.43: Rhenium diselenide structural phases.

Polymorph	Space group	a(Å)	b(Å)	c(Å)	E_{coh} (eV/atom)
Triclinic	P-1 ♯2	6.64	6.77	6.72	-6.54
Tetragonal	P42/mnm ♯136	5.72	5.72	3.86	-6.13
Monoclinic	C2/m ♯12	3.58	3.28	5.69	-6.14
Cubic	Fm-3m ♯225	6.94	6.94	6.94	-6.09
Hexagonal	P63/mmc 194	3.24	3.24	12.76	-6.25

Cohesive energy: is the negative of the energy required to decompose the solid into its constituents neutral atoms at infinite distance [176, 266], was used as a test for stability for the different possible structural phases. From the definition, the lower the cohesive energy, the more stable the considered structural modification [267, 268]. We can say that the most stable $ReSe_2$ structural phase from Table 6.43 is triclinic with *P-1* ♯2 space group, as observed experimentally [48, 50, 75].

6.7.2 Equilibrium parameters

To obtain the structural lattice parameters of the most stable structure considered, different exchange correlation functionals were used to determine the structural cohesive energy volume relationship (equation of states). Figure 6.50 shows the graph of cohesive energy (E_{coh}) against volume V_0 with sub-figures (a), (b) and (c) depicting the PBE, vdW-TS and vdW-DF results for the $ReSe_2$ (a layered structure). Different functionals were used for the structure in order to study the effect of the van der Waal's correction terms on the energy volume relation of the layered structure. It can be seen from the figure, that the PBE equation of state (EOS) curve flattens with increase in volume as the inter-layer interaction decreases to a point where the layers de-couples and the intra-layer interaction saturates. This reflects the inability of PBE functionals to describe long range dispersion forces in layered structures, suggesting the necessity for a van der Waal's correction for an accurate description of the structural parameters of

the layered structure. The lattice structural parameters obtained from the equation of states are listed in Table 6.44 and the shortest distances between the structure are listed in Table 6.45

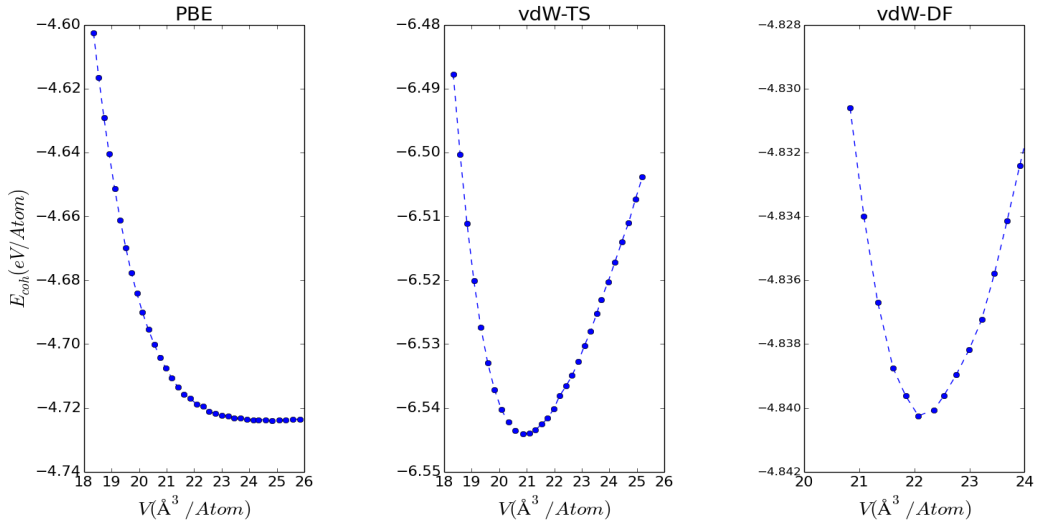


Figure 6.50: $ReSe_2$ cohesive energy-volume graph calculated using (a) PBE, (b) vdW-TS and (c) vdW-DF.

Table 6.44: $ReSe_2$ calculated and experimental equilibrium lattice parameters.

Functional	*a(Å)*	*b(Å)*	*c(Å)*	V_0/*atom* ($Å^3$)	V_0 ($Å^3$)
PBE	6.67	6.79	7.76	24.64	295.68
vdW-TS	6.64	6.77	6.72	20.93	251.16
vdW-DF	6.70	6.83	7.00	22.21	266.52
expt.	6.60 [a], 6.72 [b]	6.71 [a], 6.62 [b]	6.72 [a], 6.73 [b]		247.34 [a]

a = reference [49], b = reference [269]

In Table 6.44 we can see that vdW-TS reproduces structural lattice parameters and volume at an accuracy that is comparable to experiment, whereas the PBE and vdW-DF approximations over-estimate the equilibrium volumes. We note that, vdW-TS reproduces the better value for the *c* lattice parameter (the inter-layer separation) when compared with the experiment, and that PBE overestimates the c lattice parameter by more than 10%. The vdW-TS lattice parameters, *a* and *b*, agree quite well with that of the experimental values reported by Lamfers et al. [50] (with an error of less than 2 %) and those of Wildervank and Jellinek [49].

Table 6.45: Calculated nearest neighbour distance in (Å) units for $ReSe_2$.

Functional	Re-Re	Se-Re	Se-Se
PBE	2.69	2.39	3.15
vdW-TS	2.82	2.52	3.34
vdW-DF	2.79	2.48	3.29
expt.	2.64 [f]	2.34 [f]	3.26 [f]

f = reference [48]

From Table 6.45 we note that vdW-DF and vdW-TS overestimate the experimental nearest neighbour distances by about 6% and 8 %, respectively. PBE, on the other hand predicts nearest neighbour distance that are surprisingly in good agreement with experiment with an error of about 4%. This may be not surprising, considering the fact that nearest atoms in the $ReSe_2$ structure lies within the same layer of the structure.

6.7.3 Stability

In order to test for the stability of $ReSe_2$, elastic constants were calculated. We applied deformation uniformly to the unit cell and calculated the yield stress as implemented in VASP. Triclinic crystals have twenty one independent elastic constants as discussed in Section 5.7. Table 6.46 lists the non-zero elastic constants obtained for $ReSe_2$ using PBE, vdW-TS and vdW-DF, respectively. The Born stability criteria (necessary and sufficient conditions) are satisfied for all the functional considered [194], indicating that the configurations investigated are stable against small distortions. It is evident from the table that the type of approximation used in calculating the elastic constants affects the value of the calculated elastic constants. This relative size of the dominant elastic constants correlate inversely with the relative volumes of the equilibrium structures calculated with the different functionals.

Table 6.46: Calculated elastic constants (GPa) for $ReSe_2$.

	C_{11}	C_{12}	C_{13}	C_{14}	C_{15}	C_{16}	C_{22}	C_{23}	C_{24}	C_{25}	C_{26}	C_{33}	C_{34}	C_{35}	C_{36}	C_{44}	C_{45}	C_{46}	C_{55}	C_{56}	C_{66}
PBE	1530	319	124	-47	-384	-48	1681	97	-283	-61	-48	26	-28	-52	56	116	43	-137	138	-102	564
vdW-TS	1818	403	220	-33	-401	-44	1970	191	-328	-68	-61	314	-31	-24	52	181	32	-155	188	-99	690
vdW-DF	1718	378	224	-33	-380	-37	1806	194	-318	-68	-63	307	-13	-26	57	150	33	-145	188	-95	620

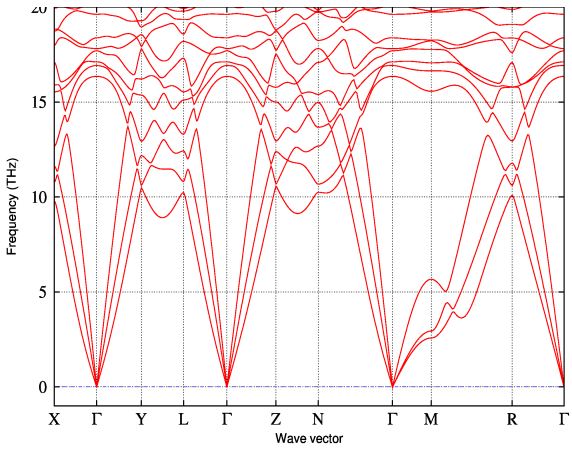


Figure 6.51: Phonon dispersion of $ReSe_2$ calculated using the vdW-TS relaxed structure.

As a further test for stability, mechanical stability test based on the phonon dispersion relation of $ReSe_2$ can be performed. Due to the similarity of the phonon density of states, we show only that calculated using vdW-TS, a functional which predicts structural parameters of this structure in good agreement with experiment. The phonon density of states revealed that the structure is mechanically stable: there are no imaginary phonon frequencies.

6.7.4 Electronic properties

Figure 6.52 shows the MBJ-DFT [3] calculated electronic band structure of $ReSe_2$. It is observed that electrons occupy spin up and down of the density of states equally, suggesting that the structure is not magnetic, as such only the spin up total density of states are shown. Sub-figure (a) show the band energies plotted along high symmetry K-points, the total density of states is depicted in sub-figure (b). Partial density of states are plotted to extract the orbital character of the bands Re (s, p, d) and Se (s, p) at the same energy level in sub-figure (c) and (d) respectively.

From Figure 6.52 we observed that the MBJ calculated electronic structure of $ReSe_2$ has valence band maximum and conduction band minimum at M points of the high symmetry k-points, resulting in a direct band gap of 1.23 eV.

Looking at the $ReSe_2$ partial density of States (PDOS), we can see that the dominant orbitals at the two band edges (valence band maximum and conduction band minimum) are Se (p) with little contribution

[3] vdW-TS relaxed structure, an approximation we identify to predict the $ReSe_s$ lattice parameters in better agreement with the experiment was used for the MBJ-DFT calculations

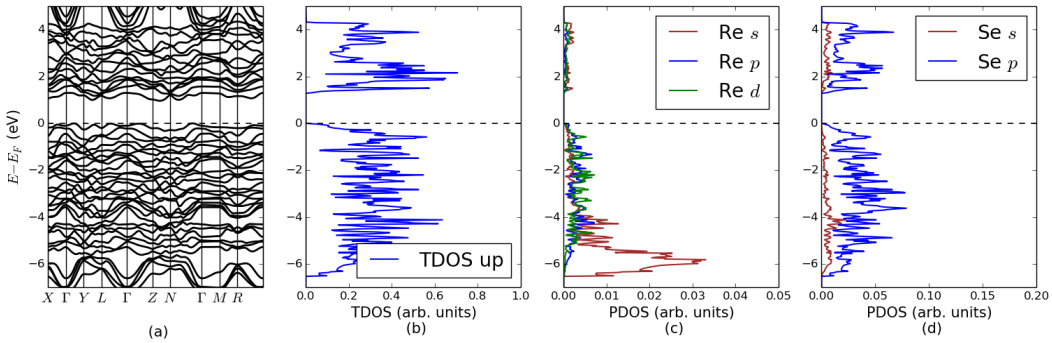


Figure 6.52: MBJ calculated $ReSe_2$ band structure (a) band structure along high symmetry K-points, (b) spin projected total density of states (TDOS), (c) partial density of states (PDOS) of Re(s,p,d) (d) PDOS of Se (s,p).

from hybridized Re (p and s).

Table 6.47: $ReSe_2$ calculated and experimental band gaps.

Functional	PBE	vdW-TS	vdW-DF	MBJ	G_0W_0	Exp.
$ReSe_2$	1.20	0.99	1.09	1.23 (1.00)	1.42	1.31, 1.32 [g, h]

g = reference [270] and h = reference [75]

Our calculated electronic band gaps of the $ReSe_2$ are listed in Table 6.47 obtained by different methods, the band gaps are compared with optical band gaps [73, 72]. The vdW-TS relaxed structure, which is observed to be in good agreement with the experimental values were used for MBJ, MBJ with inclusion of spin-orbit coupling, G_0W_0 and all subsequent calculations that come thereafter. MBJ band gap calculated with inclusion of spin-orbit coupling are in parenthesis. It is observed that due to inversion symmetry in the structure, the spin degeneracy in the structures is lifted. It is observed that the effect of spin-orbit coupling reduces the electronic band gap by about 0.23 eV. The difference between the electronic gap observed in vdW-TS and vdW-DF approximations may be connected with the difference relaxed structure of the two approximations. We observed that PBE band gaps are about 0.12 eV less than the experimental band gap. However, this may be attributed to the fact that PBE overestimated the volume of the structure and the band gap in this structure is expected to increase with an increase in volume. vdW-TS, vdW-DF and MBJ with spin orbit coupling were observed to underestimate the band gap of the structure by about 0.33 eV, 0.23 eV and 0.32 eV respectively. G_0W_0 predicts band gap that are in good agreement with experiment with an error of only about 8 %.

6.7.5 Optical properties

G_0W_0 calculation was carried out on the $ReSe_2$ structure using the vdW-TS relaxed structures. Single shot G_0W_0 was done due to limitation of our computational resources and the frequency-dependent optical spectra obtained is displayed in Figure 6.53. In the figure, the optical regions (visible part of the spectrum) is shaded.

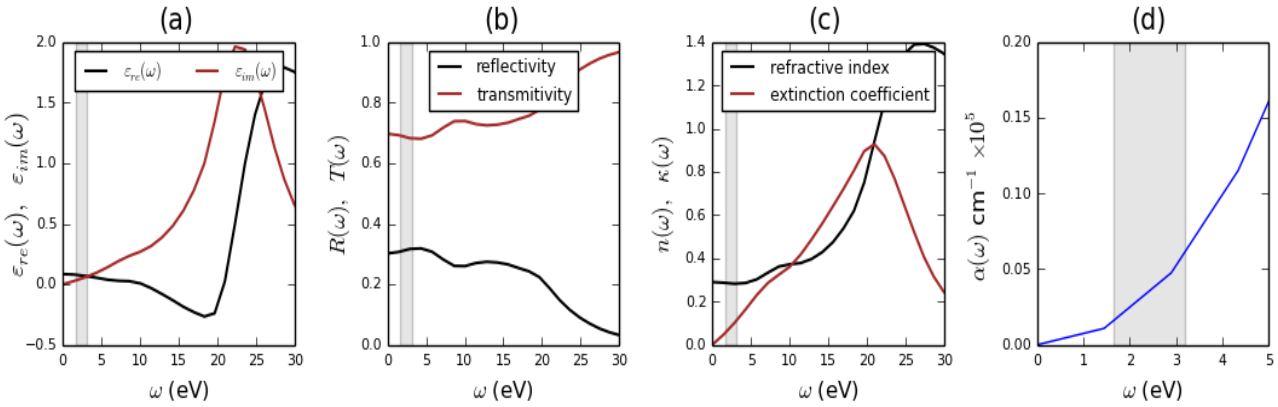


Figure 6.53: G_0W_0 $ReSe_2$ calculated frequency-dependent optical spectra (a) real $\epsilon_{re}(\omega)$ and the imaginary $\epsilon_{im}(\omega)$ parts of the dielectric function, (b) reflectivity $R(\omega)$ and transmitivity $T(\omega)$, (c) refraction $\eta(\omega)$ and extinction coefficient $\kappa(\omega)$ and (d) absorption coefficient $\alpha(\omega)$. The visible range is shaded.

From the computed G_0W_0 band gap of the $ReSe_2$ of 1.42 eV, we can conclude that the structure can be used in the manufacture of first, second and third generation photovoltaic solar cells. The optical absorption spectra of the structure, however, revealed that the structure absorbs all incident radiation within the visible range of the spectrum of light.

To the best of our knowledge, this is the first time in which the electronic and optical properties of $ReSe_2$ is reported at the GW level of approximation. In order to calculate more accurate optical properties of the structures, one needs to include electron-hole interaction in the computations and this can only be done at the BSE level of approximation.

7. Conclusions and Future Work

7.1 Conclusion

The motivation for this research was to fill in some of the missing gaps in the understanding of the structural, electronic and optical properties of the transition metal chalcogenides and provide salient information on the possible application of the structures in the electronic industry. The following have been achieved in the study:

7.1.1 TcX_2 (X = S, Se and Te)

The structural and electronic properties of the technetium dichalcogenide TcS_2, $TcSe_2$ and $TcTe_2$ have been studied using a first principles approach. Their structures were relaxed using PBE, PBEsol, vdW-DF, vdW-TS and vdW-D2. Van der Waal's correction terms were used to study the equilibrium structural properties in order to account for long range dispersion forces and find the best approximation for the structure. For all the functional considered, we found a slight overestimate of the interlayer distances in the structures, but the functionals provide reasonably accurate descriptions of lattice parameters of the structures when compared with experiment. The vdW-D2 approximation consistently give structural properties that are in better agreement with experiment.

The cohesive and formation energies for all the calculated structures indicate stability against decomposition and elastic constant and phonon dispersion studies confirm that the calculated structures are stable against distortion and small atomic displacements.

Electronic properties were examined using PBE, PBEsol and van der Waal's correction term (vdW-DF/vdW-TS/vdW-D2), modified Becke Johnson potential, HSE06 and also the many body perturbation theory at the G_0W_0 level of approximation. The results show that the DFT functionals, as expected, underestimate the band gaps of these structures. The modified Becke Johnson potential (MBJ), GW and HSE06 band gaps are expected to be closer to the experimental band gap as we have no experimental value to compare with. Spin-orbit coupling effects are expected to be negligible as a result of the symmetry of the structures.

It is important here to remark that, TcS_2 and $TcSe_2$ having electronic band gap between 0.63 to 1.59 eV and may thus be potential materials for solar photovoltaic applications and photo-catalysis. Their

layered structure open the door for quite a number of possibilities in tuning their electronic properties.

To modulate the electronic properties of TcS_2, the structure was doped with Fe. Formation and cohesive energy were used to test the possibility of formation of the new structures. It was found that the new structures have negative formation and cohesive energies, an indication that the structures are energetically possible.

MBJ, an functional observed to predict electronic properties of TcS_2 structures with an accuracy that is comparable to experiment, was used to calculate the band gap of the doped structures. It was found that the band gaps of the doped structures were less than that of the parent material and that the band gaps of the doped system depends on the position of the Fe atom and its percentage in the subset of the configurations considered.

7.1.2 MX_2(M= Zr and Hf; X= S and Se)

We have calculated the band gaps of bulk and monolayer ZrS_2, $ZrSe_2$, HfS_2 and $HfSe_2$ at both the DFT and GW level of approximation. As it is well known, DFT underestimates the band gaps of these structures, whereas GW describes the fundamental band gaps of these structures in better agreement when compared with the experimental results. We observed that moving from bulk to monolayer, the direct band gaps of these structures increase. The direct band gaps in monolayer is 0.29 eV to 0.51 eV larger than that of the corresponding bulk systems. We also observed that ZrX_2 monolayer fundamental band gaps are in the same range when compared with the energies of the A and B excitons.

Practically, GW fundamental band gaps should not be compared with the optical transition energies, because of the missing electron-hole interaction in the former. To compare them, bulk and monolayer MX_2(M= Zr and Hf; X= S and Se) optical transition energies were calculated by solving the well known Bethe-Salpeter equation (BSE). Results from the calculations show the presence of strong bound excitons in monolayer MX_2(M= Zr and Hf; X= S and Se) structures as observed in some monolayer transition metal chalcogenides like MoX_2 (X = S, Se and Te) [225, 271, 224]. The absorption spectra of the bulk and monolayer MX_2(M= Zr and Hf; X= S and Se) indicate the presence of two strongly bound excitons, the positions of the peaks range from 1.50 eV to 2.95 eV. This suggests that the structures have potential applications in the infra red and violet regions of the visible spectrum.

7.1.3 MX_3(M= Ti, Zr and Hf; X= S, Se, Te)

The structural and electronic properties of the four early transition metal trichalcogenide ZrS_3, $ZrSe_3$, $ZrTe_3$, HfS_3, $HfTe_3$, TiS_3, $TiSe_3$ and $TiTe_3$ using a-b initio approach have been reported for the first time. vdW-DF and vdW-TS van der Waal correction terms were used to study the equilibrium structural properties. In both approximations we found a slight overestimate of the interlayer distances in these structure, although these functionals provide reasonably accurate descriptions of the lattice parameters of the structures compared with the experiment. The vdW-TS approximation consistently give structural properties closer to experiment than the vdW-DF approximation.

The cohesive and formation energies for all the calculated structures indicate stability against decomposition and elastic constant and phonon dispersion studies confirm that the calculated structures are stable against distortion and small atomic displacements.

Electronic properties were examined using GGA with van der Waal's correction term (vdW-DF/vdW-TS), modified Becke Johnson potential, HSE06 and also many body perturbation theory at the GW level of approximation. The results show that the DFT GGA approximations used underestimate the band gaps of these structures by as much as 30% when compared with experiment where available. The modified Becke Johnson potential and G_0W_0 yield band gaps comparable to measured optical absorption values. Spin-orbit coupling effects were found to be negligible.

Optical properties were examined at the G_0W_0 level of approximation. The results show that ZrS_3, HfS_3, $ZrSe_3$ and $HfSe_3$ start to absorb radiation in 1.63 eV, 1.37 eV, 0.68 eV and 0.50 eV regions of the spectra, respectively. This Suggest that these compounds are promising material for third generation photovoltaic applications.

7.1.4 $ReSe_2$

The structural, electronic and optical properties of $ReSe_2$ have been investigated. PBE, vdW-DF and vdW-TS van der Waal correction terms were used to study the equilibrium structural properties. In all the approximations, we found a slight overestimate of the interlayer distances in these structure, but the functionals provide reasonably accurate descriptions of the $ReSe_2$ lattice parameters when compared with the experiment. The vdW-TS approximation consistently gave structural properties in better agreement when compared to experiment than the other approximations.

Cohesive and formation energies were used to test for other stable $ReSe_2$ structures not reported earlier. It was found that triclinic $ReSe_2$ is the most favourable structure as observed experimentally.

Mechanical stability test based on elastic constants and phonon dispersion frequencies revealed that the structure is stable against mechanical distortion.

Electronic properties of the structure investigated revealed that DFT underestimate the band gap of the triclinic $ReSe_2$ structure by about 25 $\%$. The band gap of the $ReSe_2$ was found to increase with increasing volume. Many body perturbation theory at G_0W_0 level of approximation predicts the fundamental band gaps of the $ReSe_2$ more accurately when compared with DFT. The calculated G_0W_0 band gap is, however, slightly larger than the experimental band gap by about 8 $\%$ which is a small error when compared with the DFT ones.

The optical property of the structure was investigated at the GW level of approximation, it was found that the structure start to absorb incident energy at the 0.67 eV of the spectrum. It is therefore expected that $ReSe_2$ is a potential candidate for third generation solar cell application.

7.2 Future work

The unanswered question from this work are

1. MX_3(M= Ti, Zr and Hf; X= S, Se, Te) and $ReSe_2$ optical properties investigated are based on GW level of approximations. This can not be compared with experimental optical spectra. To compare them one need to build BSE on top of the GW calculations and this requires a lot of computational resources and time.

2. To use the TcS_2 and its doped system as solar energy materials, their optical properties need to be investigated.

Appendix A. Doped TcS_2 Structures

To provide the full picture of the changes in the structural and electronic properties of the doped TcS_2 structures, we present here in table A.1, the first four coloums in the table represent the undoped unit cell of the structure and the numbers, the Tc atom replaced with Fe, the unit cell of the structure was double in x, y and z directions and technetium atoms were replaced with iron in different atomic positions. For example, dc1_0.50 refer to doubling the unit cell in the y-direction and replacing the first technetium with iron, I and D in the table refers to indirect and direct band gaps respectively.

Table A.1: Doped technetium dichalcogenides structural system, volume, volume per atom, cohesive energy E_{coh}, cohesive energy E_{coh} per atom, formation energy per atom, band gap for DFT, band gap and magnetic moment per unit cell (μ) in Bohr magnetons.

structure	Vol.	V/atom	e_{coh}/atom	f/atom	DFT-D2	MBJ	μ (vdW)	μ (MBJ)
u121	433.92	18.08	-5.22	-0.62	0.94 I	1.10 I	0.00	0.00
u211	433.44	18.06	-5.22	-0.62	0.94 I	1.10 I	0.00	0.00
u111	217.08	18.09	-5.22	-0.62	0.94 I	1.10 I	0.00	0.00
u112	434.16	18.09	-5.22	-0.62	0.938 I	1.09 I	0.00	0.00
da6_0.25	423.60	17.65	-4.96	-0.54	0.54 I	0.85 I	0.00	0.00
db9_0.375	419.28	17.47	-4.85	-0.52	0.29 I	0.80 I	1.00	1.00
da10_0.25	422.40	17.60	-4.98	-0.56	0.61 I	0.77 I	0.00	0.00
da4_0.25	422.88	17.62	-4.97	-0.55	0.60 I	0.76 I	0.00	0.00
db4_0.25	424.08	17.67	-4.97	-0.55	0.61 I	0.73 I	0.00	0.00
da2_0.25	421.44	17.56	-4.96	-0.53	0.37 D	0.72 I	0.00	0.00
da2_0.375	417.84	17.41	-4.83	-0.5 0	0.45 D	0.71 I	1.00	1.00
db6_0.25	423.12	17.63	-4.96	-0.54	0.55 I	0.70 I	0.00	0.00
db2_0.375	418.32	17.43	-4.83	-0.50	0.39 I	0.68 I	1.00	1.00
db9_0.25	424.32	17.68	-4.98	-0.56	0.53 I	0.68 I	0.00	0.00
db2_0.25	422.88	17.62	-4.95	-0.53	0.33 I	0.68 I	0.00	0.00
dc5_0.25	423.12	17.63	-4.96	-0.54	0.46 I	0.68 I	0.00	0.00
da14_0.50	411.36	17.15	-4.72	-0.48	0.48 I	0.68 I	0.00	0.00
da1_0.125	429.36	17.89	-5.08	-0.57	0.36 D	0.68 I	1.00	1.00
db1_0.25	423.12	17.63	-4.95	-0.53	0.33 I	0.68 I	0.00	0.00
db1_0.125	429.60	17.90	-5.08	-0.57	0.28 I	0.65 I	1.00	1.00
da18_0.50	411.84	17.16	-4.73	-0.49	0.37 I	0.64 I	0.00	0.00
da10_0.375	416.16	17.34	-4.85	-0.52	0.23 I	0.63 I	1.00	1.00

Continued on next page

Table A.1 – continued from previous page

structure	Volome	V/atom	e_{coh}/atom	f/atom	DFT-D2	MBJ	μ (vdW)	μ (MBJ)
dc3_0.25	423.12	17.63	-4.97	-0.55	0.59 I	0.63 I	0.00	0.00
db20_0.50	414.96	17.29	-4.72	-0.48	0.16 I	0.63 I	0.00	2.00
da2_0.125	429.84	17.91	-5.08	-0.57	0.38 I	0.63 I	1.00	1.00
dc4_0.25	422.88	17.62	-4.94	-0.52	0.14 I	0.62 D	2.00	0.68
da9_0.50	412.32	17.18	-4.71	-0.47	0.40 I	0.62 I	0.00	0.00
db6_0.50	411.36	17.14	-4.73	-0.49	0.55 I	0.62 I	0.00	0.00
db9_0.50	411.36	17.14	-4.71	-0.47	0.38 I	0.62 I	0.00	0.00
da6_0.50	411.36	17.14	-4.73	-0.49	0.54 I	0.61 I	0.00	0.00
db11_0.375	417.84	17.41	-4.83	-0.50	0.35 I	0.61 I	1.00	1.00
dc8_0.50	411.84	17.16	-4.71	-0.47	0.34 I	0.61 I	0.00	0.00
dc1_0.125	428.88	17.87	-5.08	-0.57	0.30 I	0.61 I	1.00	1.00
da1_0.25	424.80	17.70	-4.94	-0.52	0.25 I	0.61 I	2.00	2.00
db10_0.375	419.52	17.48	-4.84	-0.51	0.40 I	0.61 I	1.00	1.00
db8_0.375	417.84	17.41	-4.83	-0.50	0.31 I	0.61 I	1.00	1.00
dc7_0.50	411.84	17.16	-4.71	-0.47	0.34 I	0.60 I	0.00	0.00
d1_0.25	211.80	17.65	-4.94	-0.52	0.22 D	0.60 I	1.00	1.00
da2_0.50	411.12	17.13	-4.71	-0.47	0.29 I	0.60 I	0.00	0.00
dc5_0.50	411.36	17.14	-4.72	-0.49	0.55 I	0.59 I	0.00	0.00
db13_0.375	418.08	17.42	-4.83	-0.50	0.23 I	0.59 I	1.00	1.00
dc7_0.25	423.60	17.65	-4.98	-0.56	0.49 I	0.59 I	1.00	0.00
da11_0.375	417.36	17.39	-4.85	-0.52	0.31 I	0.59 I	1.00	1.00
db7_0.375	416.64	17.36	-4.82	-0.49	0.23 I	0.58 I	1.00	1.00
dc1_0.25	424.32	17.68	-4.95	-0.52	0.23 D	0.58 D	2.00	1.18
db5_0.375	418.08	17.42	-4.82	-0.49	0.08 I	0.57 I	1.00	1.00
da8_0.25	424.56	17.69	-4.95	-0.53	0.33 I	0.57 I	2.00	2.00
dc6_0.25	424.08	17.67	-4.98	-0.56	0.48 I	0.57 I	0.00	0.00
da20_0.50	414.48	17.08	-4.72	-0.49	0.38 I	0.57 I	0.00	0.00
da6_0.375	417.36	17.39	-4.83	-0.50	0.37 I	0.56 I	1.00	1.00
da11_0.50	411.60	17.15	-4.73	-0.49	0.41 I	0.60 I	0.00	2.00
db21_0.50	411.600	17.15	-4.73	-0.49	0.42 I	0.60 D	0.00	0.00
db17_0.50	408.72	17.03	-4.71	-0.47	0.37 I	0.56 I	0.00	0.00
db2_0.50	414.72	17.28	-4.70	-0.46	0.00 D	0.60 I	1.08	0.00
da9_0.375	418.08	17.42	-4.84	-0.51	0.35 I	0.55 I	1.00	1.00
da7_0.375	417.12	17.38	-4.82	-0.49	0.27 I	0.55 I	1.00	1.00
db8_0.50	411.12	17.13	-4.71	-0.47	0.40 I	0.55 I	0.00	0.00
dc2_0.125	430.08	17.92	-5.08	-0.57	0.41 I	0.55 I	1.00	1.00

Continued on next page

Table A.1 – continued from previous page

structure	Volome	V/atom	e_{coh}/atom	f/atom	DFT-D2	MBJ	μ (vdW)	μ (MBJ)
db5_0.50	410.40	17.10	-4.70	-0.46	0.28 I	0.55 I	0.00	0.00
db14_0.375	417.36	17.39	-4.85	-0.52	0.25 I	0.54 I	1.00	1.00
dc6_0.375	417.600	17.40	-4.83	-0.50	0.37 I	0.54 I	1.00	1.00
da13_0.375	418.32	17.43	-4.83	-0.49	0.38 I	0.54 I	1.00	1.00
db18_0.50	413.04	17.21	-4.72	-0.48	0.26 I	0.54 I	0.00	0.00
dc2_0.25	422.40	17.60	-4.95	-0.53	0.23 I	0.54 I	0.00	0.00
d2_0.25	211.92	17.66	-4.95	-0.53	0.31 I	0.54 I	1.00	1.00
da1_0.375	415.68	17.32	-4.81	-0.48	0.21 I	0.54 I	1.00	1.00
da3_0.50	409.20	17.05	-4.71	-0.47	0.36 I	0.54 I	0.00	0.00
db3_0.25	424.32	17.68	-4.94	-0.52	0.18 I	0.53 I	2.00	2.00
db3_0.50	411.84	17.16	-4.71	-0.47	0.28 I	0.53 I	0.00	0.00
da12_0.50	408.96	17.04	-4.73	-0.49	0.31 I	0.53 I	0.00	0.00
db10_0.25	422.16	17.59	-4.94	-0.53	0.25 I	0.53 I	2.00	2.00
dc9_0.375	416.40	17.35	-4.83	-0.50	0.35 I	0.53 I	1.00	1.00
da3_0.375	418.32	17.43	-4.82	-0.49	0.24 I	0.53 I	1.00	1.00
db14_0.50	411.36	17.14	-4.72	-0.48	0.44 I	0.53 I	0.00	0.00
dc10_0.375	416.40	17.35	-4.85	-0.52	0.31 I	0.52 I	1.00	1.00
db16_0.50	414.00	17.25	-4.73	-0.49	0.52 I	0.52 I	0.00	0.00
dc14_0.50	412.32	17.18	-4.72	-0.48	0.33 I	0.52 I	0.00	0.00
da7_0.50	411.84	17.16	-4.70	-0.46	0.24 I	0.51 I	2.00	2.00
dc3_0.50	411.12	17.13	-4.70	-0.47	0.22 I	0.51 I	0.00	0.00
db10_0.50	412.32	17.18	-4.71	-0.47	0.19 I	0.51 I	0.00	2.00
dc4_0.375	418.56	17.44	-4.85	-0.52	0.14 I	0.51 I	1.00	1.00
db1_0.375	416.64	17.36	-4.81	-0.48	0.19 I	0.51 I	1.00	1.00
db13_0.50	412.80	17.20	-4.72	-0.48	0.25 I	0.50 I	0.00	0.00
db12_0.375	419.52	17.48	-4.84	-0.51	0.18 I	0.49 I	1.00	1.00
db19_0.50	413.04	17.21	-4.73	-0.49	0.46 I	0.49 I	0.00	0.00
dc13_0.50	412.56	17.19	-4.73	-0.49	0.40 I	0.49 I	0.00	0.00
db7_0.50	414.24	17.26	-4.71	-0.47	0.00 D	0.49 I	2.00	0.00
db7_0.25	426.00	17.75	-4.94	-0.52	0.04 I	0.49 I	0.00	0.00
da5_0.50	410.16	17.09	-4.70	-0.46	0.27 I	0.49 I	0.00	0.00
dc5_0.375	416.88	17.37	-4.82	-0.49	0.12 I	0.49 I	1.00	1.00
db2_0.125	430.08	17.92	-5.08	-0.57	0.36 I	0.49 I	1.00	1.00
da5_0.375	414.96	17.29	-4.83	-0.50	0.28 I	0.48 I	1.00	1.00
db15_0.50	413.04	17.21	-4.71	-0.48	0.11 I	0.48 I	0.00	2.00
db12_0.50	413.52	17.23	-4.71	-0.47	0.16 I	0.48 I	2.00	4.00

Continued on next page

Table A.1 – continued from previous page

structure	Volome	V/atom	e_{coh}/atom	f/atom	DFT-D2	MBJ	μ (vdW)	μ (MBJ)
d1_0.50	204.72	17.06	-4.75	-0.51	0.36 I	0.48 I	0.00	0.00
dc1_0.375	415.68	17.32	-4.81	-0.48	0.14 I	0.47 I	1.00	1.00
dc2_0.375	415.20	17.30	-4.81	-0.48	0.14 I	0.47 I	1.00	1.00
da22_0.50	408.96	17.04	-4.75	-0.47	0.36 I	0.47 I	0.00	0.00
dc11_0.50	412.32	17.18	-4.71	-0.47	0.16 I	0.47 I	0.00	0.00
dc7_0.375	417.12	17.38	-4.85	-0.52	0.19 I	0.46 D	1.00	2.72
da8_0.50	412.80	17.20	-4.71	-0.47	0.13 I	0.46 I	0.00	0.00
db22_0.50	409.20	17.05	-4.75	-0.51	0.36 I	0.46 I	0.00	0.00
dc15_0.50	408.48	17.02	-4.75	-0.51	0.35 I	0.46 I	0.00	0.00
dc8_0.375	416.88	17.37	-4.83	-0.50	0.35 I	0.45 I	1.00	1.00
da8_0.375	417.84	17.41	-4.83	-0.50	0.35 I	0.45 I	1.00	1.00
da15_0.50	411.84	17.16	-4.70	-0.46	0.28 I	0.45 I	2.00	2.00
da1_0.50	408.48	17.02	-4.69	-0.45	0.23 I	0.45 I	0.00	0.00
db6_0.375	419.04	17.46	-4.83	-0.50	0.19 I	0.44 I	1.00	1.00
dc1_0.50	408.72	17.03	-4.69	-0.45	0.17 I	0.43 I	0.00	0.00
db1_0.50	408.72	17.03	-4.69	-0.45	0.18 I	0.43 I	0.00	0.00
dc3_0.375	417.12	17.38	-4.82	-0.49	0.16 I	0.43 I	1.00	1.00
d3_0.50	204.24	17.02	-4.69	-0.45	0.18 I	0.42 I	0.00	0.00
da9_0.25	421.44	17.56	-4.95	-0.53	0.15 I	0.42 I	2.00	2.00
da10_0.50	411.60	17.15	-4.70	-0.47	0.14 I	0.42 I	0.00	2.00
d2_0.50	205.92	17.16	-4.72	-0.45	0.20 I	0.41 I	0.00	0.00
da21_0.50	410.40	17.10	-4.71	-0.48	0.13 I	0.41 I	0.00	2.00
da19_0.50	409.92	17.08	-4.72	-0.48	0.14 I	0.40 I	0.00	0.00
da16_0.50	401.76	16.74	-4.72	-0.48	0.08 I	0.39 I	2.00	2.00
db4_0.375	419.52	17.48	-4.84	-0.51	0.24 I	0.39 I	1.00	1.00
db3_0.375	417.60	17.40	-4.82	-0.49	0.16 I	0.39 I	1.00	1.00
dc9_0.50	414.72	17.28	-4.71	-0.47	0.14 I	0.38 I	0.00	2.00
da14_0.375	415.92	17.33	-4.85	-0.52	0.24 I	0.37 I	1.00	1.00
dc10_0.50	398.16	16.59	-4.73	-0.49		0.37 I	0.00	0.00
dc12_0.50	410.88	17.12	-4.73	-0.49	0.26 I	0.37 D	0.00	4.00
dc4_0.50	410.16	17.09	-4.70	-0.46	0.14 D	0.35 I	0.00	0.00
db8_0.25	424.80	17.70	-4.95	-0.53	0.30 I	0.34 I	2.00	2.00
da4_0.375	418.80	17.45	-4.84	-0.51	0.25 I	0.33 I	1.00	1.00
da5_0.25	421.68	17.57	-4.94	-0.52	0.21 I	0.31 D	0.00	0.00
da7_0.25	421.44	17.56	-4.95	-0.53	0.25 I	0.31 I	0.00	0.00
dc6_0.50	412.8	17.20	-4.71	-0.47	0.00	0.26 I	0.00	2.14

Continued on next page

Table A.1 – continued from previous page

structure	Volome	V/atom	e_{coh}/atom	f/atom	DFT-D2	MBJ	μ (vdW)	μ (MBJ)
dc2_0.50	414.00	17.25	-4.71	-0.47	0.00	0.27 I	0.05	4.00
db11_0.50	413.28	17.22	-4.73	-0.49	0.30 I	0.22 I	0.00	0.00
da13_0.50	406.56	16.94	-4.70	-0.45	0.00	0.21 I	0.00	2.00
db5_0.25	424.08	17.67	-4.94	-0.52	0.11 I	0.20 I	0.00	0.00
da12_0.375	405.12	17.33	-4.81	-0.48	0.11 I	0.13 I	1.00	1.00
da4_0.50	411.84	17.16	-4.71	-0.47	0.20 I	0.12 I	0.00	0.00
da17_0.50	413.52	17.23	-4.72	-0.47	0.00	0.05 I	0.02	2.00
db4_0.50	413.04	17.21	-4.71	-0.47	0.00	0.05 I	0.00	0.00
da3_0.25	423.60	17.65	-4.93	-0.51	0.00	0.01 I	0.00	0.00

[0]The letters D and I in the band gap column signifies direct and an indirect band gaps respectively.

References

[1] D. Jenkinson, D. Adams, and A. Wild, "Model estimates of co2 emissions from soil in response to global warming," *Nature*, vol. 351, no. 6324, pp. 304–306, 1991.

[2] D. A. Lashof, "The dynamic greenhouse: feedback processes that can influence global warming," *Preparing for Climate Change*, p. 102, 1993.

[3] D. Schimel, W. Parton, T. Kittel, D. Ojima, and C. Cole, "Grassland biogeochemistry: links to atmospheric processes," *Climatic Change*, vol. 17, no. 1, pp. 13–25, 1990.

[4] C. J. Chen, *Physics of solar energy*. John Wiley & Sons, 2011.

[5] M. Grätzel, "Photoelectrochemical cells," *Nature*, vol. 414, no. 6861, pp. 338–344, 2001.

[6] L. El Chaar, N. El Zein, *et al.*, "Review of photovoltaic technologies," *Renewable and Sustainable Energy Reviews*, vol. 15, no. 5, pp. 2165–2175, 2011.

[7] M. Asif and T. Muneer, "Energy supply, its demand and security issues for developed and emerging economies," *Renewable and Sustainable Energy Reviews*, vol. 11, no. 7, pp. 1388–1413, 2007.

[8] J. Nelson, *The Physics of Solar Cells*. Imperial College press, 2007.

[9] R. W. Miles, G. Zoppi, and I. Forbes, "Inorganic photovoltaic cells," *Materials today*, vol. 10, no. 11, pp. 20–27, 2007.

[10] M. A. Green, "Third generation photovoltaics: solar cells for 2020 and beyond," *Physica E: Low-dimensional Systems and Nanostructures*, vol. 14, no. 1, pp. 65–70, 2002.

[11] G. Conibeer, M. Green, R. Corkish, Y. Cho, E.-C. Cho, C.-W. Jiang, T. Fangsuwannarak, E. Pink, Y. Huang, T. Puzzer, *et al.*, "Silicon nanostructures for third generation photovoltaic solar cells," *Thin Solid Films*, vol. 511, pp. 654–662, 2006.

[12] D. M. Bagnall and M. Boreland, "Photovoltaic technologies," *Energy Policy*, vol. 36, no. 12, pp. 4390–4396, 2008.

[13] M. A. Green, "Third generation photovoltaics: Ultra-high conversion efficiency at low cost," *Progress in Photovoltaics: Research and Applications*, vol. 9, no. 2, pp. 123–135, 2001.

[14] W. Shockley and H. J. Queisser, "Detailed balance limit of efficiency of p-n junction solar cells," *Journal of applied physics*, vol. 32, no. 3, pp. 510–519, 1961.

[15] M. A. Green, K. Emery, Y. Hishikawa, W. Warta, and E. D. Dunlop, "Solar cell efficiency tables (version 45)," *Progress in photovoltaics: research and applications*, vol. 23, no. 1, pp. 1–9, 2015.

[16] R. King, D. Law, K. Edmondson, C. Fetzer, G. Kinsey, H. Yoon, R. Sherif, and N. Karam, "40% efficient metamorphic GaInP/GaInAs/Ge multijunction solar cells," *Applied physics letters*, vol. 90, no. 18, pp. 183516–183900, 2007.

[17] J. Nelson, *The physics of solar cells*, vol. 1. World Scientific, 2003.

[18] S. Jenks, "Maximum efficiency of an ideal solar cell containing one and two intermediate bands," 2008.

[19] M. E. Nell and A. M. Barnett, "The spectral pn junction model for tandem solar-cell design," *Electron Devices, IEEE Transactions on*, vol. 34, no. 2, pp. 257–266, 1987.

[20] A. De Vos, "Detailed balance limit of the efficiency of tandem solar cells," *Journal of Physics D: Applied Physics*, vol. 13, no. 5, p. 839, 1980.

[21] J. Wilson and A. Yoffe, "The transition metal dichalcogenides discussion and interpretation of the observed optical, electrical and structural properties," *Advances in Physics*, vol. 18, no. 73, pp. 193–335, 1969.

[22] P. F. Weck, E. Kim, and K. R. Czerwinski, "Semiconducting layered technetium dichalcogenides: insights from first-principles," *Dalton Transactions*, vol. 42, no. 43, pp. 15288–15295, 2013.

[23] M. Benameur, B. Radisavljevic, J. Heron, S. Sahoo, H. Berger, and A. Kis, "Visibility of dichalcogenide nanolayers," *Nanotechnology*, vol. 22, no. 12, p. 125706, 2011.

[24] A. Kumar and P. Ahluwalia, "Electronic structure of transition metal dichalcogenides monolayers 1H-MX_2 (M= Mo, W; X= S, Se, Te) from ab-initio theory: new direct band gap semiconductors," *The European Physical Journal B-Condensed Matter and Complex Systems*, vol. 85, no. 6, pp. 1–7, 2012.

[25] B. McCandless and K. Dobson, "Processing options for cdte thin film solar cells," *Solar Energy*, vol. 77, no. 6, pp. 839–856, 2004.

[26] B. Radisavljevic, A. Radenovic, J. Brivio, V. Giacometti, and A. Kis, "Single-layer MoS_2 transistors," *Nature nanotechnology*, vol. 6, no. 3, pp. 147–150, 2011.

[27] K. F. Mak, K. He, C. Lee, G. H. Lee, J. Hone, T. F. Heinz, and J. Shan, "Tightly bound trions in monolayer MoS_2," *Nature materials*, vol. 12, no. 3, pp. 207–211, 2013.

[28] D. Xiao, G.-B. Liu, W. Feng, X. Xu, and W. Yao, "Coupled spin and valley physics in monolayers of MoS_2 and other group-vi dichalcogenides," *Physical Review Letters*, vol. 108, no. 19, p. 196802, 2012.

[29] Z. Yin, H. Li, H. Li, L. Jiang, Y. Shi, Y. Sun, G. Lu, Q. Zhang, X. Chen, and H. Zhang, "Single-layer MoS_2 phototransistors," *ACS nano*, vol. 6, no. 1, pp. 74–80, 2011.

[30] K. Novoselov, A. Geim, S. Morozov, D. Jiang, Y. Zhang, S. Dubonos, I. Grigorieva, and A. Firsov, "Electric field effect in atomically thin carbon films," *Science*, vol. 306, no. 5696, pp. 666–669, 2004.

[31] S. Han, H. Kwon, S. Kim, S. Ryu, W. Yun, D. Kim, J. Hwang, J. Kang, J. Baik, H. Shin, *et al.*, "Band-gap transition induced by interlayer van der waals interaction in $\mathrm{MoS_2}$," *Physical Review B*, vol. 84, no. 4, p. 045409, 2011.

[32] P. Johari and V. Shenoy, "Tuning the electronic properties of semiconducting transition metal dichalcogenides by applying mechanical strains," *ACS nano*, vol. 6, no. 6, pp. 5449–5456, 2012.

[33] R. F. Frindt, "Single crystals of MoS_2 several molecular layers thick," *Journal of Applied Physics*, vol. 37, no. 4, pp. 1928–1929, 1966.

[34] K. Novoselov, D. Jiang, F. Schedin, T. Booth, V. Khotkevich, S. Morozov, and A. Geim, "Two-dimensional atomic crystals," *Proceedings of the National Academy of Sciences of the United States of America*, vol. 102, no. 30, pp. 10451–10453, 2005.

[35] R. Tenne and A. Wold, "Passivation of recombination centers in n-WSe_2 yields high efficiency ($>$ 14%) photoelectrochemical cell," *Applied physics letters*, vol. 47, no. 7, pp. 707–709, 1985.

[36] Y. Feldman, E. Wasserman, D. Srolovitz, R. Tenne, *et al.*, "High-rate, gas-phase growth of MoS_2 nested inorganic fullerenes and nanotubes," *Science (New York, NY)*, vol. 267, no. 5195, p. 222, 1995.

[37] M. Remskar, A. Mrzel, Z. Skraba, A. Jesih, M. Ceh, J. Demšar, P. Stadelmann, F. Lévy, and D. Mihailovic, "Self-assembly of subnanometer-diameter single-wall MoS_2 nanotubes," *Science*, vol. 292, no. 5516, pp. 479–481, 2001.

[38] R. Chau, S. Datta, M. Doczy, B. Doyle, B. Jin, J. Kavalieros, A. Majumdar, M. Metz, and M. Radosavljevic, "Benchmarking nanotechnology for high-performance and low-power logic transistor applications," *Nanotechnology, IEEE Transactions on*, vol. 4, no. 2, pp. 153–158, 2005.

[39] L. Mattheiss, "Energy bands for 2 H-$NbSe_2$ and 2 H-Mo S_2," *Physical Review Letters*, vol. 30, no. 17, pp. 784–787, 1973.

[40] H. Jiang, "Structural and electronic properties of ZrX_2 and HfX_2 (X= S and Se) from first principles calculations," *The Journal of Chemical Physics*, vol. 134, p. 204705, 2011.

[41] M. Abdulsalam and D. P. Joubert, "Structural and electronic properties of MX_3 (M= Ti, Zr and Hf; X= S, Se, Te) from first principles calculations," *The European Physical Journal B*, vol. 88, no. 7, pp. 1–11, 2015.

[42] J. Wu, D. Wang, H. Liu, W.-M. Lau, and L.-M. Liu, "An ab initio study of TiS_3: a promising electrode material for rechargeable li and na ion batteries," *RSC Advances*, vol. 5, no. 28, pp. 21455–21463, 2015.

[43] J. O. Island, M. Buscema, M. Barawi, J. M. Clamagirand, J. R. Ares, C. Sánchez, I. J. Ferrer, G. A. Steele, H. S. van der Zant, and A. Castellanos-Gomez, "Ultrahigh photoresponse of few-layer TiS_3 nanoribbon transistors," *Advanced Optical Materials*, vol. 2, no. 7, pp. 641–645, 2014.

[44] J. Dai and X. C. Zeng, "Titanium trisulfide monolayer: Theoretical prediction of a new direct-gap semiconductor with high and anisotropic carrier mobility," *Angewandte Chemie*, 2015.

[45] Y.-W. Son, M. L. Cohen, and S. G. Louie, "Energy gaps in graphene nanoribbons," *Physical review letters*, vol. 97, no. 21, p. 216803, 2006.

[46] J. Kang, H. Sahin, H. D. Ozaydin, R. T. Senger, and F. M. Peeters, "TiS_3 nanoribbons: Width-independent band gap and strain-tunable electronic properties," *Physical Review B*, vol. 92, no. 7, p. 075413, 2015.

[47] Y. Li, Z. Zhou, S. Zhang, and Z. Chen, "MoS_2 nanoribbons: high stability and unusual electronic and magnetic properties," *Journal of the American Chemical Society*, vol. 130, no. 49, pp. 16739–16744, 2008.

[48] N. Alcock and A. Kjekshus, "The crystal structure of $ReSe_2$," *Acta Chem Scand*, vol. 19, no. 1, pp. 79–94, 1965.

[49] J. Wildervanck and F. Jellinek, "The dichalcogenides of technetium and rhenium," *Journal of the Less Common Metals*, vol. 24, no. 1, pp. 73–81, 1971.

[50] H.-J. Lamfers, A. Meetsma, G. Wiegers, and J. De Boer, "The crystal structure of some rhenium and technetium dichalcogenides," *Journal of alloys and compounds*, vol. 241, no. 1, pp. 34–39, 1996.

[51] J. A. Rard and E. Östhols, *Chemical thermodynamics of technetium*. North Holland, 1999.

[52] C. Fang, G. Wiegers, C. Haas, and R. De Groot, "Electronic structures of ReS_2, $ReSe_2$, and TcS_2 in the real and the hypothetical undistorted structures," *Journal of Physics: Condensed Matter*, vol. 9, no. 21, p. 4411, 1997.

[53] K. Dartigeas, L. Benoist, D. Gonbeau, G. Pfister-Guillouzo, G. Ouvrard, and A. Levasseur, "Systematic x-ray photoelectron spectroscopy and theoretical studies of disulfides of groups ivb, vb and vib transition metals," *Journal of electron spectroscopy and related phenomena*, vol. 83, no. 1, pp. 45–58, 1997.

[54] L. Mattheiss, "Band structures of transition-metal-dichalcogenide layer compounds," *Physical Review B*, vol. 8, no. 8, p. 3719, 1973.

[55] A. H. Reshak and S. Auluck, "Theoretical investigation of the electronic and optical properties of ZrX_2 (X= S, Se and Te)," *Physica B: Condensed Matter*, vol. 353, no. 3, pp. 230–237, 2004.

[56] D. Bullett, "Electronic band structure and bonding in transition metal layered dichalcogenides by atomic orbital methods," *Journal of Physics C: Solid State Physics*, vol. 11, no. 22, p. 4501, 1978.

[57] F. Aryasetiawan and O. Gunnarsson, "The GW method," *Reports on Progress in Physics*, vol. 61, no. 3, p. 237, 1999.

[58] L. Hedin, "New method for calculating the one-particle green's function with application to the electron-gas problem," *Physical Review*, vol. 139, no. 3A, p. A796, 1965.

[59] P. Rinke, A. Qteish, J. Neugebauer, and M. Scheffler, "Exciting prospects for solids: Exact-exchange based functionals meet quasiparticle energy calculations," *physica status solidi (b)*, vol. 245, no. 5, pp. 929–945, 2008.

[60] F. McTaggart, "The sulphides, selenides, and tellurides of titanium, zirconium, hafnium and thorium. iii. electrical properties," *Australian Journal of Chemistry*, vol. 11, no. 4, pp. 471–480, 1958.

[61] J. Bear and F. McTaggart, "The sulphides, selenides, and tellurides of titanium, zirconium, hafnium, and thorium. iii. chemical properties," *Australian Journal of Chemistry*, vol. 11, no. 4, pp. 458–479, 1958.

[62] F. K. McTaggart and A. Wadsley, "The sulphides, selenides, and tellurides of titanium, zirconium, hafnium, and thorium. i. preparation and characterization," *Australian Journal of Chemistry*, vol. 11, no. 4, pp. 445–457, 1958.

[63] A. Steffensen, "On the properties of TiS_3, ZrS_3, and HfS_3," *Acta Chem. Scand*, vol. 17, no. 5, 1963.

[64] S. Furuseth, L. Brattas, and A. Kjekshus, "Crystal structures of TiS_3, ZrS_3, $ZrSe_3$, $ZrTe_3$, HfS_3 and $HfSe_3$," *Acta Chemica Scandinavica*, vol. 29, p. 623, 1975.

[65] M. Traving, T. Seydel, L. Kipp, M. Skibowski, F. Starrost, E. Krasovskii, A. Perlov, and W. Schattke, "Combined photoemission and inverse photoemission study of hfs_2," *Physical Review B*, vol. 63, no. 3, p. 035107, 2001.

[66] C. Fong, J. Camassel, S. Kohn, and Y. Shen, "Wavelength-modulated spectrum and electronic properties of hfs_2," *Physical Review B*, vol. 13, no. 12, p. 5442, 1976.

[67] L. Brattas and A. Kjekshus, "Properties of compounds with $ZrSe_3$-type structure," *Acta Chemica Scandinavica*, vol. 26, no. 9, pp. 3441–3449, 1972.

[68] D. Bullett, "Variation of electronic properties with structure of transition metal trichalcogenides," *Journal of Physics C: Solid State Physics*, vol. 12, no. 2, p. 277, 1979.

[69] F. Levy and H. Berger, "Single crystals of transition metal trichalcogenides," *Journal of Crystal Growth*, vol. 61, no. 1, pp. 61–68, 1983.

[70] H. Jin, D. Cheng, J. Li, X. Cao, B. Li, X. Wang, X. Liu, and X. Zhao, "Facile synthesis of zirconium trisulfide and hafnium trisulfide nanobelts: Growth mechanism and raman spectroscopy," *Solid State Sciences*, vol. 13, no. 5, pp. 1166–1171, 2011.

[71] H. V. AirdáBriscoe, P. LucockáRobinson, and E. MauriceáStoddart, "Cxcv.the sulphides and selenides of rhenium," *Journal of the Chemical Society (Resumed)*, pp. 1439–1443, 1931.

[72] C. Ho, Y. Huang, J. Chen, T. Dann, and K. Tiong, "Electronic structure of ReS_2 and $ReSe_2$ from first-principles calculations, photoelectron spectroscopy, and electrolyte electroreflectance," *Physical Review B*, vol. 60, no. 23, p. 15766, 1999.

[73] C. Ho, P. Liao, Y. Huang, T. Yang, and K. Tiong, "Optical absorption of ReS_2 and $ReSe_2$ single crystals," *Journal of applied physics*, vol. 81, no. 9, pp. 6380–6383, 1997.

[74] D. Wolverson, S. Crampin, A. S. Kazemi, A. Ilie, and S. J. Bending, "Raman spectra of monolayer, few-layer, and bulk $ReSe_2$: An anisotropic layered semiconductor," *ACS nano*, vol. 8, no. 11, pp. 11154–11164, 2014.

[75] J. V. Marzik, R. Kershaw, K. Dwight, and A. Wold, "Photoelectronic properties of ReS_2 and $ReSe_2$ single crystals," *Journal of Solid State Chemistry*, vol. 51, no. 2, pp. 170–175, 1984.

[76] S. Tongay, H. Sahin, C. Ko, A. Luce, W. Fan, K. Liu, J. Zhou, Y.-S. Huang, C.-H. Ho, J. Yan, *et al.*, "Monolayer behaviour in bulk ReS_2 due to electronic and vibrational decoupling," *Nature communications*, vol. 5, 2014.

[77] D. Joubert, "Density functionals: theory and applications," in *Lecture Notes in Physics, Berlin Springer Verlag*, vol. 500, 1998.

[78] R. Martin, *Electronic structure: basic theory and practical methods*. Cambridge university press, 2004.

[79] A. Szabo and N. Ostlund, *Modern Quantum Chemistry: Introduction To Advanced Electronic Structure Theory Author: Attila Szabo, Neil S. Ostlund, Publ*. Dover Publications, 1996.

[80] P. Giannozzi Lecture Notes oer il Corso di strutta della materia.

[81] L. H. Thomas, "The calculation of atomic fields," in *Mathematical Proceedings of the Cambridge Philosophical Society*, vol. 23, pp. 542–548, Cambridge Univ Press, 1927.

[82] E. Fermi, "Eine statistische methode zur bestimmung einiger eigenschaften des atoms und ihre anwendung auf die theorie des periodischen systems der elemente," *Zeitschrift für Physik*, vol. 48, no. 1-2, pp. 73–79, 1928.

[83] J. Kohanoff, *Electronic structure calculations for solids and molecules*. Cambridge University Press, 2006.

[84] P. Dirac, "Note on exchange phenomena in the thomas-fermi atom," *Prot. Cambridge PhiL Sec*, vol. 26, pp. 376–385, 1930.

[85] J. C. Slater, "A simplification of the hartree-fock method," *Physical Review*, vol. 81, no. 3, p. 385, 1951.

[86] P. Hohenberg and W. Kohn, "Inhomogeneous electron gas," *Physical Review*, vol. 136, no. 3B, p. B864, 1964.

[87] W. Koch, M. C. Holthausen, and M. C. Holthausen, *A chemist's guide to density functional theory*, vol. 2. Wiley-Vch Weinheim, 2001.

[88] M. Levy, "Electron densities in search of hamiltonians," *Physical Review A*, vol. 26, no. 3, p. 1200, 1982.

[89] E. Lieb, "Density functionals for Coulomb systems," *International journal of quantum chemistry*, vol. 24, no. 3, pp. 243–277, 1983.

[90] W. Kohn and L. J. Sham, "Self-consistent equations including exchange and correlation effects," *Physical Review*, vol. 140, no. 4A, p. A1133, 1965.

[91] J. Luo, Z. Q. Xue, W. M. Liu, J. L. Wu, and Z. Q. Yang, "Koopmans' theorem for large molecular systems within density functional theory," *The Journal of Physical Chemistry A*, vol. 110, no. 43, pp. 12005–12009, 2006.

[92] W. Aulbur, L. Jönsson, and J. Wilkins, "Quasiparticle calculations in solids," *Solid State Physics*, vol. 54, pp. 1–218, 1999.

[93] J. Perdew, A. Ruzsinszky, J. Tao, V. Staroverov, G. Scuseria, and G. Csonka, "Prescription for the design and selection of density functional approximations: More constraint satisfaction with fewer fits," *The Journal of chemical physics*, vol. 123, p. 062201, 2005.

[94] J. Hafner, "Ab-initio simulations of materials using VASP: Density-functional theory and beyond," *Journal of computational chemistry*, vol. 29, no. 13, pp. 2044–2078, 2008.

[95] J. Hafner, "Materials simulations using vaspa quantum perspective to materials science," *Computer physics communications*, vol. 177, no. 1, pp. 6–13, 2007.

[96] C. Fiolhais, F. Nogueira, and M. Marques, *A primer in density functional theory*, vol. 620. Springer, 2003.

[97] R. G. Parr and W. Yang, *Density-functional theory of atoms and molecules*, vol. 16. Oxford university press, 1989.

[98] S. Ono and Y. Ohishi, "Dm ceperley and bj alder," *Phys. Rev. Lett*, vol. 45, p. 566, 1980.

[99] S. H. Vosko, L. Wilk, and M. Nusair, "Accurate spin-dependent electron liquid correlation energies for local spin density calculations: a critical analysis," *Canadian Journal of Physics*, vol. 58, no. 8, pp. 1200–1211, 1980.

[100] E. W. Brown, J. L. DuBois, M. Holzmann, and D. M. Ceperley, "Exchange-correlation energy for the three-dimensional homogeneous electron gas at arbitrary temperature," *Phys. Rev. B*, vol. 88, p. 081102, Aug 2013.

[101] J. P. Perdew and A. Zunger, "Self-interaction correction to density-functional approximations for many-electron systems," *Physical Review B*, vol. 23, no. 10, p. 5048, 1981.

[102] L. A. Cole and J. Perdew, "Calculated electron affinities of the elements," *Physical Review A*, vol. 25, no. 3, p. 1265, 1982.

[103] J. P. Perdew and Y. Wang, "Accurate and simple analytic representation of the electron-gas correlation energy," *Physical Review B*, vol. 45, no. 23, p. 13244, 1992.

[104] J. F. Dobson, G. Vignale, and M. P. Das, *Electronic density functional theory: recent progress and new directions*. Plenum Press New York, 1998.

[105] D. C. Langreth and J. P. Perdew, "Theory of nonuniform electronic systems. i. analysis of the gradient approximation and a generalization that works," *Physical Review B*, vol. 21, no. 12, p. 5469, 1980.

[106] R. Nashed, Y. Ismail, and N. K. Allam, "Recent advances in the use of density functional theory to design efficient solar energy-based renewable systems," *Journal of Renewable and Sustainable Energy*, vol. 5, p. 022701, 2013.

[107] J. P. Perdew, J. Chevary, S. Vosko, K. A. Jackson, M. R. Pederson, D. Singh, and C. Fiolhais, "Atoms, molecules, solids, and surfaces: Applications of the generalized gradient approximation for exchange and correlation," *Physical Review B*, vol. 46, no. 11, p. 6671, 1992.

[108] J. P. Perdew, K. Burke, and M. Ernzerhof, "Generalized gradient approximation made simple," *Physical review letters*, vol. 77, no. 18, pp. 3865–3868, 1996.

[109] A. D. Becke, "Density-functional exchange-energy approximation with correct asymptotic behavior," *Physical Review A*, vol. 38, no. 6, p. 3098, 1988.

[110] M. Gell-Mann and K. A. Brueckner, "Correlation energy of an electron gas at high density," *Physical Review*, vol. 106, no. 2, p. 364, 1957.

[111] J. Sun, M. Marsman, G. I. Csonka, A. Ruzsinszky, P. Hao, Y.-S. Kim, G. Kresse, and J. P. Perdew, "Self-consistent meta-generalized gradient approximation within the projector-augmented-wave method," *Physical Review B*, vol. 84, no. 3, p. 035117, 2011.

[112] J. Tao, J. P. Perdew, V. N. Staroverov, and G. E. Scuseria, "Climbing the density functional ladder: Nonempirical meta-generalized gradient approximation designed for molecules and solids," *Physical Review Letters*, vol. 91, no. 14, p. 146401, 2003.

[113] Y. Zhao and D. G. Truhlar, "A new local density functional for main-group thermochemistry, transition metal bonding, thermochemical kinetics, and noncovalent interactions," *The Journal of chemical physics*, vol. 125, no. 19, p. 194101, 2006.

[114] A. D. Becke and E. R. Johnson, "A simple effective potential for exchange," *The Journal of chemical physics*, vol. 124, no. 22, p. 221101, 2006.

[115] F. Tran, P. Blaha, and K. Schwarz, "Band gap calculations with becke-johnson exchange potential," *Journal of Physics: Condensed Matter*, vol. 19, no. 19, p. 196208, 2007.

[116] A. D. Becke, "A new mixing of hartree–fock and local density-functional theories," *The Journal of Chemical Physics*, vol. 98, p. 1372, 1993.

[117] A. D. Becke, "Density-functional thermochemistry. iii. the role of exact exchange," *The Journal of Chemical Physics*, vol. 98, p. 5648, 1993.

[118] D. C. Langreth, M. Dion, H. Rydberg, E. Schröder, P. Hyldgaard, and B. I. Lundqvist, "Van der waals density functional theory with applications," *International journal of quantum chemistry*, vol. 101, no. 5, pp. 599–610, 2005.

[119] S. Grimme, "Accurate description of van der waals complexes by density functional theory including empirical corrections," *Journal of computational chemistry*, vol. 25, no. 12, pp. 1463–1473, 2004.

[120] H. Rydberg, M. Dion, N. Jacobson, E. Schröder, P. Hyldgaard, S. Simak, D. C. Langreth, and B. I. Lundqvist, "Van der waals density functional for layered structures," *Physical review letters*, vol. 91, no. 12, p. 126402, 2003.

[121] J. Klimeš and A. Michaelides, "Perspective: Advances and challenges in treating van der waals dispersion forces in density functional theory," *The Journal of Chemical Physics*, vol. 137, no. 12, pp. 120901–120901, 2012.

[122] S. Grimme, J. Antony, S. Ehrlich, and H. Krieg, "A consistent and accurate ab initio parametrization of density functional dispersion correction (DFT-D) for the 94 elements H-Pu," *The Journal of Chemical Physics*, vol. 132, p. 154104, 2010.

[123] S. Grimme, "Semiempirical GGA-type density functional constructed with a long-range dispersion correction," *Journal of computational chemistry*, vol. 27, no. 15, pp. 1787–1799, 2006.

[124] K. Lee, É. D. Murray, L. Kong, B. I. Lundqvist, and D. C. Langreth, "Higher-accuracy van der waals density functional," *Physical Review B*, vol. 82, no. 8, p. 081101, 2010.

[125] M. Dion, H. Rydberg, E. Schröder, D. C. Langreth, and B. I. Lundqvist, "Van der waals density functional for general geometries," *Physical review letters*, vol. 92, no. 24, p. 246401, 2004.

[126] T. Bučko, S. Lebegue, J. Hafner, and J. Ángyán, "Tkatchenko-scheffler van der waals correction method with and without self-consistent screening applied to solids," *Physical Review B*, vol. 87, no. 6, p. 064110, 2013.

[127] A. Tkatchenko, R. A. DiStasio Jr, R. Car, and M. Scheffler, "Accurate and efficient method for many-body van der waals interactions," *Physical Review Letters*, vol. 108, no. 23, p. 236402, 2012.

[128] M. Shishkin, M. Marsman, and G. Kresse, "Accurate quasiparticle spectra from self-consistent GW calculations with vertex corrections," *Physical review letters*, vol. 99, no. 24, p. 246403, 2007.

[129] M. Rohlfing and S. G. Louie, "Electron-hole excitations and optical spectra from first principles," *Physical Review B*, vol. 62, no. 8, p. 4927, 2000.

[130] L. Sham and W. Kohn, "One-particle properties of an inhomogeneous interacting electron gas," *Physical Review*, vol. 145, no. 2, p. 561, 1966.

[131] J. P. Perdew, R. G. Parr, M. Levy, and J. L. Balduz Jr, "Density-functional theory for fractional particle number: Derivative discontinuities of the energy," *Physical Review Letters*, vol. 49, no. 23, p. 1691, 1982.

[132] M. Shishkin and G. Kresse, "Implementation and performance of the frequency-dependent G W method within the PAW framework," *Physical Review B*, vol. 74, no. 3, p. 035101, 2006.

[133] M. S. Hybertsen and S. G. Louie, "Electron correlation in semiconductors and insulators: Band gaps and quasiparticle energies," *Physical Review B*, vol. 34, no. 8, p. 5390, 1986.

[134] M. S. Hybertsen and S. G. Louie, "First-principles theory of quasiparticles: calculation of band gaps in semiconductors and insulators," *Physical review letters*, vol. 55, no. 13, p. 1418, 1985.

[135] R. Godby, M. Schlüter, and L. Sham, "Accurate exchange-correlation potential for silicon and its discontinuity on addition of an electron," *Physical review letters*, vol. 56, no. 22, p. 2415, 1986.

[136] J. Inkson, "Many-body theory of solids: an introduction," tech. rep., Cavendish Lab., Univ. of Cambridge, Cambridge, 1984.

[137] L. Landau and I. Khalatnikov, "The gauge transformation of the green's function for charged particles," *Soviet Phys. JETP*, vol. 2, 1956.

[138] K. Capelle, "A bird's-eye view of density-functional theory," *Brazilian Journal of Physics*, vol. 36, no. 4A, pp. 1318–1343, 2006.

[139] A. Fetter and J. Walecka, "Quantum theory of many-body systems," *New York: McGrow-Hill*, 1971.

[140] D. Pines, *Elementary excitations in solids*. Perseus, 1999.

[141] M. Shishkin and G. Kresse, "Self-consistent G W calculations for semiconductors and insulators," *Physical Review B*, vol. 75, no. 23, p. 235102, 2007.

[142] F. Fuchs, J. Furthmüller, F. Bechstedt, M. Shishkin, and G. Kresse, "Quasiparticle band structure based on a generalized kohn-sham scheme," *Physical Review B*, vol. 76, no. 11, p. 115109, 2007.

[143] G. Onida, L. Reining, and A. Rubio, "Electronic excitations: density-functional versus many-body greens-function approaches," *Reviews of Modern Physics*, vol. 74, no. 2, p. 601, 2002.

[144] M. Rohlfing and S. G. Louie, "Electron-hole excitations in semiconductors and insulators," *Physical review letters*, vol. 81, no. 11, p. 2312, 1998.

[145] S. Albrecht, L. Reining, R. Del Sole, and G. Onida, "Excitonic effects in the optical properties," *physica status solidi (a)*, vol. 170, no. 2, pp. 189–197, 1998.

[146] W. Hanke and L. Sham, "Many-particle effects in the optical spectrum of a semiconductor," *Physical Review B*, vol. 21, no. 10, p. 4656, 1980.

[147] E. Salpeter and H. A. Bethe, "A relativistic equation for bound-state problems," *Physical Review*, vol. 84, no. 6, p. 1232, 1951.

[148] M. Van Setten, R. Gremaud, G. Brocks, B. Dam, G. Kresse, and G. De Wijs, "Optical response of the sodium alanate system: GW_0-BSE calculations and thin film measurements," *Physical Review B*, vol. 83, no. 3, p. 035422, 2011.

[149] L. Sham and T. Rice, "Many-particle derivation of the effective-mass equation for the wannier exciton," *Physical Review*, vol. 144, no. 2, p. 708, 1966.

[150] S. Albrecht, L. Reining, R. Del Sole, and G. Onida, "Ab initio calculation of excitonic effects in the optical spectra of semiconductors," *Physical review letters*, vol. 80, no. 20, p. 4510, 1998.

[151] M. P. Molepo, *Computational study of the structural phase transitions and pressure dependent electronic structure of ZnO*. PhD thesis, School of Physics, University of the Witwatersrand, 2012.

[152] H. J. Monkhorst and J. D. Pack, "Special points for brillouin-zone integrations," *Physical Review B*, vol. 13, no. 12, p. 5188, 1976.

[153] D. Chadi and M. L. Cohen, "Special points in the brillouin zone," *Physical Review B*, vol. 8, no. 12, p. 5747, 1973.

[154] M. C. Payne, M. P. Teter, D. C. Allan, T. Arias, and J. Joannopoulos, "Iterative minimization techniques for ab initio total-energy calculations: molecular dynamics and conjugate gradients," *Reviews of Modern Physics*, vol. 64, no. 4, p. 1045, 1992.

[155] J. C. Phillips and L. Kleinman, "New method for calculating wave functions in crystals and molecules," *Physical Review*, vol. 116, no. 2, p. 287, 1959.

[156] M. L. Cohen and V. Heine, "The fitting of pseudopotentials to experimental data and their subsequent application," *Solid state physics*, vol. 24, pp. 37–248, 1970.

[157] N. Troullier and J. L. Martins, "Efficient pseudopotentials for plane-wave calculations," *Physical Review B*, vol. 43, no. 3, p. 1993, 1991.

[158] M. H. Cohen and J. C. Phillips, "Dielectric screening and self-consistent crystal fields," *Physical Review*, vol. 124, no. 6, p. 1818, 1961.

[159] B. J. Austin, V. Heine, and L. Sham, "General theory of pseudopotentials," *Physical Review*, vol. 127, no. 1, p. 276, 1962.

[160] L. Kleinman and D. Bylander, "Efficacious form for model pseudopotentials," *Physical Review Letters*, vol. 48, no. 20, p. 1425, 1982.

[161] T. Starkloff and J. Joannopoulos, "Local pseudopotential theory for transition metals," *Physical Review B*, vol. 16, no. 12, p. 5212, 1977.

[162] W. C. Topp and J. J. Hopfield, "Chemically motivated pseudopotential for sodium," *Physical Review B*, vol. 7, no. 4, p. 1295, 1973.

[163] P. E. Blöchl, "Projector augmented-wave method," *Physical Review B*, vol. 50, no. 24, p. 17953, 1994.

[164] J. Furthmüller, P. Käckell, F. Bechstedt, and G. Kresse, "Extreme softening of vanderbilt pseudopotentials: General rules and case studies of first-row and d-electron elements," *Physical Review B*, vol. 61, no. 7, p. 4576, 2000.

[165] G. Kresse and D. Joubert, "From ultrasoft pseudopotentials to the projector augmented-wave method," *Physical Review B*, vol. 59, no. 3, p. 1758, 1999.

[166] G. Kresse and J. Furthmüller, "Efficiency of ab-initio total energy calculations for metals and semiconductors using a plane-wave basis set," *Computational Materials Science*, vol. 6, no. 1, pp. 15–50, 1996.

[167] G. Kresse and J. Furthmüller, "Efficient iterative schemes for ab initio total-energy calculations using a plane-wave basis set," *Physical Review B*, vol. 54, no. 16, p. 11169, 1996.

[168] D. M. Ceperley and B. Alder, "Ground state of the electron gas by a stochastic method," *Physical Review Letters*, vol. 45, no. 7, p. 566, 1980.

[169] D. Sholl and J. A. Steckel, *Density functional theory: a practical introduction*. John Wiley & Sons, 2011.

[170] M. S. H. Suleiman, *A theoretical investigation of structural, electronic and optical properties of some group 10, 11 and 12 transition-metal nitrides*. PhD thesis, University of the Witwatersrand, 2013.

[171] G. Lehmann and M. Taut, "On the numerical calculation of the density of states and related properties," *physica status solidi (b)*, vol. 54, no. 2, pp. 469–477, 1972.

[172] P. E. Blöchl, O. Jepsen, and O. K. Andersen, "Improved tetrahedron method for brillouin-zone integrations," *Physical Review B*, vol. 49, no. 23, p. 16223, 1994.

[173] P. Vinet, J. H. Rose, J. Ferrante, and J. R. Smith, "Universal features of the equation of state of solids," *Journal of Physics: Condensed Matter*, vol. 1, no. 11, p. 1941, 1989.

[174] P. Vinet, J. R. Smith, J. Ferrante, and J. H. Rose, "Temperature effects on the universal equation of state of solids," *Physical Review B*, vol. 35, no. 4, p. 1945, 1987.

[175] A. F. Guillermet, "Thermodynamic properties of the generalized murnaghan equation of state of solids," *International journal of thermophysics*, vol. 16, no. 4, pp. 1009–1026, 1995.

[176] G. Grimvall, *Thermophysical properties of materials*. Elsevier, 1999.

[177] X. Zhang, G. Trimarchi, and A. Zunger, "Possible pitfalls in theoretical determination of ground-state crystal structures: The case of platinum nitride," *Physical Review B*, vol. 79, no. 9, p. 092102, 2009.

[178] N. W. Ashcroft and N. Mermin, "David: Solid state physics," *Saunders College, Philadelphia*, 1976.

[179] W. A. Harrison, *Electronic structure and the properties of solids: the physics of the chemical bond*. Courier Dover Publications, 2012.

[180] P. Philipsen and E. Baerends, "Cohesive energy of 3d transition metals: Density functional theory atomic and bulk calculations," *Physical Review B*, vol. 54, no. 8, p. 5326, 1996.

[181] V. N. Staroverov, G. E. Scuseria, J. Tao, and J. P. Perdew, "Tests of a ladder of density functionals for bulk solids and surfaces," *Physical Review B*, vol. 69, no. 7, p. 075102, 2004.

[182] M. G. Moreno-Armenta and G. Soto, "Stability and electronic structure of intrinsic and intercalated copper nitride alloys," *Solid State Sciences*, vol. 10, no. 5, pp. 573–579, 2008.

[183] Y. Mishin, D. Farkas, M. Mehl, and D. Papaconstantopoulos, "Interatomic potentials for monoatomic metals from experimental data and ab initio calculations," *Physical Review B*, vol. 59, no. 5, p. 3393, 1999.

[184] M. F. C. Ladd, *Introduction to physical chemistry*. Cambridge University Press, 1998.

[185] C. Colinet, "Ab-initio calculation of enthalpies of formation of intermetallic compounds and enthalpies of mixing of solid solutions," *Intermetallics*, vol. 11, no. 11, pp. 1095–1102, 2003.

[186] P. Atkins and J. De Paula, *Elements of physical chemistry*. Oxford University Press, 2013.

[187] H. B. Huntington, "The elastic constants of crystals," *Solid state physics*, vol. 7, pp. 213–351, 1958.

[188] R. P. Singh, R. K. Singh, and M. Rajagopalan, "Structural, elastic and electronic properties of neodymium chalcogenides (NdX, X= S, Se, Te): First principles study," *Chalcogenide Letters*, vol. 8, no. 5, pp. 325–340, 2011.

[189] M. Rabah, S. Benalia, D. Rached, B. Abidri, H. Rached, and G. Vergoten, "Prediction of stabilities phase and elastic properties of palladium carbide," *Computational Materials Science*, vol. 48, no. 3, pp. 556–562, 2010.

[190] L. Fast, J. Wills, B. Johansson, and O. Eriksson, "Elastic constants of hexagonal transition metals: Theory," *Physical Review B*, vol. 51, no. 24, p. 17431, 1995.

[191] M. Born, "On the stability of crystal lattices. i," in *Mathematical Proceedings of the Cambridge Philosophical Society*, vol. 36, pp. 160–172, Cambridge Univ Press, 1940.

[192] M. Born and K. Huang, "Dynamical theory of crystal lattices," 1954.

[193] G. Grimvall, B. Magyari-Köpe, V. Ozoliņš, and K. A. Persson, "Lattice instabilities in metallic elements," *Reviews of Modern Physics*, vol. 84, no. 2, p. 945, 2012.

[194] F. Mouhat and F.-X. Coudert, "Necessary and sufficient elastic stability conditions in various crystal systems," *Physical Review B*, vol. 90, no. 22, p. 224104, 2014.

[195] J. Van Kranendonk and G. Karl, "Theory of the rotational and vibrational excitations in solid parahydrogen, and frequency analysis of the infrared and raman spectra," *Reviews of Modern Physics*, vol. 40, no. 3, p. 531, 1968.

[196] E. Kaxiras, *Atomic and electronic structure of solids*. Cambridge University Press, 2003.

[197] L. Van Hove, "The occurrence of singularities in the elastic frequency distribution of a crystal," *Physical Review*, vol. 89, no. 6, p. 1189, 1953.

[198] S. K, "Chapter 2.2: Electrons," *International Tables for Crystallography, Volume D: Physical Properties of Crystals*, pp. 294–313, 2006.

[199] L. Sham and M. Schlüter, "Density-functional theory of the energy gap," *Physical Review Letters*, vol. 51, no. 20, p. 1888, 1983.

[200] R. Godby and R. Needs, "Metal-insulator transition in kohn-sham theory and quasiparticle theory," *Physical review letters*, vol. 62, no. 10, p. 1169, 1989.

[201] W. Knorr and R. Godby, "Quantum monte carlo study of density-functional theory for a semiconducting wire," *Physical Review B*, vol. 50, no. 3, p. 1779, 1994.

[202] W. Kohn, "Discontinuity of the exchange-correlation potential from a density-functional viewpoint," *Physical Review B*, vol. 33, no. 6, p. 4331, 1986.

[203] M. Dresselhaus and M. Dresselhaus, "Optical properties of solids," *Proc. of Int. School of Phys.Enrico Fermi*, p. 243, 1966.

[204] M. Gajdoš, K. Hummer, G. Kresse, J. Furthmüller, and F. Bechstedt, "Linear optical properties in the projector-augmented wave methodology," *Physical Review B*, vol. 73, no. 4, p. 045112, 2006.

[205] W. Schmidt, S. Glutsch, P. Hahn, and F. Bechstedt, "Efficient O (N 2) method to solve the Bethe-Salpeter equation," *Physical Review B*, vol. 67, no. 8, p. 085307, 2003.

[206] S. Baroni and R. Resta, "Ab initio calculation of the macroscopic dielectric constant in silicon," *Physical Review B*, vol. 33, no. 10, p. 7017, 1986.

[207] S. L. Adler, "Quantum theory of the dielectric constant in real solids," *Physical Review*, vol. 126, no. 2, p. 413, 1962.

[208] J. Harl, *The linear response function in density functional theory: Optical spectra and improved description of the electron correlation*. PhD thesis, University of Vienna, 2008.

[209] H. Ehrenreich and M. H. Cohen, "Self-consistent field approach to the many-electron problem," *Physical Review*, vol. 115, no. 4, p. 786, 1959.

[210] F. Mark, "Optical properties of solids," 2010.

[211] B.-C. Shih, Y. Xue, P. Zhang, M. L. Cohen, and S. G. Louie, "Quasiparticle band gap of ZnO: High accuracy from the conventional G_0W_0 approach," *Physical review letters*, vol. 105, no. 14, p. 146401, 2010.

[212] F. Tran and P. Blaha, "Accurate band gaps of semiconductors and insulators with a semilocal exchange-correlation potential," *Physical review letters*, vol. 102, no. 22, p. 226401, 2009.

[213] J. P. Perdew, M. Ernzerhof, and K. Burke, "Rationale for mixing exact exchange with density functional approximations," *The Journal of Chemical Physics*, vol. 105, no. 22, pp. 9982–9985, 1996.

[214] A. Tkatchenko and M. Scheffler, "Accurate molecular van der waals interactions from ground-state electron density and free-atom reference data," *Physical review letters*, vol. 102, no. 7, p. 073005, 2009.

[215] S. Grimme, "Density functional theory with london dispersion corrections," *Wiley Interdisciplinary Reviews: Computational Molecular Science*, vol. 1, no. 2, pp. 211–228, 2011.

[216] Y. Andersson, D. C. Langreth, and B. I. Lundqvist, "van der waals interactions in density-functional theory," *Physical review letters*, vol. 76, pp. 102–105, Jan 1996.

[217] G. S. Manyali, R. Warmbier, and A. Quandt, "First-principles study of Si_3N_2," *Computational Materials Science*, vol. 96, pp. 140–145, 2015.

[218] I. t. Brown and R. Shannon, "Empirical bond-strength–bond-length curves for oxides," *Acta Crystallographica Section A: Crystal Physics, Diffraction, Theoretical and General Crystallography*, vol. 29, no. 3, pp. 266–282, 1973.

[219] S. Baroni, S. De Gironcoli, A. Dal Corso, and P. Giannozzi, "Phonons and related crystal properties from density-functional perturbation theory," *Reviews of Modern Physics*, vol. 73, no. 2, p. 515, 2001.

[220] G. Henkelman, A. Arnaldsson, and H. Jónsson, "A fast and robust algorithm for Bader decomposition of charge density," *Computational Materials Science*, vol. 36, no. 3, pp. 354–360, 2006.

[221] W. Tang, E. Sanville, and G. Henkelman, "A grid-based Bader analysis algorithm without lattice bias," *Journal of Physics: Condensed Matter*, vol. 21, no. 8, p. 084204, 2009.

[222] E. Sanville, S. D. Kenny, R. Smith, and G. Henkelman, "Improved grid-based algorithm for Bader charge allocation," *Journal of computational chemistry*, vol. 28, no. 5, pp. 899–908, 2007.

[223] T. Cheiwchanchamnangij and W. R. Lambrecht, "Quasiparticle band structure calculation of monolayer, bilayer, and bulk mos 2," *Physical Review B*, vol. 85, no. 20, p. 205302, 2012.

[224] A. Ramasubramaniam, "Large excitonic effects in monolayers of molybdenum and tungsten dichalcogenides," *Physical Review B*, vol. 86, no. 11, p. 115409, 2012.

[225] N. G. Ondzibou, *Computational study of structural, electronic and optical properties of Molybdenum Chalcogenides*. PhD thesis, Faculty of Science, University of the Witwatersrand, Johannesburg, 2014.

[226] M. Palummo, M. Bernardi, and J. C. Grossman, "Exciton radiative lifetimes in two-dimensional transition metal dichalcogenides," *Nano letters*, 2015.

[227] H. Zeng and X. Cui, "An optical spectroscopic study on two-dimensional group-vi transition metal dichalcogenides," *Chemical Society Reviews*, vol. 44, no. 9, pp. 2629–2642, 2015.

[228] D. O. Dumcenco, H. Kobayashi, Z. Liu, Y.-S. Huang, and K. Suenaga, "Visualization and quantification of transition metal atomic mixing in $Mo_{1-x}W_xS_2$ single layers," *Nature communications*, vol. 4, p. 1351, 2013.

[229] J. Kang, S. Tongay, J. Li, and J. Wu, "Monolayer semiconducting transition metal dichalcogenide alloys: Stability and band bowing," *Journal of Applied Physics*, vol. 113, no. 14, p. 143703, 2013.

[230] Y.-W. Son, M. L. Cohen, and S. G. Louie, "Electric field effects on spin transport in defective metallic carbon nanotubes," *Nano letters*, vol. 7, no. 11, pp. 3518–3522, 2007.

[231] L. Kou, C. Tang, W. Guo, and C. Chen, "Tunable magnetism in strained graphene with topological line defect," *ACS nano*, vol. 5, no. 2, pp. 1012–1017, 2011.

[232] Y. Mao and J. Zhong, "Structural, electronic and magnetic properties of manganese doping in the upper layer of bilayer graphene," *Nanotechnology*, vol. 19, no. 20, p. 205708, 2008.

[233] D. Ma, Z. Lu, W. Ju, and Y. Tang, "First-principles studies of bn sheets with absorbed transition metal single atoms or dimers: stabilities, electronic structures, and magnetic properties," *Journal of Physics: Condensed Matter*, vol. 24, no. 14, p. 145501, 2012.

[234] J. Honolka, A. Khajetoorians, V. Sessi, T. Wehling, S. Stepanow, J.-L. Mi, B. B. Iversen, T. Schlenk, J. Wiebe, N. Brookes, *et al.*, "In-plane magnetic anisotropy of fe atoms on bi_2se_3 (111)," *Physical review letters*, vol. 108, no. 25, p. 256811, 2012.

[235] J.-M. Zhang, W. Zhu, Y. Zhang, D. Xiao, and Y. Yao, "Tailoring magnetic doping in the topological insulator bi_2se_3," *Physical review letters*, vol. 109, no. 26, p. 266405, 2012.

[236] S. Bhattacharyya and A. K. Singh, "Semiconductor-metal transition in semiconducting bilayer sheets of transition-metal dichalcogenides," *Physical Review B*, vol. 86, no. 7, p. 075454, 2012.

[237] E. Scalise, M. Houssa, G. Pourtois, V. Afanasev, and A. Stesmans, "Strain-induced semiconductor to metal transition in the two-dimensional honeycomb structure of mos2," *Nano Research*, vol. 5, no. 1, pp. 43–48, 2012.

[238] A. Ramasubramaniam, D. Naveh, and E. Towe, "Tunable band gaps in bilayer transition-metal dichalcogenides," *Physical Review B*, vol. 84, no. 20, p. 205325, 2011.

[239] K. Dolui, C. D. Pemmaraju, and S. Sanvito, "Electric field effects on armchair mos2 nanoribbons," *Acs Nano*, vol. 6, no. 6, pp. 4823–4834, 2012.

[240] W. Hicks, "Semiconducting behavior of substituted tungsten diselenide and its analogues," *Journal of The Electrochemical Society*, vol. 111, no. 9, pp. 1058–1065, 1964.

[241] D. L. Greenaway and R. Nitsche, "Preparation and optical properties of group IV–VI_2 chalcogenides having the CdI_2 structure," *Journal of Physics and Chemistry of Solids*, vol. 26, no. 9, pp. 1445–1458, 1965.

[242] L. Roubi and C. Carlone, "Resonance raman spectrum of HfS_2 and ZrS_2," *Physical Review B*, vol. 37, no. 12, p. 6808, 1988.

[243] K. Terashima and I. Imai, "Indirect absorption edge of ZrS_2 and HfS_2," *Solid State Communications*, vol. 63, no. 4, pp. 315–318, 1987.

[244] C. Gaiser, T. Zandt, A. Krapf, R. Serverin, C. Janowitz, and R. Manzke, "Band-gap engineering with HfS_xSe_{2-x}," *Physical Review B*, vol. 69, no. 7, p. 075205, 2004.

[245] S. Bayliss and W. Liang, "Symmetry dependence of optical transitions in group 4b transition metal dichalcogenides," *Journal of Physics C: Solid State Physics*, vol. 15, no. 6, p. 1283, 1982.

[246] H. Guo, N. Lu, L. Wang, X. Wu, and X. C. Zeng, "Tuning electronic and magnetic properties of early transition-metal dichalcogenides via tensile strain," *The Journal of Physical Chemistry C*, vol. 118, no. 13, pp. 7242–7249, 2014.

[247] H. Myron, B. Harmon, and F. Khumalo, "The electronic structure of $ZrSe_3$," *Journal of Physics and Chemistry of Solids*, vol. 42, no. 4, pp. 263–267, 1981.

[248] J. P. Watt, "Hashin-shtrikman bounds on the effective elastic moduli of polycrystals with monoclinic symmetry," *Journal of Applied Physics*, vol. 51, no. 3, pp. 1520–1524, 1980.

[249] Z. Wu, E. j. Zhao, H. Xiang, X. f. Hao, X. j. Liu, and J. Meng, "Crystal structures and elastic properties of superhard IrN_2 and IrN_3 from first principles," *Physical Review B*, vol. 76, no. 5, p. 054115, 2007.

[250] Y.-C. Ding, M. Chen, and W. Wu, "Phase stability, elasticity, hardness and the minimum thermal conductivity of Si_2N_2O polymorphs from first principles calculations," *Physica B: Condensed Matter*, vol. 449, no. 0, pp. 236–245, 2014.

[251] W. Schairer and M. Shafer, "Growth and optical absorption spectra of the layer-type trichalcogenides ZrS_3 and HfS_3," *physica status solidi (a)*, vol. 17, no. 1, pp. 181–184, 1973.

[252] P. Lee, G. Said, R. Davis, and T. Lim, "On the optical properties of some layer compounds," *Journal of Physics and Chemistry of Solids*, vol. 30, no. 12, pp. 2719–2729, 1969.

[253] H. Starnberg, H. Brauer, and H. Hughes, "Photoemission studies of the conduction band filling in $Ti_{1.05}S_2$ and cs-intercalated TiS_2 and $ZrSe_2$," *Journal of Physics: Condensed Matter*, vol. 8, no. 9, p. 1229, 1996.

[254] M. Moustafa, T. Zandt, C. Janowitz, and R. Manzke, "Growth and band gap determination of the ZrS_xSe_{2-x} single crystal series," *Physical Review B*, vol. 80, no. 3, p. 035206, 2009.

[255] A. Borghesi, C. Chen-Jia, G. Guizzetti, L. Nosenzo, E. Reguzzoni, A. Stella, and F. Lévy, "Thermoreflectance studies of transition-metal dichalcogenides between 1 and 9 ev," *Physical Review B*, vol. 33, no. 4, p. 2422, 1986.

[256] Y. Li, J. Kang, and J. Li, "Indirect-to-direct band gap transition of the ZrS_2 monolayer by strain: first-principles calculations," *RSC Advances*, vol. 4, no. 15, pp. 7396–7401, 2014.

[257] G. Perluzzo, S. Jandl, and P. Girard, "Optical spectra of ZrS_3," *Canadian Journal of Physics*, vol. 58, no. 1, pp. 143–145, 1980.

[258] S. Kurita, M. Tanaka, and F. Lévy, "Optical spectra near the band edge of ZrS_3 and $ZrSe_3$," *Physical Review B*, vol. 48, no. 3, p. 1356, 1993.

[259] T. Adachi, T. Goto, and Y. Nishina, "Photoluminescence from excitons in ZrS_3," *Journal of Luminescence*, vol. 21, no. 2, pp. 169–175, 1980.

[260] K. Patel, R. Vaidya, and S. Patel, "Microstructural analysis of zirconium triselenide single crystals," *Indian Journal of Pure and Applied Physics*, vol. 45, no. 6, p. 514, 2007.

[261] K. Patel, J. Prajapati, R. Vaidya, and S. Patel, "Optical and electrical properties of $ZrSe_3$ single crystals grown by chemical vapour transport technique," *Bulletin of Materials Science*, vol. 28, no. 5, pp. 405–410, 2005.

[262] G. Xiuying, G. Fengsheng, T. Yamaguchi, H. Kan, and M. Kumagawa, "Dependence of energy band gap and lattice constant of III-V semiconductors on electronegativity difference of the constituent elements," *Crystal Research and Technology*, vol. 27, no. 8, pp. 1087–1096, 1992.

[263] I. Ferrer, J. Ares, J. Clamagirand, M. Barawi, and C. Sánchez, "Optical properties of titanium trisulphide TiS_3 thin films," *Thin Solid Films*, vol. 535, pp. 398–401, 2013.

[264] Y. Jin, X. Li, and J. Yang, "Single layer of MX_3 (M= Ti, Zr; X= S, Se, Te): a new platform for nano-electronics and optics," *Phys. Chem. Chem. Phys.*, vol. 17, pp. 18665–18669, 1986.

[265] M. Fleet, S. Harmer, X. Liu, and H. Nesbitt, "Polarized x-ray absorption spectroscopy and XPS of TiS_3: S K-and Ti L-edge XANES and S and Ti 2p XPS," *Surface science*, vol. 584, no. 2, pp. 133–145, 2005.

[266] N. Ashcroft, "Nd mermin solid state physics," *Saunders College, Philadelphia*, 1976.

[267] G. S. Manyali, R. Warmbier, and A. Quandt, "First-principles studies of the structural, electronic and optical properties of dinitrides CN_2, SiN_2 and GeN_2," *Computational Materials Science*, 2014.

[268] M. S. H. Suleiman and D. P. Joubert, "Theoretical calculations on the structural, electronic, and optical properties of bulk silver nitrides," *physica status solidi (b)*, pp. n/a–n/a, 2015.

[269] W. Jeitschko and R. Rühl, "Synthesis and crystal structure of diamagnetic ReP_4, a polyphosphide with Re–Re pairs," *Acta Crystallographica Section B: Structural Crystallography and Crystal Chemistry*, vol. 35, no. 9, pp. 1953–1958, 1979.

[270] C. Ho, P. Liao, Y. Huang, and K. Tiong, "Temperature dependence of energies and broadening parameters of the band-edge excitons of ReS_2 and $ReSe_2$," *Physical Review B*, vol. 55, no. 23, p. 15608, 1997.

[271] D. Y. Qiu, H. Felipe, and S. G. Louie, "Optical spectrum of MoS_2: many-body effects and diversity of exciton states," *Physical review letters*, vol. 111, no. 21, p. 216805, 2013.

[272] R. Ruehl and W. Jeitschko, "Preparation and crystal structure of dirhenium pentaphosphide, Re_2P_5, a diamagnetic semiconducting polyphosphide with rhomboidal Re_4 clusters," *Inorganic Chemistry*, vol. 21, no. 5, pp. 1886–1891, 1982.

[273] S. Rundqvist, "The crystal structure of Re_2P," *Acta Chemica Scandinavica*, vol. 15, no. 2, pp. 342–348, 1961.

[274] S. Rundqvist, "The crystal structure of Re_3P_4," *Acta Chem. Scand*, vol. 20, no. 8, p. 5, 1966.

[275] R. Gurin, M. Potel, and M. Sergent, "Nouveau cluster plan re4: Le binaire Re_12P_26," *Materials Research Bulletin*, vol. 14, no. 10, pp. 1335 – 1344, 1979.

[276] E. Zhao and Z. Wu, "Electronic and mechanical properties of 5d transition metal mononitrides via first principles," *Journal of Solid State Chemistry*, vol. 181, no. 10, pp. 2814–2827, 2008.

[277] Y. Wang, T. Yao, H. Li, J. Lian, J. Li, Z. Li, J. Zhang, and H. Gou, "Structural stability, phase transition, and mechanical and electronic properties of transition metal nitrides MN (M= Tc, Re, Os, and Ir): First-principles calculations," *Computational Materials Science*, vol. 56, pp. 116–121, 2012.

[278] R. Rajeswarapalanichamy, K. Iyakutti, *et al.*, "First-principles study of electronic structure of transition metal nitride: ReN under normal and high pressure," *Physica B: Condensed Matter*, vol. 406, no. 17, pp. 3303–3307, 2011.

[279] S.-H. Jhi, J. Ihm, S. G. Louie, and M. L. Cohen, "Electronic mechanism of hardness enhancement in transition-metal carbonitrides," *Nature*, vol. 399, no. 6732, pp. 132–134, 1999.

[280] H.-R. Lei, J. Zhu, Y.-J. Hao, L. Zhang, B.-R. Yu, L.-Q. Chen, and Y.-C. Zou, "Theoretical study of electronic structure, phase transition, elastic, and thermodynamic properties of ReN," *Physica B: Condensed Matter*, vol. 458, pp. 124–131, 2015.

[281] F. Birch, "Finite elastic strain of cubic crystals," *Physical Review*, vol. 71, no. 11, p. 809, 1947.

[282] A. J. Cohen, P. Mori-Sánchez, and W. Yang, "Insights into current limitations of density functional theory," *Science*, vol. 321, no. 5890, pp. 792–794, 2008.

[283] F. Tran, R. Laskowski, P. Blaha, and K. Schwarz, "Performance on molecules, surfaces, and solids of the wu-cohen GGA exchange-correlation energy functional," *Physical Review B*, vol. 75, no. 11, p. 115131, 2007.

[284] P. Haas, F. Tran, and P. Blaha, "Calculation of the lattice constant of solids with semilocal functionals," *Physical Review B*, vol. 79, no. 8, p. 085104, 2009.

[285] J. P. Perdew, A. Ruzsinszky, G. I. Csonka, O. A. Vydrov, G. E. Scuseria, L. A. Constantin, X. Zhou, and K. Burke, "Restoring the density-gradient expansion for exchange in solids and surfaces," *Physical Review Letters*, vol. 100, no. 13, p. 136406, 2008.

[286] M. Born and K. Huang, *Dynamical Theory of Crystal Lattices Oxford Classic Texts in the Physical Sciences*. Clarendon Press, Oxford, 1988.

[287] S. Furuseth and H. Fjellvag, "Re-examination of the crystal structure of $ZrTe_3$," *Acta Chemica Scandinavica*, vol. 45, no. 7, pp. 694–697, 1991.

[288] F. Khumalo and H. Hughes, "Reflection spectroscopy of $ZrSe_3$-type family of layer compounds in the vacuum ultraviolet region," *Physical Review B*, vol. 22, no. 4, p. 2078, 1980.

[289] M. Usuda, N. Hamada, T. Kotani, and M. van Schilfgaarde, "All-electron GW calculation based on the LAPW method: Application to wurtzite ZnO," *Physical Review B*, vol. 66, no. 12, p. 125101, 2002.